Brief Bibliography of Radiative Transfer Papers for Dense Laboratory Plasmas

G.A. Moses

February 1987

FPA-87-1

FUSION POWER ASSOCIATES

2 Professional Drive, Suite 248
Gaithersburg, Maryland 20879
(301) 258-0545

1500 Engineering Drive
Madison, Wisconsin 53706
(608) 263-2308

BRIEF BIBLIOGRAPHY OF RADIATIVE TRANSFER PAPERS FOR DENSE LABORATORY PLASMAS

G.A. Moses

Fusion Power Associates
6515 Grand Teton Plaza
Madison, WI 53719

February 1987

FPA-87-1

This is a short summary of literature from the NRL radiation physics group concerning the transport of x-ray radiation from dense plasmas. This group is quite likely the strongest group in the U.S. in the area as it is applied to laboratory plasmas.

We have accumulated 13 papers that relate to the problem of radiation line transport (see Appendix A). These papers deal with either the theory of transport methods or the application of these methods to specific plasma conditions that relate to laboratory experiments. This should not be considered a comprehensive literature search, but only a first step toward understanding and selecting a method for implementation in analyzing KALIF generated plasmas. The methods are generally escape probability based and should be quite familiar to researchers in the nuclear reactor physics community.

The papers related to methods are:

J.P. Apruzese, "An Analytic Voigt Profile Escape Probability Approximation," J. Quant. Spectrosc. Radiat. Transfer 54, 447-452 (1985).

J.P. Apruzese, "Direct Solution of the Equation of Transfer Using Frequency- and Angle-Average Photon Escape Probabilities for Spherical and Cylindrical Geometries," J. Quant. Spectrosc. Radiat. Transfer 25, 419-425 (1981).

J.P. Apruzese, J. Davis, D. Duston and K.G. Whitney, "Direct Solution of the Equation of Transfer Using Frequency- and Angle-Averaged Photon Escape Probabilities, with Application to a Multistage, Multilevel Aluminum Plasma," J. Quant. Spectrosc. Radiat. Transfer 23, 479-487 (1980).

The papers related to applications are:

F.L. Cochran, J. Davis and J.P. Apruzese, "X-Ray Lasing in a Na/Ne Plasma Environment," J. Appl. Phys. 57, 27 (1985).

J.P. Apruzese, J. Davis and K.G. Whitney, "Plasma Conditions Required for Attainment of Maximum Gain in Resonantly Photo-Pumped Aluminum XII and Neon IX," J. Appl. Phys. 53, 4020 (1982).

J.P. Apruzese and J. Davis, "Radiative Properties of Puffed-gas Mixtures: The Case of Optically Thick Plasmas Composed of Two Elements with Similar Atomic Numbers," J. Appl. Phys. 57, 4349 (1985).

D. Duston, R.W. Clark, J. Davis and J.P. Apruzese, "Radiation Energetics of a Laser Produced Plasma," Phys. Rev. A 27, 1441 (1983).

J.P. Apruzese and J. Davis, "Kinetics of X-Ray Lasing by Resonant Photoexcitation: Fundamentals of Pumping Power and Gain for the Na X - Ne IX System," Phys. Rev. A 31, 2976 (1985).

K.G. Whitney, J. Davis and J.P. Apruzese, "Influence of Broadband Photocoupling on K-shell Excitation in Aluminum," Phys. Rev. A 22, 2196 (1980).

J.P. Apruzese, J. Davis, D. Duston and R.W. Clark, "Influence of Lyman-Series Filne-Structure Opacity on the K-shell Spectrum and Level Populations of Low-to-Medium Z Plasmas," Phys. Rev. A 29, 246 (1984).

J.P. Apruzese, P.C. Kepple, K.G. Whitney, J. Davis and D. Duston, "Collisional-Radiative-Equilibrium Spectroscopic Diagnosis of a Compressed, Optically Thick Neon Plasma," Phys. Rev. A 24, 1001 (1981).

J.P. Apruzese, J. Davis and K.G. Whitney, "Interpretation of the Spatial and Spectral Intensities of Optically Thick Resonance Lines Emitted from a Spherical Laser-Heated Plasma," J. Appl. Phys. 48, 667 (1977).

Interpretation of the spatial and spectral intensities of optically thick resonance lines emitted from a spherical laser-heated plasma

J. P. Apruzese,* J. Davis, and K. G. Whitney†

Naval Research Laboratory, Plasma Physics Division, Washington, D. C. 20375
(Received 2 September 1976)

We present interpretations of computed spatial and spectral intensities of the principal resonance lines emitted from a spherical laser-heated aluminum plasma. Our interpretations are based upon frequency-by-frequency solutions for the radiation transport equation which are coupled to a spherically symmetric time-dependent aluminum plasma model. This model solves the coupled equations for ion and electron temperatures and densities, atomic level populations, and fluid velocities for varying assumptions of energy deposition within the plasma. We find that the He K_α and H K_α resonance line profiles and intensities of the AlXII and AlXIII ions emitted during deposition are sensitive to the spatial plasma heating profile. By solving for the emitted H-like K_α line intensities along various lines of sight we generate theoretical "pinhole photographs" of the emission of this line. These spatial H-like K_α profiles are also very sensitive to the assumed laser deposition distribution. We have also compared our numerical results with those given by the escape-factor formula of Holstein. and we present an escape formula which is more accurate than Holstein's for large optical depths when the photon sources are approximately uniformly distributed in the plasma sphere.

PACS numbers: 52.25.Ps, 52.50.Jm, 52.70.—m

I. INTRODUCTION

The radiation emitted from laser-heated plasmas is a major diagnostic tool for obtaining information on the properties of the emitting plasma. The transport of radiative energy may also, in some cases, strongly influence the energy balance and evolution of the plasma. Of course in a pure DT plasma, bremsstrahlung will be the dominant form of radiation and it is not expected to decisively influence the energetics. Bremsstrahlung preheat, however, may become important when the DT is enclosed in microballoons of higher-Z material.[1] These higher-Z materials will also produce abundant line and recombination radiation, which can influence the energy balance and dynamics of the plasma.[2] One particular aspect of the energetics is the efficiency with which the original laser energy is converted to x rays by the plasma. It has been pointed out previously[3] that the effects of line self-absorption and quenching must be taken into account in an optically thick plasma to compute the conversion efficiency accurately. To provide a quantitative calculation of these phenomena and a diagnostic basis for interpreting optically thick line radiation emitted by laser-heated plasmas, we have incorporated a radiation transport scheme into our inhomogeneous hot-spot model.[4] In Sec. II the radiation transport scheme is described, and results for line profiles and intensities are presented. In Sec. III we present calculations of the spatial distributions of line radiation, and discuss the diagnostic value of limb-darkening (or limb-brightening) measurements in various lines. In Sec. IV the work is summarized and further ongoing research in laser-plasma radiative transfer is described.

II. SPECTRAL PROFILES AND LINE INTENSITIES

In the present investigation we seek to determine how the resonance line profiles (and intensities) depend upon various properties of the emitting plasma. We have shown previously[5,6] that an accurate evaluation of the line intensities requires a frequency-by-frequency solution of the transfer equation to compute the profile, followed by an integration under the profile. The use of escape factors for the lines may underestimate the emitted intensities in spherical geometry by a large factor.[6] Thus, in seeking to explain emitted intensities, we must analyze the factors which affect the underlying line profile. These factors are the line source function S_ν (its absolute value and gradient) and the line Doppler width and optical depth as a function of distance through the plasma. The line will contain information about these variables.

In solving the equation of radiative transport at each frequency we have now combined a diffusion (or Eddington) approximation with a ray-tracing scheme similar to one previously described.[7] When the plasma optical depth at line center becomes large, the radiation field in the interior of the plasma at frequencies close to line center is very nearly isotropic. The Eddington approximation[8] $K_\nu = \frac{1}{3}J_\nu$ is employed whenever these conditions are met. However, as we approach the outer boundary of the plasma, the isotropy of the radiation field is destroyed and this approximation is no longer appropriate. To take account of this fact the radiation field is computed along a series of rays in these optically thin or grey outer boundary regions. Each ray is characterized by the angle θ with which it intersects a radial at the "boundary" between the thick and thin regions. (The location of this boundary is, of course, frequency dependent.) If the source function S_ν is expanded in a Taylor series at the boundary between the thick and thin regions, and the resulting expression substituted into the formal solution to the transport equation, it is straightforward to show that[9]

$$I_\nu(\tau_\nu, \mu) = S_\nu(\tau_\nu) + \sum_{n=1}^{\infty} \mu^n \frac{d^n S_\nu}{d\tau_\nu^n}, \quad (1)$$

where τ_ν is the optical depth at the point of interest, measured radially inward, and I_ν is the specific intensity of outward-traveling radiation along the ray characterized by $\mu = \cos\theta$. The $I_\nu(\mu)$ of Eq. (1) was taken to be the specific intensity fed to each μ ray by the thick plasma interior to the outer boundary region. In practice, little or no accuracy is gained by using terms past $n=2$. When the total plasma optical depth is less than ~10, a ray-tracing network is used throughout the entire sphere. At frequencies which are very thin ($\tau_\nu \lesssim 0.05$) reabsorption can be ignored. At these frequencies the radiation transport reduces to a computation of the geometrical dilution of the radiation field caused by the radial divergence of spherical symmetry.

Radiation transport calculations have been carried out using ten frequency groups in each of the Al XII $1s^2$-$1s\,2p$ and Al XIII $1s$-$2p$ transitions. These will be referred to here as the "He-like" and "H-like" resonance lines. Feautrier's[10] method has been used to compute I_ν along each ray, and the three transport moments J_ν, H_ν, and K_ν are computed at each step by a numerical integration over angle. We note that the radiation energy density is $4\pi J_\nu/c$, the net radial flux is $4\pi H_\nu$, and the radiation pressure is $4\pi K_\nu/c$ in this notation. Using the Eddington approximation in optically thick regions represents a significant savings in computation time over the pure ray-tracing scheme previously used.[5] No angular integration is now necessary in the optically thick regions, which represent a large fraction of the plasma volume for most of the critical first 200 ps of the plasma's history. The power series of Eq. (1) allows coupling of arbitrarily high accuracy between the thick interior solution and the ray network of the outer boundary regions. The detailed mathematics of the radiation transport calculations have been described elsewhere.[11]

Once evaluated, the radiation field is coupled into the basic equations governing the behavior of the plasma.[4] These equations are

$$\partial_t \rho + \nabla\cdot(\rho \mathbf{v}) = 0, \quad (2)$$

$$\partial_t(\rho \mathbf{v}) + \nabla\cdot(\rho \mathbf{v}\mathbf{v}) = -\nabla p, \quad (3)$$

$$\partial_t(\tfrac{3}{2}N_i k T_i) + \nabla\cdot(\tfrac{3}{2}N_i k T_i \mathbf{v}) = -p_i \nabla\cdot\mathbf{v} + \dot{Q}_{ei}, \quad (4)$$

$$\partial_t(\tfrac{3}{2}N_e k T_e + \tfrac{3}{2}N_i k T_i + E_i + \tfrac{1}{2}\rho v^2) + \nabla\cdot[(\tfrac{3}{2}N_e k T_e + \tfrac{3}{2}N_i k T_i + E_i + \tfrac{1}{2}\rho v^2)\mathbf{v}] = S_e - \nabla\cdot(\mathbf{q}_e + p\mathbf{v}) - R_i - R_b, \quad (5)$$

$$\partial_t N_u + \nabla\cdot(N_u \mathbf{v}) = \sum_\nu W_{u\nu} N_\nu, \quad (6)$$

where $\nabla = \hat{e}_r \partial_r$. In these equations, N_i is the ion number density ($=\sum_u N_u$), ρ is the plasma mass density, p is the total pressure, S_e is the laser power density (assumed absorbed by the electrons), which is a prescribed function of time, and R_b and R_i represent the local rates of bremsstrahlung, and line and recombination losses, respectively. $\dot{Q}_{ei}$ represents the local flow of energy between electrons and ions due to any temperature differences between them, and $\mathbf{q}_e$ is the electron heat flow vector, equal to $-K_e \nabla T_e$.

The calculated radiation field enters the above coupled equations directly at two points—via the R_i term in Eq. (5) and in the rate matrix $W_{u\nu}$ of Eq. (6). That part of R_i which represents line losses is calculated from the moment H_ν at each frequency in the line, and integrated over frequency. More specifically, we have divided the plasma sphere into ten shells. Within each shell, the properties of the plasma are assumed homogeneous. If r_j and r_{j+1} are the boundary radii of the jth plasma shell, we have, for the jth shell

$$R_i(\text{line losses}) = (4\pi/V_j)\int_{\text{line}} (4\pi r_{j+1}^2 H_{\nu,j+1} - 4\pi r_j^2 H_{\nu,j})\, d\nu, \quad (7)$$

where V_j is the volume of the jth plasma shell, and the frequency intervals of the integrals extend over the profiles of each line considered in the model. The calculated radiation field enters the rate matrix $W_{u\nu}$ of Eq. (6) in the terms representing transitions from the ground states to the excited states of each line considered, via radiative excitation. For example, for excitation of the $2p$ level from the $1s$ level of Al XIII we have

$$W_{2p\text{-}1s} = W_{\text{collis}} + W_{\text{radiat}},$$

where

$$W_{2p\text{-}1s}(\text{radiative}) = \int_{\substack{\text{line}\\ \text{profile}}} \frac{4\pi J_\nu}{h\nu} k_\nu\, d\nu, \quad (8)$$

where k_ν is the linear line absorption coefficient (in cm^{-1}) corrected for stimulated emission. During a typical calculation described below, the radiation field is recalculated and the moments J_ν and H_ν fed into the coupled equations more than 3000 times as the plasma evolves. Changing the rate of recalculation has shown this update rate to be more than sufficient for high accuracy.

A principal effect of line self-absorption is that photons which are reabsorbed may be destroyed in the act of scattering by ionization or collisional deexcitation. This reduces the line's intensity over that which would be calculated if no reabsorption were assumed. To take account of this reabsorption, an approximate escape probability formula developed by Holstein[12] is often used. In a spherically symmetric medium, it is sometimes assumed in applying Holstein's formula that the photon escape is characterized by an average path length equal to the sphere radius. If the optical depth at line center along a radius is τ_0, Holstein's formula predicts an average photon escape probability P_H such that

$$P_H = \frac{1}{\tau_0(\pi \ln\tau_0)^{1/2}}. \quad (9)$$

It is clear that if most of the photons originate near the sphere center, Holstein's formula will be quite accurate. This situation will prevail if most of the plasma heating, by compression or laser deposition, and hence most of the line excitation, occurs in the plasma interior. However, if the heating is uniform or concentrated near the outer boundary of the plasma sphere,

most of the photon creation will not occur near sphere center, and some of the photons will be able to escape easily by traveling radially outward along a path length far shorter than the radius. This effect leads to a much higher escape probability for uniform or exterior deposition than that given by Holstein's formula, as reported earlier[6] (Fig. 1). To obtain an analytic estimate for the escape probability when the sources are not concentrated near the sphere center we may consider a sphere of unit radius with a photon source function equal to unity throughout the sphere. The optical depth at line center along the radius is τ_0. Letting x stand for the frequency displacement from line center in Doppler widths, and adopting the radiative transfer notation of Chandrasekhar,[8] we find that the total photon energy escaping the sphere is

$$E_{\text{escape}} = 4\pi \int_{-\infty}^{+\infty} 2\pi \int_{-1}^{+1} I_x(\mu, r=1)\,\mu\, d\mu\, dx. \tag{10}$$

Using the well-known solution for I_x along a finite uniform source function ray and recognizing that there is no incident radiation upon the sphere [$I_x(-1 \le \mu \le 0,\ r=1)=0$] we find

$$E_{\text{escape}} = 8\pi^2 \int_{-\infty}^{+\infty} \int_{0}^{+1} \{1-\exp[-2\mu\tau_0 \exp(-x^2)]\}\mu\, d\mu\, dx. \tag{11}$$

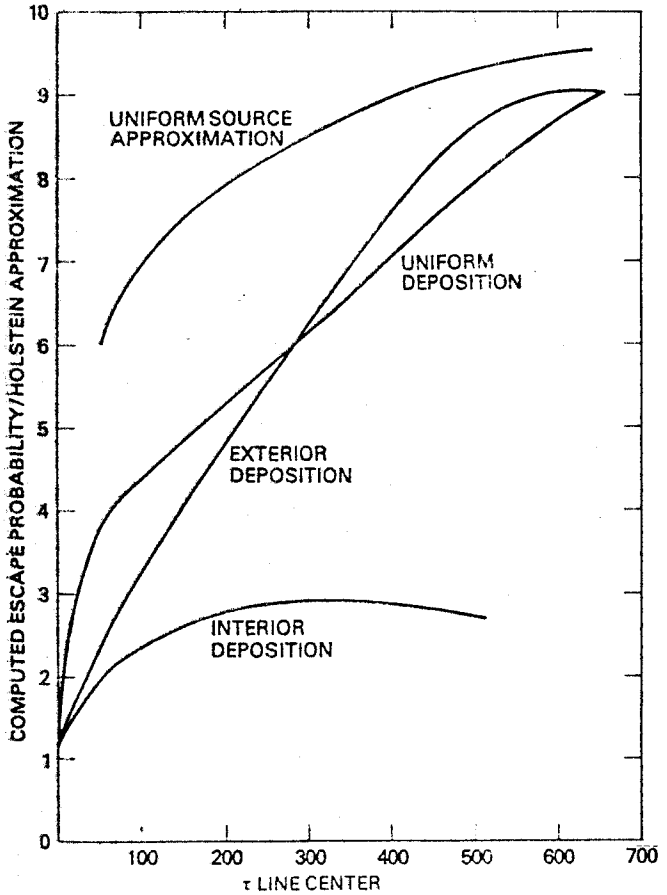

FIG. 1. The ratio of numerically calculated escape probabilities for a spherical laser plasma to that given by Holstein's formula. Results are given for cases of uniform, exterior, and interior laser energy deposition. The top curve represents the analytic estimate for the escape probability for uniform sources given by Eq. (15a).

The μ integral can be evaluated in closed form, but not the resulting x integral. To approximate the integral in the optically thick limit we note that, for *optically thick frequencies*,

$$E_{\text{escape}}(x) \approx 4\pi^2. \tag{12}$$

We now make the assumption (which is quite accurate at high τ_0) that Eq. (12) is valid for $\tau(x) \ge 1$, and that $E_{\text{escape}}(x)=0$ for $\tau(x)<1$. This corresponds to a line profile that is flat topped for frequencies of optical depth unity or greater and zero for the far wings where $\tau(x)<1$. Essentially we are ignoring those few photons escaping in the far wings of the line. Under this assumption, we have

$$E_{\text{escape}} = \int_{x=-(\ln\tau_0)^{1/2}}^{x=+(\ln\tau_0)^{1/2}} 4\pi^2\, dx = 8\pi^2 (\ln\tau_0)^{1/2}, \tag{13}$$

where the integral is confined to the core of the line such that $\tau_0 \exp(-x^2) \ge 1$. The total photon energy created internally in the plasma unit sphere is

$$\begin{aligned} E_{\text{created}} &= (\tfrac{4}{3}\pi)4\pi \int_{-\infty}^{+\infty} j_x\, dx \\ &= \tfrac{16}{3}\pi^2 \int_{-\infty}^{+\infty} \tau_0 \exp(-x^2)\, dx \\ &= \tfrac{16}{3}\pi^{5/2}\tau_0. \end{aligned} \tag{14}$$

Thus, ignoring the difference in photon energy across the line profile we find

$$P_{\text{uniform}} = \frac{8\pi^2 \ln\tau_0}{\frac{16}{3}\pi^{5/2}\tau_0} = \frac{3(\ln\tau_0)^{1/2}}{2\tau_0(\pi)^{1/2}} \tag{15a}$$

and

$$P_{\text{uniform}}/P_H = \tfrac{3}{2}\ln\tau_0. \tag{15b}$$

Equations (15a) and (15b) show that the escape probability for uniformly distributed photon sources in spherical geometry is greater than that given by Holstein's formula with the sphere radius as the characteristic escape distance. We have plotted the escape probability of Eq. (15a) in Fig. 1 in a comparison with the Holstein approximation and with the actual photon escape probabilities calculated using our numerical transport scheme at various optical depths during the aluminum plasma's evolution. It is easily seen that the present formula is preferable to Holstein's when the heating is uniform or mostly exterior. The present formula is seen to be quite accurate as τ_0 becomes greater than ~500, and more accurate than Holstein's (for uniform or exterior heating) for all $\tau_0 \ge 70$. Holstein's formula is, of course, more appropriate when the sources are mostly near $r=0$.

We have calculated time-dependent H-like and He-like resonance line profiles for varying assumptions for the region of plasma heating and for cases of uniform initial density and increasing plasma density near $r=0$. In each case we have deposited 32 J of energy into a 320-μ-radius aluminum sphere at an ion density of 7.7×10^{19} cm^{-3} with a 50-ps Gaussian pulse peaking at $t=50$ ps. Since the line profiles and intensities are sensitive to the spatial distribution of the energy deposition, we will concentrate first on the line emission which takes place during the time of deposition. Figures 2 and 3 present the time integral (to 100 ps) of the H-like and

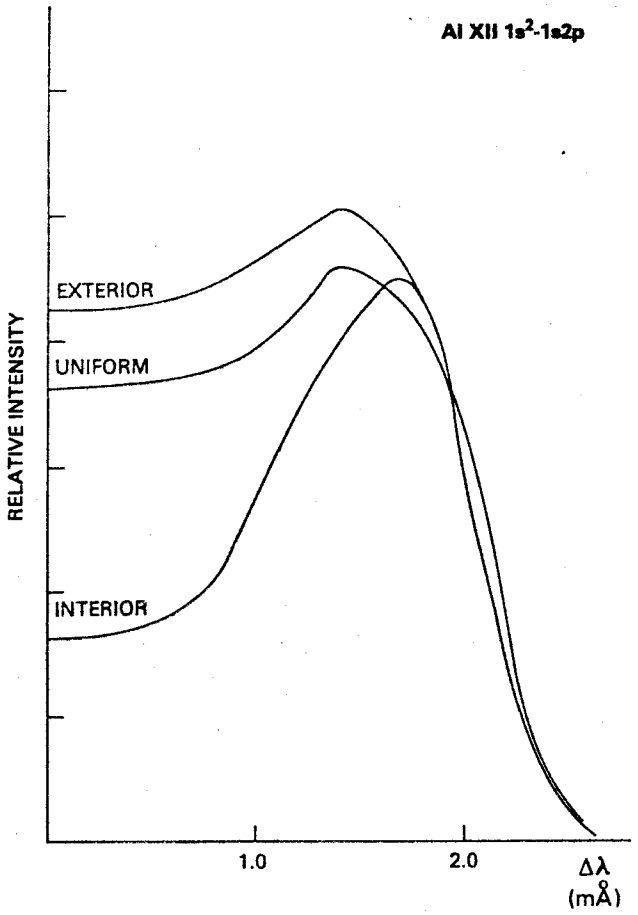

FIG. 2. The He-like resonance line profiles integrated over the time of laser energy deposition (0—100 ps) for an initially uniform plasma for the cases of interior, exterior, and uniform laser energy deposition.

He-like resonance line profiles for the cases of exterior, uniform, and interior deposition. For the exterior deposition we have deposited only 59% as much energy per unit plasma mass at $r=0$ as on the outer radius of the plasma sphere, as if the total sphere diameter represented one mean free path for laser energy absorption. Even this mild deposition gradient significantly affects the resultant resonance line emission. The "interior" deposition calculation idealizes the situation in which a microdot of preionized aluminum is heated by a laser beam whose focal spot is smaller than the sphere, or where shock or compressional heating of the core occurs. As is apparent from Fig. 2, more energy is emitted in the He-like resonance line for the cases of uniform and exterior deposition than for the case of interior deposition. This is in part a reflection of the enhanced escape probability for the former two cases as opposed to the case of interior deposition. The lowered energy emission for interior deposition appears in the line profile as a deep self-absorbed core, deeper than the self-absorption which would be produced solely by boundary effects on the line source function.[6] These calculations show that if the region of laser deposition is surrounded by a layer of the same element in which less laser energy has been deposited, the resonance line radiation losses during heating are reduced.

The development of the H-like resonance line exhibits some qualitative similarities to that of the He-like resonance line. The line first displays a near-Gaussian optically thin emission profile, which saturates and develops a self-absorbed core as the ongoing plasma ionization increases the line optical depth. The boundary effects previously noted[5] are also operative for the source function of the H-like line and are responsible for a portion of the self-absorbed core. However, we find that it is more difficult to remove the H-like self-absorbed core by depositing the laser energy in the outer regions than to similarly remove the He-like resonance line core (Fig. 3). This effect may be explained as follows. Removing or lessening the He-like absorption core is accomplished by increasing the He-like line source function in the outer layers (from where photons may easily escape). This source function enhancement results from large laser deposition in the pellet exterior. But enhancement of the He-like resonance line source function increases the relative He-like ion $2p$ population. When the $2p$ population is increased, collisional ionization to the Al XIII ground state increases also, which helps *absorb* H-like line radiation and *enhances* the self-absorbed core of the H-like line. This pumping mechanism has been referred to in a slightly different context by Whitney and Davis.[5]

When the deposition is nonuniform, Fig. 2 shows that the He-like resonance line profile changes (over the deposition time integral) to reflect the different amount

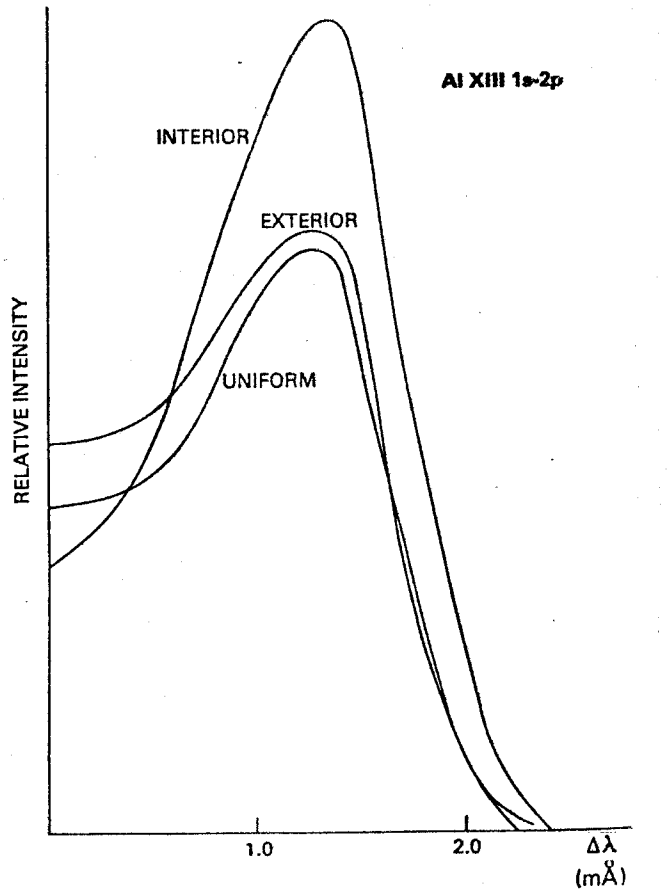

FIG. 3. Same data as Fig. 2, plotted for the H-like resonance line.

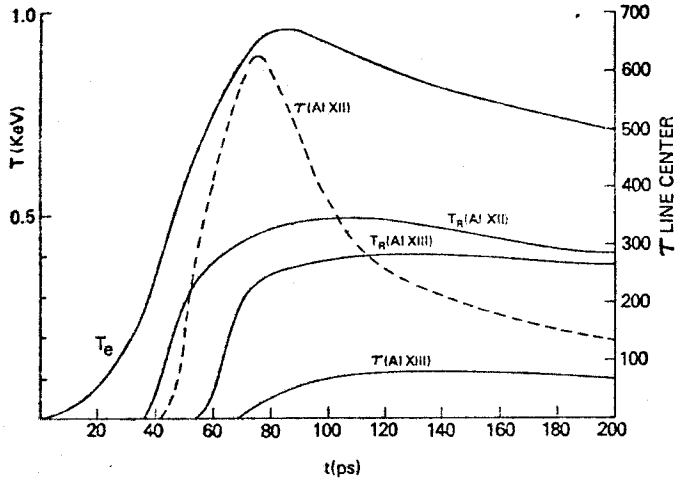

FIG. 4. Optical depth at line center in the Al XII and Al XIII resonance lines, electron temperature at plasma center, and radiation temperatures at the centers of the two lines at plasma center are plotted as functions of time. Laser energy deposition was assumed uniform in the case shown.

of self-absorption occurring in the different spatial locations of the photon sources. It is also apparent from Fig. 3 that the greater self-reversal for the H-like profile for interior deposition is not as pronounced as in the case of the He-like profile. This merely reflects the fact that the optical depth of the H-like resonance line is not as large as that of the He-like line during the deposition (Fig. 4).

In all of the calculations described to this point, we have assumed a uniform initial mass density which is chosen so that total ionization of the plasma yields an electron density of 10^{21} cm^{-3}, critical for 1.06-μ laser radiation. To determine the effect of possible density gradients upon the emitted line profiles and intensities, we have made a series of calculations in which the outer edge of the sphere is about 50% underdense, with a smooth density ramp to a 50% overdense plasma at the center. These calculations show that the dominant line profile trends described above are not upset by

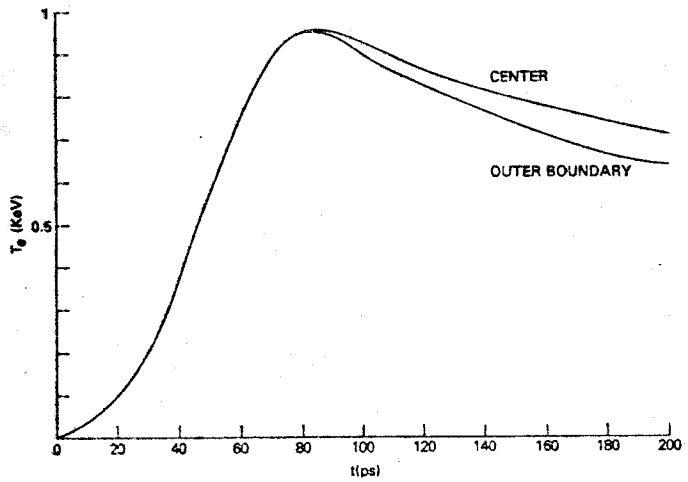

FIG. 5. The electron temperature in keV at plasma center and at the outer boundary as a function of time, for the case of uniform laser energy deposition.

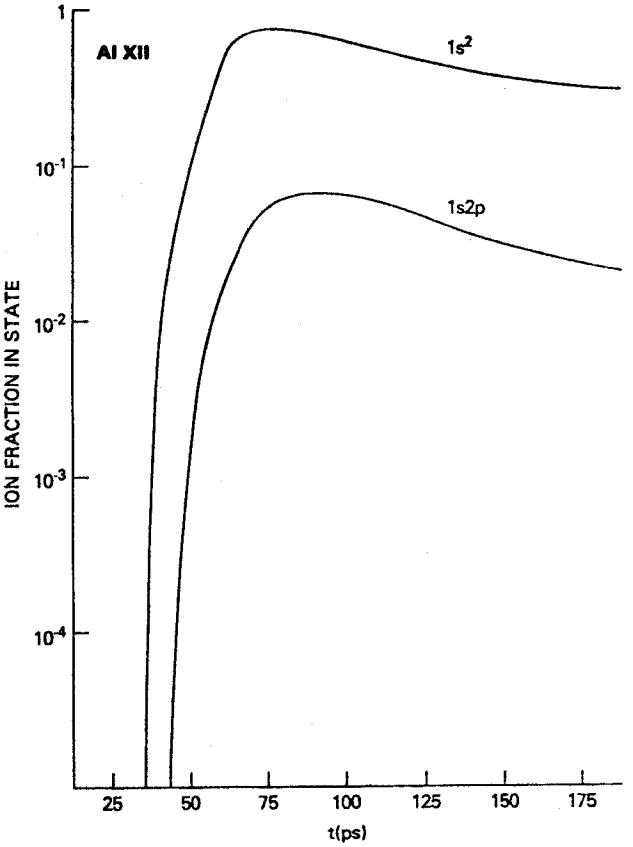

FIG. 6. The fraction of all ions in the Al XII $1s^2$ and $1s\,2p$ states at plasma center plotted against time for the case of uniform laser energy deposition.

this density gradient. The main effect is that, in each case, the degree of self-reversal is enhanced. This enhancement results from the reduced collisional excitation rates in the outer regions, which depress the line source functions, inhibit photon escape, and increase line core absorption. The *relative* self-reversals for different deposition assumptions are esentially unchanged. It should also be noted that the effects reported here, resulting from differing laser spatial heating profiles, would also occur with any plasma heating mechanism (for example, compression) which is capable of producing similar spatial temperature profiles.

We will now examine the postheating behavior of the plasma. Some of the important features of this behavior are illustrated in Figs. 4–7. The buildup of line photons in the plasma reaches a maximum around $t=120$ ps. Defining radiation temperature as the temperature of a blackbody which would produce the same mean intensity as is calculated for the two resonance lines, we note that the central radiation temperatures of the two principal resonance lines at $t=120$ ps are about 500 eV. This contrasts with the electron kinetic temperature of over 800 eV. The line optical depths do not reach sufficiently high values to allow the radiation fields to thermalize; thus the entire plasma is coupled to the boundary to some degree. The lack of photon sources outside the plasma sphere dilutes the interior photon intensity below the (blackbody) values which would prevail if the plasma were much larger.

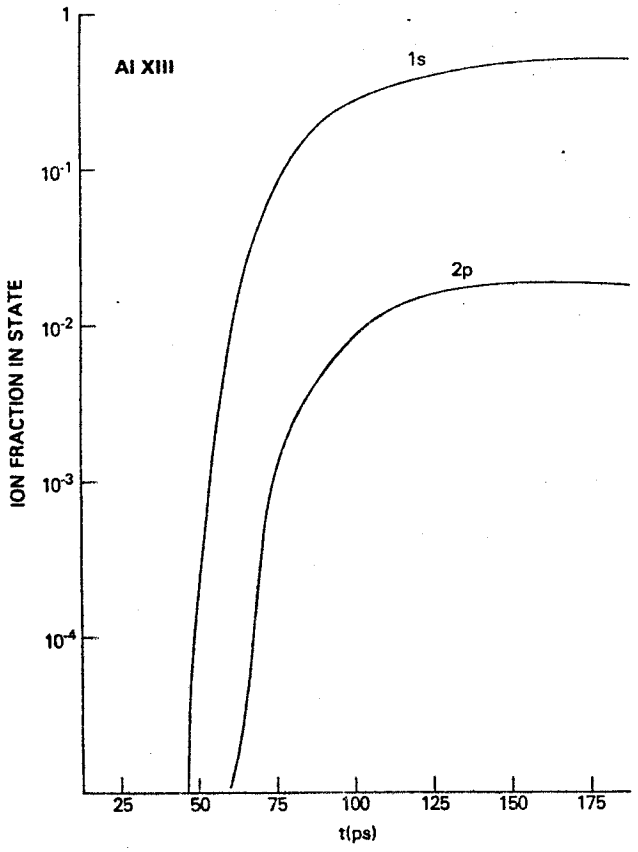

FIG. 7. Same as Fig. 6, except the ion fractions for the Al XIII $1s$ and $2p$ states are shown.

The decay of electron temperature and excited-state populations following deposition is illustrated in Figs. 5–7. During the relatively long plasma decay phase, both principal resonance lines maintain sharply self-reversed cores until the lines again become optically thin and thus quite weak. At $t \approx 80$ ps (when most of the heating is over) a significant difference between the electron temperature at plasma center and that at the outer radius develops due to radiation cooling. The outer electrons continue to cool faster than the central electrons due to these processes, resulting in a widening with time of the temperature difference.

Following the period of heating, multiple photon scattering tends to concentrate the photon source function somewhat toward the plasma center for all three different heating profiles. Thus we do not find large differences in the total radiation emitted in 200 ps in the two principal resonance lines. For the cases of uniform, interior, and exterior heating, 1.44, 1.41, and 1.45 J, respectively, are emitted in these lines in the first 200 ps of the plasma's history.

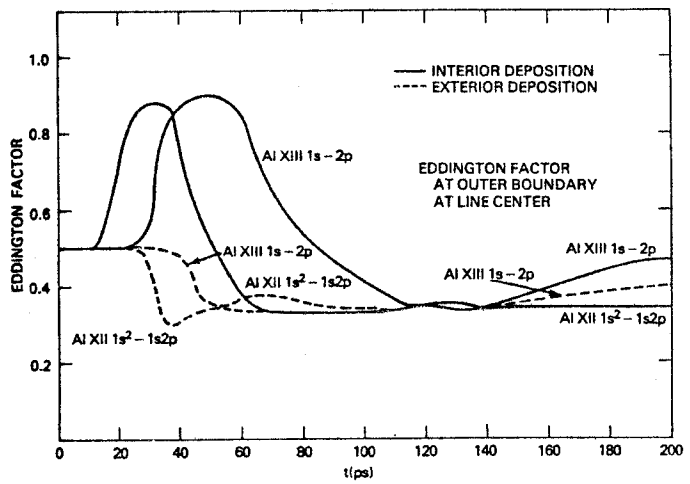

FIG. 8. The Eddington factor is given as a function of time for the cases of interior and exterior laser energy deposition. The factors plotted were computed at the outer boundary of the plasma sphere at the centers of the H-like and He-like principal resonance lines.

III. SPATIAL INTENSITY DISTRIBUTIONS

The technique of pinhole photography is an established experimental tool in the diagnosis of laser-produced plasmas. Recently, Feldman *et al.*[13] have described techniques which may lead to the experimental production of spatially and spectrally resolved images with a time resolution of a few tens of picoseconds. Our transport calculations provide a predictive and diagnostic capability for use in conjunction with such experiments. We will concentrate on the emergent radiation field and the relationship of its spatial profile to the location of

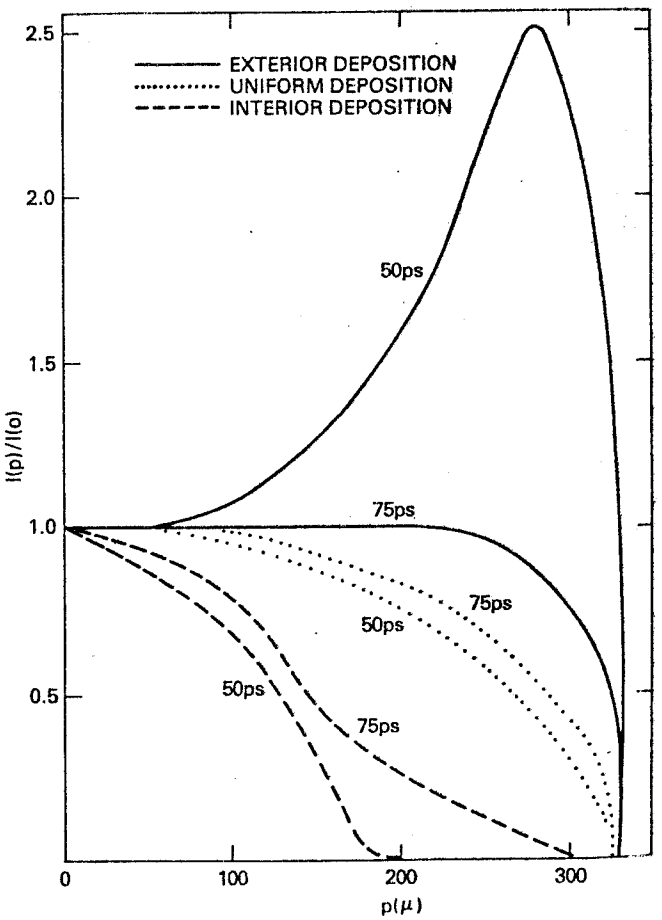

FIG. 9. The frequency-integrated spatial profiles of the principal resonance line of Al XIII. The impact parameter of the emergent ray is plotted against its intensity, which is normalized to 1.0 at $P=0$. Spatial profiles are shown for the cases of uniform, interior, and exterior deposition, at $t=50$ and 75 ps.

energy deposition and the optical depth of the plasma at the frequency of interest.

One measure of the spatial radiation distribution at the outer plasma boundary is the "Eddington factor" $f_\nu = K_\nu / J_\nu$, mentioned in Sec. II. This factor will equal $\frac{1}{3}$ for a uniform hemisphere of radiation but will equal unity if the radiation source is highly concentrated in the plasma interior, that is, in the direction $\mu = 1$. In Fig. 8 we have plotted f_ν at the centers of the principal Al XII and Al XIII resonance lines at the plasma outer boundary. We consider the contrasting cases of interior and exterior plasma heating. We note that f_ν is closer to $\frac{1}{3}$, as expected, for the exterior deposition cases. During the optically thin or grey phases of interior deposition, f_ν is about 0.7—0.8. However, as the plasma thickens, the photons emitted from the interior never reach the outer boundary and thus f_ν goes to $\frac{1}{3}$ for these interior deposition cases also. This fact is further illustrated in Fig. 9, where the H-like frequency-integrated resonance line intensity is shown as a function of the impact parameter along which the ray is emitted. We note that, for exterior deposition, the plasma is highly limb brightened in the H-like resonance line at $t = 50$ ps, when the line is thin. By 75 ps, however, the limb brightening is less pronounced due to the opaqueness at large optical depth. The same basic effects hold true for the extreme limb darkening of interior energy deposition, as is also shown in Fig. 9. We find that the uniform deposition also produces some limb darkening, and this is due to the smaller path length along very obtuse angles and boundary effects on the line source function, which we have described more fully elsewhere.[6] But the basic conclusion of Fig. 9 is that the spatial Al XIII resonance line intensity is quite sensitive to heating profiles. We have found that the Al XII He-like line spatial profiles are not quite as sensitive because the production of Al XII ions is not as sensitive to electron temperature (and thus to deposition) in this energy regime. It should be noted that the optical depth effects on limb darkening may be separated out by observing simultaneously the spatial profiles of the Al XIII $1s$-$3p$, $1s$-$4p$, and higher, thinner lines. These thinner lines should increasingly provide direct deposition information not as interwoven with self-absorption effects. By noting which line in the sequence first shows smaller limb darkening (or brightening) we might well diagnose quite accurately the line optical depths, and thus the number of Al XIII ions in the ground state along the observed path length.

IV. SUMMARY AND CONCLUSIONS

We have shown that the spatial and spectral intensities of the two principal resonance lines of Al XII and Al XIII can, even when the lines are optically thick, provide important diagnostics of the properties of the emitting plasma. We have shown that the Holstein escape-factor formula is not appropriate for spherically symmetric systems unless the photon sources are concentrated near the center of the sphere. We have derived an escape probability formula which is more accurate than Holstein's for the spherical case of uniform photon sources. The different escape probabilities for different photon source distributions result in different line profiles and intensities when the spatial distribution of energy deposition is changed. The spatial distribution of energy deposition was found to be reflected in different "pinhole photograph" spatial profiles of the line emission. These spatial profiles are also somewhat dependent on the line optical depth and, when properly interpreted, can provide information on the line optical depth as well as the spatial photon source distribution.

Consideration of certain other effects should result in a further expansion of the diagnostic potential of these lines. One such effect is the strengthening of the wings of the line profile by collisional broadening and radiation damping. This will transform the Gaussian Doppler-broadened profile considered above into a Voigt profile. This will increase j_ν and k_ν for the line at large frequency displacements from line center and thus affect the photon escape (Sec. II). Another (and potentially very important) effect is the broadening of the line profile by the frequency Doppler shift of plasma mass motions. This broadening mechanism will generally lead to a wide asymmetric line profile. Irons[14] has suggested that this effect may provide an additional diagnostic of plasma expansion or compression velocities. These additional effects are now under consideration and will be discussed in a future paper.

ACKNOWLEDGMENTS

One of us (J.P.A.) wishes to thank the National Science Foundation for support through a postdoctoral fellowship. This work was supported by the Defense Nuclear Agency and in part by the Office of Naval Research under contract No. N00014-25-C-0481.

*National Science Foundation postdoctoral fellow.
†Science Applications Inc., Arlington, Va. 22202.

[1]R.J. Mason, Nucl. Fusion 15, 1031 (1975).
[2]K.A. Brueckner, P.M. Campbell, and R.A. Grandey, Nucl. Fusion 15, 471 (1975).
[3]K.G. Whitney and J. Davis, J. Appl. Phys. 45, 5294 (1974).
[4]J. Davis and K.G. Whitney, J. Appl. Phys. 47, 1426 (1976).
[5]K.G. Whitney and J. Davis, American Physical Society Plasma Physics Meeting, Albuquerque, N.M., 1974 (unpublished).
[6]J. Apruzese, J. Davis, and K.G. Whitney, J. Appl. Phys. 47, 4433 (1976).
[7]D.G. Hummer, C.V. Kunasz, and P.B. Kunasz, Comput. Phys. Commun. 6, 38 (1973); K.G. Whitney, J. Davis, and J.P. Apruzese (unpublished).
[8]The radiation transport notation is that of S. Chandrasekhar in *Radiative Transfer* (Clarendon Press, Oxford, 1950).
[9]See, for example, D. Mihalas, *Stellar Atmospheres* (Freeman, San Francisco, 1970), p. 19.
[10]P. Feautrier, C.R. Acad. Sci. (Paris) 258, 3189 (1964).
[11]J. Apruzese and J. Davis, Naval Research Laboratory Memorandum Report No. 3277, 1976 (unpublished).
[12]T. Holstein, Phys. Rev. 72, 1212 (1947).
[13]U. Feldman, G.A. Doschek, D.K. Prinz, and D.J. Nagel, J. Appl. Phys. 47, 1341 (1976).
[14]F.E. Irons, J. Phys. B 8, 3044 (1975).

Collisional-radiative-equilibrium spectroscopic diagnosis of a compressed, optically thick neon plasma

J. P. Apruzese,* P. C. Kepple, K. G. Whitney,† J. Davis, and D. Duston
Plasma Physics Division, Naval Research Laboratory, Washington, D.C. 20375
(Received 9 May 1980; revised manuscript received 9 March 1981)

By self-consistently calculating x-ray spectra from first principles, we have delineated the relationships between the spectrum and the state of compression and heating of a neon plasma in detail. A collisional-radiative model including Stark line profiles is used to determine the highly ionized high-density states of neon. One of our calculated spectra reproduces remarkably well an experimental spectrum obtained from laser implosion by Yaakobi *et al.* and indicates compression conditions significantly different from those obtained assuming the validity of local thermodynamic equilibrium. Implications of our calculations for spectroscopic diagnoses of fusion plasmas are discussed.

I. INTRODUCTION

One of the most widely used techniques to diagnose the properties of transient fusionlike plasmas is to analyze their x-ray emissions. In an example of the use of such methods, Yaakobi *et al.*[1] have measured the K-series emission spectrum from a neon plasma produced by laser implosion of a glass microballoon filled with neon at 8.6 atm pressure. Using a methodology that assumed the ionization conditions of the plasma and that accounted for opacity and Stark broadening of the Lyman-α and Stark broadening of the Lyman-β and Lyman-γ lines, they ascribed a density of 0.26 g/cm^3 (ion density, 7.8×10^{21} cm^{-3}) to the neon emission region. From the measured line intensity ratios $I(\mathrm{Ly}\beta)/I(1s^2\text{-}1s3p)$ and $I(\mathrm{Ly}\alpha)/I(\mathrm{Ly}\beta)$, an electron temperature of 300 eV was inferred in the context of an LTE plasma model whose line radiation was assumed to be a Planck function—saturated. In this paper, we show that a theoretically self-consistent, steady-state analysis of all the main features of such spectra can be carried out that is based on a first-principles calculation in which the only free parameters are the average plasma properties of temperature, density, size, and velocity profile. This analysis leads to a set of general principles governing the relationships of high density, optically thick plasma properties to their emitted spectra. As a specific example of the application of such principles, we demonstrate that our calculations reproduce well the neon experimental spectrum discussed above and lead to a diagnosis of significantly lower density and higher temperature. Furthermore, our investigation allows an exposition of how and why a self-consistent physical model reproduces an experimental spectrum, while a simpler but inappropriate model such as LTE may lead to miscalculation and/or misinterpretation of the spectrum.

II. PLASMA MODEL

For spectrum calculations we have employed a detailed multistate, multilevel model of ionized neon in the context of collisional-radiative equilibrium and an assumed spherical geometry. Since virtually all of the neon at peak compression consists of lithiumlike or more highly stripped ions, the model includes only the ground states for Ne I–Ne VII. For lithiumlike Ne VIII, the atomic model includes the excited states $1s^2$-$2p$, -$3s$, -$3p$, -$3d$, and -$4d$. For heliumlike Ne IX, we have the excited-state manifold $1s2s\,^1S$, $1s2p\,^3P$, $1s2p\,^1P$, and the $n=3$ and $n=4$ singlet states. For Ne X, $n=2$, 3, 4, and 5 as well as $n=1$ are included. All of the lines appearing in the Rochester spectrum (Lyα, β, and γ, Ne IX $1s^2$-$1s3p\,^1P$, $1s^2$-$1s4p\,^1P$, as well as $1s^2$-$1s2p\,^1P$) are calculated by self-consistently solving fully coupled nonlinear radiation transport and rate equations.[2] Most importantly, the calculation also includes the self-consistently computed effects of Doppler, Stark,[3] and mass-motional line broadening. Additionally, the calculated spectra are convolved with 1.5 eV of experimental (Gaussian) broadening.[1] However, in most cases, as pointed out by Yaakobi *et al.*, the experimental broadening has little or no effect due to the large Stark linewidths. The rate equations and the radiative transport equation are also used to solve in detail for the continuum radiation arising from recombination from the bare nucleus to the $n=1$ and 2 states of Ne X, and from Ne X $n=1$ to Ne IX $1s^2\,^1S$ and $1s2p\,^3P$.[2]

With the exception of electron collisional excitation rate coefficients and spontaneous decay rates, the methods of calculating the various rate coefficients used in this study have been described in detail in previous papers,[4,5] and only brief reference will be made to these. Every state is coupled to the next (energetically) highest ground state, by collisional ionization and collisional re-

combination. Additionally, photoionization and radiative recombination are computed in detail for the states mentioned above. The collisional ionization rates are calculated by Seaton's prescription,[6] and the photoionization cross sections are calculated in the hydrogenic approximation[7] using effective free-bound Gaunt factors.[8] Collisional- and total-radiative recombination rates are then calculated as the detailed balance of these. However, the details of the frequency dependence of the hydrogenic photoionization cross sections are replaced by a simpler exponential profile for the recombination process.[2] In addition, adjacent ground states are coupled by dielectronic recombination[9] found by summing capture rates over a manifold of states above the ionization limit which then decay via cascade to the ground state.

Excited levels of a given ion are coupled to the other excited states in the model and to the ground state by electron collisional excitation and deexcitation, and by spontaneous radiative decay. Collisional couplings include forbidden and spin-flip transitions as well as those which are dipole allowed. For Ne X, the Coulomb-Born approximation[10] was used, while a distorted-wave calculation with exchange[11] was used to calculate the coefficients for Ne VIII and Ne IX. Comparisons of these two methods have been made for several transitions in hydrogenlike Al XIII,[12] and excellent agreement was obtained.

As mentioned above, line photon reabsorption is taken into account by solving the radiation transport equation for six selected resonance lines, five of which appear in the published Rochester spectrum[1] (taken by Yaakobi *et al.*) and are generally used as diagnostics for neon- or argon-filled pellet targets. The present model neglects the effect of radiation reabsorption for lines which couple two excited states, even though such lines are optically thick in some of the cases discussed below. This simplification, however, results in no significant error in these cases, where the density is so high that collisional rates coupling excited states vastly exceed radiative rates and thus dominate the cross coupling of these levels. Unless these lines appear in the spectrum to be analyzed, it is not necessary to perform the radiation transport calculations for them. The same principle does not apply for the resonance lines dominating most spectra, where the reduced collision rates and higher radiative rates result in comparable importance for collisions and radiation, or even radiation dominance in the couplings.

Details of the radiation transport and photocoupling calculations are given elsewhere[2,13] and will not be elaborated here. However, an additional feature—the calculation of the effects of the different Doppler shifts caused by the inhomogeneous velocity profile of a plasma implosion on the emitted line profiles—has been included in the radiation transport algorithm. These effects will be fully discussed in an upcoming paper, but in the particular results of this paper it served us mainly to confirm what had been suspected, that even at implosion velocities of 2×10^7 cm sec^{-1},[14] the effects are small due to the large Stark widths of the lines at high density. For lower density plasmas the effects can be quite significant but it is of little concern here.

In the analysis detailed below, spectra calculated for steady-state plasma conditions are used to interpret an experimental, time-integrated spectrum. While this approach may at first seem questionable, it was justified for the cases considered here—short-pulse Nd laser drivers—by Yaakobi *et al.*[15] in their letter on argon-filled glass microballoon experiments. They found from extensive hydrodynamical simulations of spherical target compressions that the most energetic emission of hydrogenlike lines occurs during a 10-psec time interval during which the plasma properties change little, spatially or temporally. These theoretical results, coupled with the fact that our analysis obtains striking agreement with experiment, indicate that this assumption can be productively employed under these conditions to interpret the emission properties of plasma cores under spherical compression.

III. COMPRESSION DIAGNOSTICS WITH CALCULATED SPECTRA

It is widely recognized that pellet compression along a low adiabat is most desirable in achieving maximum density prior to thermonuclear ignition. Hence, a major goal of laser-driven pellet compression experiments is to obtain the highest possible implosive drive while minimizing preheat. Knowledge of the degree to which this goal is met experimentally may be obtained from a variety of techniques, and one of the prime tools available is spectroscopy. For this purpose, one must know the sensitivity of the emitted spectrum to the plasma's density and temperature. Figure 1 presents three neon spectra calculated for a spherical plasma in CRE. They illustrate the evolution of the emitted spectrum as the same mass of neon is progressively compressed to higher densities and lower temperatures (i.e., along lower adiabats). The lower the adiabat, the closer to the top of the figure the spectrum appears. Increased density is primarily reflected in the widening of the lines due both to larger intrinsic Stark widths and possible opacity broadening. This effect has been utilized

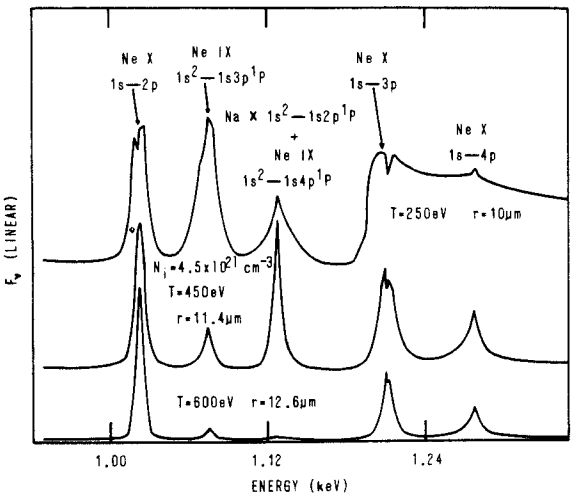

FIG. 1. Three calculated spectra are shown which illustrate, from bottom to top, the changes in spectral signature which occur as a constant neon mass is compressed to higher densities and colder temperatures. The spectra are calculated assuming that the neon plasma is in collisional-radiative equilibrium (CRE). The exterior pellet temperatures decrease from those of the core in accordance with the gradient described in the text. Only the middle spectrum includes the (negligible) pumping effect of the Na x impurity line at 1.13 keV.

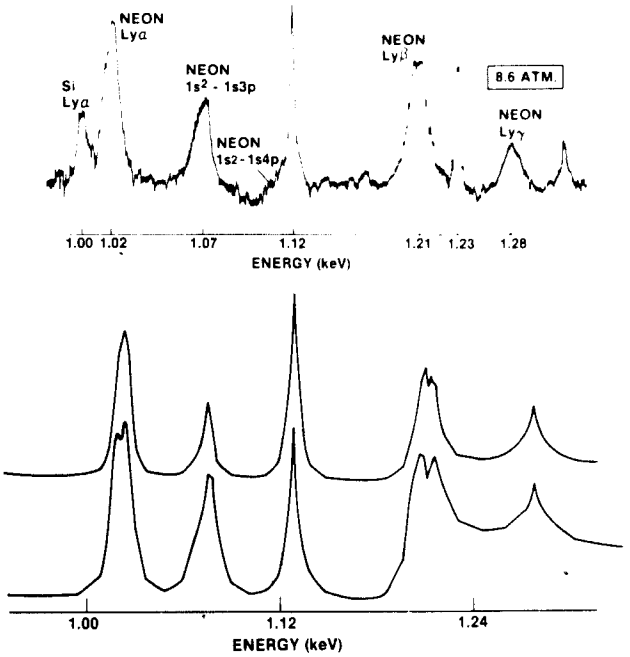

FIG. 2. The top spectrum was obtained by Yaakobi *et al.* at the University of Rochester from a laser-imploded microballoon filled with 8.6 atmospheres of neon. The bottom two spectra were calculated assuming CRE. The middle spectrum provides the best fit to the top one and arises from a plasma of $T_e = 385$ eV, $r = 11.4$ μm at $N_i = 4.5 \times 10^{21}$ cm^{-3}. The bottom spectrum would be emitted by a plasma of $T_e = 300$ eV, $r = 9.5$ μm, at $N_i = 7.8 \times 10^{21}$ cm^{-3}.

for argon compression diagnostics in the case of optically thin nonopacity broadened Stark lines.[16] The line profiles (as opposed to line intensities) are relatively insensitive to temperature.[16] However, effects of opacity broadening are specifically illustrated below in the interpretation of the Rochester neon experimental spectrum[1] taken by Yaakobi *et al.*

The pronounced temperature sensitivity of the emitted spectra is also apparent in Fig. 1. As the temperature is decreased from 600 to 450 to 250 eV, the intensity of the helium-like $1s^2$-$1s3p\,^1P$ line at 1.074 keV increases dramatically relative to the hydrogen-like Ne X lines. In the Rochester spectrum, the Ne IX $1s^2$-$1s4p\,^1P$ line (at 1.127 keV) was obscured by the impurity line Na X $1s^2$-$1s2p\,^1P$, which is equal in wavelength to 1 part in 10^5. In fact this sodium line will optically pump the Ne IX level populations to some degree due to this close resonance. In the middle spectrum of Fig. 1 the effect of this impurity line has been included—the intensity having been derived from our computed fit to the Rochester spectrum[1] (taken by Yaakobi *et al.*) in Fig. 2. We included the sodium pumping line by assuming that the flux directed inward from the microballoon toward the neon filler is the same as the inferred flux directed outward. However, by calculating the emitted neon spectrum without the pumping influence of the impurity line, we have determined that the effect is negligible for these dense plasmas with high collisional cross-coupling rates between excited states. Therefore, the line has been omitted in some of the calculated spectra presented in Figs. 1–3, since its effect on the level populations is negligible.

Equally apparent as the helium line intensity change is the relative increase in the continuum radiation arising from recombination to the ground state of Ne IX as the temperature decreases. Indeed, at a temperature of 250 eV the Lyβ and Lyγ lines which sit on top of this continuum feature (whose edge lies at 1.196 keV) are more properly regarded as "line-continuum features" rather than pure lines. The appearance of this strong continuum edge can place strong constraints on the diagnosed temperature. Also, the continuum opacity may significantly affect both the shape and strength of the observed features arising from bound level transitions. Similarly, ionization by line photons—especially important when the lines are very wide due to Stark effects—may significantly affect the ionization balance of the plasma.

Having noted the spectral differences arising

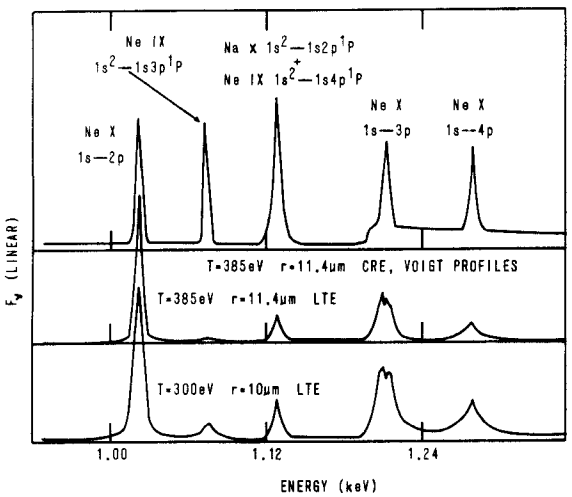

FIG. 3. The three calculated spectra shown represent the results of employing commonly used, but inaccurate, approximations. The top spectrum would be emitted by a neon plasma with pure Voigt line profiles whose conditions are those of the "best fit" of Fig. 2. The middle spectrum maintains the same physical conditions as the top, but Stark line profiles and LTE are assumed. The bottom spectrum arises from the same mass of plasma assumed to be in LTE but with a temperature of 300 eV and a radius of 10 μm. The sodium impurity line at 1.13 keV is included in these spectra.

from changes in density and temperature, we investigated the possibility of obtaining a fit to the Rochester experimental spectrum[1] using our first-principles ionization calculation, in which only temperature, density, size, and velocity variations in plasma conditions could be made.

The results of this effort are graphically summarized in Fig. 2, where the Rochester experimental spectrum (taken from Ref. 1) and two calculated spectra are displayed. The middle spectrum of Fig. 2 represents an excellent fit to the experimental spectrum displayed at the top of the figure. This "best-fit" calculated spectrum would arise from a spherical neon plasma of ion density 4.5×10^{21} cm^{-3} and radius 11.4 μm, having an electron temperature of 385 eV from $r=0$ to $r=8.8$ μm that then decreased smoothly to 296 eV at the surface. This gradient was inferred in a previous analysis of the degree of line self-reversals in such imploded plasmas,[14] and our present results support this gradient inference. Also shown in Fig. 2 (at the bottom) is the spectrum which would be emitted by a neon plasma characterized by the conditions originally inferred from the LTE analysis in Ref. 1. These conditions are $T_e=300$ eV (constant), $N_i=7.8\times10^{21}$ cm^{-3}, and $r=9.5$ μm.

The need for a higher temperature and lower density than previously diagnosed is most readily understood by comparing the predicted 300-eV spectrum to the experimental one. The presence of the prominent continuum feature—the Ne IX ground-state ionization edge—in the 300-eV predicted spectrum is not matched by a similar feature in the experimental one. An explanation for its absence is that the experimental plasma contains less Ne IX and is therefore at a higher temperature, where more of the heliumlike neon is ionized. This degree of reduction of the continuum feature as the temperature increases is clearly evident in the theoretical spectra of Fig. 1, which served as a guide in obtaining the Fig. 2 fit to the Rochester experiment. A core temperature of 385 eV was needed to lower the calculated feature which is weak or nonexistent in the experimental spectrum. Moreover, temperatures higher than 385 eV were found to produce a Ne IX $1s^2$-$1s3p\,^1P$ line which was too weak to match the experimental line. Even at $T=400$ eV, the Fig. 2 comparison of calculated and experimental spectra deteriorated noticeably in this regard. Any temperature below 385 eV raises the helium continuum again producing a significant deterioration in the agreement even at our diagnosed density of 4.5×10^{21}. Our ability to zero in on 385 eV as the likely temperature in this manner strikingly illustrates both the need and the value of utilizing all of the information in the spectrum.

The Rochester analysis yielding $T_e\sim300$ eV was based upon Planckian line ratios generated by an LTE plasma. By contrast we find that a neon plasma of $T_e=300$ eV, $N_i=7.8\times10^{21}$ cm^{-3}, and $r=9.5$ μm has not reached LTE. Of the ionic species, only the Ne X concentration is close to its LTE value. Ne XI (bare nucleus) is about half of what would be expected in LTE, while heliumlike Ne IX has twice its LTE concentration. Moreover, the excited states of Ne X, whose radiative decay dominates the spectrum, are present to a far smaller degree than would be the case in LTE. The LTE excited-to-ground-state ratios of Ne X $n=2$, 3, 4, and 5 are, respectively, 0.13, 0.16, 0.23, and 0.32. We find that the highest ratios occur in the 300-eV model plasma at $r=0$, where they are 0.05, 0.06, 0.09, and 0.13, respectively. In effect, the ionization-excitation state of the plasma lags behind what is required for LTE. At an ion density of 7.8×10^{21} cm^{-3}, collisional processes dominate the coupling of the Ne X excited states to each other. Hence, these ratios of populations of the states lying above $n=2$ to that of $n=2$ do correspond to the required LTE ratios. The Ne X excited states are also in LTE with respect to the ground state lying above (the bare nucleus) due to the strength of collisional ionization and recombination processes. However, collisional excitation from

and de-excitation to the NeX ground state from the excited states is generally at least two orders of magnitude weaker than collisional cross couplings among the excited states. Collisional deexcitation from the excited states to the ground state is also only about one-third as likely as spontaneous radiative decay to the ground state. Collisional processes are therefore not strong enough to enforce LTE between the ground and excited states of the *same* species—NeX. Moreover, due to the large Stark widths, the optical depths of Lyβ, γ, etc., are 2.2 or lower, as described below. Since these modest opacities do not permit multiple photon scattering, the states $n=3$ and above are weakly photoexcited and remain far from LTE with respect to $n=1$. However, since the optical depth of Lyα is ~200, it might at first be suspected that at least $n=2$ would be in LTE with respect to the ground state. The fact that this is not the case may be understood by applying the conditions required for LTE to the rate equations affecting the two states $n=1$ and 2. For simplicity we first consider the two-level-atom case in an optically thick plasma characterized by a line photon escape probability P_e. We let W_{21} stand for the collisional deexcitation rate coefficient and A_{21} stand for the spontaneous emission coefficient. The steady-state condition requires

$$N_2(W_{21}+A_{21}P_e)=N_1\left(W_{21}\frac{g_2}{g_1}e^{-h\nu/kT}\right), \tag{1}$$

where photon reabsorption is accounted for by diluting the spontaneous emission coefficient by a factor equal to the mean photon escape probability. From Eq. (1),

$$\frac{N_2}{N_1}=\frac{(g_2/g_1)e^{-h\nu/kT}}{1+(A_{21}P_e/W_{21})}. \tag{2}$$

For N_2/N_1 to have the LTE population ratio of these two levels, $(g_2/g_1)e^{-h\nu/kT}$, we must have

$$A_{21}P_e \ll W_{21}. \tag{3}$$

Therefore, even a very optically thick plasma can be far out of LTE if $A_{21} \gg W_{21}$ to the extent necessary to offset a small P_e. That is, the mere existence of a small P_e due to large optical depth does not ensure the validity of Eq. (3). Therefore, the fact that Lyα is quite thick in this case does not in itself justify an LTE assumption. For the plasma conditions under consideration here, $A_{21} \cong 2.5W_{21}$. Therefore, LTE will not be valid near the surface of the plasma, where $P_e \approx 0.5$, since $A_{21}P_e \gtrsim W_{21}$ in this region. Of course, the emitted spectrum of optically thick lines tends to be dominated by surface emission. Nevertheless, one still might expect LTE to prevail in the optically thick interior based on the above two-level-atom analysis. However, there are three separate effects which in this case prevent LTE conditions from being established even in the thick plasma interior. First, even though the optical depth of Lyα is ~200, the line wings are so prominent at this high density that the mean escape probability is found numerically to be 0.06. Thus, $A_{21}P_e \cong 0.15\ W_{21}$ in the interior. According to Eq. (2) this alone will reduce the N_2/N_1 ratio to 0.87 times that of LTE. The other two effects which bring the actual ratio to only 0.38 times the LTE ratio are, first, a radiative leak in the Lyβ line, where $\tau \cong 2$, and, second, another photon escape mechanism in the optically grey recombination continuum from the bare nucleus to the ground state of NeX. A multilevel analysis is necessary to clarify the detailed contributions of the latter two mechanisms.

An accurate analytic treatment is possible in this case because the very large collisional rates coupling the excited states ($n=2$, 3, 4, 5, and NeXI) force the ratios of these states to each other to equal those of LTE, as confirmed by the calculated population densities. Let L_{ij} denote the LTE ratio of state i to state j. Then, the equation for the steady-state coupling of NeX $n=1$ to the overlying states becomes

$$N_1\left(\sum_{i=2}^{6} W_{1i}\right)=N_2\Big((A_{21}P_{e21}+W_{21}) + \sum_{i=3}^{5} L_{i2}(A_{i1}P_{ei1}+W_{i1}) + L_{62}(W_{R61}N_eP_{e61})\Big). \tag{4}$$

In Eq. (4) W_{ij} is the collisional rate coupling states i and j, P_{eij} is the escape probability for the photon emitted during a radiative transition from state i to j, A_{ij} is the spontaneous transition probability, and W_{R61} is the radiative recombination rate from the bare nucleus to NeX $n=1$. Equation (4) contains all of the important processes populating and depopulating NeX $n=1$ at this temperature and density. The processes which are omitted—collisional recombination from NeXI and its inverse, and ionization and recombination processes from and to NeIX—are relatively unimportant compared to what is included, and thus their omission does not quantitatively affect this analysis. Equation (4) is easily solved for N_2/N_1. When the collisional rates and Einstein A's are inserted, the ratio N_2/N_1 is found to be a function of the escape probabilities for a particular plasma temperature, density, and size. For Lyβ, the numerical results yield $P_{e31} \cong 0.7$, and for the $n=1$ recombination continuum $P_{e61} \cong 0.3$. The Lyβ radia-

tion leak in concert with Lyα, γ, and δ would reduce N_2/N_1 to 0.65 times the LTE ratio; inclusion of the free-bound continuum leak brings the ratio down to the actual 0.05, which is 0.38 that of LTE. Photon escape in Lyγ and Lyδ makes little difference since their spontaneous transition probabilities are factors of 4.4 and 13.5, respectively, below that of Lyβ.

In summary, escape of radiation in the optically grey Lyβ and NeXI continuum transitions adds to the radiation escape in the line wings of Lyα and prevents LTE from being established even in the plasma interior. While the strong collisional coupling of the states above NeX $n=1$ forces $n=3$ and above into LTE with $n=2$, it in turn adds to the escape of radiation emitted during decays of these levels and further reduces all the excited-state populations relative to $n=1$. Fundamentally, the lack of detailed balancing of all of the NeX radiation—i.e., by reabsorption—prevents LTE conditions from being established.

The need for a reduced density in order to explain the observed spectrum (from 7.8×10^{21} to 4.5×10^{21} cm^{-3}) is implied by two features of the predicted spectrum at 7.8×10^{21} cm^{-3}; namely, the Lyα, Lyβ, and Lyγ lines are too wide, and the Lyα line exhibits a self-reversal which is not observed. We will first consider the question of the Lyβ and γ lines. As previously mentioned, the total concentration of hydrogenlike NeX in our 300-eV model plasma is roughly equal to the LTE value. However, since our excited-state densities are much less than the LTE amounts, the ground state has a greater than LTE density—varying from 75% greater at the center ($r=0$) to 2.2 times greater at the plasma surface. The reason for this spatial gradient is that the radiation field is less intense at the surface, which therefore, with less optical pumping, contains fewer bare nuclei and more hydrogenlike neon. The optical depths of Lyβ and Lyγ in collisional-radiative equilibrium are therefore about twice the previously assumed LTE values. We find a peak optical depth of 2.2 for Lyβ in contrast to the value of 1.2 that was previously used[1] to calculate the first-order opacity-broadening correction. This results in a 50% increase in linewidth because of the extra opacity broadening. Also, we do not find that the Lyγ line is optically thin; instead, it has a peak optical depth of 1.1. In summary, significantly greater opacity broadening for both Lyβ and Lyγ occurs in CRE than in LTE, which forces a reduction in density in order to reduce the Stark and opacity widths to fit the experimental spectrum.

As noted above, the 300-eV model plasma predicts an asymmetric self-reversal for Lyα. This asymmetry is due to the effects of plasma motion. The self-reversal itself is a well-known effect of large line opacity in a non-LTE plasma. Reducing the linewidth by reducing the density from 7.8×10^{21} to 4.5×10^{21} cm^{-3} turns the self-reversal into a "shoulder" which is more consistent with experiment. The increased temperature of 385 eV reduces the fraction of ground state NeX, and thus the Lyα opacity, contributing to this effect. The width of the opacity-broadened Lyα line is also in very good agreement with experiment when this lower density is assumed, as is apparent in Fig. 2.

IV. EFFECTS OF SIMPLIFYING ASSUMPTIONS ON THE CALCULATED SPECTRA

We have seen above that neither Voigt profiles nor LTE are valid assumptions for the physical state of these high-density neon plasmas. However, it is of interest to invert the analysis and examine spectra calculated using these erroneous assumptions in order to estimate the magnitude of error. Figure 3 displays three spectra which represent the results of employing commonly used, but inaccurate approximations. The top spectrum was computed using conditions identical to those of the "best fit" to the experimental spectrum at the top of Fig. 2, except that Voigt rather than Stark line profiles were used. Consequently, the much narrower lines of this spectrum bear little resemblance to the observed spectrum or to the theoretical Stark-profile spectrum in the middle of Fig. 2. The bottom two spectra of Fig. 3 were computed with Stark profiles but with the LTE assumption. Since the true excitation state of the plasma lags behind LTE, when LTE is assumed, the theoretical excitation state is increased, resulting in more ionization and less NeIX. The reduced heliumlike neon is reflected in the very weak NeIX $1s^2$-$1s3p\,^1P$ line, which for $T=300$ or 385 eV is much less intense than that which is measured. Also, the NeIX ground-state recombination continuum is much reduced, especially in the case of the 300-eV spectrum. Neither LTE spectrum agrees with experiment. It is conceivable that an LTE spectrum of neon at a much lower temperature might show a relatively increased NeIX $1s^2$-$1s3p\,^1P$ line and thus agree more closely with the experimental spectrum of Fig. 2. However, the lower temperature would reduce the collisional rates even further—meaning that LTE would be an even more inappropriate model.

V. SUMMARY AND CONCLUSIONS

We have utilized a first-principles, multistate, multilevel model of highly ionized, high-density neon to predict the emitted spectrum as a function

of the compressed state of the plasma. The appearance of the spectrum has been found to sensitively reflect this state, and the particular features which change in accordance with the various plasma properties have been noted and the underlying physics discussed. The model has been found capable of generating an excellent detailed fit to a previously published experimental spectrum, and the fitting process has led to a considerable refinement of the inferred plasma conditions, including an estimate of the extreme sensitivity of the predicted spectrum to these conditions.

One should note that the authors of Ref. 1 attempted only to obtain an approximate temperature to aid in inferring the density. On the other hand, it is our purpose here to illustrate the potential of non-LTE spectroscopic analysis for obtaining accurate temperatures as well as accurate densities. We have shown that despite the complexity of the dynamics of compression, detailed, realistic, and accurate modeling of the radiative output is both possible and fruitful.

ACKNOWLEDGMENTS

The authors wish to thank Dr. B. Yaakobi for granting permission to use his spectra and for providing a copy for reproduction here. This work was supported in part by the Defense Nuclear Agency.

*Science Applications, Inc., McLean, Va.
†Optical Sciences Division.

[1]B. Yaakobi, D. Steel, E. Thorsos, A. Hauer, and B. Perry, Phys. Rev. Lett. 39, 1526 (1977).
[2]K. G. Whitney, J. Davis, and J. P. Apruzese, Phys. Rev. A 22, 2196 (1980).
[3]H. R. Griem, M. Blaha, and P. C. Kepple, Phys. Rev. A 19, 2421 (1979).
[4]D. Duston and J. Davis, Phys. Rev. A 21, 1664 (1980).
[5]K. G. Whitney and J. Davis, J. Appl. Phys. 45, 5294 (1974); J. Davis and K. G. Whitney, *ibid.* 47, 1426 (1976).
[6]M. J. Seaton, Proc. Phys. Soc. London 79, 1105 (1962).
[7]V. L. Jacobs, J. Davis, P. C. Kepple, and M. Blaha, Astrophys. J. 211, 605 (1977).
[8]W. J. Karzas and B. Latter, Astrophys. J. Suppl. Ser. 6, 167 (1961).
[9]V. L. Jacobs and J. Davis, Phys. Rev. A 18, 697 (1978).
[10]L. A. Vainshtein and I. I. Sobel'man, Lebedev Report No. 66 (unpublished).
[11]J. Davis, P. C. Keeple, and M. Blaha, J. Quant. Spectrosc. Radiat. Transfer 16, 1043 (1976).
[12]D. Duston, J. Davis, and K. G. Whitney, NRL Memorandum Report No. 3846 (unpublished).
[13]J. P. Apruzese, J. Davis, and K. G. Whitney, J. Appl. Phys. 48, 667 (1977).
[14]S. Skupsky, University of Rochester Laboratory for Laser Energetics Report No. 80 (unpublished).
[15]B. Yaakobi, S. Skupsky, R. L. McCrory, C. F. Hooper, H. Deckman, P. Bourke, and J. M. Soures, Phys. Rev. Lett. 44, 1072 (1980).
[16]A. Hauer, K. B. Mitchell, D. B. Van Hulsteyn, T. H. Tan, E. J. Linnebur, M. M. Mueller, P. C. Kepple, and H. R. Griem, Phys. Rev. Lett. 45, 1495 (1980).

Influence of Lyman-series fine-structure opacity on the K-shell spectrum and level populations of low-to-medium-Z plasmas

J. P. Apruzese, J. Davis, D. Duston, and R. W. Clark
Plasma Radiation Branch, Plasma Physics Division, Naval Research Laboratory, Code 4720, Washington, D.C. 20375
(Received 13 July 1983)

As laboratory plasmas of increasing atomic number, temperature, size, and/or density are produced, it becomes likely that the details of the doublet opacity profiles of the Lyman series will influence the K-shell level populations and spectrum. Accordingly, we have analyzed these effects for a range of plasma parameters, confined to densities low enough for Stark broadening to be unimportant. An analytic model is developed which predicts line power enhancements and level-population changes for K-shell plasmas. This model is based upon photon escape probability and collisional quenching concepts and is valid for plasmas of atomic number ~ 13–26. Additionally, an extensive set of numerical calculations of line ratios, line profiles, and level populations has been carried out for K-shell argon plasmas. Each computation was performed both with detailed fine-structure opacity profiles and with a single-Voigt-profile approximation. The results of these calculations may be scaled for plasmas of atomic number other than 18 using a simple set of rules discussed in the text.

I. INTRODUCTION

Recent years have witnessed dramatic technological advances in laboratory production of optically thick K-shell plasmas of low-to-medium-Z elements. Consistent with these developments, considerable theoretical effort has been devoted to elucidating the effects of opacity on the spectra and intrinsic properties of such plasmas. Typically—although not exclusively—the hydrogenlike and heliumlike resonance lines of the plasma are quite optically thick but the continua are optically thin in the x-ray region. Thus it is the line opacity which has properly attracted the most concern. As is well known from astrophysical literature, the precise form of the line-opacity profile—which determines the line-photon escape probability—plays a critical role in the formation of the spectrum and determination of the level populations. It is also true that—for quite specific physical reasons—regimes exit where simplified profiles such as pure Doppler may be employed with acceptable accuracy. For instance, Fig. 5(a) of Avrett and Hummer[1] reveals little difference in the steady-state source functions obtained for Voigt and Doppler profiles up to line-center optical depths of ~ 50 with a Voigt broadening parameter of 10^{-2}. One laboratory plasma counterpart of this situation would be a 1.5-mm aluminum plasma of ion density $\sim 10^{19}$ cm^{-3} and 600-eV temperature. Detailed calculations[2] have shown that here, too, a Doppler profile is adequate as a representation for line opacity. We will consider Z scaling of all specifically quoted plasma conditions below. At higher densities and/or optical depths a Voigt profile is required to adequately describe photon transport in the line wings. At still higher densities, Stark effects must be considered.[3–7] In this paper we will delineate the plasma conditions where the doublet-opacity profile due to fine structure in the Lyman lines must similarly be taken into account. We analyze the underlying physics with both analytic and numerical models, and obtain Z-scaled expressions governing the safe use of simpler opacity approximations. In Sec. II an analytic model is developed which serves two basic functions. First, it provides a physical basis for comprehending the trends which appear in the numerical results. Second, approximate but useful Z-scaled formulas expressing some of the results are obtained. In Sec. III specific numerical results for an argon plasma ($Z=18$) are presented along with a prescription for scaling them to plasmas of different atomic numbers.

II. ANALYTIC MODEL

A. Assumptions and restrictions

Both the analytic and numerical results contained in this paper are restricted to plasma regions where Stark broadening has only a small effect on photon transport and can be neglected. The calculations encompass at most a few hundred optical depths in Ly α; hence, for only the first three lines of the Lyman series will photon transport in the far line wings be significant. Stark profiles follow approximately an inverse 2.0–2.5 power law[3] as a function of frequency separation from line center; for Voigt profiles, the asymptotic limit is an inverse power of 2.0. Therefore, if the Stark width is smaller than the Doppler width, the Stark wings will generally be considerably smaller than the Lorentz wings. This criterion is presently adopted in determining the maximum density to which our calculations can be reasonably extended. We obtain a specific density for argon from the tabulated Stark profiles of Kepple and Whitney,[5] and scale the criterion analytically for different atomic numbers.

In examining the Stark profiles for Ly α, Ly β, and Ly γ, it is clear that the upper density limit is set by the

broad, double-peaked profile of Ly β. For argon, an electron density of $\sim 2\times 10^{22}$ cm^{-3} is required for the Stark width to equal the Doppler width at temperatures of maximum Ar XVIII abundance. Accordingly, the analytic theory presented below is valid only up to this density for argon and the numerical calculations described in the next section have not been carried to higher densities.

This criterion for the negligibility of Stark effects is readily Z-scalable. Griem, Blaha, and Kepple[3] found that the Stark widths expressed in Å for analogous lines from different elements scale approximately as $Z^{-5}N_e^{2/3}$ near maximum ionic abundance temperature. The Doppler width, also expressed in Å, scales as $Z^{-1.5}$ at maximum abundance temperature. Therefore, the Stark width for the first three Lyman lines will be less than the Doppler width if

$$\left[\frac{18}{Z}\right]^5\left[\frac{N_e}{2\times 10^{22}}\right]^{2/3}\le\left[\frac{18}{Z}\right]^{1.5} \tag{1}$$

or

$$N_e\le 5.1\times 10^{15}\,Z^{5.25}\,. \tag{2}$$

Consequently, the present results are not valid at electron densities higher than those indicated by Eq. (2).

The relative populations of the $2p_{3/2}$ and $2p_{1/2}$ fine-structure levels, which are likely to prevail under different plasma conditions, have been a subject of investigation and debate for quite a few years.[8–14] Irons[13] has summarized the status of this work. Briefly, at the high- and low-density limits, ϵ, the ratio of the $2p_{1/2}$ to $2p_{3/2}$ sublevel populations, will equal 0.5, the statistical weight ratio of the states. Rapid collisional mixing ensures statistical equilibrium at high densities, and in the low-density coronal limit there is little pumping of the $2p$ states from $2s$; therefore, statistical populations prevail because only this process can cause departures from $\epsilon=0.5$. In the intermediate density regime, ϵ may reach values as high as 0.7–0.8, although the relative effects of electron-ion and ion-ion collisions are not yet precisely determined[10] and render this conclusion still somewhat uncertain. As pointed out by Sampson[12] and Irons,[13,14] substantial optical depth will reduce any tendency for a departure from statistical equilibrium. In view of the remaining uncertainties as well as the fact that the plasmas we analyze here are generally optically thick, we have assumed statistical population of the $j=\frac{1}{2}$ and $j=\frac{3}{2}$ sublevels ($\epsilon=0.5$) for all the plasmas considered here, for each hydrogenlike level. We also assume that the ion thermal velocities are sufficiently greater than the plasma differential motion to enable the plasma to be treated as stationary. Irons[13,14] has explored some of the consequences of substantial plasma differential motion for Ly-α opacity.

B. Analysis of opacity effects

The doublet splitting of the Lyman series is important as an opacity determinant when the separation of the components is comparable to the Doppler half-width ($\Delta\nu_D$) of the line. For specificity, the $\Delta\nu_D$ referred to here is the half-width of the Doppler line profile at e^{-1} of the central maximum. As pointed out by Irons,[13] the ratio of the fine-structure splitting to the Doppler half-width varies as $Z^{1.5}$ since the characteristic temperature for hydrogenlike-ion predominance varies as Z^2. Specifically, for Ly α,

$$(\Delta\nu)_f/(\Delta\nu)_D\approx 5.3\left[\frac{Z}{18}\right]^{1.5}\,. \tag{3}$$

For Ly β, the splitting relative to the Doppler width is about one-fourth the above value; for Ly γ, about one-tenth. Therefore, fine-structure opacity effects will have by far their greatest impact on Ly α, both because of its greater optical depth and because the splitting is greater relative to the Doppler line width. Our semiquantitative analytic model consequently focuses on Ly α.

Consider the $n=2$ hydrogenlike level, with the sublevels assumed statistically populated. For the moderate density plasmas considered here, this level is populated primarily by collisional excitation from the hydrogenlike ground state and by radiative excitation due to scattered Ly α photons. Depopulation occurs by a variety of processes, including spontaneous decay, collisional excitation and de-excitation, and (primarily collisional) ionization. We will follow the standard approximate procedure in accounting for radiative excitation by diluting the spontaneous decay rate A_{21} by the spatially averaged photon-escape probability P_e. This counts only those decays not resulting in re-excitation of the $n=2$ level. Letting C_{12} stand for the collisional excitation rate from $n=1$ in cm^3 sec^{-1}, D_2 represents the sum of all collisional processes depopulating the $n=2$ level; also in cm^3 sec^{-1}, a qualitatively correct equation for the steady-state population of the $n=2$ level is

$$N_1C_{12}N_e=N_2(A_{21}P_e+D_2N_e)\,. \tag{4}$$

In Eq. (4), N_1 and N_2 are the $n=1$ and 2 level population densities (cm^{-3}), N_e is the electron density (cm^{-3}), and the other symbols are defined above. It is useful to define a quenching probability P_Q—the probability that the $n=2$ level is collisionally depopulated during a Ly-α scattering

$$P_Q=D_2N_e/(A_{21}+D_2N_e)\,. \tag{5}$$

Combining Eqs. (4) and (5) leads to the following expression for the $n=2$ population density:

$$N_2=\frac{N_1C_{12}}{D_2}\left[1\Big/P_e\left[\frac{1-P_Q}{P_Q}\right]+1\right]\,. \tag{6}$$

The significance of Eq. (6) becomes apparent when considering P_e. The escape probability obtained will depend on whether the single-Voigt-profile approximation or the true fine-structure profile is used in the calculation. Letting P_e now stand for the escape probability, which would be obtained from the spurious single-Voigt-profile approximation, and P_{ef} refer to the true fine-structure-opacity escape probability, the ratio of population densities obtained with the correct opacity to that obtained with the single-profile opacity is

$$\frac{N_2(\text{with fine structure})}{N_2(\text{single Voigt})}=\frac{P_e(1-P_Q)+P_Q}{P_{ef}(1-P_Q)+P_Q}\,. \tag{7}$$

Equation (7) is obtainable from Eq. (6) with the (excellent) assumption that N_1 is not affected by fine-structure opacity. Note the limits implicit in Eq. (7). At very high densities, when $P_Q \to 1$, there is no difference in populations. Collisional processes control the level population. Also, when $P_e(1-P_Q)$ and $P_{ef}(1-P_Q)$ are both much smaller than P_Q, fine structure again has no effect on N_2. This corresponds to the effectively thick case, where most photons do not escape, even after many scatterings. The number of radiative excitations, while possibly large, is determined by collisional quenching, not by the detailed behavior of P_e or P_{ef}. However, when $P_Q \to 0$ the computed populations of $n=2$ are inversely proportional to the ratio of escape probabilities. Radiative excitation dominates the level if P_e (or P_{ef}) is substantially smaller than unity. For fine-structure opacity to be negligible (defined as having less than a 10% effect on population of $n=2$) we require

$$P_e(1-P_Q)+P_Q > 0.9P_{ef}(1-P_Q)+0.9P_Q \ . \tag{8}$$

In general, P_{ef} will exceed P_e. For Ly α, a single line of optical depth τ_0 is in effect replaced by two separate lines of optical depths $\frac{2}{3}\tau_0$ and $\frac{1}{3}\tau_0$ for $2p_{3/2}$ and $2p_{1/2}$, respectively. The escape probability at large optical depth for a Voigt profile is proportional to $\tau^{-1/2}$; hence, if there is no overlap of the doublet wings

$$\frac{P_{ef}}{P_e} = \left[\frac{1}{3}\left(\frac{\tau_0}{3}\right)^{-1/2} + \frac{2}{3}\left(\frac{2\tau_0}{3}\right)^{-1/2} \Big/ (\tau_0)^{-1/2} \right]$$

$$\approx 1.4 \ . \tag{9}$$

As discussed by Irons,[14] the assumption of no wing overlap fails for $\tau_0 \geq 10^2$; this failure will arise at lower τ_0 for small Z and higher τ_0 for large Z, according to Eq. (3) for the doublet spacing. However, since we seek a criterion for the *onset* of fine-structure-opacity effects, the ratio of Eq. (9) will be presently assumed. More exact results are given below in the section on numerical modeling. Combining Eqs. (8) and (9) yields the following criterion for the negligibility of fine-structure-opacity effects on population densities:

$$0.38\left(\frac{P_Q}{1-P_Q}\right) > P_e \ , \tag{10}$$

or employing Eq. (5)

$$0.38\left(\frac{D_2 N_e}{A_{21}}\right) > P_e \ . \tag{11}$$

To cast Eq. (11) into a more useful form, note that $A_{21} \approx 5\times 10^{13}(Z/18)^4$ sec^{-1}. Also, depopulation of the $n=2$ level is temperature, density, and Z dependent. Following Refs. 9–11, we will refer to the temperature in units of Z^2 Ry$=13.6Z^2$ eV. For temperatures of $(0.18\text{–}0.57)Z^2$ Ry (0.8 to 2.5 keV for argon) the depopulation of $n=2$, summed over the levels, has been calculated from the Coulomb-Born approximation[16] and is found to vary less than 20% from its value at $0.3Z^2$ Ry, where

$$D_2 = 2\times 10^{-10}\left(\frac{18}{Z}\right)^3 \tag{12}$$

in units of cm^{3}sec^{-1}. The temperature range $(0.18\text{–}0.57)Z^2$ Ry covers a large range of plasmas where hydrogenlike species are significantly present. Combining Eqs. (11) and (12) yields our final, Z-dependent criterion for less than 10% level population change due to fine-structure opacity

$$9.3\times 10^{-16} Z^{-7} N_e > P_e \ . \tag{13}$$

If the electron density is sufficiently high to render the inequality of Eq. (13) valid, fine-structure opacity—as compared to the single-Voigt-profile approximation—will affect the level populations by less than 10%. We again stress that Eq. (13) is to be applied to optically thick plasmas only—when the plasma is optically thin the fine-structure profiles cannot affect populations. The Voigt-profile escape probability P_e has been given in approximate analytic form by Athay.[15]

The effect on line emission of the doublet profile is perhaps of even more interest and importance than the change in population densities. Even though the populations may not be affected, the different effective escape probability can surely influence the Ly-α integrated intensity. The ratio of computed emission with fine-structure opacity to that obtained from a single Voigt profile is

$$\frac{I_f}{I_0} = \frac{N_2(\text{fine})A_{21}P_{ef}}{N_2(\text{single Voigt})A_{21}P_e} \ , \tag{14}$$

or, using Eq. (7),

$$\frac{I_f}{I_0} = \frac{P_{ef}}{P_e}\left(P_e + \frac{P_Q}{1-P_Q}\right) \Big/ \left(P_{ef} + \frac{P_Q}{1-P_Q}\right) \ . \tag{15}$$

The quantity $P_Q/(1-P_Q)$ is obtainable as above for the temperature range $(0.18\text{–}0.57)Z^2$ Ry, from Eqs. (5) and (12), and the expression for A_{21}

$$\left(\frac{P_Q}{1-P_Q}\right) \approx 2.45\times 10^{-15} N_e Z^{-7} \ . \tag{16}$$

Therefore,

$$\frac{I_f}{I_0} = \frac{P_{ef}}{P_e}\frac{P_e + 2.45\times 10^{-15} N_e Z^{-7}}{P_{ef} + 2.45\times 10^{-15} N_e Z^{-7}} \ . \tag{17}$$

Equation (17) is usable if P_e and P_{ef} can be calculated or estimated. If, as before, we assume $P_{ef} = 1.4P_e$ an approximate criterion for 10% enhancement of emission due to fine structure is obtainable,

$$5.2\times 10^{-15} N_e Z^{-7} > P_e \ . \tag{18}$$

The physical content of Eq. (18) is that, in an optically thick plasma with an electron density sufficiently high to validate the inequality, fine-structure opacity will result in a Ly-α intensity at least 10% higher than would be obtained from the single Voigt approximation.

We have demonstrated that the interplay of optical depth (as expressed by P_e) and the collisional quenching rate (as expressed by N_e), rather than either factor alone,

determines the importance of doublet-opacity effects on population densities and spectral emission. Several simple expressions obtained above express this interplay semiquantitatively and convincingly demonstrate the trends to be anticipated. We now turn to specific numerical results for further illumination of the question.

III. NUMERICAL MODEL

A. Model description

In order to validate and clarify the analytic approximations presented above, as well as provide more specific spectral diagnostics, we have performed an extensive series of numerical calculations centered on one element (argon). The calculations consist of a set of simultaneous solutions of the coupled atomic-rate and radiative-transfer equations for argon plasma cylinders where the varied parameters are temperature, density, and radius r, presumed much smaller than the length. These solutions have typically been carried out with both the more realistic doublet opacity and an assumed single Voigt profile for each parameter set.

The atomic model consists of 38 levels ranging from neutral Ar I to the bare nucleus (Ar XIX). Since our focus is on K-shell radiation, only ground states are carried through Be-like argon (Ar XV). For Li-like Ar XVI, the $1s^2 2s$, $1s^2 2p$, $1s^2 3s$, $1s^2 3p$, $1s^2 3d$, and $1s^2$, $n=4$ (composite) levels are modeled. The Ar XVII manifold includes $1s^2\,{}^1S$, $1s2s\,{}^3S$, $1s2p\,{}^3P$, $1s2s\,{}^1S$, $1s2p\,{}^1P$, the $n=3$ triplets and singlets, and $n=4$–7 composite levels. For Ar XVIII, $n=1$–5 are included. The various levels are connected through electron collisional excitation and deexcitation, collisional ionization and radiative recombination, three-body recombination, and, where appropriate, dielectronic recombination. Photoionization and photoexcitation are accounted for by solving the radiative transfer. All the modeled ionization edges are included as part of the radiative-transfer model. Additionally, all the optically thick resonance lines inherent in the level structure described above are also transported, along with the 2-3 line of Ar XVIII and the $1s2p\,{}^1P$–$1s3d\,{}^1D$ line of Ar XVII. While some of the higher levels have been omitted because of storage and efficiency considerations, the model provides a substantially complete description of the processes which form the dominant spectral lines of K-shell argon. A discussion of the atomic rate calculations is contained in Ref. 17. In all results presented below, the plasma is assumed to be in collisional-radiative equilibrium (CRE); namely, that each level-population density is in a steady state consistent with the atomic rates and photon fluxes produced by the other level populations.

Some improvements have been effected in our technique for carrying out the simultaneous, steady-state solution of the radiative-transfer and rate equations.[2,4,17–22] Reference 21 describes a multicell-coupling technique for radiative transfer in spherical and cylindrical geometries, based on frequency-integrated line escape probabilities. This method produces nearly exact solutions while employing only one ray angle and the computational equivalent of just one frequency per line. To account for doublet opacity, where escape probabilities have yet to be tabulated or fitted analytically, we have adopted a hybrid of the method of Ref. 21 and more conventional multifrequency approaches. The single-angle feature of Ref. 21 is retained but each line is divided into 17–43 frequency groups—depending on the line shape and optical depth. The coupling constants are defined in terms of individual frequencies (where the escape probability at each frequency is purely exponential) rather than individual lines. This also allows inclusion of continuum optical depths and line and continuum cross-pumping. Given the population densities a set of cell-to-cell photon coupling constants at each of more than 350 frequencies is thus obtainable.

The iteration technique by which self-consistency between the radiative-transfer and steady-state rate equations is obtained has also been significantly improved. The most straightforward and obvious procedure, using the radiation field from the previous iteration to calculate populations which then enables the radiation field to be recomputed until consistency is achieved, is known as Λ iteration. This technique is a very poor choice for low-density, high-optical-depth astrophysical problems[23] since the number of iterations required is approximately equal to the mean number of photon scatterings, which can be very large under such circumstances. However, the situation is not nearly so difficult for laboratory plasmas where the optical depths are smaller and the quenching probabilities larger than those which prevail in astrophysical situations, resulting in far fewer scatterings. We employ the mathematical equivalent of Rybicki's core-saturation method[24] and thereby render the Λ-iteration technique quite serviceable for laboratory plasma calculations. As noted by Rybicki,[24] the conceptual and computational simplicity of the technique is a very desirable feature, especially for complex multilevel problems.

To demonstrate our application of the core-saturation method for Λ iteration, we consider one line characterized by a profile-averaged photon escape probability from the plasma P_e and quenching probability P_Q. Let $N_u^{(i)}$ represent the upper level density obtained on the ith iteration and A the spontaneous decay probability. The photoexcitation rate for the ith iteration is therefore $N_u^{(i)}A(1-P_e)$. If C_u and D_u are the collisional creation and depopulation rates, respectively, for N_u, $N_u^{(i+1)}$ is obtained from the equation balancing gains and losses in the level

$$N_u^{(i+1)}(A+D_u)=C_u+N_u^{(i)}A(1-P_e)\,, \tag{19}$$

or

$$N_u^{(i+1)}=N_u^{(1)}+N_u^{(i)}(1-P_e)(1-P_Q)\,, \tag{20}$$

where $P_Q=D_u/(A+D_u)$ as before, and the upper level population for an optically thin plasma is given by the first iterative solution

$$N_u^{(1)}=\left[\frac{C_u}{A+D_u}\right]. \tag{21}$$

Equation (20) yields a recursive sum for the nth iteration's solution

$$N_u^{(n)}=N_u^{(1)}\sum_{i=0}^{n-1}[(1-P_e)(1-P_Q)]^i . \tag{22}$$

The slow convergence of the sum of Eq. (22) when $P_e, P_Q \ll 1$ precisely expresses the difficulty of Λ iteration. Note, however, that the sum is analytically evaluable to give

$$N_u^{(\infty)}=N_u^{(1)}\left[\frac{1}{1-(1-P_Q)(1-P_e)}\right] \tag{23}$$

and that this is exactly what is obtained for N_u on the *first* iteration if, in Eq. (19) A is replaced by AP_e instead of calculating excitations as $A(1-P_e)$. This is the essence of Rybicki's technique[24] of eliminating the readily absorbed line core photons. In practice, we apply the method by calculating, cell by cell, the escape probability from the plasma for each line by integrating over the absorption profile—including the continuum. The spontaneous emission coefficients are then diluted by this factor on the first iteration, which generally results in an excellent approximation to the final solution, especially near the plasma center. On subsequent iterations, the spontaneous emission coefficients are diluted in each cell by the escape probability from that cell and excitations are computed explicitly only for the line wing photons arriving from other cells. This completely general procedure usually converges within 20 iterations even for several hundred Ly-α optical depths. Convergence has been verified by starting with entirely different initial iterative solutions, and by quadrupling the number of iterations, both of which yield the same final level populations.

B. Z scaling of numerical results

In order that the results given below, specifically obtained for argon, may be readily applied to other low-to-medium-Z elements, we present the methodology for Z scaling in this section. Given a K-shell argon plasma of radius R_0, ion density N_I, and temperature T_e, the results may clearly be applied to a plasma of atomic number Z at a temperature of $T_e(Z/18)^2$. However, scaling the density and size is not quite so straightforward. To maintain the analogous level populations and spectrum, it is evident from the discussion in Sec. II that both the quenching probabilities and optical depths must remain the same. The quenching probability is determined by the ratio of collision rates—which scale as Z^{-3}—to spontaneous decay rates—which scale as Z^4. Since the quenching probability consequently scales as Z^{-7}, the electron density must scale as Z^7 to offset this. Therefore, the ion density must increase as Z^6 to maintain the same ratio of radiative to collisional rates as would prevail in an argon plasma. Finally, to maintain the same line optical depth τ_0, note that it is proportional to $R_0 N_I \lambda (M/T_I)^{1/2}$ where λ is the wavelength, M the ion mass, and T_I the ion temperature. Since $N_I \sim Z^6$, $\lambda \sim Z^{-2}$, $M \sim Z$, and $T_I \sim Z^2$, $\tau_0 \sim R_0 Z^{3.5}$. Therefore, the size must scale as $Z^{-3.5}$ to maintain the optical depth. In summary, a K-shell plasma of atomic number Z, radius $R_0(18/Z)^{3.5}$, ion density $N_I(Z/18)^6$, and temperature $T_e(Z/18)^2$ will produce the same spectrum as an argon plasma of radius R_0, ion density N_I, and electron temperature T_e. The "same" spectrum is defined as the same relative intensities of the lines. Absolute intensities will differ due to the differing line photon energies and total numbers of emitting ions. We recommend Z scaling only for $13 \lesssim Z \lesssim 26$ from the $Z=18$ results presented below, since the $Z^{1.5}$ scaling of fine-structure splitting [Eq. (3)] will spoil the applicability of the scaling far from $Z=18$.

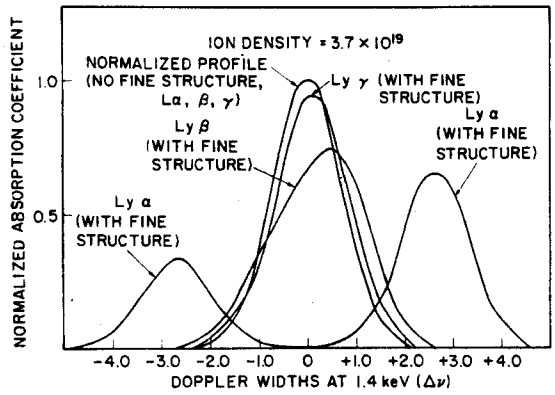

FIG. 1. Normalized fine-structure profiles of the absorption coefficients of Ar XVIII Ly α, β, and γ are compared to the single Voigt profile which would characterize the opacity in the absence of fine-structure splitting.

C. Numerical results

In Fig. 1 the doublet absorption profiles for Ar XVIII Ly α, Ly β, and Ly γ are shown along with the single Voigt profile which would characterize the line opacity in the absence of fine structure. The profiles are normalized for case of comparison. Plasma conditions of ion temperature 1.4 keV and ion density 3.7×10^{19} cm^{-3} are assumed. Note that the Ly-α profile is split into two distinct features since the doublet components are ~ 5 Doppler widths apart. However, both Ly β and Ly γ appear quasi-Gaussian, with a skewing of the profile toward the stronger of the fine-structure components. For Ly γ, the change from the single Voigt profile is quite small.

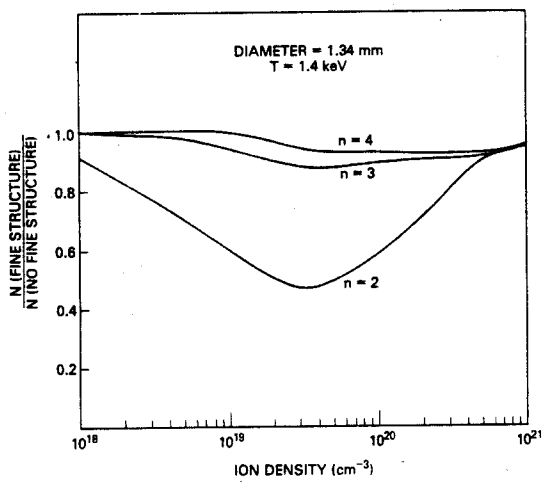

FIG. 2. Ratio of the $n=2$, 3, and 4 Ar XVIII populations obtained with the correct fine-structure profiles to those obtained using a single Voigt profile are plotted against ion density for the indicated cylindrical plasma temperature and diameter.

Therefore, the following results will concentrate on Ly-α and Ly-β power outputs and line ratios which could reflect those outputs as influenced by fine-structure opacity.

In Fig. 2 the ratio of populations calculated with realistic doublet opacities to those which would prevail in the absence of fine structure is plotted against density, for an argon plasma temperature of 1.4 keV and a diameter of 1.34 mm. The changes in $n=3$ and 4 are 15% or less, whereas, for an ion density of $\sim 3\times 10^{19}$ cm^{-3}, the $n=2$ population is reduced by a factor of 2. For all three levels, the population ratio approaches unity at both low and high densities, consistent with Eq. (7). For the $1s_{1/2}$-$2p_{3/2}$ component, the line-center optical depths are 0.14, 2, 47, and 420 at ion densities of 10^{18}, 10^{19}, 10^{20}, and 10^{21} cm^{-3}, respectively. The corresponding optical depth of a single Voigt profile, τ_0, would be 50% greater. Since $N_e \approx 18 N_I$, $\tau_0 \approx 3.5\times 10^{-20} N_e$ for ion densities between 10^{20} and 10^{21} cm^{-3}. The approximate escape probability for a Voigt profile[15] is given as a function of the damping parameter a and optical depth τ_0 for $\tau_0 \gg 1$:

$$P_e \approx 0.85 \left[\frac{a}{\tau_0} \right]^{1/2} . \tag{24}$$

The damping parameter a for a resonance line is

$$a = \frac{\Gamma}{4\pi \Delta \nu_D} , \tag{25}$$

where the upper-state inverse lifetime Γ for Ly α is mostly determined by radiative decay in this density range. The Doppler width $\Delta\nu_D$ at 1.4 keV is 2.2×10^{14} Hz. Including the collisional contribution, $a \approx 2.5\times 10^{-2}$ for these densities, and Eqs. (24) and (13) may be combined to obtain the electron density at which a 10% departure of $n=2$ population due to fine-structure opacity would be expected according to the analytic theory

$$9.3\times 10^{-16}(18)^{-7} N_e > 0.85 \left[\frac{2.5\times 10^{-2}}{3.5\times 10^{-20} N_e} \right]^{1/2} \tag{26}$$

which yields an electron density of 6.1×10^{21} cm^{-3}, equivalent to an ion density of 3.4×10^{20} cm^{-3} which is in excellent agreement, considering the approximations, with the numerically calculated value of 4.5×10^{20} (Fig. 2).

The most experimentally detectable consequence of fine structure is certainly spectroscopic effects. The analytic results presented above also contain [Eq. (18)] an electron-density criterion for 10% enhancement of Ly α. In Fig. 3 we present two line ratios which are both temperature and density sensitive: He $1s^2$—$1s4p\ ^1P$/Ly β and He $1s^2$—$1s3p\ ^1P$/Ly α, as a function of density, with and without the correct doublet opacity. The ratios decrease substantially with density even with fixed temperature (1.4 keV) and plasma diameter (1.34 mm) since higher collision rates and optical depths increase the excitation and ionization state of the plasma. However, at the highest densities the Ar XVII to Ar XVIII line ratios level off and then increase. This is primarily due to the increased opacity of the Lyman lines coupled with the decreased opacity of the heliumlike lines as the average charge state of the plasma increases with density. The double valuing of line ratios

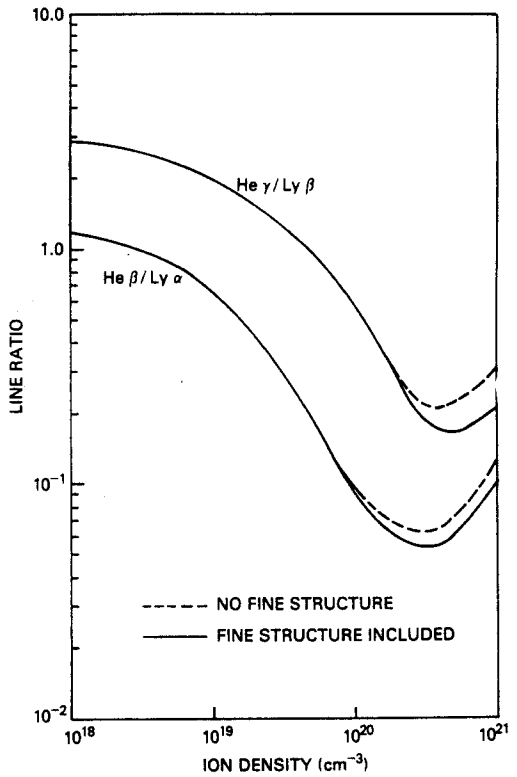

FIG. 3. Line ratios Ar XVII $1s^2$—$1s3p\ ^1P$/Ly α and Ar XVII $1s^2$—$1s4p\ ^1P$/Ly β are plotted against ion density for a plasma diameter of 1.34 mm and temperature 1.4 keV. Where fine-structure opacity results in significant differences, it is indicated.

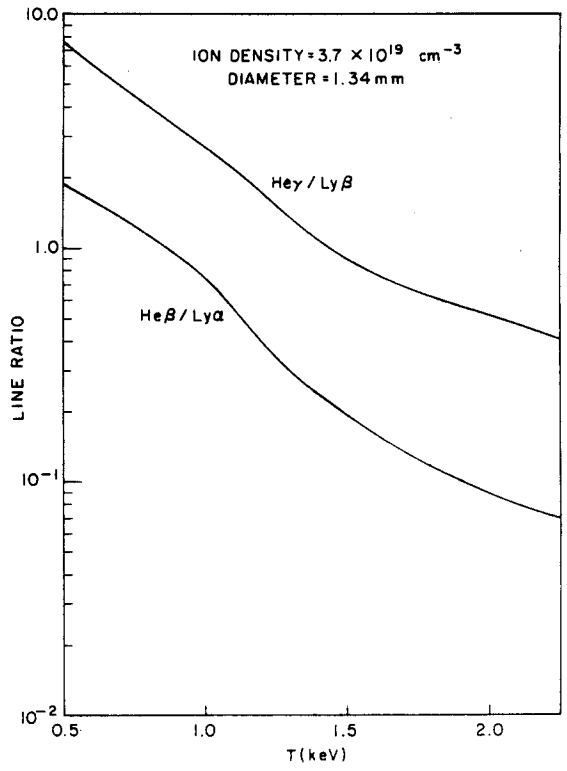

FIG. 4. Same line ratios of Fig. 3 are plotted against temperature for the same size cylindrical argon plasma (1.34 mm) at an ion density of 3.7×10^{19} cm^{-3}, where the presence of fine structure makes no difference.

due to opacity effects has been noted elsewhere.[19] At ion densities of $\sim 10^{20}$ and higher, the dichotomy between fine-structure and single-profile calculations is noticeable; it reflects the higher power outputs of both Ly α and Ly β due to the greater effective escape probabilities of the doublet profiles. For Ly α, these results provide another point of comparison with the theory of Sec. II. According to Eq. (18), the Ly-α line intensity should be enhanced by 10% when

$$5.2\times 10^{-15} N_e Z^{-7} > P_e \ . \tag{18}$$

Equation (24), plus the fact that $\tau_0 \approx 3.5\times 10^{-20} N_e$ allows Eq. (18) to be solved for N_e; the result predicts a 10% power enhancement at $N_I \approx N_e/18 = 1.1\times 10^{20}$ cm^{-3}, in excellent agreement with the numerically calculated value of 1.3×10^{20} cm^{-3} (Fig. 3).

Figures 4 and 5 present this same ratio as a function of temperature, again for a plasma of fixed diameter 1.34 mm. In Fig. 4 the ion density is 3.7×10^{19} cm^{-3}. At these relatively modest optical depths (~ 10 for Ly α) the ratios are single valued and a very good temperature indicator. Also, fine structure does not affect the power output at this density; therefore, only one curve appears for each line ratio. This may be contrasted with Fig. 5 where the same information is presented at the considerably higher ion density of 10^{21} cm^{-3}. Fine-structure opacity noticeably depresses the line ratios for the entire temperature range considered. Also, the much larger optical depths virtually eliminate the temperature sensitivity of the ratios above 1.0 keV; as the population of Ar XVIII increases with temperature, so does the opacity, which considerably reduces the tendency of the Lyman line to increase in intensity. At an ion density of 3.7×10^{19} cm^{-3}, the Lyman photons generally escape after a few scatterings; at 10^{21} cm^{-3}, they are mostly collisionally quenched.

The fact that the enhancement of Ly β is comparable to that of Ly α may seem puzzling in light of the fact that the Ly-β profile is not so drastically affected by fine structure (Fig. 1). However, the Lorentz wings of the profile are substantially enhanced by the increase in damping parameter (i.e., reduction in level lifetime) when collisions transferring population among fine-structure levels are considered. At such high opacities, substantial numbers of photons can escape only in these far wings—resulting in the Ly-β power increase. For Ly α, as noted above, the upper level lifetime is still mostly determined by its very high radiative decay rate, even when collisions among fine-structure levels are considered.

Finally, in Fig. 6 we present the evolution of the emitted Ly-α profile as a function of density for a temperature of 1.4 keV and a plasma diameter of 1.34 mm. At $N_I = 10^{18}$ cm^{-3}, the $2p_{3/2}$ component is twice the strength of the $2p_{1/2}$ since the lines are optically thin at this density. At 6×10^{18} cm^{-3}, $\tau_0 \approx 1$ and the $2p_{3/2}$ component begins to saturate to the value of the source function—allowing the $2p_{1/2}$ to begin to approach its intensity. At 3.7×10^{19} cm^{-3}, full saturation has occurred—the components are of equal intensity and a small self-reversed core is seen in each. The profiles at ion densities of 10^{20} and 3×10^{20} cm^{-3} are qualitatively similar to that at

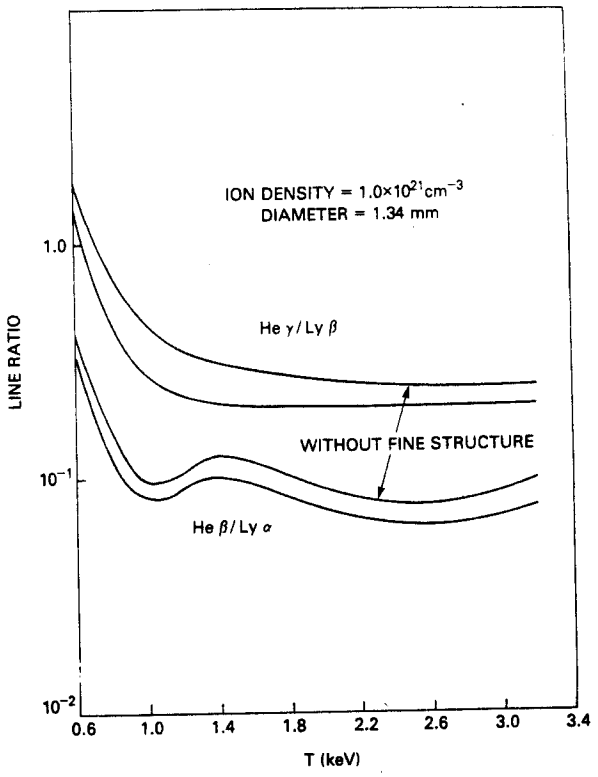

FIG. 5. Same as Fig. 4, except the density is 10^{21} ions per cm^{-3}. At this density the result depends upon the details of the fine-structure profile and such is indicated.

3.7×10^{19} cm^{-3} except that the higher optical depths produce deeper self-reversed cores. At ion densities of 7.5×10^{20} cm^{-3} and 10^{21} cm^{-3}, the profiles have a peculiar three-pronged appearance. The three peaks appear where the profile optical depth is approximately unity—one peak on each of the far wings of the components, with another emission peak occurring at the absorption minimum between the two components.

Because of this density sensitivity, the Ly-α profile is potentially an excellent density diagnostic. Since the pro-

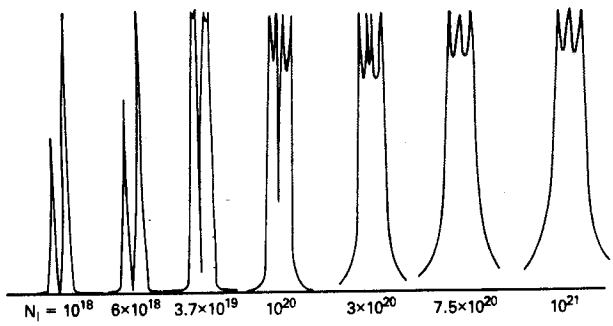

FIG. 6. Evolution of the emitted Ly-α profile is presented as a function of density for an argon plasma of 1.4 KeV and diameter 1.34 mm. The splitting of the two components (visible at the lowest density) is 5.4 mÅ and this horizontal scale is maintained throughout. The absolute intensities have been normalized for ease of comparison.

files depend on optical depth as well as density, the size of the plasma must be ascertained to fully exploit this technique. Experimental methods such as x-ray pinhole photography would be quite valuable for this purpose. Also, spectral resolution of $\sim 1-2$ mÅ will be required, independently of Z.

ACKNOWLEDGMENTS

The authors would like to express their appreciation to Dr. P. C. Kepple and Dr. H. R. Griem for several valuable discussions. This work was supported by the U. S. Defense Nuclear Agency.

[1]E. H. Avrett and D. G. Hummer, Mon. Not. R. Astron. Soc. 130, 295 (1965).
[2]J. P. Apruzese, J. Davis, D. Duston, and K. G. Whitney, J. Quant. Spectrosc. Radiat. Transfer 23, 479 (1980).
[3]H. R. Griem, M. Blaha, and P. C. Kepple, Phys. Rev. A 19, 2421 (1979).
[4]J. P. Apruzese, P. C. Kepple, K. G. Whitney, J. Davis, and D. Duston, Phys. Rev. A 24, 1001 (1981).
[5]P. C. Kepple and K. G. Whitney, Naval Research Laboratory (NRL) Memorandum Report No. 4565, 1981 (unpublished).
[6]A. Hauer, K. G. Whitney, P. C. Kepple, and J. Davis, Phys. Rev. A 28, 963 (1983).
[7]R. W. Lee, J. Quant. Spectrosc. Radiat. Transfer 27, 87 (1982).
[8]R. J. Hutcheon and R. W. P. McWhirter, J. Phys. B 6, 2668 (1973).
[9]I. L. Beigman, V. A. Boiko, S. A. Pikuz, and A. Ya. Faenov, Zh. Eksp. Teor. Fiz. 71, 975 (1976) [Sov. Phys.—JETP 44, 511 (1976)].
[10]A. V. Vinogradov, I. Yu. Skobelev, and E. A. Yukov, Fiz. Plazmy 3, 686 (1977) [Sov. J. Plasma Phys. 3, 389 (1977)].
[11]V. A. Boiko, A. V. Vinogradov, S. A. Pikuz, I. Yu. Skobelev, A. Ya. Faenov, and E. A. Yukov, Fiz. Plasmy 4, 97 (1978) [Sov. J. Plasma Phys. 4, 54 (1978)].
[12]D. H. Sampson, J. Phys. B 10, 749 (1977).
[13]F. E. Irons, Aust. J. Phys. 33, 283 (1980).
[14]F. E. Irons, J. Quant. Spectrosc. Radiat. Transfer 24, 119 (1980).
[15]R. G. Athay, *Radiation Transport in Spectral Lines* (Reidel, Dordrecht, 1974), pp. 22–24.
[16]L. A. Vainshtein and I. I. Sobel'man, Lebedev Report No. 66, 1967 (unpublished); I. I. Sobel'man, *Introduction to the Theory of Atomic Spectra* (Pergamon, New York, 1972).
[17]D. Duston and J. Davis, J. Quant. Spectrosc. Radiat. Transfer 27, 267 (1982).
[18]J. P. Apruzese, J. Davis, and K. G. Whitney, J. Appl. Phys. 48, 667 (1977).
[19]D. Duston and J. Davis, Phys. Rev. A 21, 932 (1980).
[20]K. G. Whitney, J. Davis, and J. P. Apruzese, Phys. Rev. A 22, 2196 (1980).
[21]J. P. Apruzese, J. Quant. Spectrosc. Radiat. Transfer 25, 419 (1981).
[22]D. Duston, J. Davis, and P. C. Kepple, Phys. Rev. A 24, 1505 (1981).
[23]D. Mihalas, *Stellar Atmospheres* (Freeman, San Francisco, 1970), pp. 152–155.
[24]G. B. Rybicki, Conference on Line Formation in the Presence of Magnetic Fields, National Center for Atmospheric Research Report, Boulder, 1971 (unpublished).

PHYSICAL REVIEW A VOLUME 22, NUMBER 5 NOVEMBER 1980

Influence of broadband photocoupling on K-shell excitation in aluminum

K. G. Whitney
Optical Sciences Division, Naval Research Laboratory, Washington, D. C. 20375

J. Davis
Plasma Radiation Group, Naval Research Laboratory, Washington, D. C. 20375

J. P. Apruzese
Science Applications, Inc., McLean, Virginia 22102
(Received 11 September 1979)

A detailed theoretical model of the collisional and radiative couplings within the aluminum K shell is described which has been used to self-consistently calculate the functional dependence of the excitation state of the K shell and its emission spectrum on ambient plasma conditions for a wide range of K-shell opacities. Both line and continuum couplings are included in the model over a range of photon energies from 442 eV to 6.13 keV. The approach of the interior of the aluminum plasma to local thermodynamic equilibrium has been investigated for millimeter sized plasmas where the K-shell couplings are photodominated and the plasma interior must come into radiative equilibrium. The approach of the K-series emission spectrum, which includes satellite and intercombination lines of the heliumlike resonance line, to the blackbody curve is computed. Temperature variations of the power output in continuum and line radiation are also computed and discussed. Finally, a set of calculations that relate to the ability of an external source of x radiation to selectively photopump the $3p$ state and maintain an inversion between $2p$-$3d$ levels within the heliumlike ionization stage is described. Two important effects are seen. One, the opacity of the heliumlike $L\alpha$ line plays an important role in determining the ability of the external radiation to invert levels within the plasma interior, and two, the inversion saturates with increasing pump strengths as the heliumlike ground-state population is depleted by the pump.

I. INTRODUCTION

In the gray-body approximation of radiation transport theory,[1] the detailed atomic structure of the radiating medium is, by definition, ignored so that the absorption coefficient over the broadband of the emitted radiation can be taken to be frequency independent. As a result of this assumption, appropriately frequency averaged absorption coefficients are used, the two most common being the Planck and Rosseland means corresponding to optically thin and thick physical situations, respectively, depending on the size and density of the emission region. In addition, the medium is usually restricted to be in local thermodynamic equilibrium (LTE). Then, the source function for the radiation field can be specified to be the blackbody source function, $B_\nu(T_e)$.

In this paper, we will investigate the behavior of aluminum as a broadband source of kilovolt x rays starting from a much more ambitious set of theoretical assumptions and objectives than are used in the gray-body approximation. LTE conditions will not be assumed. Rather, we shall study the approach of aluminum to LTE as a combined function of electron-ion and radiation field-ion interactions. In addition, special emphasis will be placed on the calculation of self-consistent aluminum K-shell emission spectra as they approach the blackbody curve. Thus, the detailed frequency dependence of both the source function and the absorption coefficient will have to be determined from a detailed treatment of the aluminum medium and vice versa. Steady-state conditions will be assumed in these calculations.

Because of the relative simplicity of one- and two-electron optical spectra, emission from the hydrogenlike and heliumlike ionization stages within the K shell produces one of the simplest spectra to analyze in detail. However, even in this case, approximations must be made with respect to the amount of spectral detail and energy-level structure employed in the calculations. Nevertheless, one can be guided, as we have, by experiment in order to model either the most prominent or some of the most diagnostically important features of the K-shell emission spectrum. Furthermore, only through a detailed treatment of the major photocouplings and of the competing coupled emission and absorption processes can both diagnostic and dynamic information on the aluminum plasma's collisional-radiative state be self-consistently determined.

II. IONIZATION MODEL

The K-shell spectrum we have chosen to compute as well as the couplings to the aluminum plasma that both produce and self-absorb this radiation are shown in Fig. 1. The spectrum consists of

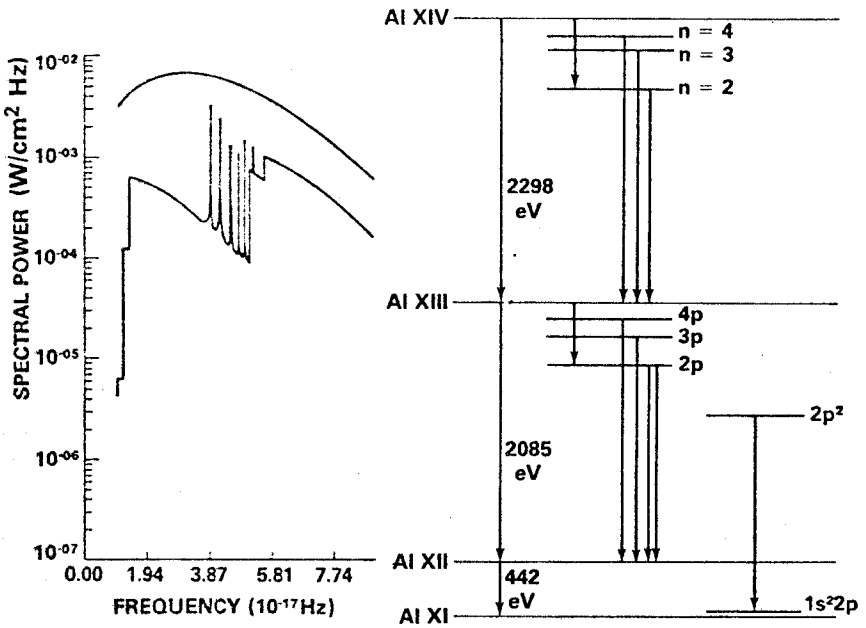

FIG. 1. The K-series aluminum spectrum on the left is calculated from the radiative transitions connecting the Al XI-XIV energy levels shown on the right. Also listed are the locations of the aluminum ground-state–to–ground-state radiative recombination emission edges.

five free-bound continua and eight lines whose upper ionic states lie in the hydrogenlike and heliumlike manifold of states. The spectrum begins at the emission edge of the Al XII to Al XI (He – Li) radiative recombination continuum at 442 eV and extends to 6.13 keV, far into the wings of the Al XIV to Al XIII (Z – H) and Al XIII to Al XII (H – He) recombination continua. Lyman α-, β-, and γ-like line emission from Al XII and Al XIII is computed along with the $1s^2$-$1s2p\,^3P$ intercombination line in Al XII and the $1s^2\,2p$-$1s2p^2\,^2D$ satellite line in Al XI. These lines lie on the background continuum which is produced by the He–Li, Z – H(n =2), and H – He($1s2p\,^3P$) recombinations. The H-like $L\gamma$ line also lies on the generally strong H – He continuum.

The excited-state structure of our aluminum ionization model consists only of the K-shell levels shown in Fig. 1 together with $1s2s\,^1S$, $1s3s\,^1S$, and $1s3d\,^1D$ states in Al XII and $2p$, $3s$, $3p$, $3d$, and $4d$ states in Al XI. Only the radiative couplings shown in Fig. 1 are included in this model, e.g., both Balmer and lithiumlike line emission are purposefully suppressed. Thus, all of our radiative couplings to the aluminum K shell can be fully detail balanced as blackbody radiation energy densities within the medium are reached. As a consequence, collisional-radiative equilibrium (CRE) calculations performed with this model can sensitively model the aluminum K shell's approach to LTE even under conditions where its radiative couplings are much stronger than the corresponding collisional couplings.

Because of the generally local nature of electron-ion interactions and in spite of the fact that the strength of many of the K-shell radiative interactions can be and often are much stronger than the corresponding strength of the collisional interactions, it has historically been the case that CRE calculations emphasize and are much fuller in their collisional than in their radiative couplings. A similar condition exists within the present state of our aluminum K-shell model, i.e., it contains a complete network of collisional transitions and only the partial (13) set of radiative transitions described above. The density and temperature behavior of the rate coefficients coupling the level structure in Al XI has been described in one of our earlier papers.[2] The 5 bound excited states are fully coupled collisionally to one another and to the Al XI and Al XII ground states. The $1s2p^2$ autoionizing state, on the other hand, is excited only by dielectronic recombination from the Al XII ground state. It decays radiatively to the $1s^2\,2p$ state and by autoionization with a rate of 1.41×10^{14} sec^{-1}, which was computed recently.[3] The excited states within the Al XII and Al XIII ionization stages are also fully coupled collisionally. The level structure and collisional couplings for this aluminum K-shell model are identical to the structure and couplings that we used in a previously described carbon K-shell ionization model.[4]

III. CRE EQUATIONS–PLASMA MODEL

Since we are interested in the full CRE behavior of the aluminum K shell for a widely varying set of plasma conditions, the ionization dynamics and K-shell emission spectrum must be computed from one another self-consistently. Hence, the major computational problem is not just to solve the radiation transport equation, but to calculate a self-consistent set of photocouplings, and to relate the strength of these couplings to the calculated emission spectrum. If we let N_a denote the population density of the ath ionization state of the plasma and W_{ab} denote the total rate of the transitions from the bth to the ath state, then in CRE, N_a must be determined by solving the following set of rate equations:

$$\sum_b W_{ab}(N_e, U_\nu) N_b = 0 , \tag{1}$$

$$\sum_b N_b = N_i , \tag{2}$$

and

$$\sum_b Z_b N_b = N_e . \tag{3}$$

N_i is the total ion density, N_e is the electron density, U_ν, the radiation energy density at frequency ν, and Z_b is the ionic charge of the bth state. Because of the rate coefficient dependence on U_ν, solutions to Eqs. (1)–(3) are geometry dependent. In a planar geometry, U_ν can be calculated by solving a transport equation for the specific intensities, $I_\nu(\mu, z)$, of the form[5]

$$\mu \frac{d}{dz} I_\nu = + k_\nu (S_\nu - I_\nu) , \tag{4}$$

where μ is the cosine of the angle between the light ray and the normal to the plane along which z is calculated. k_ν and S_ν are the absorption coefficient and source function, respectively, of the radiation at frequency ν. U_ν (in units of ergs/cm^3 Hz) is found from I_ν by averaging over the angles of the different ray directions:

$$U_\nu(z) = \frac{2\pi}{c} \int_{-1}^{1} d\mu \, I_\nu(\mu, z) . \tag{5}$$

In addition the emission spectrum $W(\nu)$ (in units of erg/cm^2 sec Hz), is calculated from the first moment of I_ν evaluated at the surface of the plasma:

$$W(\nu) = 2\pi \int_{-1}^{1} d\mu \, \mu I_\nu(\mu, z = Z_0) . \tag{6}$$

The ionization and emission behavior of aluminum that is described in this paper is obtained from solutions to Eqs. (1)–(6).

Photon coupling to a set of rate equations can be carried out through the use of Einstein A and B coefficients, which satisfy the detail balance relations,[6]

$$B_{ab}(\nu) = \frac{A_{ab}(\nu)}{(8\pi\nu^2/c^3)h\nu} , \tag{7}$$

$$B_{ba}(\nu) = (N_b/N_a)_{\mathrm{LTE}} \, e^{h\nu/kT_e} B_{ab}(\nu) , \tag{8}$$

where $(\,)_{\mathrm{LTE}}$ denotes that LTE relative values of the population densities are to be taken. The A coefficients can be factored into a total decay rate, A_{ab}^T, times a profile function $\phi_{ab}(\nu)$, where $\int \phi_{ab}(\nu) d\nu = 1$:

$$A_{ab}(\nu) \equiv A_{ab}^T \phi_{ab}(\nu) . \tag{9}$$

For free-bound continuum emission, ϕ was taken to have the form[7]

$$\phi_{ab}(\nu) = \eta_+(\nu - \nu_{ba})(h/kT_e) e^{h(\nu_{ba} - \nu)/kT_e} , \tag{10}$$

where $h\nu_{ba} \equiv E_b - E_a$ is the energy difference between the ionic states of the transition and η_+ is the Heaviside function:

$$\eta_+(\nu) = \begin{cases} 1, & \nu \geq 0 \\ 0, & \nu < 0 . \end{cases} \tag{11}$$

The total rate of radiative recombination, A_{ab}^T

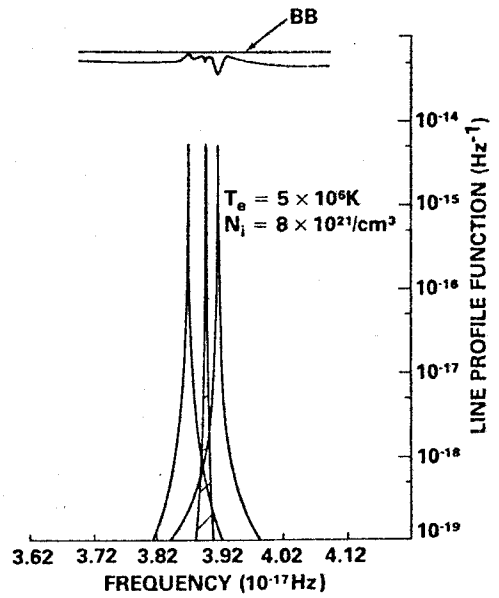

FIG. 2. On the bottom of this figure, the calculated line profile functions of the heliumlike resonance, intercombination, and satellite lines are drawn for an electron temperature of 5×10^6 K, an ion density of 8×10^{21} cm^{-3}, and a 2-mm thick planar plasma. On the top of the figure, the calculated emission spectrum of these lines under these plasma conditions is compared to the blackbody curve.

$\equiv N_e \alpha_{ab}(T_e)$, was calculated using Seaton's formula,[8]

$$\alpha_{ab}(T_e) = 5.2\times10^{-14} Z_b \lambda^{1/2}(0.43 + \tfrac{1}{2}\ln\lambda + 0.47/\lambda^{1/3}) , \quad (12)$$

where $\lambda \equiv h\nu_{ba}/kT_e$.

For line emission, energy and momentum conservation imply that ϕ_{ab} has the form, which is compatible with Eqs. (7) and (8):

$$\phi_{ab}(\nu) = e^{-h(\nu-\nu_{ba})/2kT_e}\,\phi^V_{ab}(\nu) , \quad (13)$$

where $\phi^V_{ab}(\nu)$ was taken in our calculations to be a Voigt profile whose collisional width was determined from the total lifetime, including stimulated emission (i.e., power broadening), of the excited state b.[9] Thus, at high plasma densities, where the collisional lifetime of the excited state exceeds the radiative lifetime, the Voigt parameter, $a \equiv \Delta\nu_c/\Delta\nu_D$, which is the ratio of collisional to Doppler linewidths, becomes linearly dependent on electron density. Finally, the following set of calculated values for the spontaneous radiative decay rates A^T_{ab} were used in our calculations:

	Transition	A (sec^{-1})
AlXIII	$n=1$-$n=2$	1.34×10^{13}
	$n=1$-$n=3$	1.59×10^{12}
	$n=1$-$n=4$	3.66×10^{11}
AlXII	$1s^2$-$1s2p\,^3P$	2.54×10^{10}
	$1s^2$-$1s2p\,^1P$	2.83×10^{13}
	$1s^2$-$1s3p\,^1P$	7.71×10^{12}
	$1s^2$-$1s4p\,^1P$	3.2×10^{12}
AlXI	$1s^2 2p$-$1s2p^2\,^2D$	1.3×10^{13}

Local photocoupling within the plasma occurs by means of Eqs. (1). The long-range, cross-coupled nature of the radiation interactions manifests itself in Eq. (4), which can be placed in the form,

$$\mu\frac{d}{d\tau_\nu} I_\nu = I_\nu - S_\nu , \quad (14)$$

where the increment $d\tau_\nu$ in optical depth is defined as $d\tau_\nu \equiv -k_\nu dz$. In general, S_ν and k_ν must be computed by summing over the various processes in which a photon at a given frequency is emitted or absorbed within the plasma. Each of the eight line profiles was calculated over a frequency interval that overlapped with the neighboring line profile. Thus, at high densities emission in the wings of one line is partially reabsorbed by and pumps the line nearest it in the spectrum. The greatest overlap of line and continuum processes, however, occurs in the vicinity of the resonance, intercombination, and satellite triplet of lines. Their overlapping line profiles are drawn in Fig. 2 at an aluminum ion density of 8×10^{21} cm^{-3} and at an electron temperature of 5×10^6 K. As an illustration of the net outcome of this line coupling, a calculated emission spectrum is shown above the line profiles in comparison to the 5×10^6 K blackbody emission curve. In the vicinity of these lines k_ν and $j_\nu \equiv k_\nu S_\nu$ must be calculated by summing over the different line and continuum processes that couple in this frequency interval:

$$k_\nu = k_\nu^{\mathrm{RL}} + k_\nu^{\mathrm{IL}} + k_\nu^{\mathrm{SL}} + k_\nu^{\mathrm{C}} , \quad (15)$$

$$j_\nu = j_\nu^{\mathrm{RL}} + j_\nu^{\mathrm{IL}} + j_\nu^{\mathrm{SL}} + j_\nu^{\mathrm{C}} , \quad (16)$$

where the superscripts, RL, IL, SL, and C denote resonance line, intercombination line, satellite line, and continuum, respectively. The continuum absorption and emission coefficients are, in turn, sums over the three free-bound transitions in Fig. 1 that radiate into the frequency interval around this triplet of lines. Finally, self-consistency with the photocouplings in Eqs. (1) requires that the individual absorption and emission coefficients be related to the Einstein A and B coefficients by the expressions

$$(k_\nu)_{ab} = (h\nu/c)[B_{ba}(\nu)N_a - B_{ab}(\nu)N_b] , \quad (17)$$

$$(j_\nu)_{ab} = (h\nu/4\pi)A_{ab}(\nu)N_b . \quad (18)$$

In solving Eqs. (1)–(18), we made no attempt to fully resolve the spatial variations of the population and radiation energy densities that are introduced by their mutual interactions even under the assumptions we made that the plasma had a uniform total ion density and uniform electron and ion temperatures. Nevertheless, the calculations generated a good deal of information about the aluminum plasma's radiative behavior. Moreover, they were self-consistent and demonstrated important effects of the induced spatially varying photocouplings. In all, in the calculations that were performed, a symmetric plasma problem was assumed, half of the plasma was divided into 11 cells, and the temperature dependence of 167 collisional rate coefficients was calculated along with 29 population densities, 136 radiation energy densities, and 13 photocouplings per cell.

IV. APPROACH TO THERMODYNAMIC EQUILIBRIUM

In order to reach thermodynamic equilibrium, the combined ionic radiation system must satisfy this condition: the population densities must attain their LTE values (N_a^*) enabling the source function to reach blackbody values,

$$B_\nu(T_e) = \frac{2h\nu^3/c^2}{e^{h\nu/kT_e} - 1} . \quad (19)$$

If we focus our attention, for example, on an excited state of the plasma of population density N_u which undergoes a radiative transition to a lower lying state having a population density N_l, then, in general, in collisional-radiative equilibrium,

$$(W^{CD}+W^{PD}+W^{OD})N_u=(W^{CE}+W^{PE})N_l+\sum_{p(p\neq l)}W_pN_p. \tag{20}$$

In this equation, W^{CE}, W^{CD}, W^{PE}, and W^{PD} denote the collisional and radiative excitation and deexcitation rates, respectively, that connect states l and u directly. W^{OD} represents the sum over all rates for which u deexcites to other states than l. Finally, $\sum W_pN_p$ represents the sum over all excitation processes of the upper state that originate from states other than l. We can solve Eq. (20) for the ratio of the population densities:

$$\frac{N_u}{N_l}=\frac{W^{CE}+W^{PE}+\sum_p W_p(N_p/N_l)}{W^{CD}+W^{PD}+W^{OD}}. \tag{21}$$

Then, if one defines b_{ul} to be this ratio when the plasma is in LTE,

$$b_{ul}\equiv\frac{N_u^*}{N_l^*}=\frac{W^{CE}}{W^{CD}}=\frac{g_u}{g_l}e^{-h\nu_{ul}/kT_e}, \tag{22}$$

a measure of the extent to which the plasma is out of LTE can be defined by

$$\epsilon_{ul}\equiv 1-(N_u/N_l)/b_{ul}. \tag{23}$$

From Eq. (21) one then finds that

$$\epsilon_{ul}=f^{PD}(1-s^P/b_{ul})+f^{OD}(1-s^O/b_{ul}), \tag{24}$$

where

$$f^{PD}\equiv\frac{W^{PD}}{W^{CD}+W^{PD}+W^{OD}}, \tag{25}$$

$$f^{OD}\equiv\frac{W^{OD}}{W^{CD}+W^{PD}+W^{OD}}, \tag{26}$$

$$s^P\equiv W^{PE}/W^{PD}, \tag{27}$$

$$s^O\equiv\sum_p\frac{N_p}{N_l}\frac{W_p}{W^{OD}}. \tag{28}$$

Thus, the degree to which the population densities are out of LTE is given by a weighted average over the degrees to which (1) photoexcitation and deexcitation processes and (2) other quenching processes that connect to the upper level do not separately detail balance. The weighting factors are branching ratios that determine the relative strengths of the three distinguished deexcitation processes.

A similar analysis can be carried out for the source function S_ν, which can be written, in general, in the form

$$S_\nu\equiv(j_\nu^L+j_\nu^C)/(k_\nu^L+k_\nu^C), \tag{29}$$

where j_ν^L and k_ν^L are the total emission and absorption coefficients of the eight overlapping lines in the calculation. In an infinite, uniform medium, for example, the departure of the radiation field from that of a blackbody field can be defined in terms of the departure of the source function from B_ν:

$$\epsilon_\nu\equiv 1-S_\nu/B_\nu. \tag{30}$$

Then, from Eq. (29), one finds that

$$\epsilon_\nu=F_\nu^L(1-S_\nu^L/B_\nu)+F_\nu^C(1-S_\nu^C/B_\nu), \tag{31}$$

where

$$F_\nu^L\equiv k_\nu^L/(k_\nu^L+k_\nu^C), \tag{32}$$

$$F_\nu^C\equiv k_\nu^C/(k_\nu^L+k_\nu^C), \tag{33}$$

$$S_\nu^L\equiv j_\nu^L/k_\nu^L, \tag{34}$$

$$S_\nu^C\equiv j_\nu^C/k_\nu^C. \tag{35}$$

Thus, S_ν differs from B_ν in proportion to the amount that continuum (free-bound) or line absorption is dominant and also in proportion to the degree to which the individually defined continuum or line source functions differ from B_ν.

For the K shell of an optically thin aluminum plasma to be in LTE (i.e., to be collisionally dominated), the collision theory of our model predicts that the ion density must be at least 10^{24} cm^{-3}. However, in an optically thick aluminum plasma, LTE can be reached at much lower ion densities depending, to some extent, on the line profiles. In order to investigate this phenomenon, we performed the following calculation. A planar plasma, 2-mm thick, at a uniform electron and ion temperature of 5×10^6 K, was chosen and CRE solutions to Eqs. (1)–(18) were obtained for ion densities up to 10^{23} cm^{-3}. The total ion density was taken to be uniform. The behavior of the population densities was monitored in terms of the quantities defined in Eqs. (20)–(28). Figures 3 and 4 show, respectively, the relative progressions of the population densities of the $n=1$ and $n=2$ states of Al XIII and of the $1s^2\,{}^1S$ and $1s2p\,{}^1P$ states of Al XII towards LTE at the center of the plasma ($z=0$).

In each figure the curve labeled 1 is a plot of ϵ_{ul}, curves 2 and 3, are plots of $1-s^P/b_{ul}$ and $1-s^O/b_{ul}$, respectively, the curves 4 and 5, are plots of f^{PD} and f^{OD}, respectively. The population densities for the $L\alpha$ transition in Al XIII reach LTE (to better than 1%) at an ion density of 6×10^{21} cm^{-3}, while the populations of the Al XII $L\alpha$ transition respond more slowly to the buildup in the radiation densities at the center of the plasma and require an ion density of 10^{22} cm^{-3} to come into LTE.

Note that curves 4 and 5 cross at a higher density.

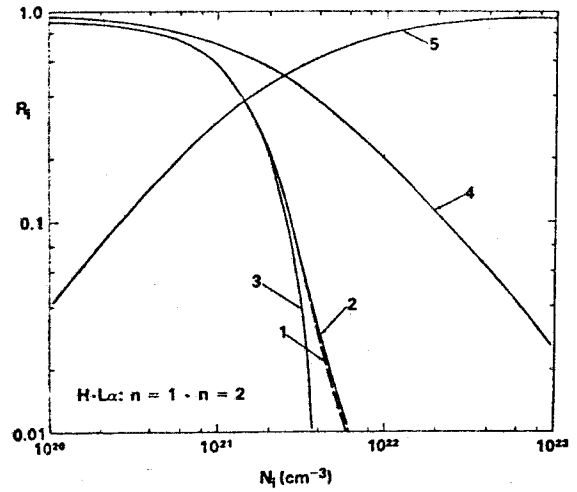

FIG. 3. The quantities appearing in Eq. (24) are computed as a function of ion density for the energy levels involved in the hydrogenlike Lyman-α emission. The quantities ϵ_{ul}, $1-s^P/b_{ul}$, $1-s^O/b_{ul}$, f^{PD}, and f^{OD}, labeled as curves 1–5, respectively, were calculated at the center of a 2-mm thick uniform-density, planar plasma at a temperature of 5×10^6 K.

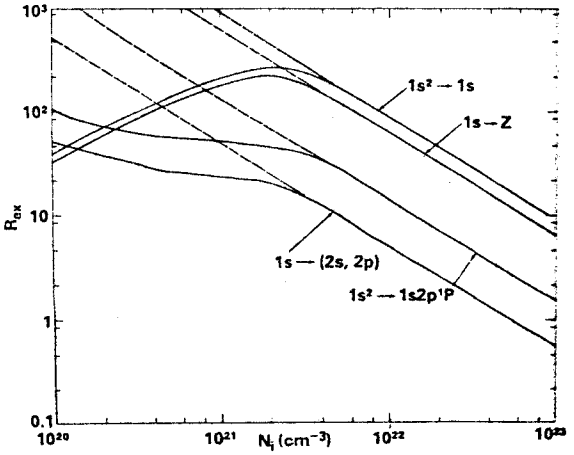

FIG. 5. Ratios of photo to collisional excitation rates (solid curves) and deexcitation rates (dashed curves) connecting upper and lower radiating states are plotted against ion density for the Lyman-α lines of Al XII and Al XIII as well as the Z → H and H → He ground-state radiative recombinations. These ratios were calculated at the center of a 2-mm thick, uniform-density plasma having a temperature of 5×10^6 K.

and after thermal equilibration has substantially occurred, in the hydrogenlike system (Fig. 3) than in the heliumlike system (Fig. 4). Thus, the influence of collisions, which connect the $2p$ states of Al XII and Al XIII to states other than the $1s^2$ and $1s$, is stronger relative to the Lyman-α couplings in Al XII than in Al XIII. Also, note that curves 2 and 3 fall together in both figures. Thus, the behavior of curves 2–5 suggests (1) that the imbalance in the photorates which define s^P reflects itself in an imbalance of the rate processes defining s^O, and (2) that the lower the density at which f^{OD} exceeds f^{PD}, the higher will be the ion density that it takes for the population densities to reach LTE. However, for a 2-mm thick planar plasma, we see that LTE is reached at an ion density 100 times lower than is required in optically thin aluminum plasmas.

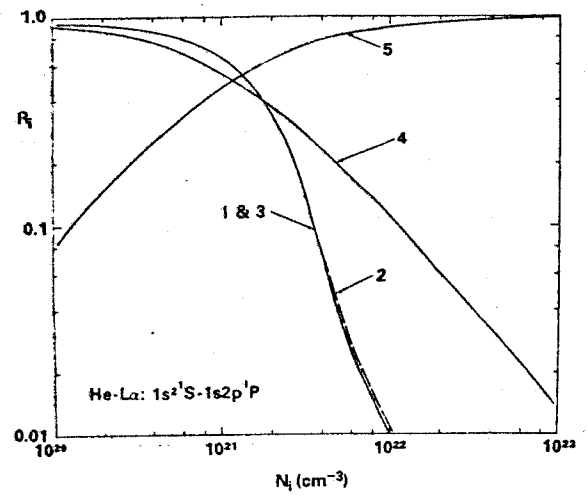

FIG. 4. The quantities appearing in Eq. (24) are computed as a function of ion density for the energy levels involved in the heliumlike Lyman-α emission. The quantities ϵ_{ul}, $1-s^P/b_{ul}$, $1-s^O/b_{ul}$, f^{PD}, and f^{OD}, labeled as curves 1–5, respectively, were calculated at the center of a 2-mm thick uniform-density, planar plasma at a temperature of 5×10^6 K.

Figure 5 provides a reason for this behavior. The solid curves are ratios of photo-to-collisional excitation at the center of the plasma for the four transitions indicated. The dashed curves are corresponding ratios of photo to collisional deexcitation. The merging of the dashed and solid curves occurs at densities where the photorates begin to detail balance. In all of the transitions, at the point where merging occurs, the line photoexcitations are more than 10 times stronger than line collisional excitations and the free-bound excitations are more than 100 times stronger than the corresponding free-bound collisional excitations. Thus, the diffusion of photons in frequency is strong, i.e., there are many photon-scatterings per collisional excitation.

Near the surfaces of the 2-mm thick plasma where the flux patterns of the radiation begin to skew outward and become hemispheric, higher densities than 10^{22} cm^{-3} are needed to bring the ion populations into LTE. Figures 6–9 illustrate this behavior in terms of the quantities in Eq. (31). These curves, of ϵ_ν, $(1-S_\nu^L/B_\nu)$, $(1-S_\nu^C/B_\nu)$, F_ν^L, and F_ν^C were calculated at an ion density of

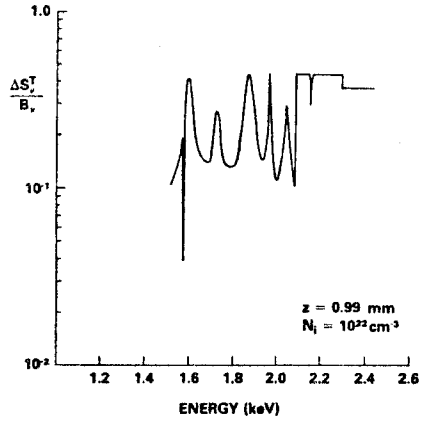

FIG. 6. The calculated percentage departure of the source function from blackbody values in the outer cell of the plasma is shown as a function of photon energy. The calculation was carried out at an ion density of 10^{22} cm^{-3} and a plasma temperature of 5×10^6 K in a 2-mm thick plasma.

10^{22} cm^{-3} in the outside cell of the plasma. The center of this cell is located 0.99 mm from the plasma center. Figure 6 shows the frequency behavior of $\epsilon_\nu \equiv \Delta S_\nu^T / B_\nu$. Near the core of the satellite line, the source function approaches B_ν to better than 5%. At other frequencies, S_ν oscillates between 10 and 40% deviations from B_ν depending on which ionization stage and which emission process contributes most heavily to S_ν. In Fig. 7, the separate contributions of $1 - S_\nu^L / B_\nu \equiv \Delta S_\nu^L / B_\nu$ and $1 - S_\nu^C / B_\nu \equiv \Delta S_\nu^C / B_\nu$ to $\Delta S_\nu^T / B_\nu$ are drawn for comparison to the $\Delta S_\nu^T / B_\nu$ curve. The $\Delta S_\nu^L / B_\nu$ curve is labeled BB and the $\Delta S_\nu^C / B_\nu$ curve, FB. One

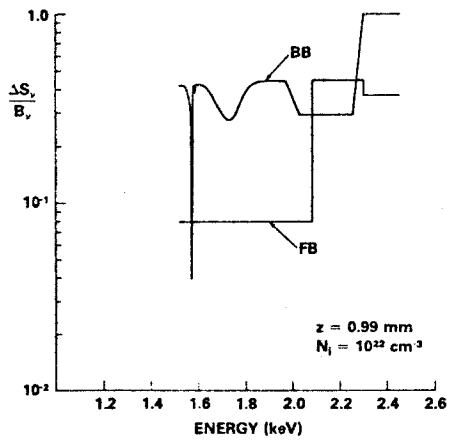

FIG. 7. The calculated percentage departures of the line source function (curve labeled BB) and the continuum source function (FB) from blackbody values in the outer cell of a 2-mm thick plasma is shown as a function of photon energy. The calculation was carried out at an ion density of 10^{22} cm^{-3} and a plasma temperature of 5×10^6 K.

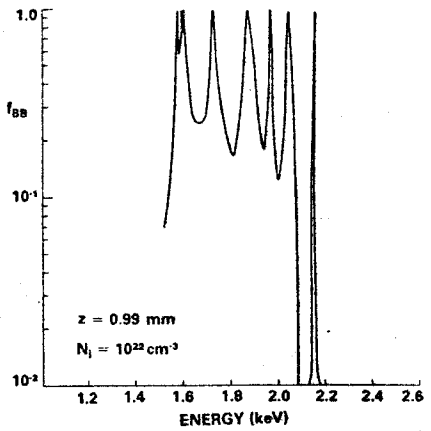

FIG. 8. The fraction by which the line source function of Fig. 7 contributes to the total source function of Fig. 6 is plotted as a function of photon energy.

can infer from Figs. 6 and 7 that the AlXIII system is closer to LTE than AlXII in agreement with Figs. 3 and 4, and that levels within AlXII and AlXIII deviate *uniformly* (i.e., by the same factor) from LTE. The fact that S_ν^L and S_ν^C are formed from sums of overlapping line and continuum emission processes can be seen from the way in which the two curves transit between the different line and continuum values. The weighting factors F_ν^L and F_ν^C (labeled f_{BB} and f_{FB}, respectively) of the $\Delta S_\nu^L / B_\nu$ and $\Delta S_\nu^C / B_\nu$ contributions to ϵ_ν are plotted in Figs. 8 and 9. In the region of overlap between the lines, far removed from the line cores, we see that photons are absorbed principally by photoionization events (80–90%), but that absorption in the wings of the highly broadened lines is still at minimum 10 to 20% of all absorptions.

The broadening of the lines as a function of ion

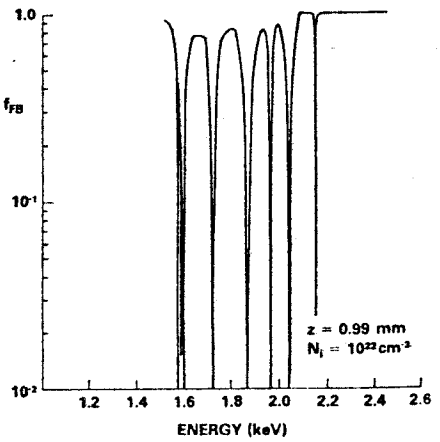

FIG. 9. The fraction by which the continuum source function of Fig. 7 contributes to the total source function of Fig. 6 is plotted as a function of photon energy.

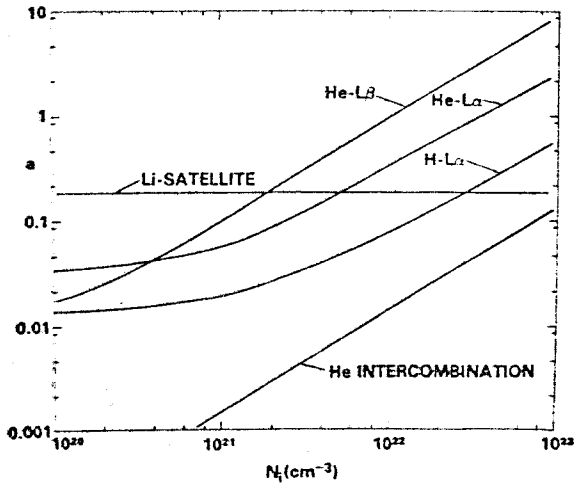

FIG. 10. The computed Voigt profile function parameter, a, which gives the ratio of collisional to Doppler linewidths, is plotted as a function of ion density for 5 of the lines in the K-series spectrum. The plasma was 2-mm thick and at a temperature of 5×10^6 K.

density is shown in Fig. 10, in which the Voigt profile parameter, a, is plotted for 5 of the transported lines. In these calculations, the Li-satellite linewidth is density independent, since it is the rate of autoionization that determines the collisional lifetime of the $1s2p^2$ level. Note that the He-like $L\beta$ line is more strongly broadened than the He-like $L\alpha$ line once collisional broadening becomes dominant since as one moves higher in the manifold of excited states, the state density becomes greater and the energy separation of the states becomes smaller leading to stronger collisional mixing and stronger interuptions of the radiative processes.

One result of the large broadening of the lines at high densities is that their opacities relative to the free-bound continuum decrease as the ion density is increased. This effect is seen in Fig. 11 where the optical depths of the two Lyman-α lines close to line center[10] are plotted as a function of ion density along with the free-bound optical depth at the emission edge of the Z – H and H – He ground-state-to-ground-state recombinations. In spite of the fact that the He – $L\alpha$ line opacity exceeded 10^5 at the end of the calculations, they were performed for a fixed set of cell spacings that were finer toward the surface of the plasma. For example, the innermost cell was taken to be 400-μm thick, while the outermost cell was only 10-μm thick. Consequently, the spatial variations of the source function were imperfectly resolved as a function of density, i.e., optical depth; however, this is an intrinsic limitation of all radiation transport calculations that are based on a finite number of plasma cells.

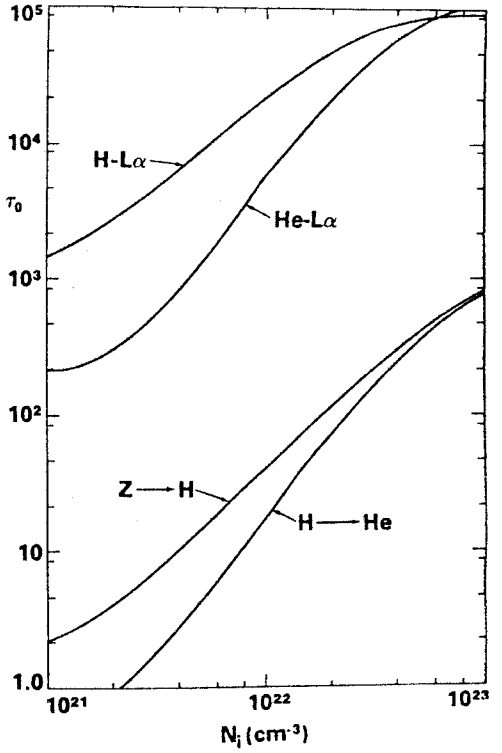

FIG. 11. The optical depths of the hydrogenlike and heliumlike Lyman-α lines near line center and of the Z → H and H → He ground-state radiative recombinations at the emission edge are plotted as a function of ion density. The plasma was 2-mm thick and at a temperature of 5×10^6 K.

When a different set of cell spacings were used to carry out the calculations, the photocouplings and emission spectra were changed somewhat, but not in a way to significantly affect the main conclusions or basic results of the calculations.

One of these basic results is the computed behavior of the emission spectrum as a function of ion density. Figures 12 and 13 contain 2 sets of spectra, at two different ion densities, of both the emergent flux and a blackbody flux calculated at the surface of the plasma (lower curves) and at 145 μm behind the surface (upper curves). Once again, these are spectra from 2-mm thick plasmas. The two sets of companion curves demonstrate a well-known phenomenon of line formation in a highly optically thick medium; namely, that line cores become self-absorbed in the surface layers of the emission region where the population can no longer be held in LTE by the decreasing strength of the radiation field as they are in the interior.[11] As can be seen in these figures, the spectrum at the points of reversal is also lowered from the blackbody curve. Figures 12 and 13, also illustrate how the K-shell spectrum changes from emission to absorption due to line-core

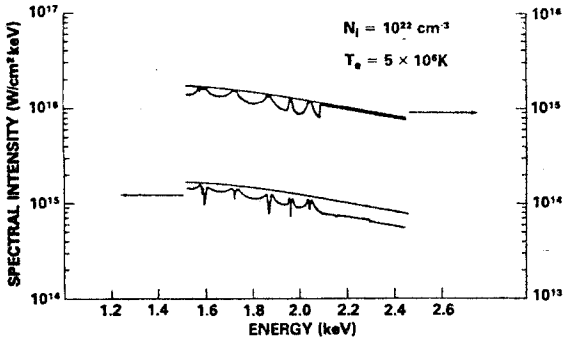

FIG. 12. The computed K-series emission spectrum from a 2-mm thick planar plasma at a density of 10^{22} ions/cm^3 and a temperature of 5×10^6 K is shown relative to the blackbody spectrum (lower set of curves). The same spectra as computed 145 μm behind the surface of the plasma are shown in the upper set of curves.

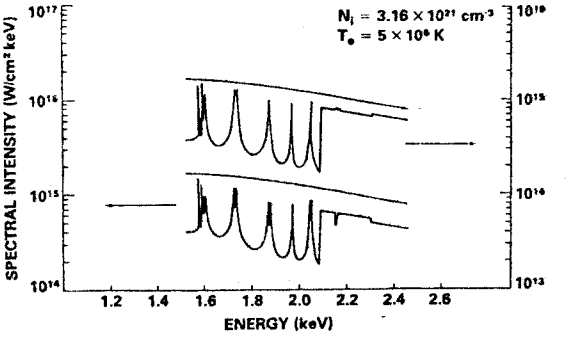

FIG. 13. The computed K-series emission spectrum from a 2-mm thick planar plasma at a density of 3.16×10^{21} ions/cm^3 and a temperature of 5×10^6 K is shown relative to the blackbody spectrum in the lower set of curves. The same spectra as computed 145 μm behind the surface of the plasma are shown in the upper curves.

reversal as the ion density is increased and the continuum and line wings move up toward the blackbody curve. The range of density values over which the plasma will produce an absorption spectrum is imperfectly predicted by these calculations since more cells are needed at the plasma surface to monitor the transition of the surface ionization state towards LTE when the plasma becomes collisionally dominated. One can infer from Fig. 5 that densities of at least 10^{24} are needed for this to occur. Note also in Fig. 13 that the lithiumlike satellite line is relatively unaffected by its passage through the surface layer, since its formation is already collisionally controlled by dielectronic recombination and autoionization. The relative populations of the two levels involved in this transition are determined essentially by the electron temperature; absorption in the continuum accounting for the remainder of the line-formation behavior (see Figs. 6–9).

K-shell spectrum formation at high density has several other interesting features. At 10^{22} ions/cm^3, for example, the Z – H and H – He continua are sufficiently opaque (Fig. 11) to become self-absorbed, like the line cores, on their passage through the surface layer. At 3.16×10^{21} ions/cm^3, H – He emission is becoming thin, while Z – H emission remains relatively thick. Consequently, both the H-like $L\gamma$ line and the Z – H emission edge appear as absorption features in the H – He continuum. Finally, note that, while all the lines in Fig. 13 have opacities larger than 20, the K-shell spectrum lies completely away from the blackbody curve due to core self-absorption and continuum absorption.

Spatial differences in the ionization state of a

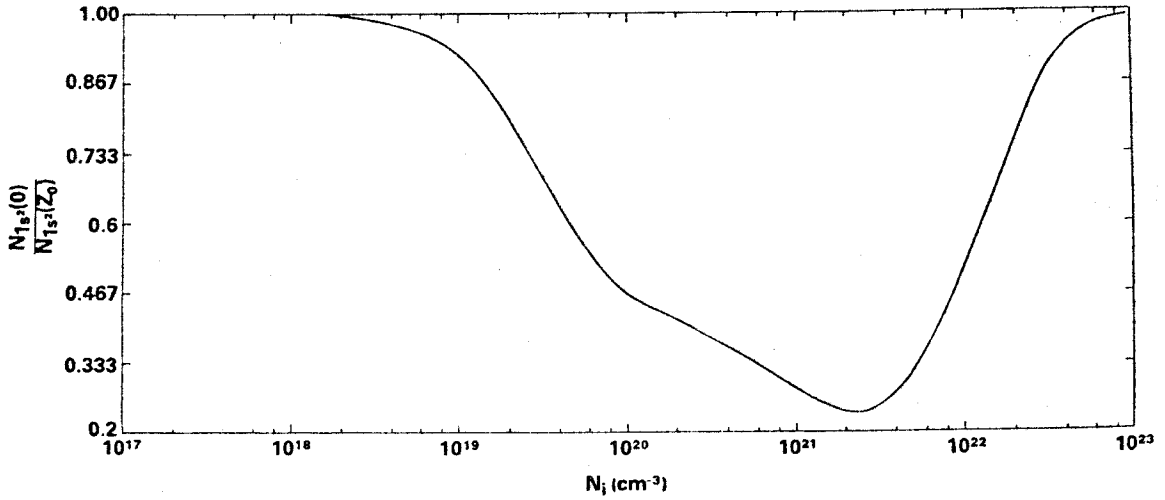

FIG. 14. The computed ratio of Al XII $1s^2\ ^1S$ population densities at the center and surface ($z = Z_0$) of the plasma is plotted as a function of ion density. The 2-mm thick plasma was at a temperature of 5×10^6 K.

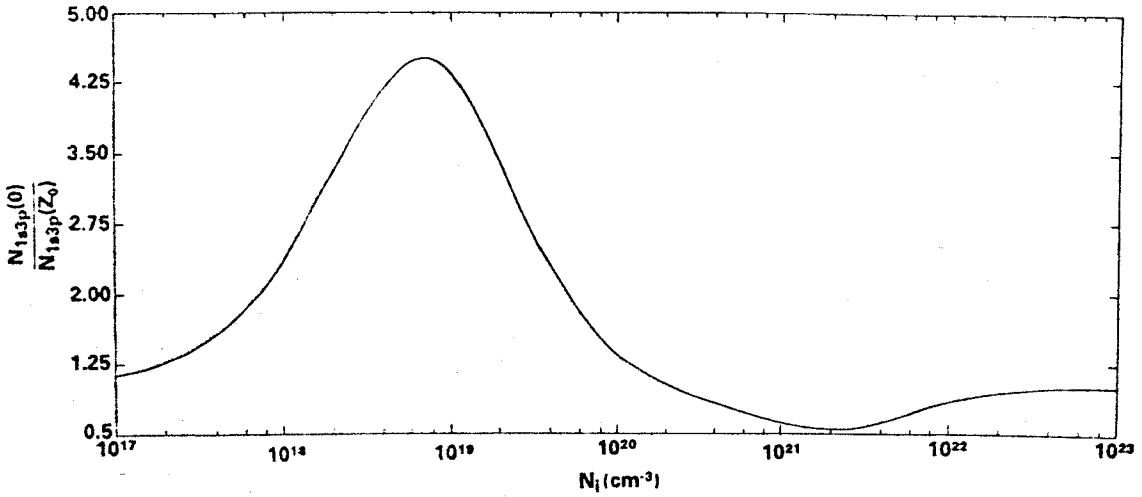

FIG. 15. The computed ratio of Al XII $1s3p\,^1P$ population densities at the center and surface ($z = Z_0$) of the plasma is plotted as a function of ion density. The 2-mm thick plasma was at a temperature of 5×10^6 K.

plasma of uniform temperature and density are induced by the radiation interactions. These ionization gradients can be inferred from the emission spectrum when line reversals are observed. However, the magnitude of the population differences is computable directly. Three examples are given in Figs. 14–16. The ratios of the population densities at the center and surface of the plasma of the heliumlike $1s^2$ ground state, $1s3p$ excited state, and the hydrogenlike $n = 2$ excited state are shown in Figs. 14, 15, and 16, respectively, as a function of ion density. They were calculated over six orders of magnitude of density change in two separate calculations; one calculation was begun at the lowest, and, the other, at the highest density value in the figures. The self-consistency of the two calculations was demonstrated by their smooth merging at the density midpoint of 10^{20} ions/cm^3. The behavior of the ground state of Al XIII and of the Al XIV population density is similar to the behavior of the $1s3p$ and $n = 2$ populations, respectively. Maximum gradients in the hydrogenlike and heliumlike excited-state manifolds occur at around 10^{19} ions/cm^3 while the maximum gradient in the heliumlike ground state occurs above 10^{21} ions/cm^3. At these maxima, from 4 to 7 times as many ions may exist at the center or surface of the plasma as exist at the surface or center, respectively.

V. TEMPERATURE DIAGNOSTICS

One important reason for calculating x-ray emission from optically thick aluminum plasmas

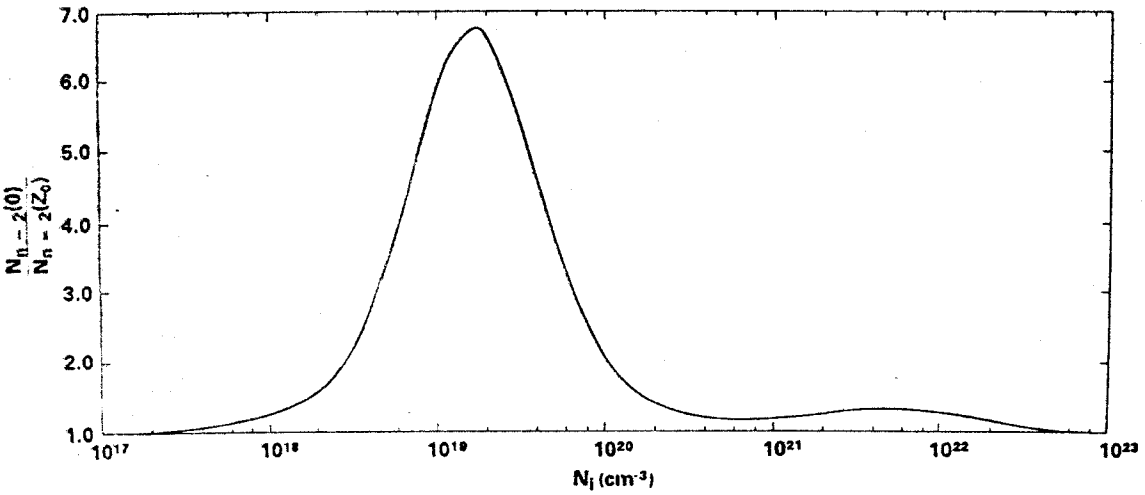

FIG. 16. The computed ratio of Al XIII $n = 2$ population densities at the center and surface ($z = Z_0$) of the plasma is plotted as a function of ion density. The 2-mm thick plasma was at a temperature of 5×10^6 K.

of well defined sizes, shapes, ion densities, temperatures, and ionization states is that it is common experimental practice either to assume or to infer such information from x-ray spectral data obtained from laboratory experiments where the plasmas generated are short-lived ($\lesssim 0.1$ μsec) and small ($\lesssim 1$ mm).[12] If the size and temperature of the emission region are known, as they were in the preceding calculations, the strength of the line reversals, the relative strengths of the continuum background to the line, linewidths, the height of collisionally controlled satellite lines, and the existence of absorption features in the continuum background all provide important density information about the medium. On the other hand, if the size and density of the emission region are known, the problem of deriving "a temperature" from spectral data appears to be much more complicated.

To begin with, in most laboratory situations, it is generally impossible to sustain the plasma in a steady state at a reasonably well-defined temperature, hence, the plasma's temperature will at first be rising and later falling (perhaps rapidly) during emission, and an assumption of collisional-radiative equilibrium may itself be of limited validity. Furthermore, the peak temperature reached may often be a function of the rates of heating and radiative cooling. Since time-integrated spectra are usually measured during short-lived experiments, variations of the emission spectrum with temperature must be known in order to properly time integrate different spectral features. In addition, most spectra are recorded on film, which generally has a dynamic range on the order of 100. Thus, it may not always be possible to simultaneously resolve the line and continuum structure. This recording problem is illustrated in Figs. 17 and 18.

Both spectra in Figs. 17 and 18 were calculated from a 2-mm thick planar plasma. The spectrum in Fig. 17 was calculated at an ion density of 3.16×10^{19} cm^{-3} and an electron temperature of 5×10^6 K, while, in Fig. 18, the ion density and electron temperature were 10^{20} cm^{-3} and 1.88×10^7 K, respectively. In both figures, a dashed horizontal line is drawn, roughly 50 to 100 intensity units below the peak line intensity of each figure. In Fig. 17, none of the free-bound continuum lies above this line; in Fig. 18, only a small portion does. Film recordings of these spectra, therefore, would not necessarily detect any of the continuum background unless they were saturated at the lines.

The absolute intensities of the lines, and the relative intensities of the satellite to intercombination to resonance lines can be used to provide other spectral diagnostic information which is

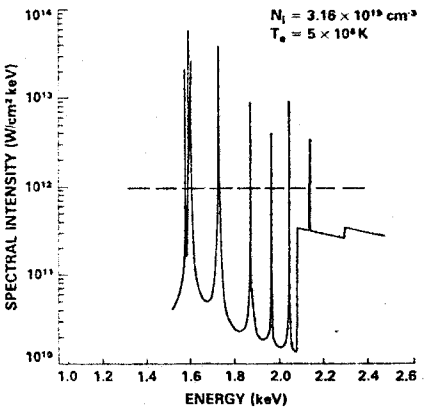

FIG. 17. Calculated K-series aluminum spectrum from a 2-mm thick plasma at an ion density of 3.16×10^{19} cm^{-3} and a temperature of 5×10^6 K.

sensitive to the temperature and opacity of the emission region. The intercombination line in Fig. 17, for example, is twice as intense as it is in Fig. 18; whereas, the resonance lines of Fig. 17 is more than 5 times as weak as it is in Fig. 18. Moreover, the intensity ratios of the satellite, intercombination, and resonance line are usually observed as they appear in Fig. 18.[13]

If line ratios are used to make temperature estimates of an optically thick transient emission region, it will be undoubtably important to locate the background continuum relative to the line peaks as well as to know the size of the emission region in order to have good estimates of both the density of the medium and of the relative amounts of collisional and opacity broadening of the lines. Figure 19 provides some information about these aspects of the problem of spectral interpretation. In this figure, seven calculated power output curves are drawn (per a unit of surface area) as a function of the plasma temperature for two cases

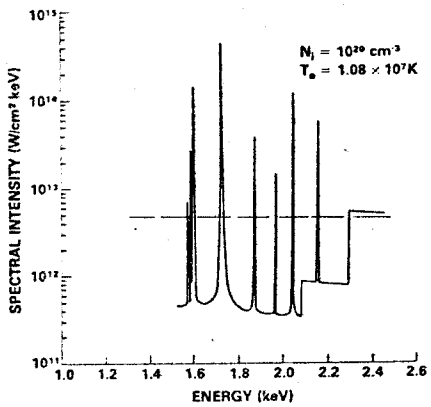

FIG. 18. Calculated K-series aluminum spectrum from a 2-mm thick plasma at an ion density of 10^{20} cm^{-3} and a temperature of 1.08×10^7 K.

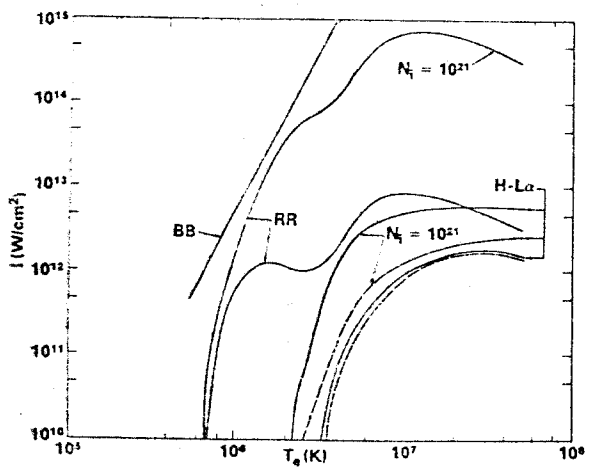

FIG. 19. The spectrally integrated intensity from a blackbody emitter (BB) is compared to the calculated integrated K-series emission into the continuum (RR) and hydrogen Lyman-α line (H $L\alpha$) from 2-mm thick plasmas at ion densities of 10^{20} cm^{-3} and 10^{21} cm^{-3}. The solid H $L\alpha$ curves represent integrations of the line emission further into the wings of the line than the dashed H $L\alpha$ curves.

in which the ion density was 10^{21} cm^{-3} and 10^{20} cm^{-3}. Again the plasma thickness was 2 mm. The curves labeled RR represent the integrated intensity under the K-shell spectrum (from 440 eV to 6.1 keV) exclusive of line-core radiation. Four curves of intensity output from the H – $L\alpha$ line are also drawn; the dashed curves represent symmetrical integrations of the intensity under this line to 2.3 average Doppler widths (7.25×10^{13} Hz) from line center (which is at 4.17×10^{17} Hz); the solid curves are integrations to 17.8 Doppler widths. At 10^{20} ions/cm^3, the dashed and solid curves of H – $L\alpha$ emission are nearly identical and indicate that little emission occurs in the wings of this line; however, at 10^{21} ions/cm^3 the dashed and solid curves show there is considerable emission in the wings of the H – $L\alpha$ line. The final curve on the figure, labeled BB, is a plot of the σT_e^4 blackbody emission rate. The closeness of approach of the total K-shell emission curve at 10^{21} ions/cm^3 to the blackbody curve indicates the strength of the continuum emission from the He – Li recombination in the sub-kilovolt spectral range. Per cm^2 of surface area, an input power of 10 TW would be needed to sustain a plasma of this size and density at temperatures around 300 to 400 eV against its x-ray energy loss.

If one compared experimentally only the intensity output curves of the H – $L\alpha$ emission at the two densities of Fig. 19 one would overlook the approximate N_i^2 increase in K-shell x-ray yield due to the rise in continuum emission from the plasma. At 10^{20} ions/cm^3, our calculations show that continuum emission from the K shell dominates over the line emission, although a film recording of this x-ray spectrum might indicate strong line and virtually no continuum emission. The reason for this recording phenomenon can be found in the relative sizes of the frequency intervals encompassed by the lines and by the continuum. For example, the frequency interval over which the solid emission curves of the $H\alpha$ line in Fig. 19 were computed was 2.67×10^{15} Hz. On the other hand, the total frequency interval that is covered in our K-shell spectrum calculations is 1.37×10^{18} Hz.

VI. PHOTOPUMPING

We have seen that for 2-mm thick, planar aluminum plasmas photoabsorption is the dominant means of exciting the K shell (see Fig. 5) at moderate densities and temperatures ($10^{19} \leq N_i \leq 10^{22}$, $T_e \sim 5\times10^6$). One might expect, therefore, to produce a population inversion within the aluminum K shell by selective photoexcitation. In fact, a scheme in which the $1s^2$-$1s2p$ resonance line in silicon is used to pump the $1s^2$-$1s3p$ transition in aluminum was proposed recently.[14]

One method of studying this proposal in its most ideal form is to pump a planar aluminum plasma symmetrically at both surfaces with a blackbody flux of photons that is filtered outside of a frequency interval surrounding the $1s^2$-$1s3p$ line at frequency ν_0. The strength of the pump radiation can then by characterized by a radiation temperature T_{pump}, where

$$I_\nu^{\text{pump}} \equiv \frac{2h\nu^3/c^2}{e^{h\nu/kT_{\text{pump}}}-1}$$

for $\nu \in [\nu_0 - \Delta\nu, \nu_0 + \Delta\nu]$. $I_\nu = 0$ otherwise. If the thickness of the aluminum plasma is sufficiently small and its density is sufficiently low, the pump radiation will penetrate the medium and produce an inversion between the $1s2p$ and $1s3d$ states in Al XII. Results from such a calculation are shown in Figs. 20–23. The calculation was carried out for the following uniform set of plasma conditions. The electrons were relatively cool for K-shell excitations at 2×10^6 K. The ion density was 2×10^{19} cm^{-3}, and the aluminum plane was 1-mm thick, i.e., the distance the pump radiation has to penetrate to invert all of the Al XII populations was 500 μm. The gain coefficient for the $1s2p\ ^1P$-$1s3d\ ^1D$ line was calculated assuming no feedback on the population densities from this line radiation.

Figure 20 shows the computed emergent flux from the plasma when the strength of the pump radiation is defined by $T_{\text{pump}} = 1.58\times10^6$ K, slightly

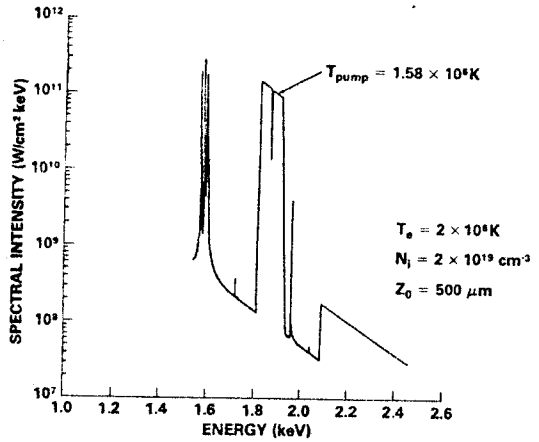

FIG. 20. Calculated K-series emission spectrum from a 1-mm thick plasma at an ion density of 2×10^{19} cm^{-3} and a temperature of 2×10^{6} K in the presence of an external, filtered, blackbody pump of 1.58×10^{6} K strength.

below the ambient electron temperature. The frequency interval, $2\Delta\nu$, is sufficiently small so that only the $1s^2$-$1s3p$ line is pumped. The strength of the pumping is indicated by the depth of the hole in the pump radiation spectrum following its passage through the relatively cool plasma.

At a slightly higher blackbody pump temperature, the Al XII ions at the plasma surface acquire a $1s2p$-$1s3d$ inversion (see Fig. 21). The gain coefficient rises steeply to a value of 50 cm^{-1} at a pump "temperature" 3 times the electron temperature. However, T_{pump} must reach values in excess of 10^7 K in order for the pump radiation to sufficiently penetrate the plasma to invert the $1s2p$ and $1s3d$ states in the center cell and to generate

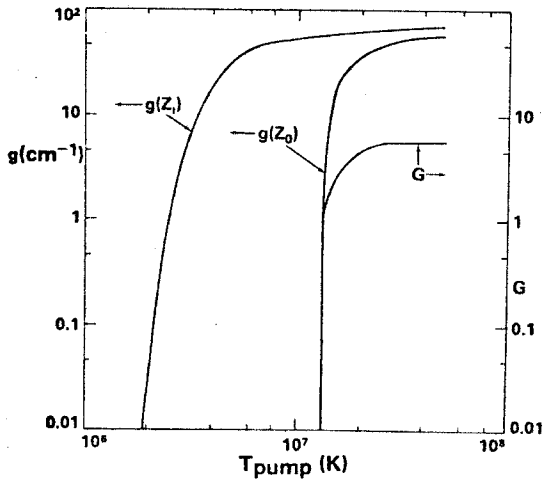

FIG. 21. The calculated gain coefficient at the surface of the plasma ($z=Z_1$) and near the center of the plasma ($z=Z_0$) is shown as a function of the strength of the external pump radiation. The integrated gain in the direction perpendicular to the plasma surface is also drawn.

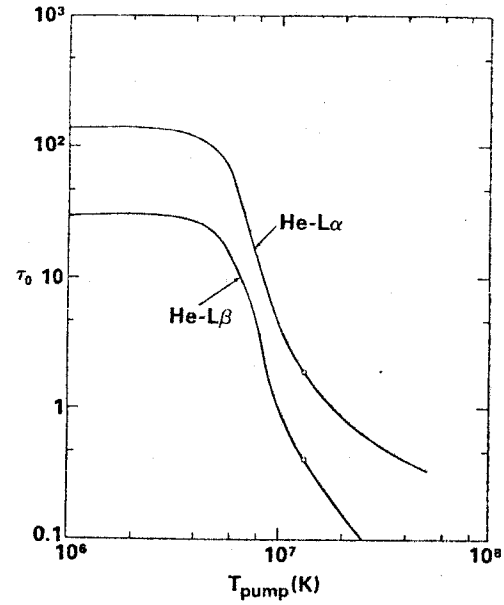

FIG. 22. Calculated optical depths of the heliumlike Lyman-α and Lyman-β lines near line center and at plasma center as a function of pump strength.

an integrated gain $G\equiv\int_0^{z_0} g\,dz$ in the direction perpendicular to the surface. [Because of the thickness of the center cell in these calculations (150 μm), the rise in G followed closely the rise in $g(z=0)$.]

The behavior of G is correlated to the behavior of the optical depths at the center of the plasma of the $1s^2$-$1s2p$ and $1s^2$-$1s3p$ lines, which are shown in Fig. 22 as a function of T_{pump}. Below 8×10^6 K, the optical depth of the He-$L\beta$ line is too large for much of the pump radiation to pene-

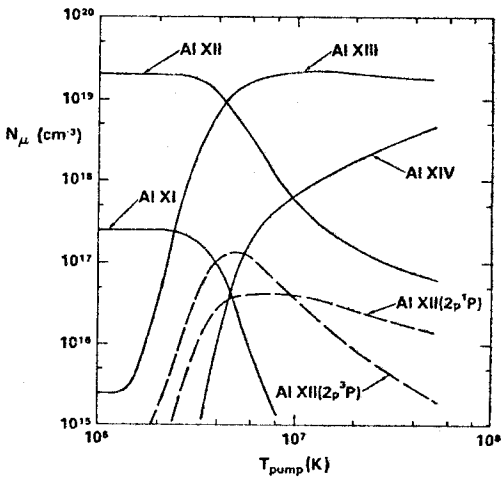

FIG. 23. Calculated population densities at the surface of the plasma as a function of the strength of the external pumping radiation. The electron temperature in the plasma was 2×10^6 K.

trate into the plasma. At $T_{pump} \gtrsim 10^7$ K, the He-$L\beta$ optical depth finally drops to one and the plasma center volume is pumped; however, self-absorption of the He-$L\alpha$ line is still sufficiently high to populate the $1s2p$ state and quench the $1s2p$-$1s3d$ inversion. A further increase in the pump strength is needed to diminish He-$L\alpha$ absorption and invert the $1s2p$-$1s3d$ populations in the plasma interior.

The decrease in opacity of the Al XII Lyman lines with pump strength is related to the dual effect of this radiation to populate the upper energy levels and to deplete the heliumlike ground state of the aluminum plasma in CRE. These effects are illustrated in Fig. 23, where the population densities of the Al XI through Al XIV ground states and the $1s2p\,^1P$ and $1s2p\,^3P$ excited states at the plasma surface are plotted as a function of T_{pump}. At a plasma temperature of 2×10^5 K and for $T_{pump} \lesssim 10^6$ K, the plasma consists mainly of the ground state of Al XII and is primed for pumping. As T_{pump} is increased, Al XII is excited to the $1s2p\,^1P$ state, where electron collisions are sufficiently energetic and frequent to populate other excited levels in Al XII as well as the ground state of Al XIII. When Al XIII decays radiatively to the Al XII ground state, the emitted free-bound continuum acts to pump the $n=3$ state in Al XIII. Electron collisions ionize this state and Al XIV ions are formed. Also, once $1s2p\,^3P$ states are produced through collisional mixing of Al XII excited states, they become photoionized by the pump radiation, i.e., the $1s2p\,^3P$ state is the only excited state in Al XII that is photocoupled to Al XIII in our present analysis. Hence, the more rapid fall of the $1s2p\,^3P$ than the $1s2p\,^1P$ population density with increasing T_{pump} is an artifact of our model.

VII. SUMMARY AND CONCLUSIONS

In recent years, several new experimental methods have been developed to generate high-energy-density plasmas in the laboratory, two of the most notable being laser produced and exploding wire plasmas.[15] While they are similar in many ways to astrophysical plasmas, these laboratory plasmas differ in two important respects from their astrophysical counterparts. One, they are highly transient, and two, their sizes are of the order of x-ray absorption lengths. Hence, during the course of their evolution, they enter and leave regimes where the frequency-by-frequency opacity of the radiation they generate enter significantly into the physics of their evolution.

Because of the similarities of plasma conditions, however, it is natural that the techniques of x-ray data analysis, commonly employed in astrophysics, should be utilized to aid in the interpretation of the x-ray data that is being acquired in the laboratory. However, because of the important space-time differences, the x-ray analysis techniques of astrophysics must also be refined and further developed to be applied with the required generality as a laboratory analysis tool.

In the calculations that were described in this paper, the photocoupling physics was an integral element of not only the energy flow within small, highly excited, dense aluminum plasmas, but of the excitation states of these plasmas as well. We were able, nevertheless, to self-consistently compute the aluminum K-shell emission spectrum in a simple planar geometry and to thereby establish that techniques can be developed to analyze theoretically generated x-ray spectra in analogy to the techniques that are used to analyze experimental spectra, e.g., densitometry, the measurement of line ratios, widths, etc. The advantage in the theoretical case, of course, is that all of the underlying conditions of the emitting medium are known and can be monitored directly. In fact, we have also made movies which demonstrate in time, for example, how the spectra of Figs. 12 and 13 slowly evolve into one another as the ion density is changed. To paraphrase from Scott's article,[16] just as the graphical display of data, which replaced the tabulation of numbers, was a major past scientific advancement, similar benefits may occur as scientific movie making allows one to correlate changes of these graphical data displays in time. Since the variability of plasma conditions is very large, simple physical systems must be analyzed, at first, before one can progress sensibly in directions of more complex physical situations. For this reason, the plasma conditions that were used in the calculations of this paper were purposely chosen to be uniform.

Four important effects were seen as the ionization stages of the K shell approached LTE and the plasma approached radiative equilibrium. First of all, in a millimeter sized aluminum plasma, the LTE approach is made under conditions where, for example, photo-excitation rates are 10 to 100 times larger than corresponding collisional excitation rates. Secondly, the collisional widths of the lines begin to exceed their Doppler widths as the K-shell emission spectrum approaches the blackbody curve. Broadly self-absorbed line cores result and the line emission begins to strongly overlap. At frequencies midway between the lines, where normally one expects continuum emission to dominate, the lines account for 10 to 20% of the source function. Thirdly, in contradistinction to the two-level atom approximation, which is often used in astrophysics at low ion densities

and low x-ray fluence levels, the quenching contributions of collisional transitions to and from levels outside of the two undergoing the radiative transition were found to have an equal influence, along with the photocouplings, on the rate of approach of the population densities to LTE. Finally, the ability of spatial gradients in the energy density of the radiation field to induce spatial gradients in the population densities was found to extend over at least 6 to 7 orders of magnitude in ion density.

Two calculations were also described where the plasma temperature was varied at two different fixed ion densities and where continuum emission in the K shell was found to increase as N_i^2 while the corresponding line emission increase was less than N_i (Fig. 19). In these calculations, continuum emission was found to exceed line emission (at ion densities $\gtrsim 10^{20}$ cm^{-3}). Moreover, at 10^{21} ions/cm^3, continuum emission totally dominated the energy flow from the plasma and approached the rate of blackbody emission at temperatures around 2×10^6 K, where He→Li recombination was the major emission process. The inclusion of L-shell radiation into the calculation will no doubt lead to the conclusion that aluminum at the plasma conditions of this calculation is a blackbody radiator.

The importance of the continuum background was seen for both temperature and density diagnostics even though on film this measurement may be difficult. Because of the time-dependent nature of x-ray emission processes in the laboratory, a "temperature estimate" of the plasma from x-ray data, if based on considerations other than an energy-level diagram, might easily be meaningless or at best misleading. This statement will be especially true if the size and density of the emission region are changing with time in addition to the temperature.

Finally, in order to more dramatically illustrate the radiation field's ability to drive the aluminum K shell, a calculation was performed in which the $1s^2$-$1s3p$ transition in Al XII was pumped by an idealized external source that was designed to produce an inversion of the $1s2p\,^1P$ and $1s3d\,^1D$ states. The results of the calculation suggested that x-ray lasers based on x-ray optical pumping schemes may need to be designed as surface lasers[17] if CRE conditions are approximated and opacity effects are important. We found in the test situation under study that, as the pump strength was increased, the gain coefficient at the surface of the plasma saturated. This effect was caused by the depletion of the Al XII ground state as the pump radiation penetrated further into the plasma. In fact, beyond equivalent blackbody pump strengths of twice the background electron temperature, the ionization of the K shell was determined as much by the pump photons that bathed these ions as by the ambient electron gas.

ACKNOWLEDGMENT

This work was supported by the Defense Nuclear Agency.

[1] D. H. Sampson, *Radiative Contributions to Energy and Momentum Transport in a Gas* (Interscience, New York, 1975).
[2] J. Davis and K. G. Whitney, J. Appl. Phys. 47, 1426 (1976).
[3] V. Jacobs and M. Blaha, Phys. Rev. A 21, 525 (1980).
[4] J. Davis, K. G. Whitney, and J. P. Apruzese, J. Quant. Spectros. Radiat. Transfer 20, 353 (1978).
[5] S. Chandrasekhar, *Radiative Transfer* (Dover, New York, 1960), p. 12.
[6] D. Mihalas and P. B. Kunasz, Astrophys. J. 219, 635 (1978).
[7] For simplicity, the ν^{-1} dependence of the free-bound emission profile was neglected along with Gaunt factor frequency dependences.
[8] M. Seaton, Mon. Not. R. Astron. Soc. 119, 81 (1959).
[9] Two approximations were involved in this procedure. The lifetimes of the lower states were ignored and, in Al XIII, mixing rates between the degenerate levels were not calculated and hence the identification of the lifetimes of the radiating substates was not made.
[10] Our frequency grid did not include exact line-center frequencies, so, for convenience, line optical depths were computed at those frequencies which lay closest to the line centers.
[11] E. H. Avrett and D. G. Hummer, Mon. Not. R. Astron. Soc. 130, 295 (1965); D. G. Hummer, *ibid.* 138, 73 (1968).
[12] P. Burkhalter, J. Davis, J. Rauch, W. Clark, G. Dahlbacka, and R. Schneider, J. Appl. Phys. 50, 705 (1979).
[13] These theoretical spectra will generally not be observed as shown in Figs. 17 and 18 depending on the amount of instrumental or source broadening, i.e., the narrow satellite and intercombination lines of Fig. 17 will also generally be observed to be much less intense than the resonance line as they are in Fig. 18.
[14] A. V. Vinogradov, I. I. Sobelman, and E. A. Yukov, Kvant. Electron. (Moscow) 2, 105 (1975) [Sov. J. Quantum Electron. 5, 59 (1975)]; see also J. P. Apruzese, J. Davis, and K. G. Whitney, J. Phys. B 11, L643 (1978).
[15] P. Burkhalter *et al.*, Ref. 12; K. B. Mitchell, D. B. van Husteyn, G. H. McCall, P. Lee, and H. R. Griem, Phys. Rev. Lett. 42, 232 (1979); B. Yaakobi, D. Steel, E. Thorsos, A. Hauer, and B. Perry, Phys. Rev. Lett. 39, 1526 (1977); C. M. Lee and A. Hauer, Appl. Phys. Lett. 33, 692 (1978).
[16] J. T. Scott, Phys. Today 32, No. 1, 46 (1979).
[17] F. Varsanyi, Appl. Phys. Lett. 19, 169 (1971).

Kinetics of x-ray lasing by resonant photoexcitation: Fundamentals of pumping power and gain for the Na X—Ne IX system

J. P. Apruzese and J. Davis
Plasma Radiation Branch, Code 4720, Plasma Physics Division, Naval Research Laboratory, Washington, D.C. 20375-5000
(Received 30 November 1984)

Two of the most fundamental aspects of the sodium-neon resonantly photopumped x-ray laser system are examined: the functional dependencies of the sodium-plasma pumping-line power output and the atomic-level kinetics in the neon which determine gain. For sodium, the growth of pumping power with size, temperature, and density of the plasma is quantified with numerical and analytic calculations. In the neon an analytic model of the gain kinetics is developed which allows quantitative assessments of the effects of each important rate and process on the gain. Both analytic models should be applicable to similar resonantly pumped systems by using the appropriate rates for those systems. In addition, a novel way of depleting the lower lasing state in an optically thick laser medium is presented.

I. INTRODUCTION

About a decade ago it was suggested[1,2] that population inversions in highly ionized plasmas could be obtained by radiative pumping of closely matched lines from different elements or different ionization stages of the same element. Some experimental success[3,4] has been achieved in inverting the $n=4$ and $n=3$ levels in Mg XII and Mg XI by pumping with resonant Ly-α and $1s^2-1s2p\ ^1P$ transitions in C VI and C V. More recently, enhanced ultraviolet fluorescence has been demonstrated[5] using matched-line pumping of C II by Al III. Quite a few other promising matched-line pairs have been identified.[1,2,6–9] In evaluating the practicality of any of the matched-line schemes, one must first be concerned with the level of pumping photon flux which can be obtained with a given plasma. In general, the greater the pumping flux, the larger the achievable gain in the pumped plasma. Delineating the relationship of various pumping-plasma properties to the achieved output power is a principal subject of this paper. Also of great importance to the viability of this technique are the essentials of the level kinetics in the pumped plasma. This determines the actual gain in conjunction with the impinging photon flux. We show below that it is possible to develop analytical parametrizations for the photon transport of the pumping radiation as well as the kinetics of the gain medium. These analytic models exhibit clearly the influence of all the important plasma and atomic parameters. They are also useful for quantitative assessments.

In this paper we consider one of the most promising of the proposed systems: the Na X $1s^2\ ^1S_0-1s2p\ ^1P_1$ line at 11.0027 Å pumps the Ne IX $1s^2\ ^1S_0-1s4p\ ^1P_1$ line at 11.0003 Å. The strongest potential lasing lines in the pumped neon plasma are $2p\ ^1P_1-3d\ ^1D_2$, $2p\ ^1P_1-4d\ ^1D_2$, and $3d\ ^1D_2-4f\ ^1F_3$. The attractiveness of this scheme stems from several features. Both ions are heliumlike, a closed-shell configuration which is present over a relatively wide range of plasma conditions. The line wavelength match is excellent—two parts in 10^4—which is about one Doppler width. Also, both ions are readily producible in either laser plasmas or Z pinches driven by high-power pulsed generators. In previous work[10] we have demonstrated that substantial power in the sodium line was achieved in a laser-fusion implosion experiment at Rochester[11] in which sodium impurities were unintentionally included in the glass microballoon. In this experiment a brightness temperature of 227 eV was achieved in the pumping line. No numerical modeling of the sodium was possible since the impurity concentration was unknown. The line intensity was obtained by modeling the neon spectrum emitted by the compressed microballoon, and inferring the sodium-line intensity from its strength relative to the modeled neon lines. The neon model was used[10] to numerically demonstrate that temperatures of 50—100 eV and electron densities of $10^{19}-10^{20}$ cm^{-3} in the neon component would produce substantial gains when exposed to the 227 eV sodium radiation. In Sec. II, an analytic model of the Ne IX kinetics is developed which has been found to reproduce in considerable detail and to clarify the previous numerical results. In Sec. III, a numerical atomic model of the pumping sodium-plasma component is detailed, and quantitative results of the power output in the pump line are given as a function of the basic plasma properties. An accurate analytic parametrization is developed for the pump-line photon transport which greatly influences the power output.

II. BASIC KINETICS OF THE PUMPED NEON PLASMA

Even though contiguous sodium-neon components will ultimately influence each other's properties, it has been found possible to minimize this by use of a transparent thermal buffer separating them.[12] It is useful conceptually, and reasonable physically, to consider the neon plasma separately and characterize its interaction with the sodium solely by its absorption of a given pumping-line *flux*. Let us assume this flux is impinging from one side—i.e., it fills 2π steradians. If T(eV) is the effective brightness temperature of the sodium line, the associated net flux, as-

suming isotropic emission from the illuminated 2π steradians, and that $T \ll 1127$ eV, is

$$\mathcal{F}_\nu = 2\pi \int_0^1 B_\nu(T)\mu\, d\mu$$
$$= \pi B_\nu(T)$$
$$\simeq 9.4\times 10^5 e^{-(1127\text{ eV})/T} \text{ ergs/cm}^2\text{ sec Hz}, \quad (1)$$

where in Eq. (1), μ is the cosine of the ray angle. The projection factor $\mu=\cos\theta$ averaged over the hemisphere reduces the net directional flux $\pi B_\nu(T)$ by a factor of 2 from the angle integrated specific intensity $2\pi B_\nu(T)$. Although it is the net flux which is usually measured in the laboratory, the pumping rate is independent of the angle at which the photons flow. Therefore the equivalent pumping rate per neon ion in the heliumlike ground state is

$$P_4 = \int_{-\infty}^{+\infty} \frac{2\pi B_\nu(T)}{h\nu}\sigma_\nu d\nu \text{ sec}^{-1}, \quad (2)$$

where σ_ν the cross section for photoabsorption in the Ne IX $1s^2$—$1s4p\ ^1P$ line is given by

$$\sigma(\nu) = \frac{\pi e^2}{mc} f\phi(\nu). \quad (3)$$

In Eq. (3), f is the line absorption oscillator strength (0.056) and $\phi(\nu)$ is the normalized-line profile. Our calculations show that sodium-line fluxes intense enough to pump significant inversions in the neon arise from sodium plasmas optically thick enough to cause substantial opacity broadening and saturation in the emitted-line profile. Therefore we may reasonably assume that the sodium flux is constant across the absorption profile of the Ne IX $1s^2$—$1s4p\ ^1P$ line. Hence

$$P_4 = \frac{2\pi B_\nu(T)}{h\nu}\frac{\pi e^2}{mc} f \text{ sec}^{-1}, \quad (4)$$

where T refers not to the kinetic temperature of the sodium plasma but the equivalent blackbody temperature of the pumping Na X $1s^2$—$1s2p\ ^1P$ line. Inserting the appropriate numerical values in Eq. (4) leads to

$$P_4 = 1.54\times 10^{12}\, e^{-(1127\text{ eV})/T} \text{ sec}^{-1}. \quad (5)$$

For an equivalent flux temperature of 227 eV, as found in the Rochester experiment,[10,11] Eq. (5) yields a pumping rate P_4 of 1.1×10^{10} sec^{-1} for the $1s4p\ ^1P$ level of Ne IX per ground-state neon ion. At the highest neon-plasma temperature conducive to substantial gain[10] ($\sim$100 eV), the collisional excitation rate coefficient $1s^2$—$1s4p\ ^1P$ is 2×10^{-16} cm^{3}sec^{-1}. The highest ground-to-excited collisional rate coefficient is to the $1s2p\ ^1P$ level (1.4×10^{-14} cm^{3}sec^{-1}). At electron densities of 10^{20} cm^{-3}, these rates are equivalent to pumping of 2×10^4 sec^{-1} and 1.4×10^6 sec^{-1}, far below any reasonably achievable sodium photon-pumping rate. Recombination rates to form the Ne IX excited states depend upon the Ne X fraction. However, for a plasma which is half hydrogenlike and half heliumlike, with $N_e = 10^{20}$ cm^{-3}, the highest collisional and radiative recombination rates at 100 eV are 2 orders of magnitude below the photon-pumping rate quoted above. Thus, in a properly prepared sodium-neon system, excited-state population of the neon levels is dominated by the pumping photons. This fact provides the basis for the analytic description below.

In the following equations, numerical subscripts refer to the singlet levels of Ne IX. For convenience the ground-state population $N(1s^2\ ^1S_0)$ is set to unity. With this convention, the creation rate of the $n=4$ singlets is given by P_4, exactly as in Eq. (5). The D's refer to the destruction rate of the level, i.e., the sum of all the collisional and radiative rates out of the level. F_i is the fractional population (relative to the ground state) of level i. The singlet sublevels are assumed to be statistically distributed and the justification for this assumption is the agreement the model produces with previous numerical results.[10] Equilibration time of the excited states relative to the ground state is controlled by the spontaneous decay rates, which greatly exceed the collisional deexcitation rates at densities suitable for gain ($N_e < 10^{21}$ cm^{-3}). The equilibrium time is approximately A^{-1} where A is the spontaneous decay rate. Averaged over the $n=4$ singlet sublevels, A^{-1} equals 5 psec. Therefore the steady-state assumption provides a reasonably accurate description of level populations in these plasmas whose hydrodynamic time scales are at least an order of magnitude larger. In steady state, the fractional population is equal to the creation rate divided by the destruction rate, i.e.,

$$F_4 = P_4/D_4. \quad (6)$$

The $n=2$ and $n=3$ singlet levels are ultimately controlled by the pumping of $n=4$. As shown above, coupling upward from the ground state is negligible. However, radiative decay to the ground state is very important. Let C_{ij} and A_{ij} stand for the collisional rate coefficients and radiative rates coupling the $n=i$ and $n=j$ singlet levels, respectively. The $n=4$ level is the highest level which need be considered when radiative population of this level dominates the kinetics. Define

$$R_{ij} = C_{ij}N_e + A_{ij} \text{ sec}^{-1}, \quad (7a)$$

$$D_i = \sum_{j=1}^{4} C_{ij}N_e + A_{ij} \text{ sec}^{-1}. \quad (7b)$$

The $n=2$ and $n=3$ singlet-level populations are given by the following simple steady-state equations:

$$F_2D_2 = F_4R_{42} + F_3R_{32}, \quad (8a)$$

$$F_3D_3 = F_4R_{43} + F_2R_{23} \quad (8b)$$

which, given Eq. (6), have the following solutions:

$$F_2 = \frac{P_4}{D_4D_2}\frac{R_{42}+R_{32}R_{43}/D_3}{1-R_{32}R_{23}/D_2D_3}, \quad (9a)$$

$$F_3 = \frac{P_4}{D_4D_3}\frac{R_{43}+R_{23}R_{42}/D_2}{1-R_{23}R_{32}/D_2D_3}. \quad (9b)$$

Equations (6), (9a), and (9b) exhibit all the important interactions and processes which control the presence or absence of gain in the Ne IX system. The fractional populations, hence gain, are all directly proportional to the pumping rate due to sodium photons P_4. The results for

gain given by Eqs. (6), (9a), and (9b) have been compared with the numerical results presented in Ref. 10 by using $T=227$ eV for P_4 in Eq. (5) and doubling the resulting value to account for the two-sided illumination assumed in Ref. 10. Generally good agreement is obtained with this previous work for the three strongest potential lasing lines ($2p\,^1P_1-3d\,^1D_2$, $2p\,^1P_1-4d\,^1D_2$, and $3d\,^1D_2-4f\,^1F_3$). The cutoff densities, above which lasing is impossible due to collisional spoiling of the inversion, are well represented by this analytic model. The densities of the lower states ($n=2$ and $n=3$ singlets) increase with R_{43} and R_{42} which in turn increase with electron density. Not surprisingly, all of the populations, hence the gain, are inversely proportional to the destruction rate D_4 of the $n=4$ singlets.

The results of Ref. 10 as well as the above analytic model have been developed under the assumption that the neon component of the plasma is optically thin. One of the most serious effects working against the practical achievement of gain in such a photon-pumped system is the potential presence of radiation trapping in the strong lines Ne IX $1s^2-1s2p\,^1P$ and $1s^2-1s3p\,^1P$. Such trapping will increase the populations of the $n=2$ and $n=3$ lower lasing states once the neon plasma becomes optically thick to these two lines. A neon plasma of characteristic width $w(\mu\text{m})$ will reach optical depth of approximately unity in the $1s^2-1s2p\,^1P$ line when $w\approx 5\times 10^{20}/N_e$ μm. For the $1s^2-1s3p\,^1P$ line the size would be 5.6 times greater before optical depth unity would be reached. The effect of radiation trapping on gain can be straightforwardly calculated with the above analytic model. The decay rates A_{21}, A_{31}, and A_{41} are replaced in Eqs. (7) by $A_{21}P_{e21}$, $A_{31}P_{e31}$, and $A_{41}P_{e41}$ where the P_e's are the spatially averaged photon-escape probabilities for the three resonance lines. For neon plasmas where significant gain is achievable (moderate optical depths and densities) a Doppler profile[13] provides an adequate P_e. In Fig. 1 are presented results for gain versus optical depth in the Ne IX 1-2 line. In this case a one-sided illumination with a sodium pump flux of 1330 ergs/cm^2 sec Hz is assumed. The neon plasma is assumed planar, as would be appropriate if either the target were planar or a thin shell of neon surrounded a cylinder or sphere containing the sodium pump. This is an effective pumping rate an order-of-magnitude smaller than that achieved in the Rochester experiment.[10,11] At $N_e=10^{19}$ cm^{-3} the gain exceeds 7 cm^{-1} in the 4-3 line up to optical depth 10. At $N_e=10^{20}$ cm^{-3} collisional mixing of the states has reduced the fractional inversion even for the optically thin case. Therefore, as the optical depth increases the gain in the 4-3 and 3-2 lines drops more sharply than in the corresponding lower-density case. The assumed neon-plasma temperature is 65 eV for these calculations. Direct attenuation of the pumping radiation is taken into account using the 1-4 optical depth from the center to the edge of the neon plasma. The gains at zero optical depth are an order-of-magnitude smaller than those of Ref. 10, exactly as expected for such a reduction in pump flux. Our assumed pumping flux of 1330 ergs/cm^2 sec Hz is readily achievable as is demonstrated below.

As seen from Fig. 1, radiation trapping will substantially reduce the gain although at $N_e=10^{19}$ cm^{-3}, neon plasmas of width $w=500$ μm could be tolerated before the gain drops to less than 7 cm^{-1} in the 4-3 line. One possibility for reducing this effect would be to intersperse the neon target with spatially discrete regions containing fluorine or a fluorine compound instead of neon. The hydrogenlike F IX line $1s$-$6p$ lies at 11.56 Å, compared to Ne IX $1s^2-1s3p\,^1P$ which is at 11.544 Å. Thus the fluorine line could intercept the trapped 1-3 photons and possibly prevent their further diffusion in the neon plasma and subsequent repopulation of $n=3$. This scheme would not work if decay of F IX $n=6$ to $n=1$ always followed photoexcitation of $n=6$ by the trapped Ne IX photons. In that case the photons would re-enter the radiation field. However, once F IX $n=6$ is excited, decay to $n=1$ is very unlikely compared to the sum of the other possible processes such as radiative decay to $n=2$–5, and especially collisional transfer to $n=5$ and $n=7$. The overall fluorine quenching fraction for absorbed Ne IX photons is greater than 0.99 even at $N_e=10^{19}$ cm^{-3}. The major questions relating to this proposed technique are, can targets be designed to effectively intersperse sufficient absorbing fluorine in the neon plasma; and, also, would the F IX $1s$-$6p$ profile be sufficiently broadened by Stark and other effects to bridge the 16 m Å gap between it and the trapped Ne IX $1s^2-1s3p\,^1P$ line photons? A more definitive assessment is reserved for a future paper.

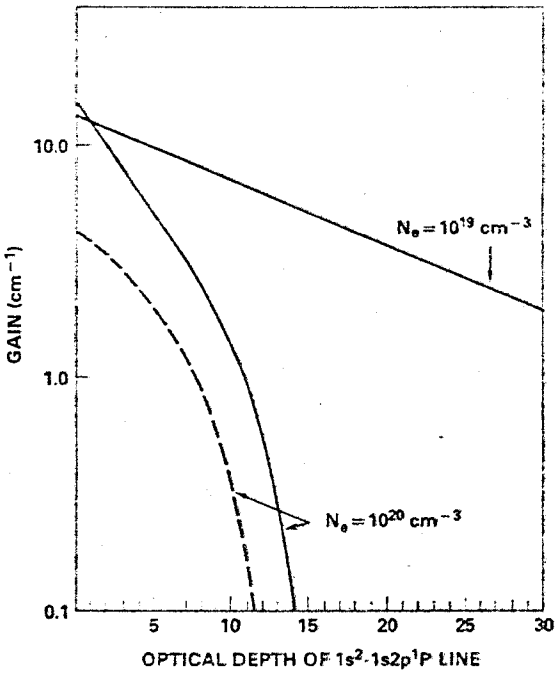

FIG. 1. Gain in the Ne IX $3d\,^1D-4f\,^1F$ (solid line) and $2p\,^1P-3d\,^1D$ (dotted line) lines is plotted against optical depth in the $1s^2-1s2p\,^1P$ line. The planar neon plasma is assumed to have a temperature of 65 eV and is pumped on one side by a matched-line sodium flux of 1.3×10^3 ergs/cm^2 sec Hz.

III. SODIUM PUMPING POWER AS A FUNCTION OF PLASMA PROPERTIES

As has been detailed in Sec. II, the pumping power in Na X $1s^2-1s2p\,^1P$ photons at 11.0027 Å is the principal

determinant of achievable gain in the neon laser-medium plasma. Therefore we turn our attention in this section to the question of the sensitivity of the pumping power to the basic properties of the sodium plasma—temperature, density, and size. To perform such an assessment we employ a numerical atomic model which assumes the sodium plasma to be in collisional-radiative equilibrium and includes radiation transport for all optically thick lines.

A. Atomic model and rates

We consider only sodium plasmas of such temperatures and densities that the K shell dominates the ionic species. Hence, only ground states are included in this model for all stages below lithiumlike. For the lithiumlike stages, the $1s^2 2s\ ^2S$ (ground), $1s^2 2p\ ^2P$, $1s^2 3s\ ^2S$, $1s^2 3p\ ^2P$, $1s^2 3d\ ^2D$, $1s^2 4l$, and $1s^2 5l$ levels are included. The heliumlike stage carries, in addition to the ground state, the $1s2s\ ^3S$, $1s2s\ ^1S$, $1s2p\ ^3P$, $1s2p\ ^1P$, $1s3l\ ^3L$, $1s3l\ ^1L$, $1s4l$, and $1s5l$ levels. The hydrogenlike levels include $n=1$–5.

The atomic processes populating and depopulating the levels are spontaneous radiative decay, electron collisional excitation and deexcitation, collisional ionization, and three-body, radiative, and dielectronic recombination. The continuum is optically thin in these plasmas; hence photoionization is neglected. Line photoexcitation is calculated by the radiative-transfer model discussed in the next section. The sources and calculational techniques used to obtain the rates are discussed elsewhere.[14]

B. Radiation transport

Continuum radiation is treated as optically thin, which is a good approximation for the plasmas considered below. Many lines are optically thick, however. For such lines, radiation transport is calculated self-consistently with the atomic-level populations for all of the optically thick lines which occur in the atomic model described above. For all of the sodium lines except the pumping $1s^2$–$1s2p\ ^1P$ line of the heliumlike stage, a probabilistic coupling-constant technique is used. This method has been presented in detail elsewhere,[13,15] hence, only a brief description is given here. For each of these lines a set of coupling constants is calculated which is a matrix of probabilities C_{ij} that if a photon is emitted in the ith spatial cell, it is absorbed in the jth cell. This calculation is based on simple but acceptably accurate expressions for the escape probability for a Voigt profile[16] as a function of optical depth. This technique accurately describes the photon pumping and escape, but since the escape factors are averaged over the line profile, the detailed frequency profile of the line emission is lost in this simplification.

For the pumping line Na X $1s^2$–$1s2p\ ^1P$ we need to know the detailed emitted profile to obtain the flux at the exact frequency where the pumped neon line occurs. Therefore, for this line only, a numerical frequency grid spanning the profile is established. Coupling constants are calculated at each frequency using the exponential escape probability which describes the transport of monochromatic radiation. Overall photon pumping is obtained by integrating over the line profile; since the emission at each frequency is known, the pumping flux at the neon line's frequency is obtainable. The iteration technique which is used to obtain self-consistency between the level populations and the radiation field is described in Ref. 17.

C. Numerical results

In a thermal plasma (Maxwellian particle distributions) the maximum attainable pumping flux at frequency ν is given by the Planck function. For the Na X $1s^2$–$1s2p\ ^1P$ line at 11.0027 Å this is given by Eq. (1):

$$\mathcal{F}_{\nu,\max} \approx 9.4\times 10^5 e^{-(1127\ \mathrm{eV})/T}\ \mathrm{ergs/cm^2\,sec\,Hz}\ , \quad (1')$$

where it is assumed that $\exp[(1127\ \mathrm{eV})/T] \gg 1$. To actually obtain the flux given by Eq. (1) from a plasma of kinetic temperature T(eV) requires that the plasma be in local thermodynamic equilibrium (LTE) and be optically thick in the line. To reach LTE requires either very high density, very high optical depth, or sufficient combination of high density and high optical depth. Note also that $\mathcal{F}_{\nu,\max}$ is a strongly increasing function of temperature in the 200–500 eV range where the heliumlike species of sodium ion predominates. Therefore, one expects that the pumping power would increase with density, size, and plasma temperature.

Quantitative results for such increases obtained with the numerical model described above are presented in Figs. 2 and 3. In Fig. 2 the emergent flux in the pumping line is plotted as a function of total ion density for an assumed cylindrical plasma diameter of 1.4 mm and temperature 400 eV. In Fig. 3 the same quantity is shown as a function of temperature with the ion density held constant at 10^{20} cm^{-3}. In Fig. 4 the flux is given as a function of plasma size with the temperature (400 eV) and ion density (10^{20} cm^{-3}) held constant. For Figs. 2 and 3, the

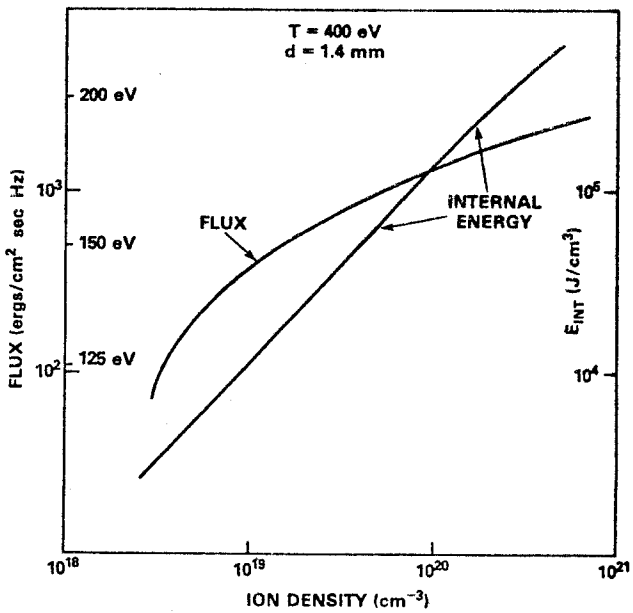

FIG. 2. Output flux in the Na X $1s^2$–$1s2p\ ^1P$ line at the frequency position of the pumped Ne IX $1s^2$–$1s4p\ ^1P$ line is shown as a function of ion density for a cylindrical plasma of temperature 400 eV and diameter 1.4 mm. Also shown is the internal energy per unit volume, as well as the equivalent blackbody brightness temperature of the emitted flux.

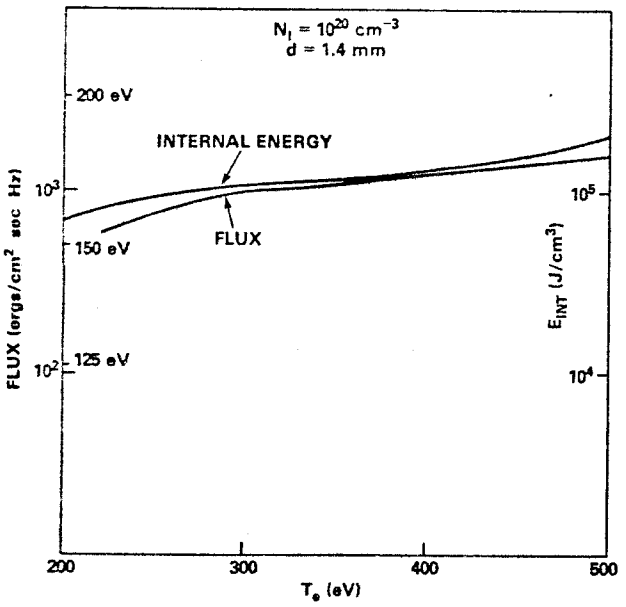

FIG. 3. Same as Fig. 2, except that the ion density is held constant at 10^{20} cm^{-3} and the quantities are plotted as a function of temperature.

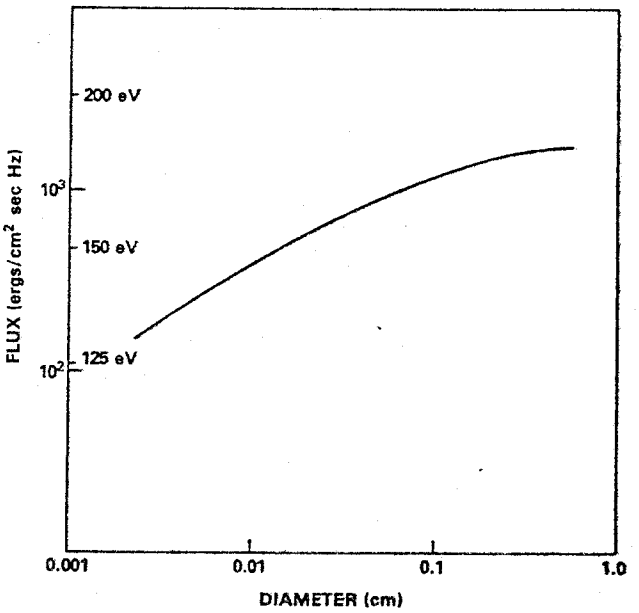

FIG. 4. Output flux in the Na X pumping line is given as a function of cylindrical-plasma diameter for a constant temperature of 400 eV and total ion density 10^{20} cm^{-3}.

plasma internal energy is also shown as a rough indication of the energetic price which must be paid by the experimenter to reach a given pumping power.

The pumping-line flux increases monotonically with temperature, density, and size, as expected. However, the growth is somewhat weaker than linear in these quantities, the strongest increase occurring as a function of density and the weakest as a function of temperature. The greatest pump flux calculated for a 400 eV, 1.4 mm plasma of ion density $\sim 10^{21}$ cm^{-3}, is 3×10^3 ergs/cm^2 sec Hz, about half that inferred from the Rochester pellet experiment.[10,11] Even at a diameter of 0.5 cm, Fig. 4 indicates that the pumping flux is more than an order-of-magnitude below the level of a 400 eV blackbody. The necessity for extremely high optical depth to achieve true LTE is detailed in Ref. 18. This flux is still quite adequate to pump neon, however. We have not carried our calculations to densities equivalent to those obtained at Rochester due to the uncertain effects of Stark broadening. Any pump flux above $\sim 10^3$ ergs/cm^2 sec Hz is sufficient to obtain gains exceeding 5 cm^{-1} in a properly prepared neon plasma.

Much insight into the functional behavior of the pumping power is obtained from studying the curves of Fig. 5. In Fig. 5 we display the fraction of all sodium ions in the heliumlike stage as a function of the same three basic plasma parameters—density, temperature, and size. Note that this fraction decreases monotonically as density, temperature, and size increase. The decrease with temperature is a straightforward consequence of the increasing ionization to the hydrogenlike and bare-nucleus stages. The pumping power is determined by the competition between the increasing collisional excitation rate for the $1s2p\ ^1P$ level and the decreasing fraction of ground-state ions available for excitation. As shown in Fig. 3, the increased collisional rate more than offsets—but barely—the reduction is ground-state ions. Thus the line intensity continues to increase with temperature.

The behavior with density and size is controlled by somewhat more subtle effects. As is evident from Fig. 5, the Na X heliumlike fraction decreases almost as strongly with increased size and density as it does with increased temperature. Also, the optical depth increases with both size and density, so surely more line photons are absorbed. Therefore, as before, the functional behavior of the line power output is governed by the interplay of increased total excitations in the plasma (due to increased size or density) and other factors. In this case the other factors are increased self-absorption and decreased ground-state fraction. The detailed behavior of these processes determines the resultant curves of Figs. 3 and 4, a slower-than-linear increase in power output with size and density.

The decrease in the heliumlike fraction with both density and size is perhaps surprising. It is due to the nature of the ionization process. At a temperature of 400 eV, the electron-impact ionization rate coefficient from the $1s^2\ ^1S_0$ ground state is 1.2×10^{-12} cm^{3}sec^{-1}. From the $1s2p\ ^1P$ level the rate coefficient is 6.3×10^{-11} cm^{3}sec^{-1}, and from the $n=5$ levels the rate coefficient exceeds 10^{-9} cm^{3}sec^{-1}. Because the ionization rates are much higher from the excited states which lie much closer to the continuum, any process which increases the population of the excited levels will increase the ionization state of the plasma. Increasing the size of the plasma increases the excited-state populations through the increased photon pumping which results from greater optical depth. Increasing the density also increases the optical depth and photon pumping of the excited states, and an additional increase in the excited-state populations also occurs through the increase in collisional excitation. This accounts for the increased ionization and decreased heliumlike fraction with size and density shown in Fig. 5. We note that for a 1.4 mm sodium plasma of temperature 400

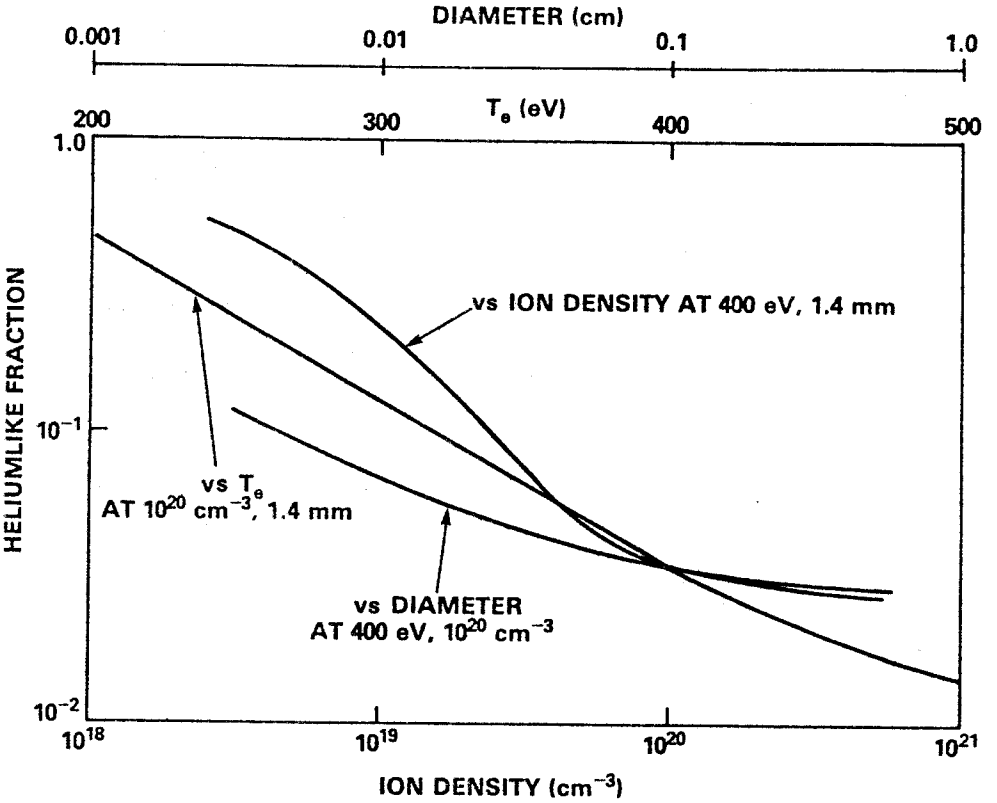

FIG. 5. The fraction of all sodium ions in the heliumlike stage is plotted as a function of ion density, plasma temperature, and plasma diameter. In each curve the remaining plasma parameters are held constant with the indicated values.

eV and ion density 10^{20} cm^{-3}, 80% of the ionization from the heliumlike to the hydrogenlike stage occurs from the excited states rather than the $1s^2\,{}^1S_0$ ground state. Even though size has no effect on the atomic rates, the increase in optical depth with size results in greater excited-state populations through photon pumping and greater ionization from the more highly populated excited-states. This underscores the importance of the excited-state populations to the overall ionization balance.

The transport of pump-line photons is clearly of great importance in determining the emitted-line power. In analyzing the transfer of line photons in laboratory plasmas, the following conceptual picture is often useful.[17] A line photon is "created" when the upper level of the transition is collisionally populated and then decays radiatively. Following its creation in an optically thick plasma the photon will generally be reabsorbed and reemitted a considerable number of times before ultimately escaping the plasma. During each reabsorption there is a finite probability P_Q that the level will be collisionally depopulated and the line photon destroyed. This probability P_Q is given by $D/(D+A)$ where D is the sum of the collisional rates out of the upper transition level, and A is the spontaneous decay rate for the line. Following the initial level excitation, collisional quenching or ultimate photon escape from the plasma will occur. We denote the probability of eventual escape by P_u; the probability of escape on any single flight is given by P_e. The quantity P_e is calculable given the optical depth and line profile; it is used, as described above, for calculating the coupling constants in radiative transfer. The quantity P_u may be obtained by considering the condition for a steady-state population density N of the upper level. Letting C stand for the collisional creation rate, this condition is

$$C = N(D + AP_e)\ \text{cm}^{-3}\,\text{sec}^{-1}\,, \tag{10}$$

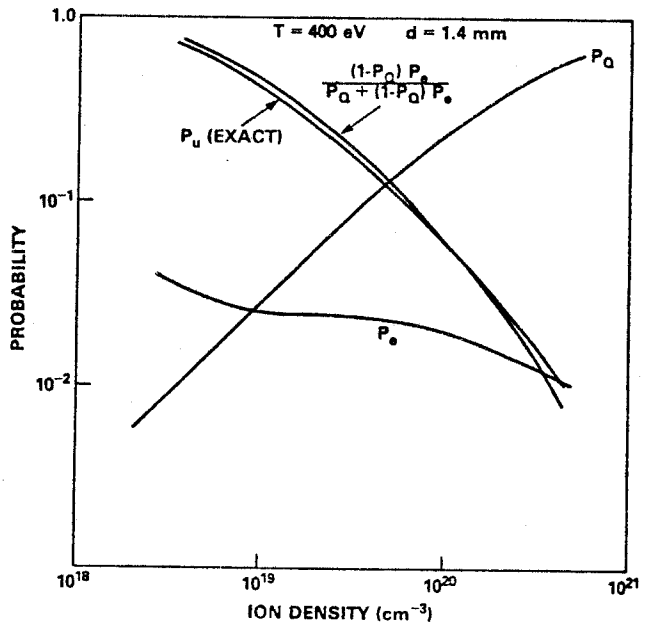

FIG. 6. The spatially averaged single-flight photon-escape probability P_e, the collisional photon-quenching probability per scattering P_Q, and the approximate analytic ultimate escape probability are plotted as a function of ion density for a 400 eV cylindrical sodium plasma of diameter 1.4 mm. Also shown is the exact computed numerical ultimate photon-escape probability P_u.

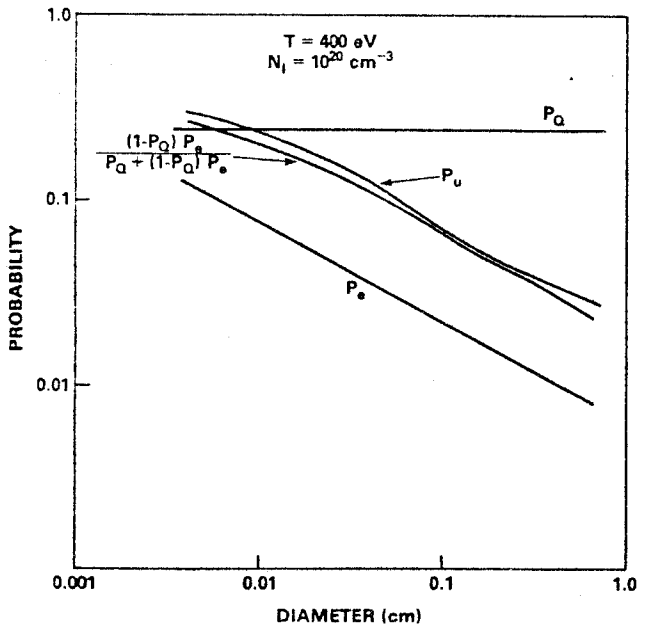

FIG. 7. Same as Fig. 6, except that the same quantities are plotted against plasma diameter for a total ion density of 10^{20} cm^{-3} at a temperature of 400 eV.

where in Eq. (10), radiative reabsorption of the line photons is taken into account by diluting the decay rate by the single-flight photon-escape probability. Even in a uniform plasma, P_e varies with position—Eq. (10) is intended as a spatially averaged approximate description of the photon transfer. After a few simple manipulations, Eq. (10) yields, taking into account that $P_Q = D/(A+D)$,

$$\frac{NAP_e}{C} = \frac{P_e(1-P_Q)}{P_Q+(1-P_Q)P_e} . \tag{11}$$

However, the left-hand side of Eq. (11) is the total photon emission divided by the total upper-level excitation rate; that is, precisely the ultimate escape probability. Therefore,

$$P_u = \frac{P_e(1-P_Q)}{P_Q+(1-P_Q)P_e} \tag{12}$$

in this approximation.

In Figs. 6 and 7 we have plotted the quantities P_e, P_Q, and $P_e(1-P_Q)/[P_Q+(1-P_Q)P_e]$ versus sodium ion density and diameter, respectively. These parameters are displayed for the Na X $1s^2-1s\,2p\ ^1P$ line for a temperature of 400 eV and, for Fig. 6, a fixed diameter of 1.4 mm. Figure 7 reflects calculations for a fixed sodium ion density of 10^{20} cm^{-3}. P_e and P_Q are obtained from Voigt profile formulas and the atomic rates, respectively. The accuracy of the spatial-average approximation is indicated in both Figs. 6 and 7 by also plotting P_u as numerically calculated from the actual computed line photon output power. As is obvious, excellent correspondence is obtained with the probabilistic, spatial-average approximation of Eq. (12). This is especially significant in light of the fact that even though the plasma temperature and density are assumed spatially uniform, the presence of a boundary ensures a significant degree of nonuniformity in both the photon field and the spatial profile of the level populations.

The important feature of Figs. 6 and 7 relevant to the line power output is the monotonic decrease of the ultimate photon-escape probability P_u with density and plasma size. Together with the decreasing heliumlike ionic fraction, this increased photon absorption results in the relatively weak pump power increase with size and density. Were the ionization and reabsorption phenomena not present, the pumping power would increase as the square of the density and linearly with the diameter of a cylindrical plasma. The ultimate escape probability P_u is seen from Figs. 6 and 7 to decrease faster with density than with size. This is a consequence of the fact that as size increases, only P_e, the single-flight escape probability, decreases if the density is constant. As the density increases, P_e decreases and P_Q increases which, according to Eq. (12), results in a faster decrease of P_u.

IV. CONCLUDING REMARKS

The most important plasma atomic processes which determine the viability of resonantly photoexcited x-ray laser schemes have been investigated in detail with both analytic and numerical models. The well-known and promising Na X—Ne IX system was chosen for specific analysis, although the general trends discovered would be valid for similar matched-line schemes.

For the pumped neon plasma, the rate and level kinetics which determine the presence or absence of gain in the lasing lines were shown to be amenable to an accurate analytic treatment which displays in a few simple equations all the important dependencies. The technique is also capable of calculating the deleterious effects of radiation trapping on achievable gain. We suggest that use of fluorine in the neon plasma may assist in removing photons trapped in the $1s^2-1s\,3p\ ^1P$ line thereby counteracting some of the unwanted effects.

For the pumping sodium plasma, the behavior of the power output in the pumping line Na X $1s^2-1s\,2p\ ^1P$ has been quantified as a function of plasma size, temperature, and density. The functional behavior is explained as resulting from the interplay of increased collisional excitation and photon reabsorption with decreased heliumlike ionic fraction. The photon transport has also proven amenable to an analytic treatment in which the ultimate photon-escape probability is given in terms of a single-flight photon-escape probability and collisional quenching parameter.

Another result of the investigation has been the determination that two physically separate neon- and sodium-plasma components are required for significant gain. Numerical calculations have shown that mixing the sodium and neon ions cannot produce conditions conducive to lasing. When the mixture is hot and dense enough to produce adequate sodium pump radiation the neon is overionized well past the heliumlike stage. This occurs

because pumping of the $1s4p\ ^1P$ level in Ne IX greatly facilitates ionization. Conversely, a mixture cool enough and tenuous enough for proper lasing conditions does not produce enough pumping radiation. The scheme appears to be very promising, however, if spatially separate sodium and neon components are used.

ACKNOWLEDGMENTS

The authors have appreciated the invaluable assistance with the atomic rates and coding provided by D. Duston and C. Agritellis. This work was supported by the U.S. Defense Advanced Research Projects Agency.

[1]A. V. Vinogradov, I. I. Sobelman, and E. A. Yukov, Kvant. Elektron. (Moscow) **2**, 105 (1975) [Sov. J. Quantum Electron. **5**, 59 (1975)].
[2]B. A. Norton and N. J. Peacock, J. Phys. B 8, 989 (1975).
[3]V. A. Bhagavatula, Appl. Phys. Lett. **33**, 726 (1978).
[4]V. A. Bhagavatula, IEEE J. Quantum Electron. **16**, 603 (1980).
[5]J. Trebes and N. Krishnan, Phys. Rev. Lett. 50, 679 (1983).
[6]P. L. Hagelstein, University of California Report No. UCRL-53100, 1981 (unpublished).
[7]W. E. Alley, G. Chapline, P. Kunasz, and J. C. Weisheit, J. Quant. Spectrosc. Radiat. Transfer **27**, 257 (1982).
[8]P. G. Burkhalter, G. Charatis, and P. D. Rockett, J. Appl. Phys. **54**, 6138 (1983).
[9]R. H. Dixon and R. C. Elton, J. Opt. Soc. Am. B **1**, 231 (1984).
[10]J. P. Apruzese, J. Davis, and K. G. Whitney, J. Appl. Phys. **53**, 4020 (1982).
[11]B. Yaakobi, D. Steel, E. Thoros, A. Hauer, and B. Perry, Phys. Rev. Lett. **39**, 1526 (1977).
[12]F. L. Cochran, J. Davis, and J. P. Apruzese, J. Appl. Phys. **57**, 27 (1985).
[13]J. P. Apruzese, J. Quant. Spectrosc. Radiat. Transfer **25**, 419 (1981).
[14]D. Duston, J. Davis, and C. Agritellis, J. Appl. Phys. **57**, 785 (1985).
[15]J. P. Apruzese, J. Davis, D. Duston, and K. G. Whitney, J. Quant. Spectrosc. Radiat. Transfer **23**, 479 (1980).
[16]J. P. Apruzese (unpublished).
[17]J. P. Apruzese, J. Davis, D. Duston, and R. W. Clark, Phys. Rev. A **29**, 246 (1984).
[18]J. P. Apruzese, P. C. Kepple, K. G. Whitney, J. Davis, and D. Duston, Phys. Rev. A **24**, 1001 (1981).

Radiation energetics of a laser-produced plasma

D. Duston, R. W. Clark, J. Davis, and J. P. Apruzese
Plasma Radiation Branch, Plasma Physics Division, Naval Research Laboratory, Washington D.C. 20375
(Received 16 August 1982)

The energy transport in a laser-heated thin foil is investigated with the use of a detailed radiation-hydrodynamic model. The calculation is performed for a long laser pulse (3 nsec full width at half maximum) at relatively low irradiance (10^{13} W/cm^2), incident on an 8-μm-thick aluminum foil, and results confirm earlier experimental hypotheses that the dense plasma at the rear side of the foil is heated predominantly by radiation. The model couples a one-dimensional, planar hydrodynamic calculation with a detailed description of the radiation-ionization dynamics in a totally self-consistent manner, thereby assuring that the dominant physical processes determining the energy transport are characterized accurately. The specific radiative mechanisms responsible for energy transfer from the front to the back surface of the foil are found to be quite complex and are described in detail. The front and rear spectral emission are presented and discussed from the point of view of both energetic and diagnostic considerations. Shifting absorption edges due to ionizing plasma are shown to be responsible for many interesting phenomena affecting the energy transport. Time integration of the K-shell spectral features is also studied and its effects on the temperature and density diagnostics are analyzed. Finally $K\alpha$ emission lines are shown to be a promising new diagnostic in determining the time development of the temperature near the foil ablation surface.

I. INTRODUCTION

Recent experiments[1–7] involving the laser heating and subsequent ablative acceleration of thin foil targets have been performed to demonstrate that velocities necessary for sufficient compression of laser-fusion fuel can be attained with present technology. Also of great interest is the degree of preheat of the fuel[8] preceding the main compression phase in inertial confinement fusion experiments. This preheat is due to a number of effects, viz., suprathermal electrons, strong shocks, thermal conduction, and radiation. It has been suggested[2] that the degree of preheat can be assessed from the foil rearside temperature in laser-foil experiments. In addition, measurement of the rearside temperature provides information useful in determining the dominant heating process.

In an effort to explain the details of the relevant physics involved in laser heating of thin foils, we have investigated this phenomenon with a hydrodynamic model designed to reliably calculate the radiation physics in more detail than has been hitherto attempted. The competing processes of energy transfer are studied for a low-irradiance, long-pulse laser beam in order to quantitatively verify, as experimental evidence indicates, that radiative heating is the dominant transport mechanism to the foil backside under these conditions. It is neither our intent nor purpose to corroborate or criticize conclusions drawn from previous measurements. However, comparisons will be made with experimental results whenever possible to provide insight into the role played by radiation in laser-foil heating.

In studying the laser heating of a thin foil, we discuss several interesting phenomena affecting energy transport. Although an abundant amount of radiation is emitted via K-shell lines in the plasma blow-off region of the ablating foil, the mechanism of down-conversion in photon frequency as photons are absorbed and reemitted deeper into the plasma was found to play a major role in the backside heating. The relative timings of laser pulse, backside emission, and backside temperature behavior show interesting but puzzling relationships in the experimental results, and this theoretical study offers explanation for all of these observations. Our investigation of so-called "foil burn-through" shows that an ionization wave can propagate through the plasma (much like a combustion wave), causing shifts in inner-shell photon absorption edges and strongly time-dependent energy transport in the dense plasma regions. We attempt to explain the details of these radiative mechanisms and the way in which they affect the energy transport in the target and escaping photon emission. Since the results of a calculation of this type depend critically on the theoretical model employed, the details of this model are discussed in depth in the section that follows.

II. THEORETICAL MODEL

For discussion purposes, the model can be conveniently partitioned into three aspects: (i) hydrodynamics and laser absorption, (ii) ionization and atomic physics, and (iii) radiation emission and transport. Many of the finer details of the method of solution of the relevant equations have been discussed at length in previous work. These studies are referenced where applicable, but the model is described accurately below in order to present a complete picture of the investigation reported on here.

A. Hydrodynamics and laser absorption

The basic hydrodynamic variables of mass, momentum, and total energy are transported in one dimension using a numerical scheme with a sliding-zone version of flux-corrected transport.[9] A special gridding algorithm is used which moves zones in a Lagrangian fashion and adjusts the mesh in order to resolve steep gradients in the flow. The hydrodynamic equations solved are

$$\frac{D\rho}{Dt}=\frac{\partial\rho}{\partial t}+\frac{\partial}{\partial x}(u\rho)=0\,, \tag{1}$$

$$\frac{D(\rho u)}{Dt}=-\frac{d\bar{p}}{dx}\,, \tag{2}$$

$$\frac{D\epsilon_T}{Dt}=-\frac{\partial}{\partial x}(u\bar{p})+\dot{\epsilon}_{\rm rad}+\dot{\epsilon}_{\rm dep}+\frac{\partial}{\partial x}\left[\eta N\frac{\partial}{\partial x}T\right]\,, \tag{3}$$

where ρ is mass density, u is velocity, $\bar{p}$ is pressure, ϵ_T is total energy, $\dot{\epsilon}_{\rm rad}$ is the rate of energy loss or gain due to radiation, $\dot{\epsilon}_{\rm dep}$ is the rate of energy gain due to the laser deposition process, η is the thermal conductivity, and N is the ion density. The thermal conductivity is calculated implicitly, using an iterative Crank-Nicholson scheme. For each finite difference time-step, the temperature and temperature-dependent conductivities are iterated on until the maximum local relative error is less than one percent.

Since densities did not much exceed solid density in this study, a simple equation of state was assumed with

$$\bar{p}=\tfrac{2}{3}(\epsilon_T-\tfrac{1}{2}\rho u^2-\epsilon_I)\,, \tag{4}$$

where ϵ_I is the ion potential energy due to ionization and excitation. A single temperature model was employed where

$$kT=\frac{\bar{p}}{(\rho/m_I)(1+\bar{z})}\,, \tag{5}$$

where m_I is ion mass, T is temperature, and $\bar{z}$ is the effective ion charge. The ionization energy, ϵ_I, radiation energy, $\epsilon_{\rm rad}$, and effective charge, $\bar{z}$, are calculated from the ionization-radiation equations and are explained below. A single temperature assumption is valid in the cold dense target as well as in the laser deposition region, since thermal equilibration times are short compared with the time scales of the energy input and changes in the hydrodynamic variables. It is not a very good approximation in the hot, tenuous blowoff region of the frontside, but since the density of this region is relatively low, it is expected to have a negligible effect on the energy transport to the rear of the foil.

Since the main motivation for this study was to investigate the role of radiation in the energy transport and not to study the laser absorption mechanism in detail, the laser energy deposition was modeled via classical inverse bremsstrahlung. The absorption coefficient used in the calculation is defined in the usual way,

$$\kappa_{\rm IB}=\frac{\omega_{pe}^2}{\omega^2 ct_{ei}(1-\omega_{pe}^2/\omega^2)^{1/2}}\,, \tag{6}$$

where ω_{pe} is the electron plasma frequency, t_{ei} is the electron-ion collision time, and ω is the laser frequency. For simplicity, the asumption was also made that any incident radiation not absorbed before reaching the cell containing the critical surface was dumped in that cell; hence, no reflection of the laser radiation was allowed. This means that these results would be more appropriately compared to experiments with laser irradiances slightly higher than the theoretical value used here, since we, in effect, assume 100% absorption of the incident energy.

The laser pulse was assumed to have a time dependence approximating a Gaussian shape with a full width at half maximum of about 3.0 nsec and reaching a peak intensity of 10^{13} W/cm^2 at a time of 4.0 nsec after initiation of the simulation. The laser wavelength was 1.06 μm, modeling the input from a Nd:glass laser driver. The time history of the laser power is shown in Fig. 4.

B. Ionization model

The atomic model used in determining the plasma ionization and excitation state has been presented elsewhere,[10] and a more complete description can be found in that work. A set of atomic rate equations of the form

$$\frac{df_i}{dt}=\sum_j W_{ji}f_j-\sum_j W_{ij}f_i \tag{7}$$

is used to characterize the ionic populations in the plasma. Here, f is the fractional population of level i, and W_{ji} is the reaction rate describing the collisional processes from initial state j to final state i. An equation of this type is constructed for each of the atomic levels included in the model. In this calculation we considered the plasma to be in collisional-radiative equilibrium (CRE),[11] making the assumption that the plasma ionization state is immediately responsive to changes in hydrodynamic quantities [the explicit time dependence is omitted in Eq. (7)]. This assumption is an excellent one in the high-density regions of the plasma (behind the laser critical surface), where particle-particle collision times are extremely short, but it is a marginal assumption in the hot, rarefied blowoff region. Since the temperature of the blowoff rises quickly to almost 1 keV and is maintained at this value (where K-shell ions are the dominant species) for several nanoseconds, little ionization or recombination takes place on even a 10-nsec time scale after the peak in the laser pulse. Hence, we have chosen to apply the equilibrium condition everywhere in this study. Preliminary results from a study of time-dependent effects on the ionization state in laser plasmas indicate slight effects on the frontside emission, but we leave the details of that investigation for future work.

The atomic level structure employed in this model includes all 14 ground states of aluminum plus 84 selected excited states, somewhat evenly distributed from Al III to Al XIII (the details of the level structure and energy level values are found in Ref. 10). With such an extensive atomic structure, the level distribution of the plasma can be accurately described from temperatures of a few eV to several keV. The excited-state structure included in this study was selected to best represent the radiation energetics for the plasma conditions under investigation, and we believe that this model takes into account almost all of the energetic transitions required to accurately describe the emission resulting from laser-foil interaction phenomena.

The rate coefficients that are used to calculate the populating and depopulating rates, W_{ji}, are calculated using various scattering techniques. The processes included in this calculation and the methods used in calculating the corresponding rate coefficients are summarized below.

(1) *Collisional ionization*—exchange classical impact-parameter (ECIP) method[12] (the effect of autoionizing resonances on the cross sections has been ignored).

(2) *Photoionization*—hydrogenic approximation with Karzas-Latter Gaunt factors.[13,14]

(3) *Dielectronic recombination*—the detailed calculations of Jacobs *et al.*[15] are used.

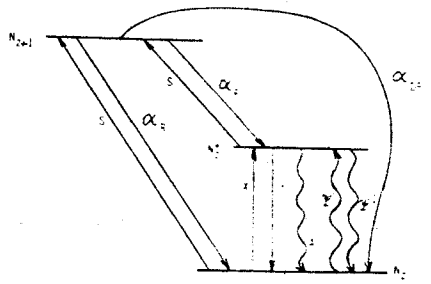

FIG. 1. Simple three-level diagram used to depict the atomic processes included in this ionization model. S is collisional and photoionization, α_R is radiative recombination and three-body recombination, α_{DR} is dielectronic recombination, X is electron collisional excitation, Y is collisional deexcitation, A is spontaneous decay, and ψ and ψ^{-1} are stimulated absorption and emission.

(4) *Collisional excitation*—Coulomb-Born distorted-wave approximation including exchange effects,[16] or the semiclassical impact-parameter (SCI) technique.[17]

(5) *Spontaneous radiative decay*—oscillator strengths are taken from several calculations and measurements.[10]

(6) *Photoexcitation*—oscillator strengths used are those quoted above to determine optical depths (see the next section on radiation transport).

Finally, collisional and radiative recombination, collisional deexcitation, and stimulated emission are all calculated as the detailed balance of the corresponding opposite rate listed above. A simplified level diagram using two ground states and a single excited state is shown in Fig. 1 to show schematically the collisional processes included in the model.

An important question to be addressed regarding the rate coefficients is how well the cross sections are known, since the radiative emission is strongly influenced by this accuracy. An extreme upper limit of a factor of 2 can be globally placed on the rates. However, most of them are correct to much better accuracy, particularly electron-impact ionization, collisional excitation, and the oscillator strengths. A complete referencing of these coefficients can be found in other papers.[18,19]

Once the set of rate equations (including the radiation transport) has been solved for the level populations, f_i, the electron density can be calculated,

$$N_e = \sum_i z_i f_i N_I \ , \tag{8}$$

where z_i is the ionic charge of level i and N_I is the total ion density.

The ionization and excitation energy can also be calculated by

$$\epsilon_I = \sum_i \chi_i f_i N_I \ , \tag{9}$$

where χ_i is the energy of level i, measured from the ground state of the neutral atom.

C. Radiation emission and transport

The radiation emission from plasmas is strictly dependent on the atomic level population densities. Once these state densities are accurately known, the radiative source functions can be calculated directly. Except for optically thin plasmas, however, the level populations also depend on the radiation field since optical pumping of states by photon reabsorption can cause significant redistribution of the populations, not only from ground to excited states but between ionization stages via both photoionization and electron-impact ionization of excited states whose populations have been enhanced by photoexcitation. Thus, the ionization and radiation equations are strongly coupled and must be solved self-consistently. In this model, this is done iteratively by first calculating the level populations at a time step using the radiation field from the previous time step, then using these populations to calculate a new radiation field and recalculating populations until convergence is reached. Any technique which does not allow for this important optical pumping of the levels is unsatisfactory, since this feedback mechanism can be critically important for both energetic and diagnostic accuracy.

The transport scheme used in this study is based on a probability-of-escape for the photons.[20] The transport method for photon absorption by valence electrons is described first. For line photons, the probability is determined by the line shape; for a Doppler profile at large optical depth,

$$P_e \simeq [\tau_0(\pi \ln \tau_0)^{1/2}]^{-1} \ , \tag{10}$$

while for a Voigt profile,

$$P_e \simeq \tfrac{2}{3}(a_{ij}/\tau_0)^{1/2} \ , \tag{11}$$

where τ_0 is the line center optical depth and a_{ij} is the Voigt damping parameter

$$a_{ij} = \frac{\sum_k A_{ik} + \sum_k C_{ik} + \sum_k A_{jk} + \sum_k C_{jk}}{4\pi \Delta \nu_D} \ . \tag{12}$$

Here, A and C are radiative and collisional depopulation rates of the lower and upper levels, i and j, of the radiative transition. Since the Voigt profile reduces to a Doppler core at low densities, the model calculates both probabilities and uses the largest value (see Ref. 20 for a fuller discussion). An expression has recently been developed for Stark profiles within the probability-of-escape formalism but it has not yet been implemented in our model.

Continuum photons due to radiative recombination processes are also transported by probability-of-escape techniques. An emission profile of the form

$$\phi_e \sim \exp[-h(\nu - \nu_0)/kT] \tag{13}$$

is assumed with an absorption profile of the form

$$\phi_a \sim (\nu_0/\nu)^3 \ , \tag{14}$$

where ν_0 is the frequency of the continuum edge. The exact probability integral

$$P_e = \frac{\int \phi_e e^{-\tau_0 \phi_a} d\nu/\nu}{\int \phi_e d\nu/\nu} \tag{15}$$

has been solved for a wide range of values for τ_0 (the optical depth at the edge) and $h(\nu - \nu_0)/kT$; the results have been fit to Chebychev polynomials and are then reconstructed on-line in the model. The free-free emission is transported by solving the equation of transfer explicitly over a grid of photon frequencies; this can be done efficiently because of the smooth nature of the emission function. To calculate the absorption coefficient, the following expression is used[21]:

$$\kappa_{ff}(\nu) = (\text{const}) N_e N_I T^{-1/2} \times \sum_i z_i^2 f_i \left[\frac{1 - \exp(-h\nu/kT)}{\nu^3} \right] . \tag{16}$$

Then, by integrating over frequency, probabilities of escape from zone to zone can be calculated in a straightforward fashion.

The methods described above deal with photon absorption by valence electrons through photoexcitation or photoionization. However, effects due to inner-shell photon absorption must also be taken into account. This is particularly important for laser-foil interaction models, since the neglect of these processes leads to a gross underestimate of the x-ray deposition in the cold, dense plasma regions, as would be seen by the presence of intense, unattenuated lines and continua in the calculated backside spectrum. Thus, what is potentially the major energy transport mechanism to the backside would be omitted.

In this model, each emission line or continuum edge characterized by the ionization model is attenuated by an inner-shell opacity as well as the valence electron line and continuum opacity described above. The inner-shell photoionization cross section for neutral aluminum is taken from the fits by Biggs and Lighthill,[22] and the inner-shell op-

tical depth can be calculated in a straightforward manner from

$$\tau_{IS}=\sum_n \sigma_{PI} d_n N_n \ , \tag{17}$$

where σ_{PI} is the photoionization cross section for inner-shell processes, d_n is the zonal path length, and N_n is the zonal ion density.

In general, the dense plasma which strongly attenuates photons via collisions with inner-shell electrons is *not* neutral, and to accurately account for x-ray deposition in the rearside of the foil, the cross section must be adjusted as a function of ionization state as well as photon energy. We have chosen to use the numerical values of the neutral aluminum cross sections and simply shift the M, L, and K absorption edges with ionization state. This is a good approximation for electrons occupying the $1s$, $2s$, and $2p$ inner shells for medium- and high-Z materials.[23] A plot of the photoionization cross sections versus photon energy for the different ionization stages of aluminum is shown in Fig. 2. The position of the various absorption edges was taken from the Hartree-Fock calculations of Clementi and Roetti.[24] Note the importance of the edge shift with ionization state; the K edge lies below the Al XII resonance line energy of 1.598 keV (one of the strongest emission lines) for Al I-Al III, and above it for higher ionization stages. Thus, as the backside heats up, the inner-shell optical depth of this line can drop by an order of magnitude and significantly decrease the x-ray heating rate.

One advantage of using an ionization model which explicitly calculates the level populations is that the inner-shell attenuation of photons can be calculated state by state rather than using a zonal effective charge to determine the cross section. As a simple illustration, consider Al XII resonance line photons (1.598 keV) incident on a dense zone in the foil backside in which the ions consist of $\frac{1}{3}$ Al III, $\frac{1}{3}$ Al IV, and $\frac{1}{3}$ Al V. The effective ionization is $Z_{eff}=3$; hence if one were to use a more simplistic calculation of Z_{eff}, the K edge would seem to be shifted to the position corresponding to Al IV at 1.626 keV, above the resonance line photon energy, and the opacity would be reduced markedly. Thus, the K-line attenuation which actually occurs in that zone by the 33% Al III concentration would not be taken into account, and the heating rate would be underestimated severalfold if only an average zonal charge were used. Knowledge of the state distributions in the dense plasma regions is therefore often necessary for accurate energy transport. The technique by which inner-shell and valence electron opacities are combined to determine a total probability-of-escape is too detailed to present here and can be found in a separate work.[25]

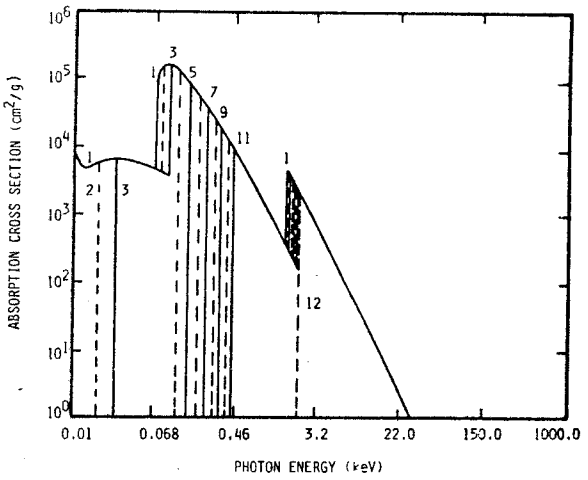

FIG. 2. Inner-shell photoionization cross section versus photon energy for aluminum. Numbers refer to the absorbing atom or ion (5 ≡ Al V or Al^{4+}).

Using the above expressions, coupling constants linking each numerical zone to every other zone are calculated for each line or recombination edge, and the photon transport from zone to zone and also escaping the plasma is determined. Thus, the bound-bound emission power is calculated by

$$P_{bb}=\sum_m \sum_n N_{mn} A_m F_{mn} \Delta E_m \ , \tag{18}$$

where A_m is the radiative decay rate for line m, N_{mn} is the upper-state population for line m in zone n, ΔE_m is the transition energy, and F_{mn} is the probability factor that a photon from line m, emitted in zone n, escapes to the outer boundary of the plasma. A similar expression can be written for the bound-free emission

$$P_{bf}=\sum_m \sum_n N_{mn} \alpha_{mn} N_{en} F_{mn} \chi_m \ , \tag{19}$$

where α_{mn} is the radiative recombination rate coefficient for recombination edge m, N_{en} is the electron density in zone n, χ_m is the ionization energy of edge m, and F_{mn} is the zonal escape probability factor for edge m, similar to that for the lines in Eq. (18).

The free-free radiation is calculated using

$$P_{ff}=(\text{const})\sum_n N_{en} N_{In} T_n^{-1/2} \sum_i z_i^2 f_{in} \int \exp(-h\nu/kT_n) F_n(\nu) d\nu \ , \tag{20}$$

where $F_n(\nu)$ is the probability that a photon of frequency ν escapes the plasma from zone n. Hence, the total radiation power emitted from the plasma is

$$P_{\rm rad}=P_{\rm bb}+P_{\rm bf}+P_{\rm ff}\ . \tag{21}$$

If Eqs. (18), (19), and (20) are rewritten to give the net photon transport from zone n to zone n', instead of that which escapes to the plasma outer boundary, the various radiative loss or gain rates $\dot{\epsilon}_{\rm bb}$, $\dot{\epsilon}_{\rm bf}$, and $\dot{\epsilon}_{\rm ff}$, can be calculated along with the total, $\dot{\epsilon}_{\rm rad}$, which occurs in the expression for the total energy, Eq. (3). In this way, the net cooling and heating by radiation emission and absorption among the various zones of the plasma is accurately accounted for, and a totally self-consistent radiation-ionization-hydrodynamic calculation can be performed.

D. $K\alpha$ emission

It was shown in the last section that line and continuum spectral features are calculated in this model by explicitly treating the bound-bound and bound-free collisional processes. In this section, a method of calculating $K\alpha$ emission is described which differs slightly from the methods used on other spectral features. Spectral lines identified as $K\alpha$ emission are often seen in experimental spectra when high-energy photons or particles are incident on cold target material.[5,26–33,35] For shorter wavelength lasers, hot-electron generation is suppressed, hence, $K\alpha$ emission may be due predominantly to X-ray reabsorption (see Mizui *et al.*[34] and Nishimura *et al.*,[6] and Yaakobi *et al.*[35]). This is the case considered here; the laser-heated front surface emits energetic x-rays back into the cold foil on the other side of the ablation surface. These photons penetrate the electron shells of low charge state ions and can strip off an inner-shell electron. If the photon energy is sufficiently large, a K-shell vacancy is created, which can be filled by either an Auger (radiationless) transition or by resonance fluorescence. For a K-shell Auger transition, an L-shell electron can decay to fill the K-shell vacancy, with the excess energy going to ionize an outer electron. Fluorescence, on the other hand, occurs when an outer (L- or M-shell, in aluminum), electron decays to fill the K-shell vacancy with the excess energy carried off by a $K\alpha$ photon.[36] A technique to accurately account for these processes in an equilibrium plasma has been described recently by Jacobs *et al.*[37] In our work, however, several simplifying assumptions have been made in modeling the $K\alpha$ emission from laser-foil interactions.

Using the expressions from Sec. II C above describing the inner-shell opacity calculation along with the photon field from the frontside of the foil, we calculate a K-shell vacancy creation rate, V_K, for each plasma zone. Since the photoionization cross section is known as a function of ionization stage as well as photon energy, and the ionic population densities are calculated explicitly by our ionization model, this K-shell vacancy creation rate is determined also as a function of ionization state. The K-shell fluorescence yield, ω_K, the proportion of K-shell vacancies which are filled by fluorescence ($K\alpha$ emission), has been calculated by McGuire.[38] Hence, the intensity of $K\alpha$ photons emitted from zone n and ionization stage z can be calculated simply from the following expression:

$$P_K(n,z)=V_K(n,z)\omega_K(z)\Delta E_K(z)\ , \tag{22}$$

where $\Delta E_K(z)$ is the $K\alpha$ transition energy for ion z. Shown in Table I are the K fluorescence yields and the transition energies for the lowest nine charge states of aluminum.

TABLE I. Transition energies and fluorescence yields for the ionization stages of aluminum included in the $K\alpha$ emission model, taken from McGuire's calculations.

Ionization stage	Transition energies (keV)	Fluorescence yields
Al^{0+}	1.486 99	0.033 3
Al^{1+}	1.487 52	0.046
Al^{2+}	1.488 24	0.045
Al^{3+}	1.488 95	0.043 4
Al^{4+}	1.499 58	0.047 9
Al^{5+}	1.511 64	0.052 2
Al^{6+}	1.525 40	0.061 9
Al^{7+}	1.540 37	0.070 0
Al^{8+}	1.557 01	0.062 3

It has been shown[32] experimentally for aluminum that the $K\alpha$ emission from Al^{0+}-Al^{3+} is usually seen as a single unresolved feature in the spectrum due to the small energy difference ($\sim$2 eV) separating the four lines. After the first L-shell electron has been removed, however, the lines from the next ions shift measurably to higher energies due to the significantly reduced screening from the missing L electron. Thus, the remaining lines will be seen in the spectrum at higher energy, well resolved from the main $K\alpha$ peak but still below the Al XII resonance and intercombination lines at about 1.59 keV. It is apparent that these lines are clear indicators of the ionic distribution in the cold backside of the foil; a discussion of this diagnostic in the context of the results of this study is found in the next section.

Although opacity effects may alter the $K\alpha$ emission from the backside plasma, the analysis in the following section assumes that all the $K\alpha$ emission escapes the plasma unattenuated. Using solid densi-

ties for aluminum, the photon cross section at 1.5 keV from Fig. 2, and a path length of 8 μm, one calculates the optical depth of the $K\alpha$ lines due to photoionization alone to be of order unity, neglecting the resonant effects present in a warm, ionized plasma. However, we leave the problem of $K\alpha$ photon transport through laser-heated foils for future investigations.

III. RESULTS

In this section, the results of a specific laser-foil interaction experiment are discussed. Since the focus of our interest is in the radiation physics, emphasis is placed on that analysis as opposed to a detailed study of laser deposition, suprathermal electron generation and transport, flux-inhibited transport, etc. Previous studies have shown that the onset of suprathermal electrons and flux-inhibited transport occurs at high laser irradiances.[5] To minimize the effects of these phenomena in this study, a relatively low-irradiance laser pulse, 10^{13} W/cm^2 at 1.06 μm wavelength, was assumed to be incident on a thin (8.0 μm) aluminum foil.

The results of this calculation are presented in four sections. First, a qualitative picture of the fundamental physical processes occurring in this calculation are presented. Second, a more detailed analysis of the energy transfer from laser to thermal energy in the foil is given. Third, the calculated frontside and backside spectra are presented to illustrate the qualitative and quantitative nature of the radiation, considering not only what escapes, but what is trapped internally also. Finally, the $K\alpha$ emission is studied and its role as an indicator of the dense rearside plasma conditions is analyzed.

A. The nature of laser-heated foils

When intense laser radiation strikes a thin medium-z foil, the physical mechanisms which play a role in the transport of that energy are extremely complex. The radiation is absorbed in a relatively thin surface layer, determined by the laser wavelength. The plasma is strongly heated locally by this energy deposition and ablates away from the foil surface creating a large density gradient. Simultaneously with material ablation, energy is transported into the foil by shock heating, thermal conduction, suprathermal electrons, and secondary radiation emission. In order to more clearly explain the results of this calculation, the foil plasma is considered to be comprised of three regions, as shown in Fig. 3. (1) A high-temperature, low-density "blowoff" plasma formed as heated material ablates from the frontside of the foil, (2) a central "transition" zone in which the laser energy is absorbed, characterized by large temperature and density gradients resulting from the local deposition and transport of energy, and (3) a cold, dense "backside" region into which energy is transported from the blowoff and transition zones by one or more of the processes mentioned above.

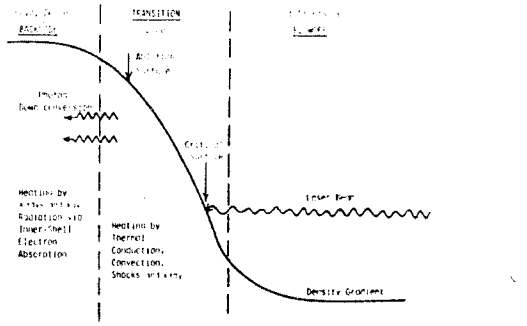

FIG. 3. Simple schematic of the major physical processes taking place in laser-foil interaction at low irradiance, showing the three regions referred to in the text.

Much work has been done in an effort to model plasma heating by thermal conduction, shock and compression waves, and suprathermal electrons, and the physical mechanism of each of these processes is at least qualitatively understood if not, as yet, quantified exactly. Although several workers have studied laser plasmas using hydrodynamic codes coupled with radiation models,[39–43] no detailed study of the role of secondary radiational heating has been reported on in laser-heated foils; hence, we concentrate our investigation on this aspect of the problem.

Laser heating of the plasma in the vicinity of the critical surface ($N \approx 10^{20}$ ions/cm^3 for 1.06 μm laser light in aluminum) results in radiation emission by this heated plasma in both the forward and rear directions. In aluminum, this radiation will consist mainly of soft x-ray and xuv photons. The soft x rays, with energies above 1.5 keV, are emitted from the plasma heated to electron temperatures above at least 250 eV, and result mainly from bound-bound transitions due to excitation of K-shell electrons. The xuv photons, with energies below about 1.0 keV, are emitted from plasma between about 10 and 150 eV and result mainly from bound-free transitions and, to a slightly lesser degree, bound-bound transitions of L-shell electrons, depending on the plasma density. Between photon energies of about 0.5 and 1.5 keV, continuum emission dominates the spectrum; no strong lines are found in this region due to the large difference in excitation energies of L- and K-shell electrons.

The radiation emitted in the forward direction suffers some attenuation due to resonant photoexcitation processes, but most escapes through the low-

density blowoff region. That which is emitted back into the foil, however, is strongly attenuated by both valence electron photoexcitation and inner-shell electron photoionization, due to the large optical depths in this dense region. Since the backside plasma is of much higher density and highly collisional, much of this absorbed radiation is collisionally quenched, resulting in increased temperature and ionization of the cold matter. This matter will, of course, reradiate much of its energy, but at lower photon energies corresponding to the dominant ionization stages of the colder material. This process continues throughout the transition and backside regions, with photons being absorbed and reemitted at lower frequencies. Hence, the radiation reaching the rear surface of the plasma is comprised of a wide spectrum of photons, from frontside soft x rays, which manage to penetrate the total extent of the foil, to transition and backside photons which have been born in the xuv range via progressive *down-conversion* in frequency of the incident soft x rays. It is this progressive down-conversion process which makes the radiational heating of the dense backside plasma such a complex process, and renders the simple technique of turning the measured forward spectrum back onto the cold, dense plasma to obtain estimates of the radiational heating, somewhat inaccurate.

The photons born in the transition and blowoff regions and emitted to the rear tend to be absorbed in the dense backside primarily by inner-shell processes. This creates K- and L-shell vacancies which have to be filled by the decay of a bound electron. Since K and L fluorescence yields are so small for aluminum, most of these vacancies are filled by Auger processes. Hence, the radiation absorbed in the backside region tends to be predominantly channeled into ionization along with thermalization via the ejected Auger electrons, i.e., the ejected-electron energy is arbitrarily dumped into the thermal reservoir in this calculation.

B. Energy transport in the foil

To elucidate the role played by radiation in the transport of energy through the foil, a discussion of both the spatial and temporal distribution of the emission is necessary. Although a large fraction of the radiated photons are reabsorbed before ever escaping the plasma, much can be learned from the gross characteristics of the radiation that does get out. In Fig. 4, we show the total forward and backward radiation power as a function of time, along with the temporal laser pulse shape. The emission in the forward direction is typically two orders of magnitude more intense than that from the back-

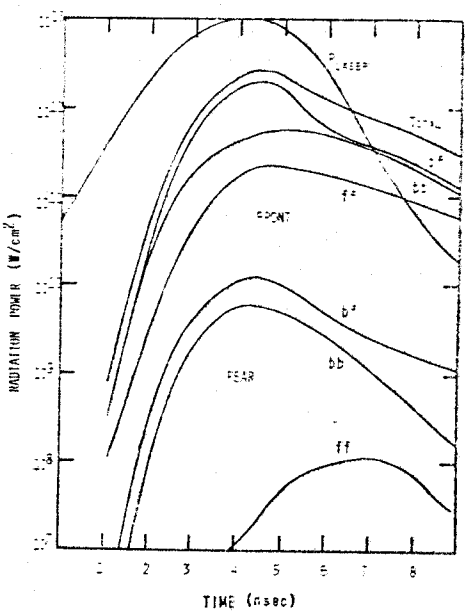

FIG. 4. Time evolution of the laser power and total radiative power of the laser-heated foil. The total power is also separated into lines (bb), radiative recombination (bf), and bremsstrahlung (ff) in the forward and rearward directions.

side. Also shown in the figure are the three components of the total: bound-bound (line emission), bound-free (radiative recombination emission), and free-free (bremsstrahlung) radiation. Both front and back directions are dominated by bound-free processes, while bremsstrahlung plays only a minor role in the foil energetics, accounting for only 10% of the total emitted radiation. The roughly $\frac{1}{2}$ nsec delay between the peaks in the laser profile and the radiation pulse is of no significance other than representing the difference between the temporal laser power and the integrated power or laser energy deposition. Thus, the plasma radiation responds quickly to changes in energy deposition. This is rather what one would expect from the frontside emission, but it is not so intuitive as regards the backside radiation, where one might expect some "lag time" between laser and radiation power. It will be shown later that the bulk of the calculated rearward emission is comprised of secondary K-line x rays above a kilovolt shining through the foil from the blowoff and transition regions and hence responds quickly to laser power. Compare this with the backside bremsstrahlung component which is born in the dense rearside of the foil; the response is much slower for these photons which are truly emanating from the rear of the foil. However, with only a calorimeter or bolometer at his disposal, an experimentalist would see only the response of the more energetic shine-through component from the

front. Of course, with thicker foils, the rearside spectrum changes accordingly, and fewer x rays from the front penetrate through the foil to overshadow the true backside emission.

An important question we wanted to address with this model was "How much of the backside heating is attributable to thermal conduction, how much to radiation, how much to shocks, etc.?" To answer this, a graph of the spatial variation of several pertinent parameters can be illuminating. In Fig. 5 is shown a snapshot (at a time near peak emission) of the plasma temperature, density, and net radiative cooling, along with the position of the laser deposition critical surface (the original foil position was at $d=0$). The radiational cooling follows the density profile closely in the blowoff region, whereas it drops sharply just forward of the ablation surface where the plasma temperature starts to fall off. Further into the foil, the plasma becomes heated by radiation, i.e., it absorbs more energy from photons than it emits. By comparing the values for the rate of heating, we find that radiation is *two to three orders of magnitude* more effective than thermal conduction in the dense backside region. In addition, the assumed laser irradiance was low enough that only a small shock wave was propagated and contributed little to the backside heating. The radiational heating of the backside region can be seen clearly in the temperature curve. Without radiation, the curve would drop smoothly to near zero at the backside; in Fig. 5, however, a noticeable hump is present near the original foil position and the temperature drops to about 5 eV at the backside. The flat temperature profile in the blowoff region is a consequence of the one-dimensionality of the model, since it cannot take account of the actual-two-dimensional cooling of the ablating plasma.

Another point of interest in the energy transfer physics is the temporal behavior of the backside temperature; this is shown in Fig. 6 along with the

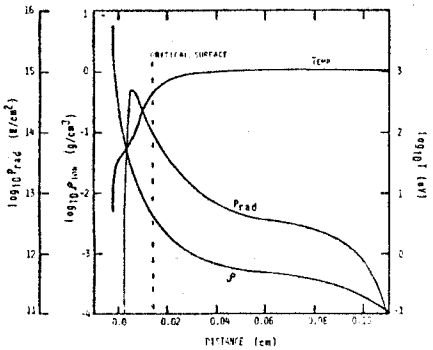

FIG. 5. Temperature, mass density, and radiative cooling as a function of position in the laser-heated foil, at a time near peak radiative emission ($\sim$5 nsec).

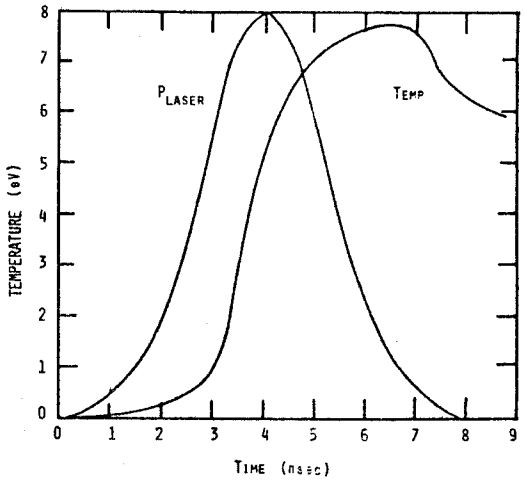

FIG. 6. Backside temperature of the laser-heated foil as a function of time. The laser power is shown for reference.

laser pulse shape. The lag time between the laser peak and the peak in the backside temperature is about 2.5 nsec, and the temperature reaches a maximum of about 7.5 eV. These values are in reasonable agreement with those quoted by McLean *et al.*,[2] although their measurements were taken for slightly different laser and foil parameters than ours. Knowing that radiation is responsible for backside heating, one would expect the temperature there to have a temporal behavior similar to the rearward radiation profile. However, the total backward radiation pulse (as well as the bound-bound and bound-free emission) is characteristic of the emission which *passes through* the backside, not what is *stopped* in the backside. The backside bremsstrahlung tells the story of the rearside temperature history, since it truly originates in the backside; this can be seen in Figs. 5 and 6. What causes the time lag, then? Why does the backside not respond immediately to the frontside radiation shining back into the foil? The answer is that ionization-dependent inner-shell opacity controls the time dependence of the backside temperature. A simpler way of stating this is that, like a combustion wave, radiation incident on the backside region must first "burn" its way through to the rear surface before it can heat it via the photoionization-Auger-thermalization cycle. "Burn" in this context means "ionize," since the inner-shell opacity must be reduced before the radiation can penetrate deeper into the plasma. How is this accomplished in the laser-heated foil? Since the strongly emitted features of a material are also strongly absorbed by that material when cold and dense, a changing temperature profile on the frontside will not appreciably alter the heat-

ing by shifting the intense features of the spectrum away from absorption edges. What does occur, however, is the shifting of absorption edges. As the region between the ablation surface and the rear surface slowly heats up, it ionizes, causing the absorption edges to shift according to Fig. 2. In this way, radiation from the front slowly burns its way through to the rear surface. Thus, the upward drift in rearside temperature after termination of the laser pulse reported by McLean *et al.*[2] is probably not due to thermal conduction, but, more likely, is due to "ionization burn-through" of the dense backside region by secondary x rays and xuv photons from the ablation and blowoff regions.

The temporal behavior of the backside temperature can have serious consequences on fuel preheat in laser pellets, and a common question is when the backside becomes hot enough to heat the fuel. Perhaps another question to consider is the effect of the prompt shine-through radiation on the fuel. Depending on the pellet shell material (which dictates the emitted spectral distribution), and the radiative absorption characteristics of the fuel, radiation preheat could be a more serious threat to efficient fuel compression on a low isentrope than backside plasma temperature.

One final point in regard to the energy transfer through the foil is the energy partitioning. In Fig. 7 are shown the various energy terms as they progress in time. These include the laser deposition, particle kinetic energy, radiation energy loss, internal energy, and energy of the ions due to ionization and excitation. The final percentages at the end of the run ($t = 8.3$ nsec) are shown in Table II. Most of the energy has been converted into kinetic energy of the foil, as it is accelerated by the ablating plasma in the blowoff region. However, over a quarter of the absorbed energy has been radiated away, most of it out

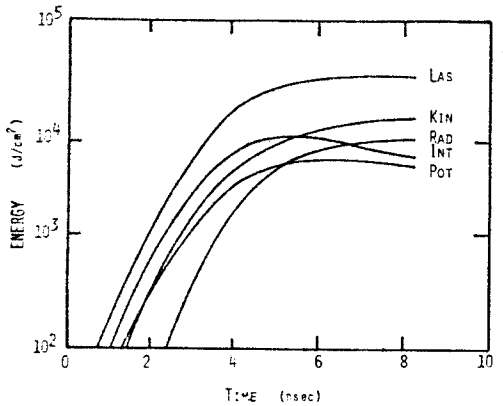

FIG. 7. Laser-foil energy partitioning as a function of time, including laser deposition (LAS), kinetic energy (KIN), radiative cooling (RAD), internal energy (INT), potential energy (POT).

TABLE II. Energy partitioning of the laser-heated foil at the end of the theoretical simulation ($t = 8.3$ nsec).

Mechanism	Energy (joules)	Percentage
Laser deposition	2.94×10^4	100%
Kinetic energy	1.20×10^4	40.8
Radiative loss	7.76×10^3	26.4
Internal energy	5.34×10^3	18.2
Potential energy	4.29×10^3	14.6

the front of the foil. The internal energy peaks near the maximum of the laser pulse and drops thereafter as the plasma commences cooling. The ionization energy has been maintained at a constant level since the peak of the laser pulse, indicating little ion recombination has taken place during this time. This seems a bit contradictory in view of the decreasing internal energy. Most of the ionization energy is in the dense backside regions of the foil, where plasma cooling changes the temperature only a few electron volts; this has little effect on the ionization state there. On the other hand, the thermal energy is more evenly distributed throughout the backside and transition zones where the cooling has more noticeable effects on the internal energy. Ionization energies in the transition zone are larger and a large decrease in the temperature there will greatly decrease the total plasma potential energy.

C. Spectral energetics

In this section we analyze the details of the forward and rearward spectral emission and attempt to explain how radiation is transported through the foil. The emphasis here will be on the energetics of the gross spectrum, whereas spectral diagnostics are discussed in Sec. III D.

Shown in Fig. 8 is the total, time-integrated radiation spectrum from the frontside of the foil, over a range from 10 eV to 10 keV. There are several interesting details in this plot which merit further discussion. At low photon energies, the emission is predominantly bremsstrahlung; to illustrate, the free-free portion of the spectral intensity is shown as a broken dotted curve. Also, few lines are present below 30 eV, since photons from most lines in this range are born of lower ionization stages found in the dense backside region, and are strongly attenuated before reaching the front of the foil. Above 50 eV, many strong lines are present, sitting on a continuum baseline made up of recombination radiation. This bound-free component is also shown in the figure as a broken curve. Between 450 eV and 1.5 keV, no lines are present since this range falls in

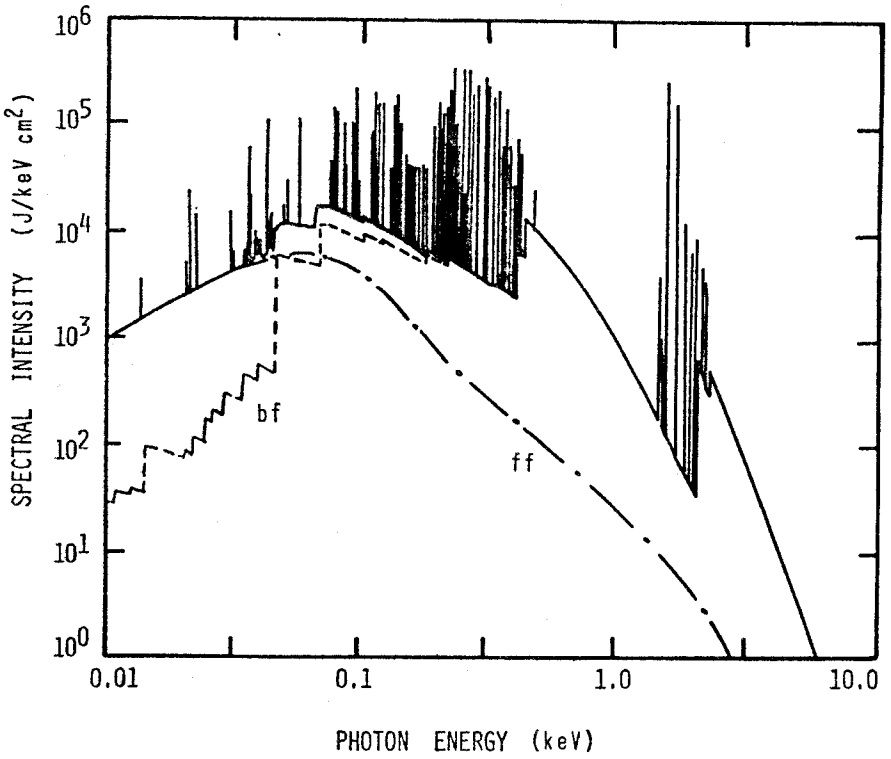

FIG. 8. Full time-integrated spectrum from the frontside of the laser-heated foil. Also shown are the bound-free (bf) and free-free (ff) components of the radiation.

the energy gap between the K and L lines; the emission here is bound-free radiation from heliumlike aluminum. Above 1.5 keV is the K-shell radiation: $K\alpha$ emission and hydrogenlike and heliumlike lines. The continuum level rises at energies above 2 keV due to the recombination edges of Al XIII and Al XIV. A more detailed analysis of the K-shell spectrum will be presented in the diagnostic section following.

An interesting question that often occurs in spectroscopy is the degree to which the spectra change during the time development of the plasma. If one could substantiate that the "snapshot" power spectrum at a time near peak emission was qualitatively similar to the time-integrated spectrum, the frequently used approach of inferring that the plasma parameters obtained by diagnosing the time-integrated spectrum are typical of the plasma at peak emission could be validated. In Fig. 9, we show a snapshot of the frontside spectrum at a time near peak emission. Comparison with Fig. 8 shows little qualitative difference in terms of the slope of continuum features and strong line intensities. The only noticeable difference is the slope of the Al XII recombination continuum between 0.45 and 1.5 keV. In general, most of the frontside snapshot spectra that were generated (at various times during the main emission pulse) looked qualitatively similar to the time-integrated spectrum; essentially only the intensity levels change slightly with time. In the next section, the K-shell x-ray spectra will be examined in detail to assess the finer discrepancies between time-integrated and time-resolved spectra.

We now turn our attention to the radiation spectrum from the rearside of the foil. The full time-integrated spectrum is shown in Fig. 10, and substantial differences are found compared to the frontside emission shown in Fig. 8, the most noticeable being the absence of radiation between 80 and about 650 eV. The opacity due to inner-shell photoionization strongly attenuates all photons in this energy band. Below the L absorption edge, two superimposed features are seen: (1) The continuum radiation emanating from the dense backside region and approximating a Planckian function at low temperature (about 6.0 eV), (2) a small recombination feature, cut off at the L edge, consisting of photons from the transition region, which manage to escape through the backside. The high-energy component of the spectrum is all shine-through radiation from the frontside blowoff region and consists of attenuated K lines and bound-free continuum from L and K electrons. Notice the distorted appearance of these continuum features due to opacity, which

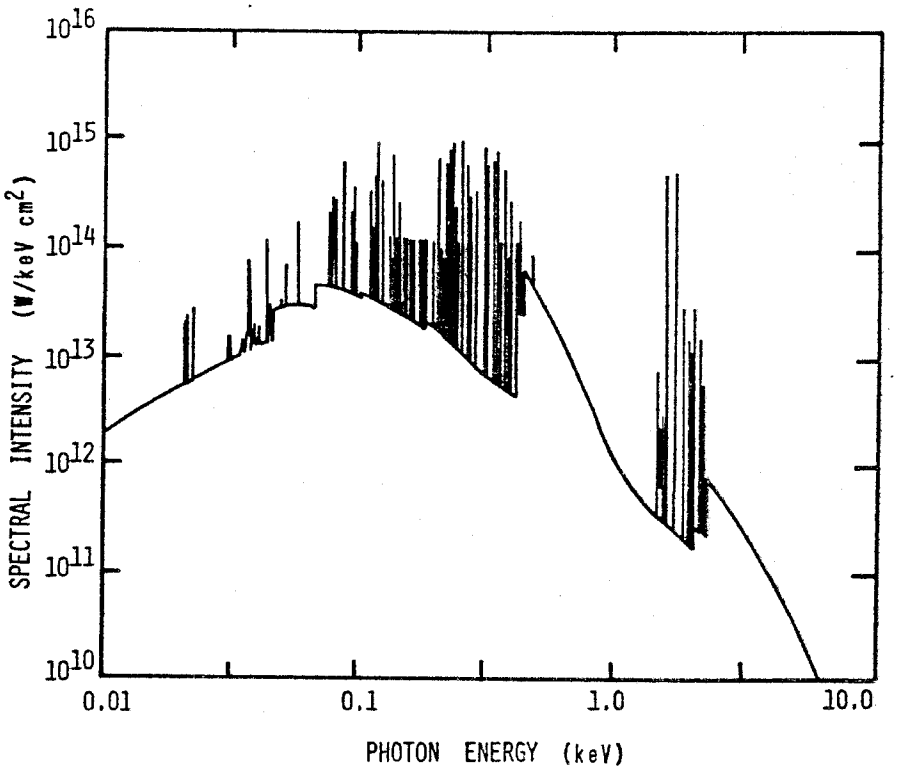

FIG. 9. Full snapshot spectrum from the frontside of the laser-heated foil at $t = 4.59$ nsec.

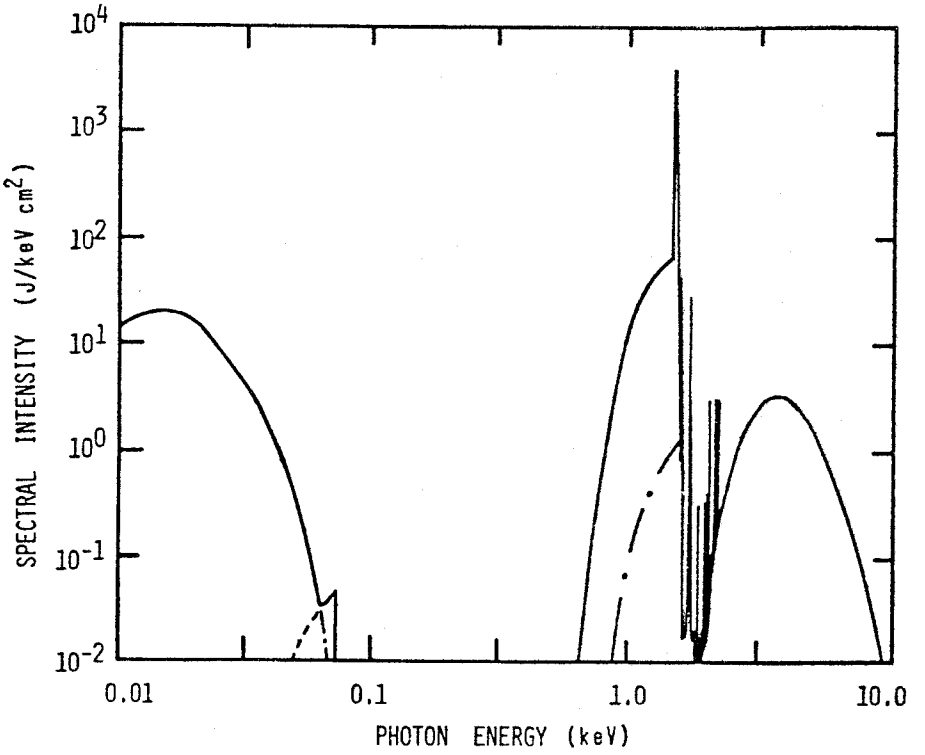

FIG. 10. Full time-integrated spectrum from the rearside of the laser-heated foil. Bound-free contribution is shown as a dashed line, while free-free is shown as alternating dots and dashes.

shifts the frequency at which most bound-free photons escape from the actual recombination edge frequency. The shift can be approximated by the expression

$$E_{\text{shift}} \approx E_0^{3/4}(3\tau_0 kT)^{1/4}, \tag{23}$$

where $E_0 = h\nu_0, \nu_0$ is the edge frequency, and τ_0 is the optical depth at the recombination edge. This calculated spectrum was verified by comparing it with the predicted instantaneous emission spectrum from a more detailed transport calculation[44] which solves the exact equation of transfer for a large-frequency grid, and agreement between the two models was excellent. Superimposed on the continuum is the $K\alpha$ emission which appears as a single large spike with the coarse resolution of Fig. 10. The $K\alpha$ radiation comes from regions where K-shell photons are strongly absorbed by inner-shell processes. Only the low-energy continuum radiation constitutes actual backside region emission, from within a few optical depths of the rear surface. The other features are shine-through from beyond the ablation surface.

Although few qualitative differences were found in time-integrated and time-resolved spectra in the frontward direction, substantial differences are seen in the rearward spectra. In Fig. 11, the full backside snapshot power spectrum is shown at five times during the emission pulse, and significant differences are evident. At t_1 (3.0 nsec), only L-shell bound-free emission is strong, appearing just below the K edge. The K-shell lines and continuum are barely evident. The sharp spike at 1.5 keV is the blend of $K\alpha$ lines. At t_2 (3.9 nsec) and t_3 (5.0 nsec), two changes are seen: (1) continuum radiation appears at low photon energies as the backside plasma begins to heat up, (2) more K-shell radiation is emitted and the emission penetrates the dense plasma more easily as the inner-shell opacity is slowly reduced by burn-through in the transition zone and forward-most zones of the backside region. Also shown in these spectra is the blackbody (BB) curve (broken line) corresponding to the temperature of the last backside zone. The actual emission in these spectra tracks the BB curve very well up to the L edge. This is due to the strong opacity at these low photon energies, predominantly free-free, but with a non-negligible bound-free opacity contribution. Thus, at low frequency the backside plasma looks like a blackbody emitter and validates the procedure of McLean *et al.* in obtaining backside temperatures from time-dependent spectroscopy at several low photon frequencies and fitting the result to the appropriate BB profile.

At t_4 (6.4 nsec), the frontside blowoff is beginning to cool due to expansion and reduced laser power,

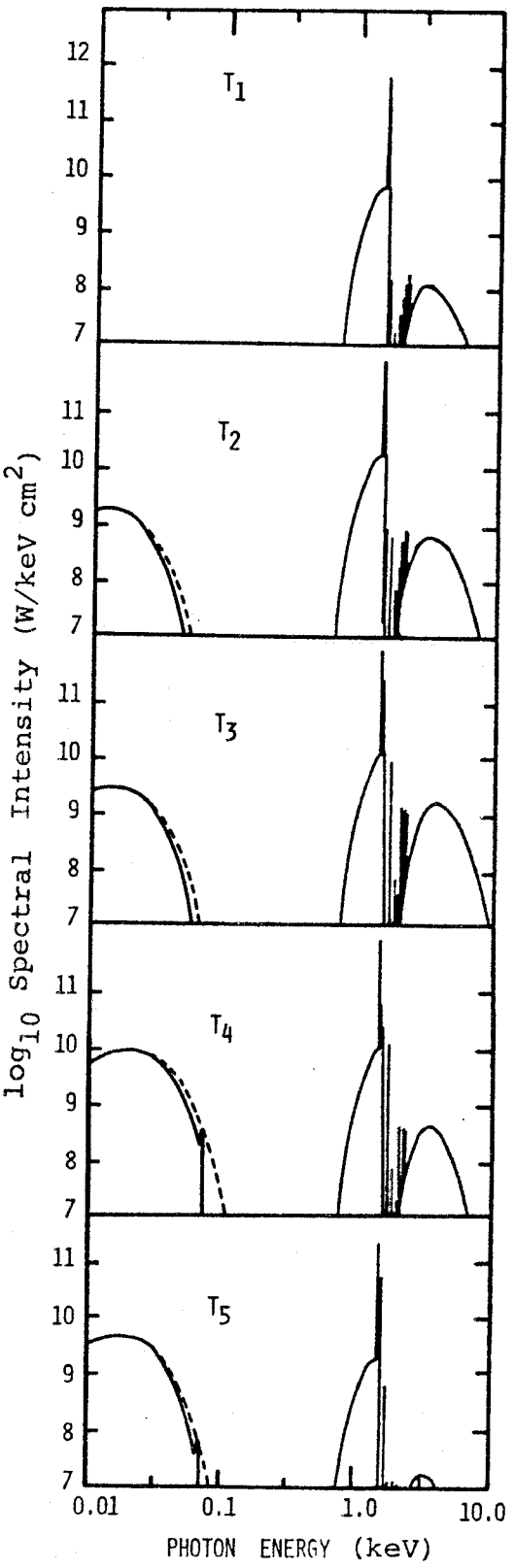

FIG. 11. Full snapshot spectra from the rearside of the laser-heated foil at five different times: $T_1 = 3.0$ nsec, $T_2 = 3.9$ nsec, $T_3 = 5.0$ nsec, $T_4 = 6.4$ nsec, $T_5 = 8.4$ nsec.

which is evident from the decrease in the K-shell shine-through. The transition zone is still maintaining its temperature, however, and the L-shell continuum, just below the K edge, is still strong. The bremsstrahlung intensity level at low frequency is still increasing since the backside temperature reaches a maximum at 6.5 nsec (see Fig. 6); in addition, it still maintains close proximity with the Planck function, determined by the backside temperature. Also present is a very weak bound-free continuum feature just below the L edge, which rises to the vicinity of the BB curve. It should be emphasized here that the BB curve corresponding to the rear surface temperature does not represent an upper limit to this continuum emission, since this radiation is emitted from several optical depths into the backside region and at frequencies where the plasma is not a perfect absorber. The time-integrated spectrum in Fig. 10 most resembles the snapshot spectrum at this time.

Finally, at t_5 (8.4 nsec) the K-shell contribution is negligible, and only bremsstrahlung, L-shell bound-free continuum, and $K\alpha$ emission are present. Note that the L edge is still a major absorption mechanism, as evidenced by the large gap in the emission. From a "plasma" point of view, this spectral gap is an indication that the laser has still not burned through the foil, since the foil backside region has yet to be heated to high temperatures. From a radiation standpoint, however, burn-through is not so clearly defined, since secondary emission from the frontside is the strongest radiational component through the backside and it commences promptly after laser-plasma interaction begins. Thus, if the absorption cross section for the fuel (or intermediate tamper) is large at frequencies corresponding to this shine-through emission, and the shine-through radiation is sufficiently intense, as in thinner foils, parameters such as foil burn-through time can be of minor consequence when considering target preheat.

To more quantitatively assess the radiative output of this laser-foil interaction, the frontside and backside radiative components are shown in Table III; the emission is separated by both energy bins and atomic mechanism as well as direction, and is expressed as a percentage of the total radiation in the appropriate direction. The total forward emission is approximately a factor of 100 times more intense than the total rearward emission. For the most part, the table is self-explanatory. A few points need to be emphasized, however. The low-energy bremsstrahlung from the backside accounts for less than a percent of the rearward emission; almost all lies in photons above a kilovolt. The bremsstrahlung component (both front and back) as a whole is energetically unimportant, comprising only about 10% of the foil radiation, while radiative recombination is the most important radiative process. Conversion efficiencies are often numbers of interest in experiments of this sort. The total laser-to-radiation conversion efficiency was 26.4%, hence, from Table III, the conversion to x rays above 1.5 keV is only 5.3%, and above 0.5 keV it is 12%.

D. K-shell diagnostics

Many previous papers[45] have dealt with the subject of K-shell radiation diagnostics in dense plasmas. However, most have employed stationary atomic models uncoupled from the plasma dynamics for the sake of simplicity. With this model we are able to make detailed comparisons between time-integrated and time-resolved spectral emission for the K-shell region to determine what portion of the plasma evolution is characterized by the time-integrated spectrum. Granted, with the recent advent of spectroscopically resolving x-ray streak cameras, this new advanced technology has made it possible to obtain time-resolved K-shell spectra for the first time. However, this will be a successful diag-

TABLE III. Total time-integrated radiation energy in the forward and rearward directions, separated by various photon energy bins and by the atomic process responsible for the emission (values are given as percentages of the total in that direction).

Photon	Forward spectrum				Backward spectrum			
energy (eV)	bb	bf	ff	total	bb	bf	ff	total
1–40	0.0	0.1	1.2	1.3	0.0	0.0	0.6	0.6
40–125	1.2	8.0	5.1	14.3	0.0	0.3	0.0	0.3
125–300	7.0	11.3	2.2	20.5	0.0	0.0	0.0	0.0
300–500	3.3	14.0	0.5	17.8	0.0	0.0	0.0	0.0
500–1560	0.6	25.1	0.3	26.0	30.9	50.9	0.0	81.8
1560–5000	15.6	4.3	0.2	20.1	1.2	16.1	0.0	17.3
Total	27.7	62.8	9.5	100.0	32.1	67.3	0.6	100.0

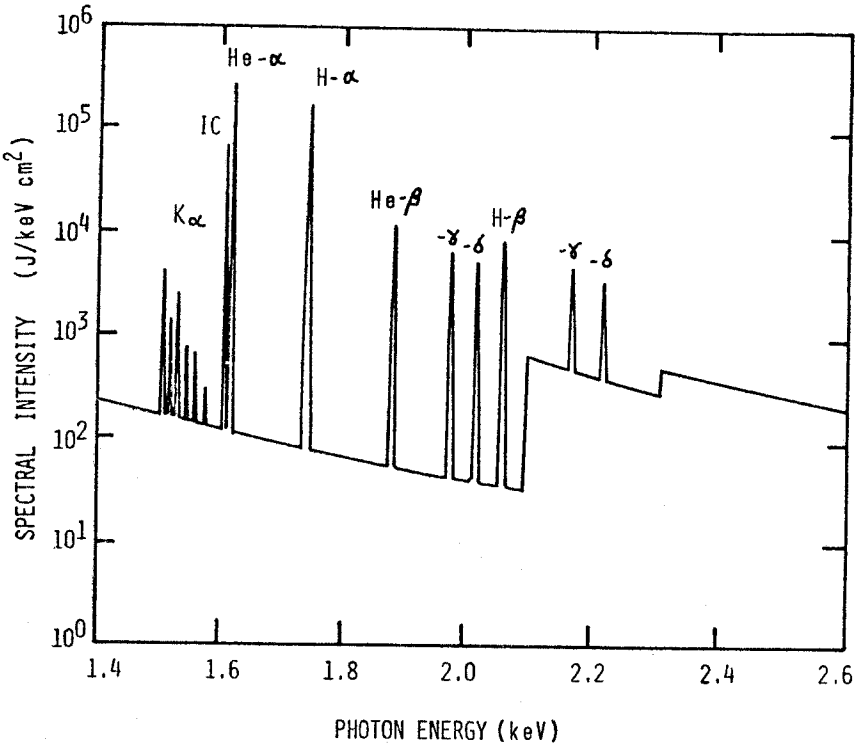

FIG. 12. Time-integrated K-shell spectrum from the frontside of the laser-heated foil.

nostic tool only if intensities are sufficiently high. Other valuable diagnostic techniques, e.g., impurity doping,[46] tracer-dot implantation,[47] and slitting to obtain spatially resolved information, often limit the measured intensity of the emission, making time-resolved measurements difficult and uncertain. Thus, the relationship between time-integrated measurements and the evolution of various plasma parameters of interest is still an important unanswered question.

The time-integrated K-shell frontside spectrum, shown in Fig. 12, contains Rydberg series lines from hydrogenlike Al XIII and heliumlike Al XII, resulting from the spontaneous decay of np states ($n \leq 5$) to the $1s$ orbitals. In addition, the density-sensitive $1s^2(^1S)$-$1s\,2p(^3P)$ intercombination (IC) line is also shown, as well as the two recombination continua Al XIV-to-Al XIII and Al XIII-to-Al XII, seen as sharp edges above 2 keV. At slightly lower energies, the $K\alpha$ series of lines is shown; as stated earlier, they are treated as optically thin in this study. Thus, their intensities here are identical to those predicted in the rearward spectrum, and it will suffice to discuss their relative intensities as seen in Fig. 12 without showing a K-shell backside spectrum.

In order to allow for comparison, the frontside snapshot spectra for several times are shown in Fig. 13. Since the real K lines (as opposed to the $K\alpha$ lines) are valence electron transitions from highly ionized aluminum, they are emitted entirely from the frontside blowoff and the transition zone just in back of the critical surface. As thermal conduction of deposited laser energy back into the foil becomes ineffective as a heating mechanism, the temperature drops and the K lines are no longer emitted; this probably occurs at some point between the critical and ablation surfaces, at a temperature around 150–200 eV. Hence, the K-line emission is characteristic of somewhat dense as well as rarefied regions of the foil plasma. Limiting this first discussion to the K lines, very little difference is evident between the five spectra in Fig. 13 and the one in Fig. 12. The intensities fall off at t_5 (7.35 nsec), but relative line intensities vary only slightly. To magnify these differences, we have plotted three line ratios commonly used for plasma diagnostics as a function of time in Fig. 14. Curve 1 is the H-β/He-δ[$1s$-$3p/1s^2$-$1s\,5p(^1P)$] ratio, curve 2 is the H-α/He-α[$1s$-$2p/1s^2$-$1s\,2p(^1P)$] ratio, and curve 3 is the IC/He-α[$1s^2$-$1s\,2p(^3P)/1s^2$-$1s\,2p(^1P)$] line ratio. The first two are temperature sensitive, while the third is density sensitive. A complete discussion of these line diagnostics in isothermal, isodense plasmas can be found in Ref. 18, while the effects of density and temperature gradients on these ratios has been described in Ref. 19.

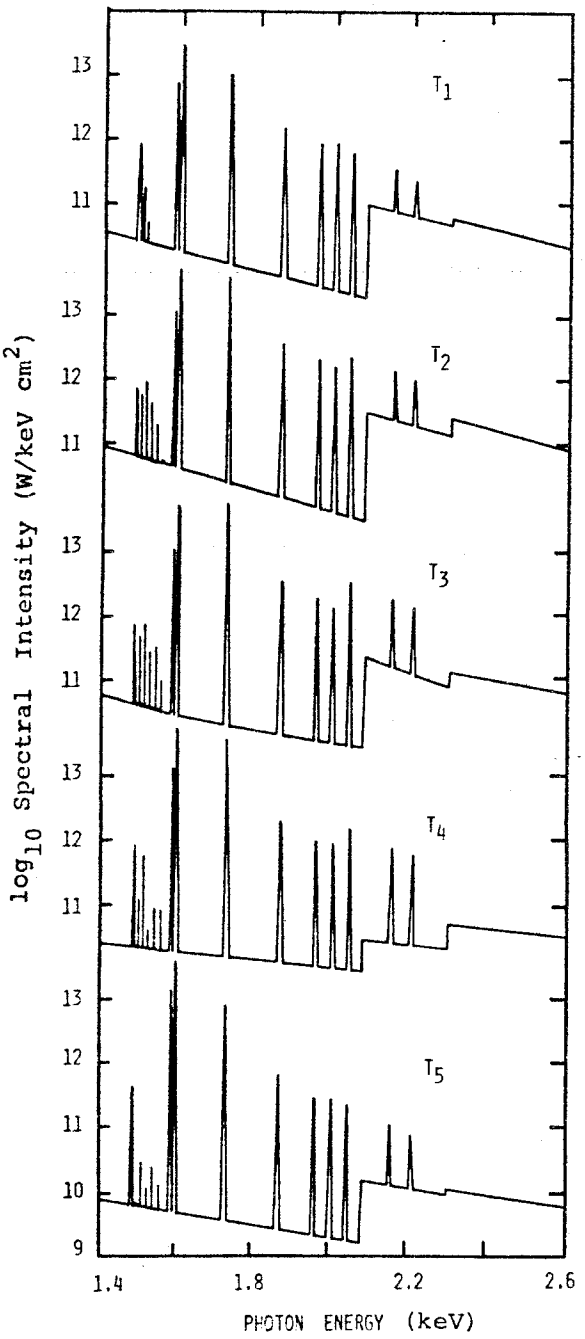

FIG. 13. *K*-shell snapshot spectra from the frontside of the laser-heated foil at five different times: $T_1=2.9$ nsec, $T_2=3.9$ nsec, $T_3=4.6$ nsec, $T_4=5.9$ nsec, and $T_5=7.4$ nsec.

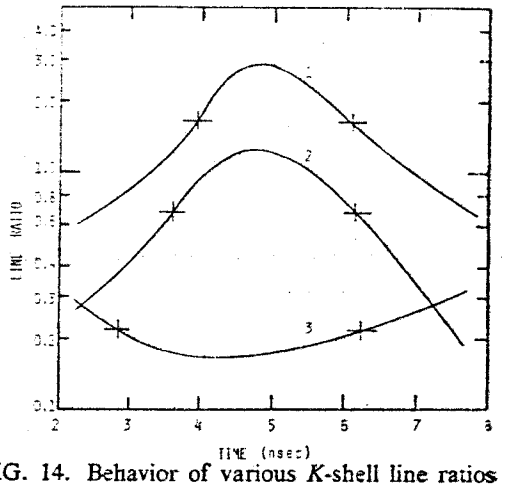

FIG. 14. Behavior of various *K*-shell line ratios as a function of time: curve 1 H-β/He-δ, curve 2 H-α/He-α, curve 3 IC/He-α.

What we seek to determine here is the effect of time integration on these diagnostics. Namely, what can we expect to learn from a time-integrated spectrum which has been obtained from a plasma which changes significantly during the radiation pulse time? Examining the time behavior of curves 1 and 2, they display maxima at 4.8 nsec when the blowoff plasma is the hottest and the greatest abundance of hydrogenlike aluminum ions, relative to heliumlike ions is attained. Curve 3 shows a minimum corresponding to the peak plasma density in the blowoff region, which occurs at 4.2 nsec, slightly earlier than the time peak temperature is reached. Superimposed on the curves are crosses which indicate the values for these ratios from the time-integrated spectrum in Fig. 12. It seems to indicate that the time-integration averages the values obtained for plasma parameters over a time period comparable to the total radiation pulse width, which is what one would intuitively expect rather than a significant weighting by the ratios in either the pre- or post-maximum direction. However, the more interesting question is what is the *difference* in temperatures (or densities) between the peak values attained in the plasma and those indicated by the time-integrated diagnostics? Using theoretical line-ratio calculations generated for the study in Ref. 19, ratios 1 and 2 indicate time-integrated values for the temperature roughly *200 eV lower* than those indicated by a time-resolved spectrum at the time of maximum temperature. Similarly, the time-integrated density as determined by ratio 3 is 25% lower than that predicted by the time-resolved spectrum at maximum emission time. What impact does this have on spatially and temporally integrated diagnostics? As seen in the study on plasma gradients, a laser-heated slab plasma will be diagnosed significantly cooler than the actual spatially averaged temperature due to spatial integration of the line spectrum over gradients normal to the target. Couple this with the result above due to time integration, and the net result from spectral diagnostics can be expected to be several hundred electron volts below the maximum average tempera-

ture attained in the plasma. Combined effects of spatial and temporal integration on the density determination are nearly as strong, and the values obtained are at least a factor of 2 lower than the maximum average density attained in the K-shell emitting region.

Our final goal in this work was to make some definitive contribution in the use of $K\alpha$ emission to diagnose cold, dense matter. In this initial effort to study these features, the $K\alpha$ emission was not transported; hence, every K vacancy that was created resulted in a measured $K\alpha$ as dictated by the appropriate fluorescence yield. The $K\alpha$ emission is seen most clearly in Fig. 12, the time-integrated, frontside, K-shell spectrum. As was stated in Sec. II, each ionization stage will emit $K\alpha$ radiation at a different frequency, since the shielding due to outer electrons is different. Since the first four ions have similar ionization energies, the $K\alpha$ lines corresponding to them are usually unresolvable, and appear in Fig. 12 as a single strong line, followed by the other five $K\alpha$ lines included in this model from the remaining ionization stages. The time evolution of these lines is represented in Fig. 13, where the higher lines are seen to grow in intensity and then fall off as time progresses. This can be seen more clearly in Fig. 15, where the $K\alpha$ intensities are plotted as a function of time. The actual time-integrated line ratios, relative to the intensity of the first and strongest $K\alpha$ feature are 1:0.23:0.59:0.12:0.11:0.03.

At the outset, we anticipated we would be able to make quantitative statements about the dense plasma based on the time-integrated $K\alpha$ emission. In fact, this proved to be quite difficult, since each line is emitted over a widely varying pulse width as seen in the figure. This pulse width corresponds to the period during which the respective ionization state is in abundance somewhere in the dense plasma region. The reason the dense plasma region dominates is a function of the inner-shell opacity. At densities much below solid, the creation rate of K-shell vacancies per unit volume at this laser power is not large enough to generate $K\alpha$ lines intense enough for measurement. However, Fig. 15 shows that to fully understand the $K\alpha$ radiation diagnostics, the time history of the lines must be known, hence, time-resolved spectroscopy is probably necessary. In addition, for this information to be useful, one must know from what regions of the plasma these lines emanate. If they all had come from the dense region very close to the foil backside, as we initially anticipated, Fig. 15 would look like a typical ionization abundance curve versus plasma temperature, with each ionization stage dominating at later and later times, until the backside began to cool, whence $K\alpha$ from lower ionization stages would reappear in reverse order. Since this is not the case in Fig. 15, the emission region must be different from what we had originally guessed.

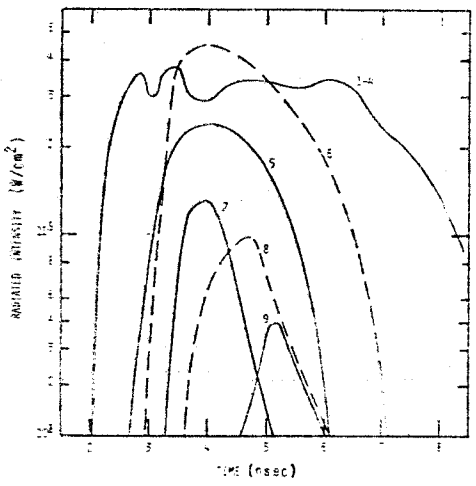

FIG. 15. Time behavior of the various $K\alpha$ line intensities in the laser-heated foil (optically thin approximation). Numbers refer to the atom or ion before photoionization occurs (5 ≡ Al V or Al^{4+}).

From the time history of these lines we see that successive ionization stages do "turn on" at progressively later times, as initially expected. However, the lower ionization stages do not disappear and reappear later, but sustain themselves over significant time intervals. The sustained nature of the lower ionization stages is due to the fact that the $K\alpha$ lines are coming from different regions of the plasma. The lowest ionization stages are coming from the far backside, while the higher ionization stages emit $K\alpha$ lines almost to the ablation surface in the transition zone. This is an interesting phenomenon from a diagnostic point of view and there are basically two reasons for it. Obviously, the temperature increases as one moves into the plasma from the backside, hence, the ionization abundances change predictably. Second (and a very necessary criterion), the K absorption edge shifts to higher photon energies with temperature, allowing the intense helium-like resonance line, for example, from the frontside to penetrate deeper and deeper into the plasma as it heats up. The Ly-α line, on the other hand, will be attenuated along with the other Rydberg series lines by the first dense zone it encounters, just beyond the ablation surface, since the K edge rarely shifts that much in the dense plasma region. Therefore, instead of yielding diagnostic information about the temperature of the far backside of the foil, we find that, knowing the $K\alpha$ line time histories, one can determine the dominant ionization stage (and, therefore, the approximate temperature) of the plasma region in the vicinity of the *ablation surface* and how that

temperature behaves in time. From Fig. 15 we know that at its hottest point, near $t=5$ nsec, the region in the vicinity of the ablation surface was mostly Al VIII and Al IX. Hence from CRE aluminum ionization abundance plots (see, e.g., Ref. 18), the temperature must have reached approximately 50–60 eV at this time. At the peak of the laser pulse ($t=4$) nsec), on the other hand, Al VII was dominant in that region, and the temperature was probably nearer to 40 eV at the ablation surface.

Of course, opacity effects may disturb the relative intensities of these lines, and work is underway to include these effects in our model. However, their time behavior appears to be more significant than their relative intensities as a useful diagnostic tool.

IV. CONCLUSIONS

The purpose of this investigation was to study the radiation dynamics of a medium-z material, heated to x-ray emitting temperatures by a laser. Although some physical mechanisms were not included in the theoretical model, the laser power was chosen so as to minimize the effect of these processes and allow us to concentrate on the radiative aspects of the problem. Therefore, we believe this model to be quite adequate to allow us to study the processes emphasized in this report in a detailed way and draw meaningful conclusions.

Several interesting conclusions were drawn from this work which are worthwhile summarizing. Our primary goal was to determine how important radiation was as an energy transport mechanism. For the conditions here, i.e., 10^{13} W/cm^2 glass laser pulse with a 3 nsec pulse width incident on an 8 μm thick aluminum foil, radiation was several orders of magnitude more efficient in transporting energy past the ablation surface than the second most important process, thermal conduction. (Recently, Yaakobi *et al.*,[35] in an interesting study of intense 0.35 μm laser light on saran targets, concluded that radiation, not suprathermal electrons, was responsible for heat transport past the ablation surface.) It was found that the heating in this region was caused by photoionization of inner-shell electrons in the dense backside plasma and that the incident photons transporting the energy consisted of down-converted xuv photons ($h\nu<1$ keV) from the transition zone as well as secondary x-rays ($h\nu>1$ keV) from the frontside blowoff region. Thus, the backside heating process is a complex one, not easily characterized by simpler models of the dense plasma, driven solely by K lines. The delay in the backside temperature rise after termination of the laser pulse was found to be totally radiative in nature and not attributable to thermal conduction eventually burning through the plasma. As secondary xuv and soft x-ray photons from the frontside and transition zones heat the dense, cold backside plasma, it slowly heats up and ionizes, shifting absorption edges to higher photon energies. This allows deeper and deeper penetration of these photons with time, resulting in a moving ionization (or temperature) front toward the rear of the plasma. Of course, the process is a continuous one across the entire spectrum, so the far backside temperature rises smoothly in time as increasing numbers of photons are able to penetrate. Hence, the concept of "prompt" x-ray heating of the backside is probably incorrect in all but very thin foils, and in these cases, thermal conduction will most likely dominate the heating. Summing up, "ionization burn-through" proved to be most important to radiative heating of the backside for the conditions considered here.

Concerning the general nature of the emitted radiation, about $\frac{2}{3}$ can be attributed to bound-free atomic processes (radiative recombination), about $\frac{1}{4}$ to line emission, and only $\frac{1}{10}$ to bremsstrahlung photons. The radiation directed out the frontside of the plasma was almost 100 times more intense than that in the rearward direction, but this will be strongly dependent on the foil thickness and laser wavelength. The rearside spectrum consists of a low-energy continuum, emitted directly from the backside region after the peak in the laser pulse, along with a higher energy prompt component shining through from the frontside and consisting of K lines and continuum and some L-shell continuum from the transition zone. In addition, strong $K\alpha$ features were present, emitted in the dense plasma region. The rearside low-energy continuum closely follows the curve for a blackbody emitter at the rearside temperature, up to photon energies well below the L edge, and the ion populations in the dense plasma are very nearly in local thermodynamic equilibrium (LTE). Depending on the absorption characteristics of the fuel constituents in a microballoon, this transmitted radiation may or may not represent a serious source of preheat in the fuel region.

Two main points are to be made regarding spectroscopic plasma diagnostics. First, the time-integration of the spectral emission has a large effect on line-ratio diagnostics from laser-produced plasmas. The final time-integrated intensities of K-shell emission lines indicated average temperatures and densities significantly lower than the maximum actually achieved in the plasma for these conditions. Thus, time-integration coupled with spatial gradients in these plasma parameters can have a serious effect on spectroscopic techniques used to diagnose them.

Finally, it was found that the $K\alpha$ lines can be a promising diagnostic tool in laser-produced plasmas. Since these features are emitted throughout the dense backside region, all the way up to very near the ablation surface, their time histories can be used to determine the temporal behavior of the electron temperature in the vicinity of the ablation surface. In principle, crystal-diffraction streak camera spectroscopy should be able to track the time-dependence of the $K\alpha$ components of the higher ionization stages in the dense plasma, and convert this information to temperature using ion abundance plots at high densities. Of course, no opacity effects were included when transporting the $K\alpha$ in our model, and fast electrons can also create K vacancies which give rise to these lines, but these factors should not in principle detract from the use of the $K\alpha$ lines to determine the time evolution of the plasma temperature deep in the plasma. In fact, the $K\alpha$ features emitted near the ablation surface may be more easily detectable in the forward spectrum than in the rearward.

In conclusion, we have tried to show the importance of plasma radiation to the energy transport in laser-heated foils. The radiation model employed in this study is one of the most detailed ever to be used in such a way, incorporating a comprehensive treatment of level population dynamics and radiation emission and transport. Although this model may lack the detail of other hydrodynamic codes used to address this problem, we believe our fluid treatment of the plasma medium to be quite sufficient to study the phenomenon of laser-foil interaction, and the conclusions drawn are valid ones for the initial conditions assumed. More detailed analysis of the comparison between various ionization-radiation models and the impact of neglecting radiation on the plasma modeling is the subject of another study presently nearing completion, and will be presented in another paper to follow.

ACKNOWLEDGMENTS

The authors would like to thank P. C. Kepple and H. R. Griem for helpful discussions and suggestions regarding the manuscript. This research was supported by the U.S. Defense Nuclear Agency.

[1]B. H. Ripin *et al.*, Phys. Fluids 23, 1012 (1980); 24, 990 (1981).
[2]E. A. McLean *et al.*, Phys. Rev. Lett. 45, 1246 (1980).
[3]J. A. Stamper *et al.*, J. Appl. Phys. 52, 6562 (1981).
[4]B. H. Ripin, E. A. McLean, and J. A. Stamper, Phys. Fluids 25, 2128 (1982).
[5]H. Nishimura *et al.*, Phys. Rev. A 23, 2011 (1981).
[6]H. Nishimura, M. Yagi, F. Matsuoka, K. Yamada, T. Yamanaka, S. Nakai, and C. Yamanaka, Appl. Phys. Lett. 39, 592 (1981).
[7]J. W. Murdoch, J. D. Kilkenny, D. R. Gray, and W. T. Toner, Phys. Fluids 24, 2107 (1981).
[8]J. Nuckolls, L. Wood, A. Thiessen, and G. Zimmerman, Nature 239, 139 (1972).
[9]J. P. Boris and D. Book, J. Comput. Phys. 11, 38 (1973).
[10]D. Duston and J. Davis, Phys. Rev. A 23, 2602 (1981).
[11]D. R. Bates, A. E. Kingston, and R. W. P. McWhirter, Proc. R. Soc. London, Ser. A 267, 297 (1962).
[12]A. Burgess, in Proceedings of the Symposium on Atomic Collision Processes in Plasmas, Culham, England, Report No. 4818, 63, 1964 (unpublished); and A. Burgess, H. P. Summers, D. M. Cochrane, and R. W. P. McWhirter, Mon. Not. R. Astron. Soc. 179, 275 (1977).
[13]V. L. Jacobs, J. Davis, P. C. Kepple, and M. Blaha, Astrophys. J. 211, 605 (1977).
[14]W. J. Karzas and B. Latter, Astrophys. J. Suppl. Ser. 6, 167 (1961).
[15]V. L. Jacobs and J. Davis, Phys. Rev. A 18, 697 (1978).
[16]J. Davis, P. C. Kepple, and M. Blaha, J. Quant. Spectrosc. Radiat. Transfer 16, 1043 (1977).
[17]E. Oran and J. Davis, J. Appl. Phys. 45, 2480 (1974).
[18]D. Duston and J. Davis, Phys. Rev. A 21, 1664 (1980).
[19]D. Duston and J. Davis, Phys. Rev. A 24, 1505 (1981).
[20]J. P. Apruzese, J. Davis, D. Duston, and K. G. Whitney, J. Quant. Spectrosc. Radiat. Transfer 23, 479 (1980).
[21]C. W. Allen, *Astrophysical Quantities* (Athlone, London, 1955), p. 102.
[22]Frank Biggs and Ruth Lighthill, Sandia Laboratories Report No. SC-RR-71 0507, 1971 (unpublished).
[23]R. G. Reilman and S. T. Manson, Phys. Rev. A 18, 2124 (1978).
[24]E. Clementi and C. Roetti, At. Data Nucl. Data Tables 14, 177 (1974).
[25]J. Davis, R. W. Clark, D. Duston, and J. P. Apruzese (unpublished).
[26]B. Yaakobi, I. Pelah, and J. Hoose, Phys. Rev. Lett. 37, 836 (1976).
[27]K. B. Mitchell and R. P. Godwin, J. Appl. Phys. 49, 3851 (1977).
[28]A. Zigler, H. Zmora, and J. L. Schwob, Phys. Lett. 63A, 275 (1977).
[29]J. D. Hares, J. D. Kilkenny, M. H. Key, and J. G. Lunney, Phys. Rev. Lett. 42, 1216 (1979).
[30]R. D. Bleach, D. J. Nagel, D. Mosher, and S. J. Stephanakis, J. Appl. Phys. 52, 3064 (1981).
[31]E. Nardi, E. Peleg, and Z. Zinamon, Appl. Phys. Lett. 39, 46 (1981).
[32]E. Nardi and Z. Zinamon, J. Appl. Phys. 52, 7075 (1981).
[33]A. Hauer, W. Priedhorsky, and D. van Hulsteyn, Appl. Opt. 20, 3477 (1981).
[34]J. Mizui, N. Yamaguchi, T. Yamanaka, and C. Yama-

naka, Phys. Rev. Lett. 39, 619 (1977).
[35]B. Yaakobi, J. Delettrez, L. M. Goldman, R. L. McCrory, W. Seka, and J. M. Soures, Opt. Commun. 41, 355 (1982).
[36]For a more complete discussion, the reader is referred to the review article by W. Bambynek *et al.*, Rev. Mod. Phys. 44, 716 (1972).
[37]V. L. Jacobs, J. Davis, B. F. Rozsnyai, and J. W. Cooper, Phys. Rev. A 21, 1917 (1980).
[38]E. J. McGuire, private communication.
[39]P. J. Mallozzi *et al.*, in *Fundamental and Applied Laser Physics, proceedings of the Esfahan Symposium,* edited by M. S. Feld, J. Javan, and N. A. Kurnit (Wiley, New York, 1973), p. 165.
[40]D. Colombant and G. F. Tonon, J. Appl. Phys. 44, 3524 (1973).
[41]D. G. Colombant, K. G. Whitney, D. A. Tidman, N. K. Winsor, and J. Davis, Phys. Fluids 18, 1687 (1975).
[42]G. L. Payne, J. D. Perez, T. E. Sharp, and B. A. Watson, J. Appl. Phys. 49, 4688 (1978).
[43]H. Yasuda and T. Sekiguchi, Jpn. J. Appl. Phys. 18, 2245 (1979).
[44]J. P. Apruzese and R. W. Clark (unpublished).
[45]See, for example, the extensive reference list in the review article C. DeMichelis and M. Mattioli, Nucl. Fusion 21, 677 (1981).
[46]B. Yaakobi, D. Steel, E. Thorsos, A. Hauer, and B. Perry, Phys. Rev. Lett. 39, 1526 (1977).
[47]M. J. Herbst, P. G. Burkhalter, J. Grun, R. R. Whitlock, and M. Fink, NRL Memorandum Report No. 4812, Rev. Sci. Instrum. 53, 1418 (1982).

Radiative properties of puffed-gas mixtures: The case of optically thick plasmas composed of two elements with similar atomic numbers

J. P. Apruzese and J. Davis
Plasma Radiation Branch, Plasma Physics Division, Naval Research Laboratory, Washington, D.C. 20375

(Received 29 November 1984; accepted for publication 18 January 1985)

Using detailed atomic and radiative transfer calculations, we consider the K-shell radiative properties of optically thick plasmas composed of two different elements with nearly the same atomic number. A sodium-neon mixture is chosen for specificity, and the plasma conditions considered are similar to those achieved in puffed-gas or exploding-wire Z pinches. The emissivity of an individual K-shell line is parameterized in terms of an "ultimate" photon escape probability which is a function of both the single-flight photon escape probability and the collisional quenching probability. Holding the total ion density (sodium plus neon) constant, we have evaluated the total K-shell emissivity as a function of sodium-to-neon ratio. In contrast to the optically thin case the emitted K-shell power peaks at values of this ratio intermediate between pure neon and pure sodium. The opacity effects responsible for this phenomenon are analyzed using the escape parameterization.

I. INTRODUCTION

In recent years, much attention has been devoted to measuring, understanding, and interpreting the x-ray emissions of laboratory plasmas produced by high-voltage pulse-power Z-pinch-like discharges through wires or gas puffs.[1–13] The bulk of experiments using such Z pinches have normally been concerned with a single material to form the plasma, neon, aluminum, and argon being perhaps the most frequently employed elements. Due to the numerous applications of such x-ray sources such as x-ray spectroscopy, x-ray lithography, and x-ray lasers, tailoring of the emitted power and photon energy spectrum is highly desirable. In an effort to develop novel techniques to achieve such tailoring the radiative properties of optically thin plasma mixtures have recently been studied in detail.[14] The mixtures selected for study in Ref. 14 were of two gases of widely divergent atomic number (i.e., neon/argon, argon/krypton, helium/argon, and helium/krypton). In that study it was found that no enhancement of radiative power would occur due to mixing, but that the utilization of two materials provided an effective technique to fill in naturally occurring spectral gaps between electron-shell emissions of various elements. The present paper is concerned with a considerably different mixture scenario: the plasma is optically thick and the atomic numbers are very close. In this case, opacity effects do influence the total yield at the expense of spectral filling since the spectral lines from the various shells of the two elements lie fairly close in energy. As seen below, the effects produced by this type of mixture differ considerably from optically thin mixtures of significantly different atomic number such as those considered in Ref. 14.

II. DESCRIPTION OF MODEL AND CALCULATION

A. Basic considerations

We consider sodium and neon ions, mixed in varying ratio, and heated to temperatures at which the helium and hydrogenlike ionization stages are by far the dominant species. The choice of sodium and neon is of significant interest not only because of the close atomic numbers, but also because the Na X $1s^2$-$1s2p\,^1P$ line at 11.0027 Å virtually coincides with Ne IX $1s^2 - 1s4p\,^1P$ at 11.0003 Å. Therefore, the effect of direct overlap of high-opacity spectral regions may be ascertained. Of course, this line coincidence also provides the basis for suggested x-ray laser configurations,[15–19] but this feature will not be considered here. Nor will we consider the technological problems of including sodium in a Z pinch with neon—our principal objective is the delineation of the radiation physics of an optically thick plasma composed of two elements of neighboring atomic number.

As explained in Ref. 14, the temperatures and densities attained in a pinch with a given current-voltage pulse are largely dependent on the plasma mass which is accelerated. Therefore, a reasonable comparison of the radiative emissivity of a mixture with that of a one-element plasma may be made by holding the mass constant. Since sodium and neon have nearly the same mass, in the cases presented below we have kept the total ion density constant while varying the sodium/neon ratio, to remain reasonably faithful to the prescription for a meaningful comparison.

For a plasma of a given size, total ion density, temperature, and sodium/neon ratio, we solve for the level populations and emitted radiation. The plasmas, which persist for tens of nanoseconds, are assumed to be in collisional-radiation equilibrium (CRE); that is, the level populations reach values which permit them to be in a steady state consistent with the other level populations, atomic rates, and the ambient radiation field. To perform this calculation the critical elements required are the atomic level model and rates, and a radiation transport algorithm which accounts for two-element opacity overlap.

B. Atomic model and rates

We consider only sodium-neon plasmas of such temperatures and densities that the K shell dominates the ionic species. Hence, only ground states are carried in the model for all stages below lithiumlike. For the lithiumlike stage, the $1s^22s\,^2S$ (ground), $1s^22p\,^2P$, $1s^23s\,^2S$, $1s^23p\,^2P$, $1s^23d\,^2D$,

$1s^2 4l$, and $1s^2 5l$ levels are included. The heliumlike stage carries, in addition to the ground state, the $1s2s\ ^3S$, $1s2s\ ^1S$, $1s2p\ ^3P$, $1s2p\ ^1P$, $1s3l\ ^3L$, $1s3l\ ^1L$, $1s4l$, and $1s5l$ levels. The hydrogenlike levels include $n = 1$ through $n = 5$.

The atomic processes populating and depopulating the levels are spontaneous radiative decay, electron collisional excitation and deexcitation, collisional ionization, and three-body, radiative, and dielectronic recombination. The continuum is optically thin in these plasmas; hence photoionization is neglected. Line photoexcitation is calculated by the radiative transfer model discused in the next section. The sources and calculational techniques used to obtain the rates are discussed in Ref. 14.

C. Radiation transport

Continuum radiation is treated as optically thin, which is a good approximation for the plasmas considered below. Many lines, however, are optically thick. They may be separated into two categories: lines whose region of significant opacity coincides with all or part of the profile of a line from the other element (overlapping lines), and those lines containing no source of opacity from the other element (nonoverlapping lines). The latter category contains most of the lines: even for sodium-neon the only overlapping pair of lines in the K shell is the one mentioned above.

For the nonoverlapping lines, radiation transport is calculated self-consistently with the atomic level populations for all of the optically thick lines contained within the atomic model. The numerical technique has been described previously[20–22]; hence only a brief summary is provided here. For each nonoverlapping line, a set of "coupling constants" is calculated which is a matrix of probabilities C_{ij} that a line photon emitted in the ith spatial cell is absorbed in the jth cell. This calculation is based on simple but acceptably accurate expressions for the escape probability of a Voigt profile[23] as a function of optical depth. For each overlapping line pair (lines A and B), the calculation of four matrices is necessary. These matrices may be denoted as C_{ij}^{AA}, C_{ij}^{AB}, C_{ij}^{BA}, and C_{ij}^{BB}. The matrix C_{ij}^{AA} is the set of probabilities that a photon emitted in cell i by line A is absorbed in cell j by the same line A. The matrix C_{ij}^{AB} is the set of probabilities that a photon emitted in cell i by line A is absorbed in cell j by the overlapped line B. The generalization to C_{ij}^{BA} and C_{ij}^{BB} is obvious. Calculation of the four coupling-constant matrices for the overlapped line pair cannot be done efficiently with precalculated escape probability formulas like those of Refs. 20 and 21. The line centers do not in general coincide exactly, and the profile parameters such as Doppler width and Voigt broadening constant usually differ, which precludes such a computational technique. A multifrequency approach is necessary for the overlapped lines. In this case a grid of 35 frequencies is established which covers the entire region where significant opacity exists in either the Na X $1s^2$-$1s2p\ ^1P$ line (A) at 11.0027 Å or the Ne IX $1s^2$-$1s4p\ ^1P$ line (B) at 11.0003 Å.

The absorption coefficients for each line at a given frequency $\nu(k_\nu^A, k_\nu^B)$ are summed to yield the total optical depth at each frequency ν along the single chosen ray through the plasma. The choice of ray angle is elaborated in Ref. 21. A "master matrix" of coupling constants at each frequency, C_{ij}^{ν} is then readily calculable since the monochromatic escape probability is exponential in optical depth. We let $\phi_{\nu i}^A$ and $\phi_{\nu i}^B$ represent the respective line emission profiles in cell i, normalized so that their frequency integral is unity. Letting $k_{\nu i}^A$ and $k_{\nu i}^B$ stand for the respective absorption coefficients (cm^{-1}), the four coupling constant matrices for the overlapped line pair are then given by

$$C_{ij}^{AA} = \int \frac{\phi_{\nu i}^A k_{\nu j}^A}{k_{\nu j}^A + k_{\nu j}^B} C_{ij}^{\nu}\, d\nu, \tag{1a}$$

$$C_{ij}^{AB} = \int \frac{\phi_{\nu i}^A k_{\nu j}^B}{k_{\nu j}^A + k_{\nu j}^B} C_{ij}^{\nu}\, d\nu, \tag{1b}$$

$$C_{ij}^{BA} = \int \frac{\phi_{\nu i}^B k_{\nu j}^A}{k_{\nu j}^A + k_{\nu j}^B} C_{ij}^{\nu}\, d\nu, \tag{1c}$$

$$C_{ij}^{BB} = \int \frac{\phi_{\nu i}^B k_{\nu j}^B}{k_{\nu j}^A + k_{\nu j}^B} C_{ij}^{\nu}\, d\nu. \tag{1d}$$

In Eq. (1) the integral is taken over the line profiles. The frequency distribution of the emission in cell i by either line A or B is accounted for by the presence of ϕ; the apportionment of absorbed photons of frequency ν in the receiving cell j is given by the ratio of the absorption coefficient of the receiving line to the sum of the absorption from both lines. Having obtained all the relevant radiative coupling constants for both the overlapping and nonoverlapping lines, the steady state solution for the ionic species and level population is obtained by an iteration procedure, the details of which are described in Ref. 22.

III. RESULTS AND INTERPRETATION

A. K-shell power output

Calculations have been performed for a variety of assumed plasma conditions to determine the total K-shell resonance line power as a function of the sodium/neon ratio. In each case a cylindrical plasma of length 4 cm of fixed total (sodium plus neon) ion density is assumed. The temperature, diameter, and sodium/neon ratio were varied, and the results are summarized in Fig. 1 and Table I. In Fig. 1 the K-shell power output in J/ns is plotted as a function of the fractional abundance of sodium ions for a variety of plasma conditions. Note that generally the power output (equivalent to K-shell emissivity) peaks at a sodium ion concentration of 50–75%, and the emissivity in some cases substantially exceeds that obtained either for pure neon or for pure sodium. The effect is more pronounced as the line opacity of the plasma (roughly proportional to the product of ion density and diameter) increases. Therefore, the K-shell emissivity of an opaque plasma mixture may exceed that for either element alone for similar atomic number elements. The precise nature of this effect is illuminated in Table I, where the power outputs for sodium and neon Ly α and He α ($1s^2$-$1s2p\ ^1P$) lines are given for various plasma conditions. These two lines usually account for more than 65% of the K-shell power. Were the composition of an optically thin plasma to be changed from pure neon to 50% neon, for instance, the neon line power output would decrease by 50%—ignoring small changes in the electron density due to sodium. However,

TABLE I. Power outputs (J/ns) for Ly α and He α.

	Pure Na	75Na, 25Ne	50Na, 50Ne	75Ne, 25Na	Pure Ne
	$d = 5.6$ mm, $T_e = 400$ eV, $N_I = 5\times10^{19}$ cm^{-3}				
Ne IXHe α	...	58	74	85	94
Ne XLy α	...	286	364	420	467
Na XHe α	303	251	197	133	...
Na XILy α	867	759	638	467	...
	$d = 2.8$ mm, $T_e = 400$ eV, $N_I = 10^{20}$ cm^{-3}				
Ne IXHe α	...	36	44	50	54
Ne XLy α	...	171	214	245	270
Na XHe α	167	141	112	79	...
Na XILy α	480	423	357	268	...
	$d = 1.4$ mm, $T_e = 400$ eV, $N_I = 10^{20}$ cm^{-3}				
Ne IXHe α	...	14	18	20	22
Ne XLy α	...	68	85	97	106
Na XHe α	63	53	43	31	...
Na XILy α	183	159	134	100	...
	$d = 2.8$ mm, $T_e = 400$ eV, $N_I = 10^{19}$ cm^{-3}				
Ne IXHe α	...	6	10	13	16
Ne XLy α	...	29	45	57	66
Na XHe α	51	39	28	15	...
Na XILy α	87	67	46	23	...

inspection of the table reveals that the neon line's output never drops by as much as 50% and in fact usually drops by only about 20%. The one exception is the least-opaque plasma of ion density 10^{19} cm^{-3}, where the Ne IX He α power drops by nearly 40%. In this least-opaque plasma the Ly α optical depth is ~ 50. The same effect exists for sodium. The change of the photon output is controlled by opacity effects. This results in the greatest emissivity occurring for an intermediate mixing ratio of sodium-to-neon, where there are twice as many lines radiating as in the pure-element case and the optical depths of the radiating lines are smaller than for the pure-element case.

B. Analysis of power output

In analyzing the transfer of line photons in laboratory plasmas, the following conceptual picture is often useful.[22] A line photon is "created" when the upper level of the transition is collisionally populated. Following its creation in an optically thick plasma the photon will generally be reabsorbed and reemitted a considerable number of times before being quenched or ultimately escaping the plasma. During each reabsorption there is a finite probability P_Q that the level will be collisionally depopulated and the line photon destroyed. This probability P_Q is given by $D/(D+A)$, where D (s^{-1}) is the sum of the collisional rate coefficients out of the upper transition level times the electron density, and A is the spontaneous decay rate for the line. Following the initial collisional excitation the photon will ultimately suffer one of two fates: destruction or eventual escape from the plasma. We denote the probability of eventual escape by P_u; the probability of escape on any single flight is given by P_e. The quantity P_e is calculable given the optical depth and line profile; it is used, as described in Sec. II C, for calculating the coupling constants in radiative transfer. The quantity P_u may be obtained by considering the condition for a steady-state population N of the upper level. Letting C stand for the collisional excitation rate this condition is

$$C = N(D + AP_e) \quad (\text{cm}^{-3}\,\text{s}^{-1}), \tag{2}$$

where, in Eq. (2), radiative reabsorption of the line photon is taken into account by diluting the decay rate by the single-flight photon escape probability. Even in a uniform plasma, P_e varies with position; Eq. (2) is intended as a spatially averaged approximate description of the photon transfer. After a few simple manipulations, Eq. (2) yields, taking into account that $P_Q = D/(D+A)$,

$$\frac{NAP_e}{C} = \frac{P_e(1-P_Q)}{P_Q + (1-P_Q)P_e}. \tag{3}$$

However, the left-hand side of Eq. (3) is the total photon-emission rate divided by the total upper-level-excitation rate; that is, precisely the ultimate escape probability. Therefore,

$$P_u = \frac{P_e(1-P_Q)}{P_Q + (1-P_Q)P_e} \tag{4}$$

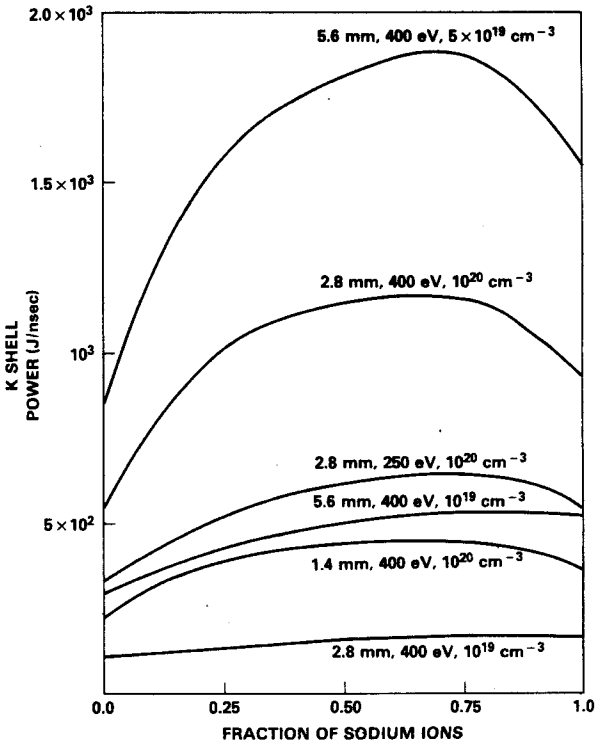

FIG. 1. Total K-shell power output in J/ns from a sodium-neon plasma plotted against fractional abundance of sodium for a range of indicated plasma conditions. In each case the plasma is assumed to be a 4-cm-long cylinder with fixed total ion density (sodium plus neon ions).

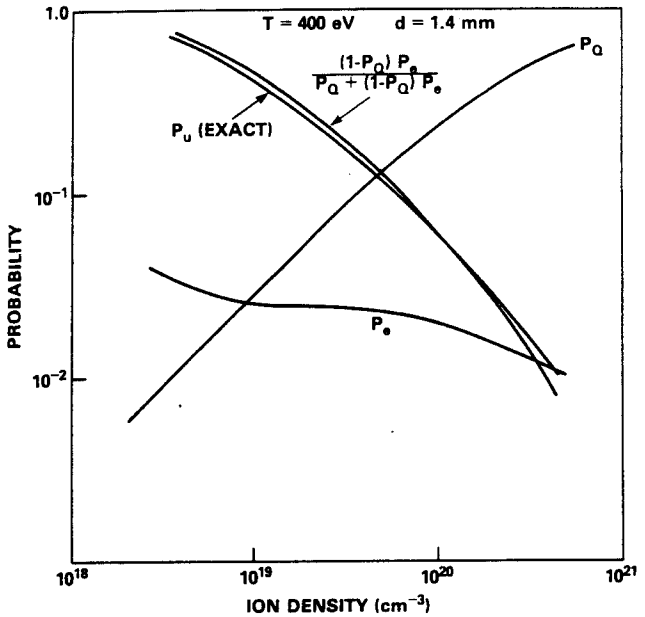

FIG. 2. Spatially averaged single-flight escape probability P_e, collisional photon quenching probability per scattering P_Q, and approximate analytic ultimate escape probability plotted against ion density for a 400-eV cylindrical sodium plasma of diameter 1.4 mm. Also shown is the exact computed numerical ultimate escape probability P_u. All these quantities apply to the Na X $1s^2 - 1s2p\ ^1P$ line.

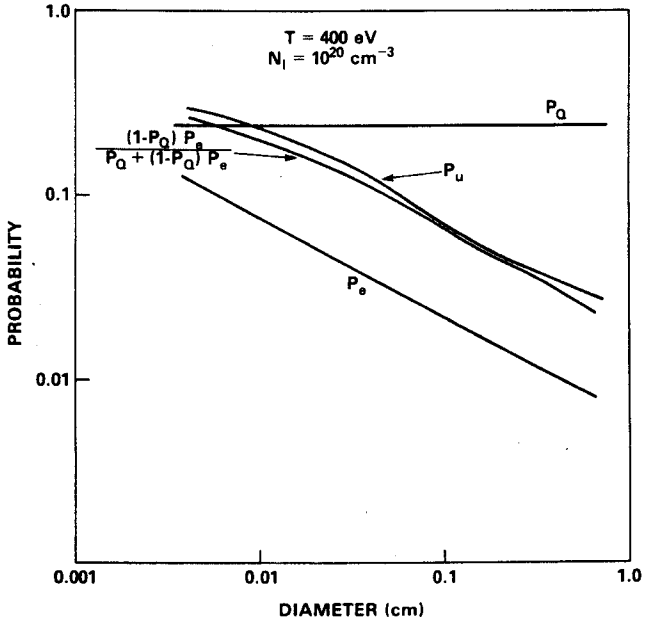

FIG. 3. Same as Fig. 2, except the quantities are plotted against cylindrical plasma diameter for a sodium ion density of 10^{20} cm^{-3} at a temperature of 400 eV.

is the approximate probability that collisional excitation of the upper transition level results in the ultimate escape of a photon from the plasma.

In Figs. 2 and 3 we have plotted the quantities P_e, P_Q, and $P_e(1-P_Q)/[P_Q+(1-P_Q)P_e]$ versus sodium ion density and diameter, respectively. These parameters are displayed for the Na X $1s^2$-$1s2p^1P$ line for a temperature of 400 eV and, for Fig. 2, a fixed diameter of 1.4 mm. Figure 3 reflects calculations for a fixed sodium ion density of 10^{20} cm^{-3}. P_e and P_Q are obtained from Voigt profile formulas and the atomic rates, respectively. The accuracy of the spatial-average approximation is indicated in both Figs. 2 and 3 by also plotting P_u as numerically calculated from the actual computed line photon output power. As is obvious, excellent correspondence is obtained with the probabilistic, spatial-average approximation of Eq. (4). This is especially significant in light of the fact that even though the plasma temperature and density are assumed spatially uniform, the presence of a boundary guarantees a significant degree of nonuniformity in both the photon field and the spatial profile of the level populations.

The important feature of Fig. 3 relevant to the mixture emissivity is the behavior of P_u with respect to opacity. Optical depth varies approximately linearly with plasma diameter. The electron density in a sodium-neon plasma is very nearly constant with sodium/neon mixing ratio provided the total ion density is constant. Therefore, halving the diameter of a pure sodium plasma would lead to an increase in P_u very similar to that which is obtained by comparing a pure sodium plasma to one of the same ion density which is half sodium, half neon. The profile of Fig. 3 indicates that $P_u \sim \tau^{-1/2}$ for optically thick K-shell sodium plasmas of ion density 10^{20} cm^{-3} in the 1–10-mm range. Therefore, halving the optical depth by reducing the sodium fraction from 1.0 to 0.5 results in P_u increasing by 40%. The other sodium and neon lines experience a similar—though not identical—increase in P_u, which accounts for the curves of Fig. 1.

IV. SUMMARY AND CONCLUSION

We have examined the K-shell line emissivity of optically thick sodium-neon plasmas with properties similar to those produced in Z pinches driven by higher-power generators. It was found that, in contrast to the optically thin case with two elements of dissimilar atomic number, the utilization of two elements rather than one can actually increase the expected radiative power output. Given the assumptions of fixed plasma properties, this is an exact numerical result. However, we have found that the line photon creation and ultimate escape may be accurately parameterized by a simple probabilistic model, and that such a model accounts intuitively for the results.

We conclude that when a laboratory plasma is of substantial optical depth its radiative emissivity can be increased by employing mixtures of elements to form the plasma. Conceivably, the use of more than two elements could, by increasing the photon escape probability even more, result in even greater increases in power output than reported here.

ACKNOWLEDGMENTS

The authors express their appreciation of D. Duston and C.Agritellis for assistance in coding and the compilation of rates. This work was supported by the Defense Nuclear Agency.

[1]P. G. Burkhalter, C. M. Dozier, and D. J. Nagel, Phys. Rev. A **15**, 700 (1977).
[2]W. L. Baker, M. C. Clark, J. H. Degnan, G. F. Kiuttu, C. R. McClenahan, and R. H. Reinovsky, J. Appl. Phys. **49**, 4694 (1978).
[3]J. Davis, D. Duston, and P. Kepple, NRL Memorandum Report 3879, November 1978 (unpublished).
[4]J. Shiloh, A. Fisher, and N. Rostoker, Phys. Rev. Lett. **40**, 515 (1978).
[5]P. Burkhalter, J. Davis, J. Rauch, W. Clark, G. Dahlbacka, and R. Schneider, J. Appl. Phys. **50**, 705 (1979).
[6]P. G. Burkhalter, J. Shiloh, A. Fisher, and R. D. Cowan, J. Appl. Phys. **50**, 4532 (1979).
[7]C. Stallings, K. Childers, I. Roth, and R. Schneider, Appl. Phys. Lett. **35**, 524 (1979).
[8]J. D. Perez, L. F. Chase, R. E. McDonald, L. Tannenwald, and B. A. Watson, J. Appl. Phys. **52**, 670 (1981).
[9]M. Gersten, J. E. Rauch, W. Clark, R. D Richardson, and G. M. Wilkinson, Appl. Phys. Lett. **39**, 148 (1981).
[10]R. F. Benjamin, J. S. Pearlman, E. Y. Chu, and J. C. Riordan, Appl. Phys. Lett. **39**, 848 (1981).
[11]W. Clark, M. Wilkinson, J. Rauch, and J. LePage, J. Appl. Phys. **53**, 1426 (1982).
[12]W. Clark, M. Gersten, J. Katzenstein, J. Rauch, R. Richardson, and M. Wilkinson, J. Appl. Phys. **53**, 4099 (1982).
[13]W. Clark, R. Richardson, J. Brannon, M. Wilkinson, and J. Katzenstein, J. Appl. Phys. **53**, 5552 (1982).
[14]D. Duston, J. Davis, and C. Agritellis, J. Appl. Phys. **57**, 785 (1985).
[15]A. V. Vinogradov, I. I. Sobelman, and E. A. Yukov, Sov. J. Quantum Electron. **5**, 59 (1975).
[16]B. A. Norton and N. J. Peacock, J. Phys. B **8**, 989 (1975).
[17]P. L. Hagelstein, Lawrence Livermore National Laboratory Report UCRL-53100 (1981).
[18]J. P. Apruzese, J. Davis, and K. G. Whitney, J. Appl. Phys. **53**, 4020 (1982).
[19]F. L. Cochran, J. Davis, and J. P. Apruzese, J. Appl. Phys. **57**, 27 (1985).
[20]J. P. Apruzese, J. Davis, D. Duston, and K. G. Whitney, J. Quant. Spectrosc. Radiat. Transfer **23**, 479 (1980).
[21]J. P. Apruzese, J. Quant. Spectrosc. Radiat. Transfer **25**, 419 (1981).
[22]J. P. Apruzese, J. Davis, D. Duston, and R. W. Clark, Phys. Rev. A **29**, 246 (1984).
[23]J. P. Apruzese (unpublished).

Plasma conditions required for attainment of maximum gain in resonantly photo-pumped aluminum XII and neon IX

J. P. Apruzese, J. Davis, and K. G. Whitney[a)]
Plasma Physics Division, Naval Research Laboratory, Washington, D. C. 20375

(Received 3 August 1981; accepted for publication 9 March 1982)

We present a detailed analysis of the plasma conditions required to optimize gain in two proposed x-ray lasing schemes using resonant photo-pumping. In one proposed configuration, the Si XIII line $1s^2$-$1s2p^1P$ at 6.650 Å pumps Al XII $1s^2 - 1s3p^1P$ at 6.635 Å, inverting the Al XII $n = 3$ and $n = 2$ levels which are separated by 44 Å. A similar approach which utilizes the Na X $1s^2$-$1s2p^1P$ line at 11.00 Å would invert the $n = 4$, 3, and 2 levels of Ne IX. Conditions in the pumped neon and aluminum plasmas, and in the pumping silicon plasma, are calculated using a multistage, multilevel atomic model with multifrequency radiation transport. For modeling the pumping sodium line we have inferred the intensity from a spectrum of a neon filled, laser-imploded glass microballoon containing sodium impurities obtained at Rochester. The pump line intensities calculated for Si and inferred for Na are equivalent to blackbodies of 252 and 227 eV, respectively. It is found that peak gain for the 3-2 lines of about 100 cm^{-1} occurs at ion densities of 10^{20} cm^{-3} and 4×10^{20} cm^{-3} in the pumped neon and aluminum plasmas, respectively. Temperatures required to maximize gain in the pumped plasmas are found to be 50 and 100 eV, for neon and aluminum, respectively. Finally, since the silicon and aluminum lines are slightly off resonance, we have investigated the effect of streaming the plasmas toward each other at various velocities to offset some or all of the wavelength difference. It is found that a streaming velocity of 6.8×10^7 cm sec^{-1}—fully offsetting the wavelength difference—will approximately triple the achieved gain compared to the zero velocity case. Lesser increases in gain occur with partial velocity offsets.

PACS numbers: 42.55.Hq, 52.25.Ps, 42.60.By

I. INTRODUCTION

It has been suggested[1-4] that population inversions in plasmas may be efficiently pumped by opacity broadened lines from different ionization stages of the same element or from different elements in a two component plasma. Experimental evidence[5,6] has been presented for inversions of the $n = 4$ and $n = 3$ levels in Mg XII and Mg XI, which were pumped by resonant *Lyα* and $1s^2$-$1s2p^1P$ radiation in C VI and C V. The above mentioned lasing transitions in Mg lie at ~130 and 156 Å for Mg XII and Mg XI, respectively. In this paper we present a detailed analysis of the plasma conditions which would be needed to optimally implement two promising lasing schemes utilizing resonant photoexcitation with considerably shorter lasing wavelengths (down to 44 Å). The radiation field—critical in a photoexcitation process—is modeled in detail. The pumped and pumping transitions—as well as other key optically thick lines—are calculated on a frequency grid allowing for accurate modeling of broadening processes and frequency-dependent absorption. Previous efforts at modeling short-wavelength resonantly photoexcited lasing processes have employed assumed linewidths,[1] line profiles arising from uniform source functions,[2] assumed power densities,[3,5] or probability-of-escape approximations.[4] In another study,[7] the pumped plasma was modeled with a fine frequency grid but the pumping spectrum was assumed to be a filtered Planckian. In Sec. II our atomic model is described along with the methodology for its employment for calculations for both the pumped and pumping plasmas. In Sec. III the equilibrium results are presented for optimum plasma densities, temperatures, and relative velocities and the relevant physical processes controlling these effects are analyzed. Finally, we summarize the work and present our basic conclusions in Sec. IV.

II. DESCRIPTION OF MODEL AND CALCULATIONS

A. Basic details of models

The photon pumping schemes to be analyzed are the following. Scheme 1 would employ the Si XIII $1s^2$-$1s2p^1P$ resonance line at 6.650 Å to pump the Al XII $1s^2$-$1s3p^1P$ resonance line at 6.635 Å, creating an inversion of the $n = 3$ and $n = 2$ levels of Al XII. Scheme 2 utilizes the Na X $1s^2$-$1s2p^1P$ line at 11.00 Å to pump the Ne IX $1s^2$-$1s4p^1P$ line at 11.001 Å, creating an inversion in the 3-2, 4-2, and 4-3 singlet lines of Ne IX. Scheme 1 results in stimulated emission at 44 Å and scheme 2 at 82 Å for the 3-2 inversion, 58 Å for the 4-2, and 230 Å for the 4-3 transitions. Ionic state and level densities as well as the radiation field are computed for Al using the model described in Ref. 7. For Si, a precisely analagous model to Al—the same level structure and transitions—is employed. The Ne atomic model is described in Ref. 8. This model possesses an extra degree of sophistication in that self-consistent Stark profiles[9] are used for the line opacity rather than the Voigt profiles employed for Al and Si. For Na, no atomic model is employed. Rather, the profile of the pumping line at 11.00 Å is utilized as it was experimentally measured from glass impurities in a laser implosion

[a)] Optical Sciences Division.

 0021-8979/82/064020-08$02.40

experiment at the University of Rochester.[10] The multifrequency measured profile is modified within the pumped neon plasma by absorption and reemission in the Ne line and this phenomenology is computed in detail using the flux profile of the Na line as an input condition on the Ne plasma. Further details are given in Sec. II C. Results given below are calculated for collisional-radiative equilibrium (CRE).

B. Pumped plasma calculation

One of the major difficulties arising in resonant photoexcitation inversion mechanisms is the need to prevent overpopulation of the lower level by photon trapping. For Al XII, trapping in the strong resonance line $1s^2$-$1s2p^1P$ could spoil the 3→2 inversions by increasing the $n = 2$ populations well above their optically thin values. Similar considerations arise in the sodium-neon scheme. Hagelstein[11] has determined that optical depths greater than five in the principal resonance line will generally ruin the inversions. We find that the line center absorption coefficients for Al XII $1s^2$-$1s2p^1P$ and Ne IX $1s^2$-$1s2p^1P$ are approximately 1.2×10^{-16} N_I and 1.6×10^{-16} N_I (cm^{-1}), respectively. These approximate relationships for a total ion density N_I are obtained at optimally low plasma temperatures discussed below. Assuming for simplicity that $k = 1.4\times10^{-16}$ N_I for both Al and Ne, an optical depth $\tau\leqslant5$ implies that

$$r(\mu\mathrm{m})\leqslant\frac{3.6\times10^{20}}{N_I}, \tag{1}$$

where r is the characteristic plasma radius in μm and N_I the total ion density. Satisfaction of Eq. (1) also guarantees sufficient penetration by the pump radiation whose characteristic opacity is lower than that of the $1s^2$-$1s2p^1P$ line. At ion densities $\sim10^{20}$, the total width of the pumped plasma must be <10 μm, which rules out the use of a Z pinch at high density with present technology whose characteristic smallest structures are $\geqslant100$ μm.[12] However, such spatial resolution and control has been achieved with laser plasmas at even higher density[10] and some success in resonant photoexcitation at lower densities[5] in laser plasma experiments has been reported. Of course a Z pinch may be employed at $N_I\leqslant10^{19}$ but there will still be a need for a high degree of control of the lasing medium geometry. Without minimizing these difficulties or the strong possibilities of future advances in experimental control of plasma geometries, we have performed the computations assuming that the lasing medium can be maintained small enough to prevent deleterious trapping. The radiation field is calculated in a planar plasma of infinite area with thickness small enough to insure an optically thin regime over a broad angular range of specific intensities. Our objectives—given an optically thin lasing medium—are to determine a range of temperatures, densities, and for scheme 1, streaming velocities in which maximum gain occurs and to determine some of the tradeoffs involved in establishing this maximum.

The pumped plasma is assumed to be bathed symmetrically in the pumping radiation which is calculated (for Si) or measured (for Na). The penetration of the pumping radiation into the pumped plasma is calculated in a straightforward manner. At the outer boundaries of the pumped plasma the inward specific intensity along each ray at each frequency I_ν^- is taken to be that emitted from the pumping plasma which is also assumed to be planar. The radiative transfer equation is then solved in the pumped plasma with this particular boundary condition for I_ν^- applied at each of the chosen rays at its outer boundaries. The calculation then proceeds by iteration until steady state conditions are obtained. Since fully coupled radiative transport and rate equations are solved in this model, the steady state obtained is a self-consistent collisional-radiative equilibrium. The quantity of primary interest here—the gain coefficient of the lasing transition—is obtained as a linear function of the computed densities of the upper and lower states. Finally, the temperature, density, and (for Al) velocity of the pumped plasma was varied in order to obtain the functional dependence of the gain coefficient on these quantities. We make no attempt to calculate the depletion of excited states by lasing, and thus are computing only the linear amplifier behavior (small signal gain).

C. Treatment of the pumping plasma

Since our principal objective is to determine the effect of varying conditions in the pumped plasma on the achieved gain, we selected only one set of pumping conditions for each of the Si and Na plasmas. Because the $1s^2$-$1s2p^1P$ Si XIII and $1s^2$-$1s3p^1P$ Al XII lines are off resonance by 0.015 Å, the profile of the $1s^2$-$1s2p^1P$ line must be wide enough to produce significant intensity at 0.015 Å (i.e., 13 Doppler widths at 400 eV) from line center. Thus, for a stationary plasma the line must be opacity broadened.[2] If the resonance line is very thick at line center, the Lorentz wings will still exceed optical depth unity many Doppler widths from line center, guaranteeing a wide profile. Such conditions can be obtained in a moderate energy Si plasma of 1.5 mm width, temperature 400 eV, and ion density 8×10^{19} cm^{-3}. Plasmas similar to this have been realized in the laboratory.[12] Most importantly, the CRE calculation for this plasma indicates that, depending on position, 62%–82% of the ions are in the active (helium-like) stage. Furthermore, the optical depth of the pumping resonance line $1s^2$-$1s2p^1P$ is ~500, which produces a very wide profile, as shown in Fig. 1. The maximum flux in this profile is 2.58×10^3 ergs/(cm^2 sec Hz), equivalent to a 252-eV blackbody. This pump brightness is quite reasonable considering that the kinetic temperature of the radiating plasma is 400 eV and it is quite optically thick. In addition to the calculated emission profile the intrinsic absorption profile for the $1s^2$-$1s3p^1P$ Al XII line is shown for typical conditions in the aluminum plasma. In this case, the Si resonance line is sufficiently broadened by opacity to overcome the resonance defect. Therefore, under the reasonable assumption that these equilibrium Si plasma conditions can be achieved, the Si/Al lasing scheme will be viable at least in the sense that the resonance defect can be overcome.

To obtain a radiation source to pump Ne, we have analyzed the spectrum of a laser-imploded neon filled glass microballoon obtained at Rochester.[10] One of the strongest lines appearing in this spectrum is the Na X $1s^2$-$1s2p^1P$—which arose from sodium impurities in the glass. Since we have been able to reproduce the observed spectrum with a

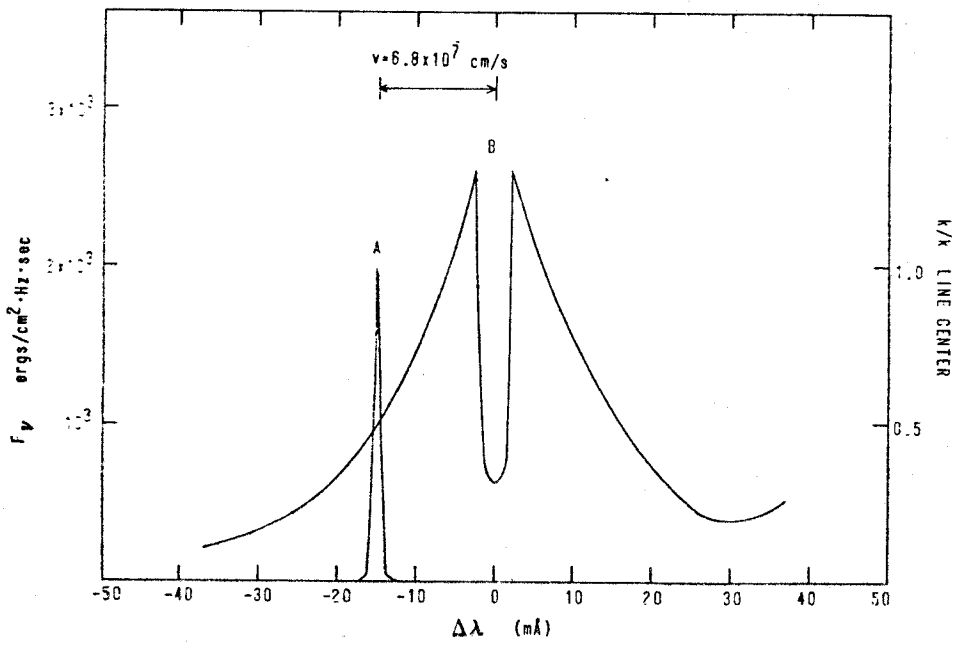

FIG. 1. Line profile of the Si pumping line (B) calculated to arise from the plasma conditions described in section II C is shown on the same wavelength scale as the intrinsic absorption profile of the pumped Al line (A). The left vertical scale applies to the flux of the emitted Si line; the right vertical scale applies to the absorption coefficient of the Al line.

first-principles non-LTE calculation of the line and continuum intensities,[8] the theoretical calculation which matches the observed spectrum also yields the absolute intensities of the lines—flux in ergs/(cm^2 sec Hz) at the outer surface of the pellet. Knowing the absolute intensities of the Ne lines, one may infer the Na line intensity profile from its measured value relative to the Ne lines. Its value at the central peak is 6.6×10^3 ergs/(cm^2 sec Hz). This is equivalent to a 227-eV blackbody flux, which is again quite reasonable from a dense, optically thick plasma of kinetic temperature 300–385 eV.[10] The actual intensity profile which we use as our pump source in the Na/Ne calculations is the one appearing in the published spectrum,[10] where experimental sources of broadening are relatively small. In any event deconvoluting any experimental broadening would result in a sharper central peak, which, since the lines are perfectly resonant, would give a better pump source.

In the next section it is shown that this experimentally observed Na X $1s^2$-$1s2p\,^1P$ intensity profile is sufficient to substantially invert the Ne X $n=2$, 3, and 4 levels. This finding is significant in light of the fact that this radiation was merely a consequence of sodium impurities in the glass; i.e., no effort was made to increase its intensity in the experiment. We note that only the Na resonance line was used to irradiate Ne, whereas all of the calculated Si radiation, pumping plus other lines plus continuum, were included in the Al calculation.

III. RESULTS OF GAIN CALCULATIONS

A. Density dependence

A principal question related to the time varying conditions in the pumped plasma is: at what density is gain maximized? As has been often pointed out,[3,4,6,13] there exists for each lasing scheme contemplated a density above which no inversion is possible, due to the tendency of collisional processes to bring the state densities into LTE. In the opposite, low-density limit the plasma will be controlled entirely by radiative pumping and depletion. In this situation the medium may have its largest fractional inversion, although the gain may be reduced due to the smaller number of lasing ions in a given linear distance. In the limit that collisions are unimportant the ratio of the optically pumped level population (N_u) to the ground state population (N_g) is easily calculable from the equivalent blackbody temperature of the radiation T_B. If $B_\nu(T_B)$ is the pumping intensity, assumed flat across the normalized absorption profile ϕ_ν and the stimulated absorption and emission coefficients are denoted by B_{gu} and B_{ug}, the net pumping rate of the upper state is

$$\int_{\text{profile}} B_\nu(N_g B_{gu} - N_u B_{ug})\phi_\nu \, d\nu = B_\nu(N_g B_{gu} - N_u B_{ug}). \tag{2}$$

Setting this rate equal to the depletion rate $N_u A_{ug}$ in the collisionless limit one finds

$$\frac{N_u A_{ug}}{N_g B_{gu} - N_u B_{ug}} = B_\nu(T_B). \tag{3}$$

Substituting for $B_\nu(T_B)$ and utilizing the Einstein relations leads, as expected, to

$$\frac{N_u}{N_g} = \frac{g_u}{g_g} e^{-(h\nu/kT_B)}. \tag{4}$$

Thus, for a given ion density N_I the population density of the pumped level may be obtained from Eq. (4) in terms of T_B, the pump brightness temperature, and the fractional helium-like ion population f. Furthermore, the lower level of the lasing transition is negligibly populated at very low density and the gain coefficient is then a function only of N_u, i.e., of f, N_I, and T_B. For the Al XII $2p$-$3d$ line at 44 Å with an oscillator strength of 0.71, the gain coefficient in the low-density limit for a 100-eV Doppler profile is

$$k = 5.2\times10^{-15} f(\text{Al XII}) N_I e^{[-1864.4\ \text{eV}/T_B(\text{eV})]}\ \text{cm}^{-1}. \tag{5}$$

In Eq. (5) statistical equilibrium among the $n = 3$ singlet sublevels has been assumed. For a fractional Al XII population of 0.5 and our silicon pump $T_B = 252$ eV, the low density gain is ideally a linear function of N_i. This line is plotted in Fig. 2 along with the detailed computational results. Note that the CRE result approximately parallels the ideal gain until well past 10^{20} cm^{-3} where collisional processes begin to spoil the inversion. Computed results are given for the enforced statistical equilibrium of the $n = 3$ singlet sublevels as well as for a rate-by-rate calculation of the $3d$ and $3p$ populations. The assumption of statistical equilibrium leads to an overestimate of gain at low densities; however, for densities near the predicted peak gain, around 4×10^{20} cm^{-3}, the overestimate is very slight. This effect is of course due to the greater accuracy of the statistical equilibrium assumption at higher densities. The factor of ~3 reduction in the computed gain as opposed to the ideal case at lower densities is due almost entirely to the resonance mismatch of the pumped and pumping lines. As seen below, the gain would be very close to the ideal value if the resonance defect could be made up by streaming the plasmas toward each other at 6.8×10^7 cm sec^{-1}. The chosen temperature of 100 eV corresponds approximately to maximum gain—this point is discussed further in the next section.

Finally, it is clear from Eq. (5) that the low-density gain coefficient will rapidly increase with T_B; indeed, if T_B is changed from 252 eV to 1 keV, the gain increases by a factor greater than 10^2. Thus, in principle, extremely high gains such as we obtained in Ref. 4 are achievable. However, when we predicted such gains, a photon probability-of-escape technique was used to model the line radiation only. More recent calculations with our multifrequency model of both line and continuum radiation show that when the Si plasma is hot enough and opaque enough to produce a 1-keV pump field, the continuum radiation photoionizes the Al past the helium-like stage and little or no gain is obtained. Therefore some kind of selective filtering of the Si nonresonant radiation is required to achieve gain of the magnitudes previously suggested in Ref. 4. However, even with the presently calculated pump radiation the gain is substantial as seen from Fig. 2. Fractional populations of the levels are presented in Table I for the maximum gain point at 4×10^{20} cm^{-3} ion density. The $3p/1s^2$ population ratio is 4.6×10^{-4}; the ideal ratio as given by Eq. (4) is 1.8×10^{-3}. At this point the gain coefficient is 10^2.

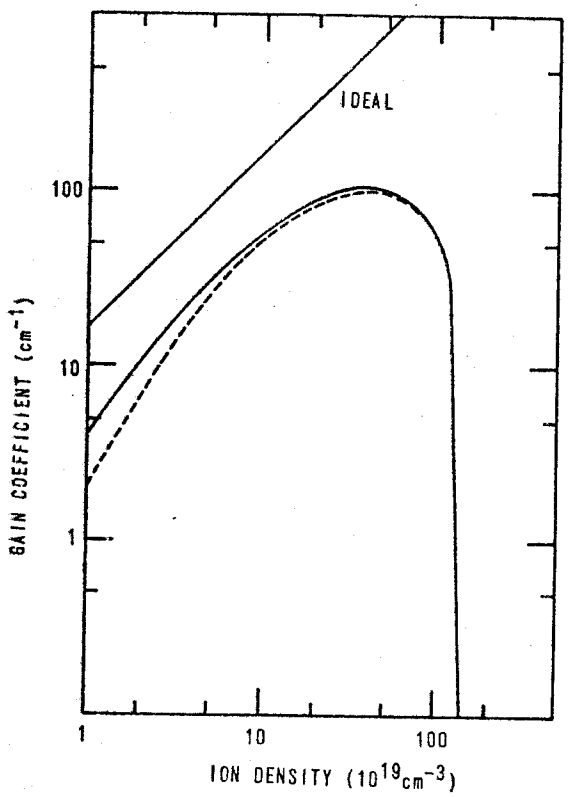

FIG. 2. Line center gain coefficient in the Al XII $2p\,^1P$-$3d\,^1D$ line is plotted vs Al plasma ion density, with an assumed pumped plasma temperature of 100 eV. Dual results for the assumption of collisional equilibrium between the $3p$-$3d$ states and for a general, rate-by-rate treatment of these states (dotted line) are displayed. Characteristics of the pumping Si plasma are discussed in the text. The line marked "ideal" describes the gain achievable for a purely radiative plasma, as described in the text.

For helium-like Ne IX the strongest lines where gain might be expected are $3d\,^1D$-$4f\,^1F$ at 230 Å with an absorption oscillator strength of 1.02, the $2p\,^1P$-$4d\,^1D$ line at 58 Å with an oscillator strength of 0.12, and the $2p\,^1P$-$3d\,^1D$ line at 82 Å with oscillator value 0.703. Figure 3 presents results for gain versus density for these three lines obtained from the detailed model as well as for an ideal, radiatively dominated system. In all cases statistical equilibrium among the singlet sublevels is assumed. For none of the three lines is the actual gain as close to that of the ideal case as was obtained for Al XII $2p$-$3d$. In this case, even though the pumping is closely resonant, the pumped $1s4p\,^1P$ level lies only 69 eV from the continuum and is easily collisionally ionized. This large ionization, whose rate is plotted in Fig. 4, prevents the $1s4p$ level from reaching its theoretically largest ratio, $(g(4p)/g(1s^2))e^{-h\nu/kT_B}$, with respect to the ground state. The fractional populations of Table II (at the temperature and ion density which approximately maximizes $2p$-$3d$ gain) demonstrate this; the ratio of $4p$ to $1s^2$ is 1.09×10^{-3}, whereas for a 227-eV sodium pump twenty times this ratio is expected in the absence of the extremely high collisional ionization rate at this density. Since the $3d$ population is also strongly coupled to the $4p$ level, this effect exists for all of the population inversions. The remainder of the deviation from ideality is due to the non-negligible population of the lower levels. Even though gain is obtained for the widest range of densities for the $2p$-$3d$ line, the falloff at low density is quite sharp because collisions become increasingly ineffective in transferring population from the pumped $4p$ level to the $3d$. This necessity for collisional mixing between the $3d$ and $4p$ levels results in the $2p$-$3d$ gain reaching its maximum at the highest ion density of 10^{20} cm^{-3} of the 3 lasing lines. By

TABLE I. Al XII fractional populations.

$N_i = 4\times10^{20}$	$T = 100$ eV
$1s^2\,^1S$	5.4×10^{-1}
$1s2p\,^1P$	9.4×10^{-5}
$1s3p\,^1P$	2.5×10^{-4}
$1s3d\,^1D$	3.9×10^{-4}

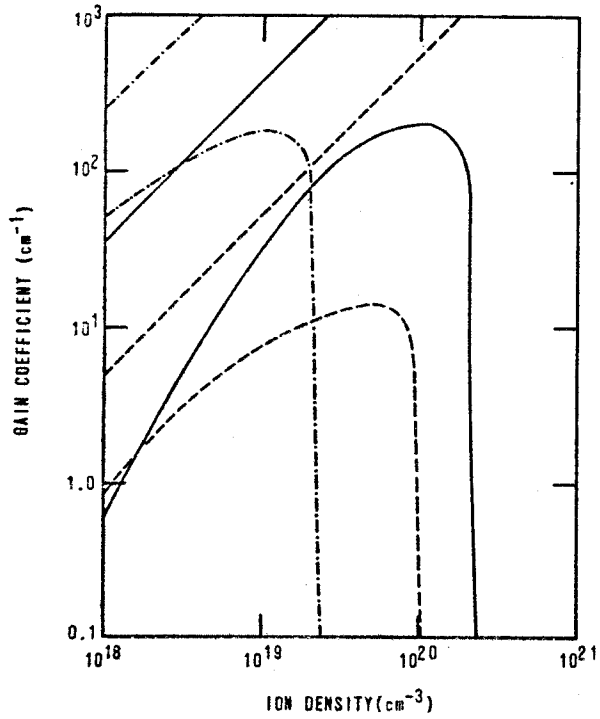

FIG. 3. Line center gain coefficients for the Ne IX $2p^1P$-$3d^1D$ (———), $2p^1P$-$4d^1D$ (——), and $3d^1D$-$4f^1F$ (– – –) lines are plotted against ion density. The corresponding overlying straight lines describe the gain achievable with an ideal radiatively dominant plasma, as described in the text. The assumed plasma temperature is 65 eV.

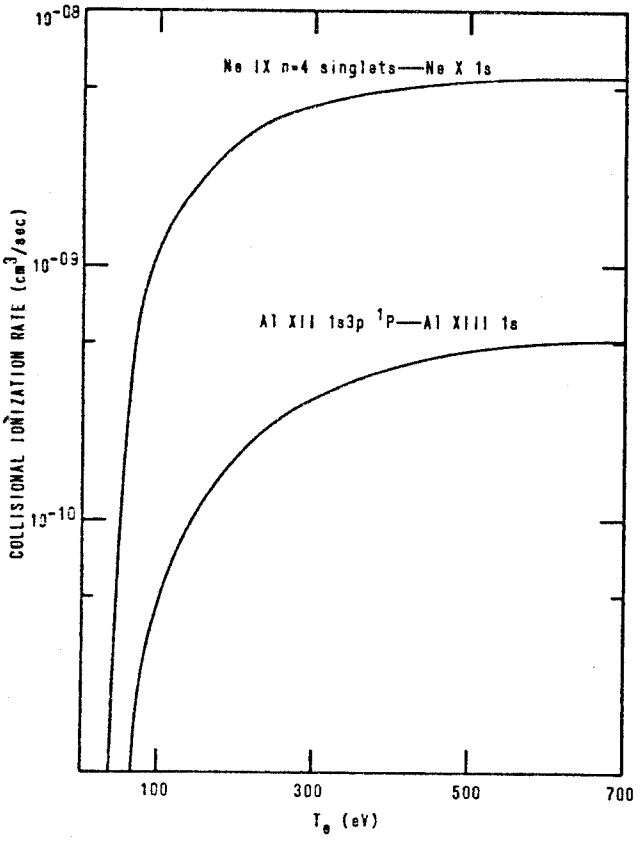

FIG. 4. Collisional ionization rates for Ne IX $n = 4$ singlets (assuming statistical population of the sublevels) and Al XII $1s3p^1P$ are shown as a function of electron temperature.

TABLE II. Ne IX fractional populations.

$N_i = 10^{20}$	$T = 65$ eV
$1s^2\,^1S$	6.4×10^{-1}
$1s2p\,^1P$	5.0×10^{-4}
$1s3p\,^1P$	1.1×10^{-3}
$1s3d\,^1D$	1.8×10^{-3}
$1s4p\,^1P$	7.0×10^{-4}
$1s4d\,^1D$	1.2×10^{-3}
$1s4f\,^1F$	1.7×10^{-3}

$3d$-$4f$ gain is maximized at $\sim10^{19}$ cm^{-3}; at higher densities collisional mixing already begins to spoil the inversion.

For Al, peak gain occurs at an ion (electron) density of 4×10^{20} (4.2×10^{21}) cm^{-3}, for Ne the corresponding numbers are 10^{20} (8.1×10^{20}) cm^{-3}. For hydrogenic lasing schemes, Bhagavatula[3,6] has presented reduced variable equations which demonstrate that the dependence of electron density at peak gain on Z is Z^7. We note with interest that the Z dependence of electron density at peak gain implied by the above numbers for our helium-like schemes is fairly similar, $Z^{6.3}$.

B. Temperature dependence

In Figs. 5 and 6 results for gain versus temperature are plotted for the 3-2 lines of the Si/Al and Na/Ne systems for fixed ion densities of 5×10^{19} and 10^{20} cm^{-3}, respectively. The gain dependence on temperature is similar to that on density in that a maximum is exhibited with a sharp falloff on one side caused by the variation of the active ion species' populations with temperature. Note, however, that the tem-

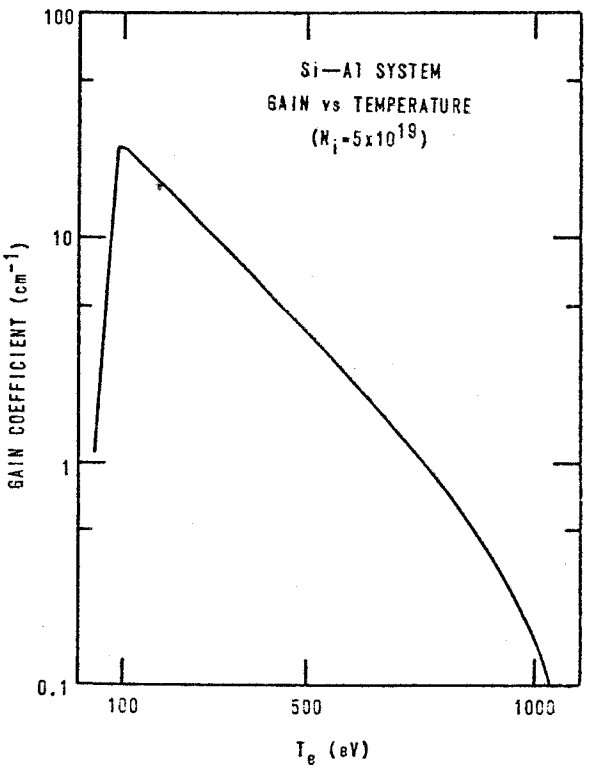

FIG. 5. Line center gain coefficient in the Al XII $2p^1P$-$3d^1D$ line is plotted vs Al plasma temperature for a fixed Al ion density of 5×10^{19} cm^{-3}.

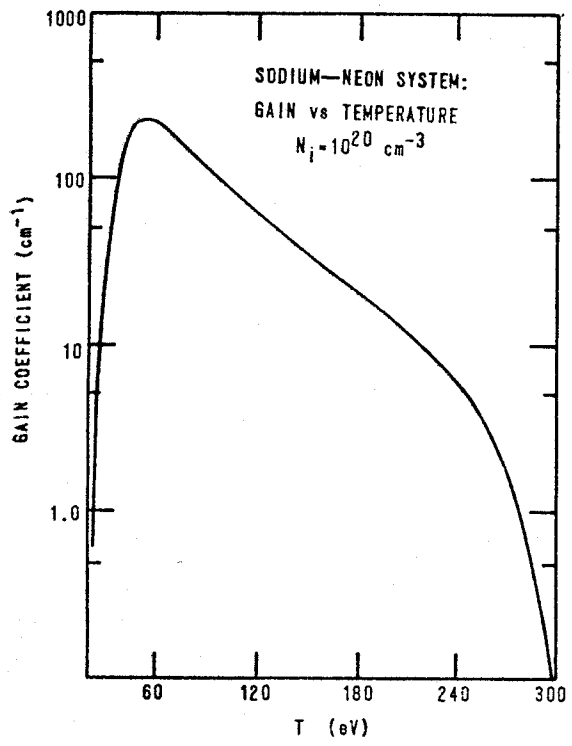

FIG. 6. Line center gain coefficient in the Ne IX $2p^1P$-$3d\ ^1D$ line is plotted vs Ne plasma temperature for a fixed Ne ion density of 10^{20} cm^{-3}.

perature of maximum gain is much lower than one would expect from coronal model calculations of the ionic species abundances. Such calculations[14] reveal that helium-like ion concentrations peak at 120 and 330 eV for Ne and Al, respectively. The present calculations predict corresponding peak gains at 50 and 100 eV, since radiative pumping to the $n = 4$ and $n = 3$ bound levels in the two schemes greatly facilitates collisional ionization (Fig. 4). Hence peak lasing ion abundance occurs at much lower temperatures where fewer electrons are capable of ionizing these bound states. Ion species abundances at a fixed total ion density as a function of temperature are shown for resonantly pumped Al and Ne in Figs. 7 and 8, respectively. In each case the shape of the gain versus temperature curve is similar to that of the helium-like species abundance function. Because of the rapid collisional ionization of the helium-like species, hydrogen-like Al XIII and Ne X exhibit large abundances over a wide range of temperature, a property usually possessed by helium-like species in the absence of a nonequilibrium photon field. For the $n = 3$ singlet of Al XII and the $n = 4$ singlets of Ne IX, the collisional ionization rate at $T_e \sim 400$ eV is approximately equal to the sum of the collisional excitation and de-excitation rates to the other levels. Thus the pumped plasma must be kept cooler (50–100 eV) to preserve a substantial helium-like abundance. At still lower temperatures a sharp gain and abundance falloff occurs as the plasma assumes a more normal configuration when the "extra" ionization becomes small. In these two lasing systems, the strength of the pump-

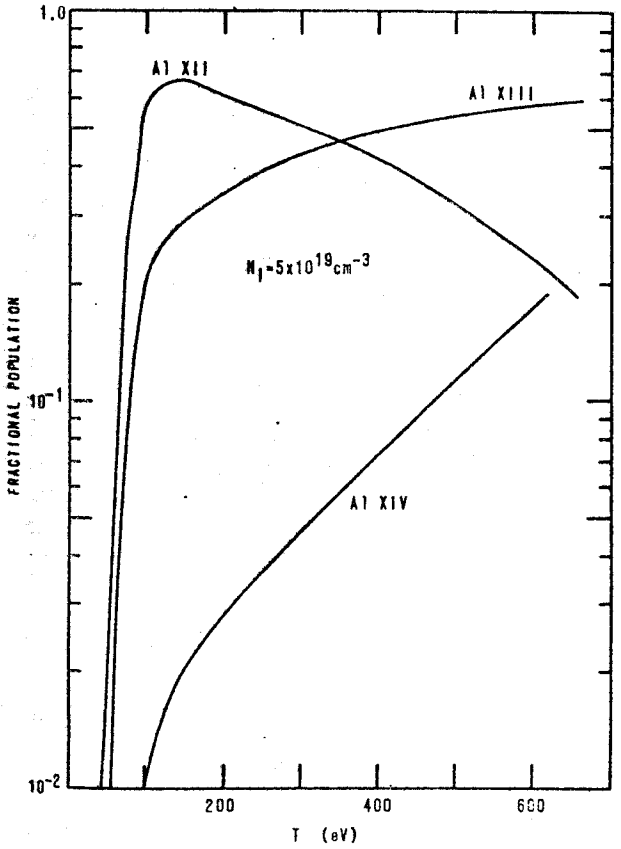

FIG. 7. Ionic species abundances for an optically thin Al plasma under the influence of the Si pump radiation of Fig. 1 are shown vs temperature at an ion density of 5×10^{19} cm^{-3}.

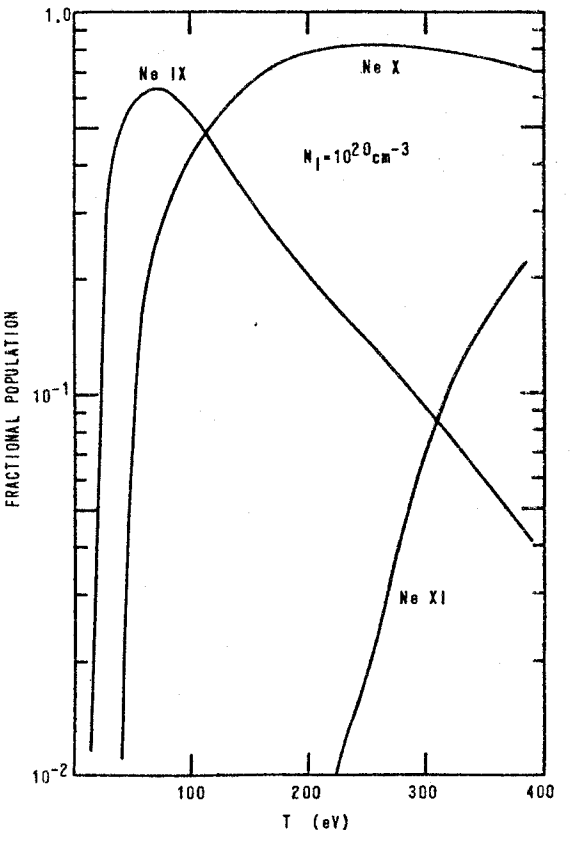

FIG. 8. Ionic species abundances for an optically thin Ne plasma under the influence of the Na pump radiation described in the text are shown vs temperature at an ion density of 10^{20} cm^{-3}.

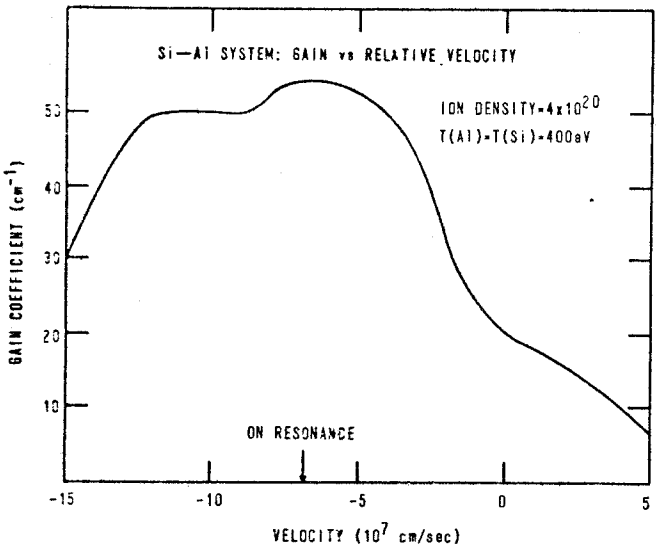

FIG. 9. Line center gain coefficient in the Al XII $2p\,^1P - 3d\,^1D$ line is plotted vs velocity of approach of the Si and Al plasmas. The Al ion density is 4×10^{20} cm^{-3} and its temperature (the same as that of the pumping Si plasma) is assumed to be 400 eV.

ing decisively affects the temperature at which the pumped plasma must be prepared for maximum gain to occur. Such effects have been noted elsewhere[6,7] in somewhat different contexts.

C. Velocity dependence

For the Na/Ne system, the pumped and pumping lines are within resonance to 1 part in 10^5, and thus there is no question as to the adequacy of the wavelength coincidence. For Si/Al, however, the wavelength difference of 0.015 Å amounts to 13 Doppler widths at 400 eV. For a photon traveling at normal incidence to the pumped plasma, this resonance defect could be made up if the two plasmas stream toward each other at 6.8×10^7 cm sec^{-1}. But given the wide opacity broadened pumping line profile (Fig. 1) the functional dependence of gain on plasma streaming velocity must be calculated; this result is presented in Fig. 9. In these calculations, the frequencies of the radiation incident on the pumped plasma were shifted angle by angle to reflect the streaming velocities indicated. Even though there is a substantial self-reversal at the center of the pumping line, peak gain does indeed occur for the matched streaming velocity of 6.8×10^7 cm sec^{-1}. This is due to the fact that most of the pumping radiation is not normally incident on the pumped plasma and therefore a range of velocity shifts are sampled (due to the cos θ effect) at any one physical streaming velocity. At the perfectly matched streaming velocity of 6.8×10^7, gain is $\simeq$3 times that of zero streaming velocity because the very highest pumping line intensities just outside the self-reversed core are sampled to the greatest degree. Such a velocity is somewhat higher than those experimentally produced to date, but not prohibitively so. Laser plasma ablation velocities of 3.3×10^7 cm sec^{-1} have been reported,[15] and Z-pinch implosion velocities of 2×10^7 cm sec^{-1} were deduced from spectroscopic evidence.[16] In any event, counter-streaming of the plasmas is helpful, but not essential to produce significant gain.

IV. FURTHER REMARKS AND CONCLUSIONS

We have determined, through a series of detailed calculations, the conditions under which significant gain at x-ray wavelengths, employing the Na/Ne and Si/Al plasmas for resonant photon pumping, should be attainable in the laboratory. Substantial gain at 58-230 Å and 44 Å for Na/Ne and Si/Al, respectively, is in principle achievable. However, the task of setting up the correct plasma conditions is not trivial for a number of reasons. First, there are the deleterious radiative trapping effects described in Sec. II. Also, for optimum employment of both schemes, the temperature of the pumped plasma should be maintained well below that of the pumping plasma to avoid excessive ionization in the lasing medium. This could perhaps be accomplished by keeping the two components as physically separate as possible to reduce conductive temperature equilibration. Similarly, the pumping plasma might be heated first, and then the pumped medium activated through use of a delayed heating pulse or laser beam to assure that the pumped plasma passes through the optimal temperature range while being exposed to the intense pumping radiation. Also, in previously successful experiments,[17] stepped targets using metal plates as heat sinks have allowed experimenters to tune the plasma temperature downward at certain distances from the initial plasma formation surface. Perhaps similar techniques could be employed for the present schemes. Even though a lower pumped plasma temperature is essential for optimum steady state gain, substantial gain is still achievable for equal pumped and pumping plasma temperatures (Fig. 9).

In the case of the Na/Ne system, pumping radiation was generated in an actual pellet implosion experiment at Rochester for which the ion density of the pellet has been diagnosed as 4.5×10^{21} cm^{-3}, which is more than an order of magnitude greater than the neon ion density required for maximum gain. In short, a very dense sodium plasma is desirable to obtain high pumping power, but a relatively tenuous neon medium is needed to prevent collisional processes from neutralizing the pumped inversion. Therefore, a configuration which is the reverse of a normal pellet suggests itself. One might compress a cylindrical glass rod (with a cylindrically focussed laser, perhaps) which has been heavily doped with sodium impurities. This rod would initially be encased in neon, which would form a more tenuous blowoff plasma. Or, alternatively two physically separate Na and Ne plasmas could be created with intensities and pulse widths tailored to produce optimum gain characteristics. This would certainly allow different densities to be produced in the separate components, and would minimize or eliminate conductive temperature equilibration.

ACKNOWLEDGMENT

This work was supported in part by the Office of Naval Research.

[1] A. V. Vinogradov, I. I. Sobelman, and E. A. Yukov, Kvant. Electron. (Moscow) 2, 105 (1975) [Sov. J. Quantum Electron. 5, 59 (1975)].
[2] B. A. Norton and N. J. Peacock, J. Phys. B 8, 989 (1975).
[3] V. A. Bhagavatula, J. Appl. Phys. 47, 4535 (1976).

[4]J. P. Apruzese, J. Davis, and K. G. Whitney, J. Phys. B **11**, L643 (1978).
[5]V. A. Bhagavatula, Appl. Phys. Lett. **33**, 726 (1978).
[6]V. A. Bhagavatula, IEEE J. Quantum Electron. **16**, 603 (1980).
[7]K. G. Whitney, J. Davis, and J. P. Apruzese, Phys. Rev. A **22**, 2196 (1980).
[8]J. P. Apruzese, P. C. Kepple, K. G. Whitney, J. Davis, and D. Duston, Phys. Rev. A **24**, 1001 (1981).
[9]H. R. Griem, M. Blaha, and P. C. Kepple, Phys. Rev. A **19**, 2421 (1979).
[10]B. Yaakobi, D. Steel, E. Thorsos, A. Hauer, and B. Perry, Phys. Rev. Lett. **39**, 1526 (1977).
[11]P. Hagelstein, "Physics of Short Wavelength Laser Design," Ph.D. thesis, Lawrence Livermore Laboratory, 1981 (unpublished).
[12]P. Burkhalter, J. Davis, J. Rauch, W. Clark, G. Dahlbacka, and R.Schneider, J. Appl. Phys. **50**, 705 (1979).
[13]K. G. Whitney, J. Davis, and J. P. Apruzese, "Some Effects of Radiation Trapping on Stimulated VUV Emission in Ar XIII," in *Cooperative Effects in Matter and Radiation*, edited by C. M. Bowden, D. W. Howgate, and H. R. Robl (Plenum, New York, 1977).
[14]V. L. Jacobs, J. Davis, J. E. Rogerson, and M. Blaha, Astrophys. J. **230**, 627 (1979); also unpublished calculations for Al.
[15]R. Decoste, S. E. Bodner, B. H. Ripin, E. A. McLean, S. P. Obenschain, and C. M. Armstrong, Phys. Rev. Lett. **42**, 1673 (1979).
[16]J. D. Perez, L. F. Chase, R. E. McDonald, L. Tannenwald, and B. A. Watson, J. Appl. Phys. **52**, 670 (1981).
[17]V. A. Bhagavatula and B. Yaakobi, Opt. Commun. **24**, 331 (1978).

X-ray lasing in a Na/Ne plasma environment

F. L. Cochran
Berkeley Research Associates, Springfield, Virginia 22105

J. Davis and J. P. Apruzese
Plasma Radiation Branch, Plasma Physics Division, Naval Research Laboratory, Washington, D.C. 20375

(Received 25 July 1983; accepted for publication 13 August 1984)

An investigation has been conducted to determine the feasibility of generating conditions favorable to population inversion, gain, and x-ray lasing in a two-component plasma consisting of sodium and neon. An intense laser beam is assumed incident on both sides of a Na/Ne slab target separated by a carbon thermal buffer. Temperature and density profiles of the laser target interaction are calculated using a Lagrangian hydrodynamics model. Level populations and radiative emissions are evaluated using a collisional-radiative equilibrium model including opacity effects. It appears possible to achieve measurable gain at 82, 58 and 230 Å from the 3-2, 4-2, and 4-3 transitions of heliumlike neon, respectively. Additionally, by pulse tailoring and target design, it should be possible to enhance the Na pumping power.

I. INTRODUCTION

For many years now, there have been a variety of proposed schemes suggesting ways to create a population inversion and subsequent gain in the x-ray region.[1–7] One such scheme involves the flashlamp concept where the radiated flux from one plasma pumping another plasma creates conditions which result in coherent radiation in the soft x-ray regions.[4–7] There are several cases where the coincidence between the pumping and absorbing lines is close enough to merit strong consideration as a possible lasing combination. For example, K-shell lines from Mg, Al, or Si are reasonably well matched to several fluorinelike Kr lines. Two such schemes utilizing a Si-XIII–Al-XII system and a Na-X–Ne-IX system are modeled in detail in Ref. 1. The Na-Ne scheme is particularly interesting because the lines match to two parts in 10^4 at a wavelength of 11 Å. An energy level diagram of this scheme is shown in Fig. 1. In this paper we will consider a scheme which is currently under study and consists of a target design made up of planar layers of sodium and neon. We have also found that it is necessary to use an intermediate layer of another material which acts as a thermal buffer but allows the pumping radiation to pass through relatively unimpeded. We will concentrate on the hydrodynamic and thermodynamic aspects of creating the proper plasma conditions which should be favorable to achieving gain. The basis of the assumptions which we employ are taken from Ref. 1, which will hereafter be referred to as ADW.

In Sec. II a description of the proposed two-component plasma configuration is given along with a discussion of the considerations which must go into the design of such a system. Section III gives the results of our numerical modeling. A summary and conclusions are presented in Sec. IV.

II. DESCRIPTION OF THE DYNAMICS OF THE Na-Ne SYSTEM

The method proposed for creating the proper conditions in the Na-Ne system is to use two high-power laser beams to "tune" the hydrodynamics and thermal properties of the two plasma components.[7] The first laser acts to create a tenuous neon blowoff while the second laser provides an energy source to heat the sodium. The sodium then acts as a backlighting flashlamp for the neon. Lasers which operate today in the 0.25–1.0-μm range are well suited for this task since absorption of the beam can be tailored to the requirements of the system. First, absorption of one laser operating at a relatively low intensity will ablate the neon at a low temperature, typically about 100 eV. Second, a higher-powered laser will heat the sodium plasma to a higher temperature which then serves as the backlighting pump source. Of course, within a finite time, the thermal wave will propagate through the sodium and into the neon. This isothermal state precludes the necessary conditions which are necessary for achieving gain. This is particularly disastrous if the neon

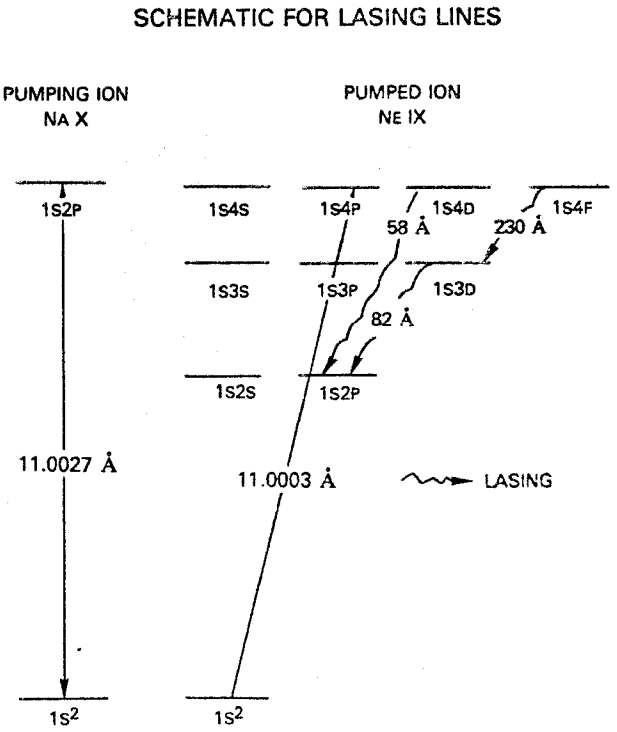

FIG. 1. Key energy levels diagramed for the Na-Ne scheme.

 0021-8979/85/010027-06$02.40

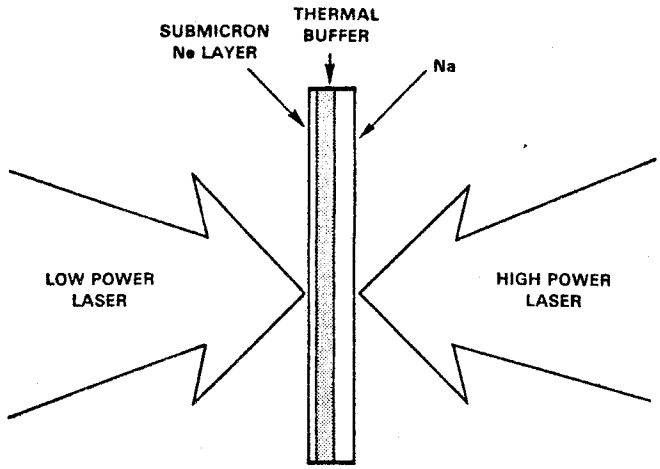

FIG. 2. Schematic of the proposed Na-Ne x-ray laser experiment. A thermal buffer region is also shown.

is in contact with the sodium. However, if the two materials are separated by any appreciable distance, then the efficiency in the system can be lost due to solid angle effects. A schematic of this configuration is shown in Fig. 2. Note here that the two lasers are pointing in opposite directions.

An analysis of a system where the strong laser is propagated through the neon before heating the sodium shows that the neon will be overheated very quickly because it serves as the underdense laser corona for the sodium material. In such a situation, the corona is nearly isothermal at temperatures which cause excessive neon ionization beyond the heliumlike stage, and thus permits little or no gain. This forces one to look at schemes which involve two-sided illumination.

Several constraints in this problem are revealed by considering the plasma properties which are needed to achieve gain in a resonant photopumped medium. The line absorption coefficients are linear in ion density. Therefore, for a fixed optical depth, the width d of the ablated neon can be scaled as $d = A/N$ where A is a constant and N is the ion density. The maximum 1-2 resonance line optical depth before significant reduction in population inversion occurs has been determined by Hagelstein[2] to be approximately 5. This is probably somewhat relaxed for the 4-3 transition (see Fig. 1). However, for the purposes of the paper, we will use this value as the maximum allowed optical depth. The approximation given in ADW is that this requires an ablated blowoff with a scale length not greater than 10 μm for ion densities on the order of 10^{20} cm^{-3}. This scale length can increase to greater than 0.1 cm for ion number densities on the order of 10^{18} cm^3. For the inverted levels discussed in ADW, the gain coefficients for the Ne IX $2p^1P$-$3d\ ^1D$ and $2p^1P$-$4d\ ^1D$ transitions peak near an ion density of 10^{20} cm^{-3}. The $3d\ ^1D$-$4f\ ^1D$ gain which peaks near 10^{19} cm^{-3}, subsequently drops off dramatically to less than unity at 10^{16} cm^{-3} but is still greater than 10 at 10^{18} cm^{-3}.

A second constraint is placed on the temperatures of the two plasmas. The temperature of the lasing neon must be kept low enough to prevent burnout of the Ne IX population. At a density of 10^{18} cm^{-3} the maximum fractional population for Ne IX occurs at approximately 65 eV in the presence of the pump radiation. On the other hand, the pumping plasma (in this case Na) is most favorable when it is an optically thick plasma with a kinetic temperature of about 300 eV. In short, one would like a hot dense pumping plasma irradiating a cooler lasing plasma which is optically thin along one axis.

As indicated above, the density requirements of the 3-2 and 4-2 transitions differ from the requirements of the 4-3 transition. Therefore, we can separate the following discussion into two parts. First, we will examine the 3-2 and 4-2 scaling requirements. We consider cryogenic neon with density of 1.2 g/cm^3 on the outside of a planar target. In order to prevent photon trapping and meet the conditions given above, a layer of 2.79×10^{-2} μm of Ne is needed. This assumes a uniform ion blowoff density of 10^{20} cm^{-3} with a width of 10 μm. Ablation velocities in laser-produced plasmas typically are on the order of 10^7 cm/sec. It can therefore be expected that expansion out to 10 μm occurs on a time scale of roughly 100 psec. Both the pumping material and the lasing material must reach the proper conditions for gain in this time frame. The strong dependence of the gain coefficient on density results in the existence of a window of approximately 300 psec before the 3-2 and 4-2 transitions yield a gain coefficient less than unity.

On the other hand, the 4-3 transition has a gain coefficient of 1.0 at approximately 10^{16} cm^{-3} and hence the expansion time can be up to 1 μsec. This time is much greater than any other time of interest in this problem. At peak gain (i.e., 10^{19} cm^{-3}) this allows 1 nsec for the blowoff to develop. Again, this assumes a uniform expansion velocity of 10^7 cm/sec.

We now consider the propagation of the thermal wave from the hot dense sodium plasma into the neon plasma which is, at both, a lower density and temperature. The electron heat flux is given by

$$\mathbf{q} = -K\nabla T_e. \tag{1}$$

The conductivity K can be written in the form

$$K = Cn_e k\lambda_c v_e, \tag{2}$$

where C is a constant of order unity, n_e is the electron density, k is Boltzmann's constant, λ_c is the electron-ion collision mean free path, and v_e is the electron thermal speed. The heat flux can be rewritten in the form

$$\mathbf{q} = Cn_e kT_e\left(\frac{\lambda_c}{L_T}\right)v_e(-\mathbf{e}_T), \tag{3}$$

where L_T is the temperature gradient length and $-\mathbf{e}_T$ is given by $\nabla T/|\nabla T|$. If $L_T < \lambda_c$, the heat flux will be carried in the direction $-\mathbf{e}_T$ at a rate which is greater than the electron thermal speed. This is an unphysical result and indeed, the derivation of the conductivity given by Eq. (2) is predicated on the assumption that $\lambda_c < L_T$. The problem of steep gradients has been studied extensively in the laser fusion literature.[8–11] The approach which has been used most often in connection with this difficulty has been to limit the flux whenever $\lambda_c > fL_T$ to

$$\mathbf{q} = N_e kT_e fv_e(-\mathbf{e}_t), \tag{4}$$

where f, the so-called "flux limiter", is less than one. There-

fore, we can base our estimate of the propagation speed of the thermal wave based on a flux-limited value of v_e.

This propagation speed is particularly important at the Na-Ne interface if the dense hot sodium is close to the Ne. It is important to note here that the portion of sodium facing the neon must be at a temperature which is a significant fraction of the pumping temperature (i.e., 300–400 eV). Otherwise, the central portion of the sodium line will be self-absorbed with the resultant emerging flux greatly reduced. Thus, the optimum pumping condition occurs when the sodium is experiencing burn-through at the time the ablation wave has reached the sodium interface. The transit time across the neon of this thermal front will be given by some limited value of v_e times the neon plasma length. For a temperature of 400 eV, this velocity approaches 10^9 cm/sec if $f = 1$. If the flux limiter concept is invoked, this velocity will be reduced to something on the order of 10^8 for $f = 0.1$. In all cases, because of the low density of the neon compared to the high sodium density which acts as a large thermal reservoir, we can expect the neon plasma to become isothermal at the sodium temperature on a rapid time scale (i.e., 10–100 psec).

To alleviate this problem, a third material can be placed between the Na-Ne interface. This will act as a thermal buffer while allowing the pumping radiation to pass through without significantly reducing the pumping intensity. First, the material is chosen to be a solid which is both thick enough to absorb the thermal wave and keep it from reaching the neon. Thus, a material of approximately the same thickness and density as that of the original sodium is appropriate. Second, the material should be relatively low in Z so that opacity effects do not significantly impede the pumping line. A material such as carbon is ideal for this purpose. For example, the photon cross section of cold carbon at 11 Å (i.e., the pumping line) is approximately 2×10^3 cm^2/g.[12] Thus, for linear distances less than 2.2 μm, solid carbon (2.2 g/cm^3) can be considered to be thin to the pumping line. This distance can be lengthened if, for instance, CH is used in which case the corresponding carbon density is decreased.

III. NUMERICAL MODELING

In order to assess the validity of this scheme in a more detailed fashion, we have used a 1-D Lagrangian hydrodynamics code to model the Na-Ne and Na-C-Ne target configurations. This code treats the electron and ion temperatures separately. Equation of state models are used for both the ions and electrons. We use the IONEOS model[13] to treat the ions and a quantum statistical treatment for the electronic equation of state.[14] Of course, the gaseous neon tends to behave nearly as a perfect gas. At the beginning of each run, the target is initialized as a solid sodium slab (or solid sodium-carbon slab) coated with a thin layer of neon. The Ne layer contains enough particles so that for a uniform expansion width of 10 μm, the ion density will be 10^{20} cm^{-3}. These values are dictated by the self-absorption criteria discussed earlier. As solid or liquid densities, this gives a submicron layer of uniform thickness.

The Lagrangian hydrodynamic equations are

$$\frac{dM}{dt} = 0, \tag{5}$$

$$\rho\frac{d\mathbf{v}}{dt} = -\nabla(P_e + P_i + Q), \tag{6}$$

$$c_{v_e}\rho\frac{dT_e}{dt} = -\nabla\cdot\mathbf{q}_e + \frac{1}{\rho}\left(P_e - \rho^2\frac{d\epsilon_e}{d\rho}\right)\frac{d\rho}{dt} + \dot{C}_{i,e}(T_i - T_e) + \dot{\epsilon}_s, \tag{7}$$

$$c_{v_i}\rho\frac{dT_i}{dt} = -\nabla\cdot\mathbf{q}_i + \frac{1}{\rho}\left(P_i + Q - \rho^2\frac{d\epsilon_i}{d\rho}\right)\frac{d\rho}{dt} - \dot{C}_{i,e}(T_i - T_e), \tag{8}$$

where M is the zonal mass, ρ is the density, v is the velocity, $P_{e,i}$ are the pressures, $T_{e,i}$ are the temperatures, $c_{v_{i,e}}$ are the specific heats, $\epsilon_{i,e}$ are the specific internal energies, and Q is an artifical viscosity. The $\dot{\epsilon}_s$ and $\dot{C}_{i,e}$ terms, represent energy sources and energy transfer terms, respectively. The initial zone sizes are varied in the transition region so that the zonal masses of the neon are nearly equal to those of the solid material at the interface. Velocities and positions are defined on zone boundaries. Density, temperature, and laser absorption are computed at zone centers. The electron temperature is flux-limited according to Eq. (4). At the intensities which are considered in this study, there is experimental evidence that $f = 0.1$ gives good agreement between numerical simulation and targets irradiated at 1.06 μm.[15] Therefore, in all cases which are discussed here, a flux limiter of $f = 0.1$ has been used. The simulation starts with both sides of the target (see Fig. 2) being irradiated by layers operating at 1.06 μm. The intensity on the neon side is well below that on the sodium side and is typically on the order of 10^{12} W/cm^2. During this early phase, the neon plasma expansion and heating by the laser begin to set up the proper conditions discussed earlier. Because in this design the heating processes for the two materials are independent, the low power laser on the neon side can be shut off to prevent overheating the corona and burning through the Ne heliumlike stages.

TABLE I. Parameters for three Na-C targets.

Case	Na/C thickness (μm)	Peak laser intensity (W/cm^2)	Pulse time FWHM (psec)	Line center pumping intensity (ergs/cm^2 sec Hz)	Pump line width at half center value (Hz)
I	0.5/0.5	5×10^{13}	200	2.0×10^3	3.0×10^{14}
II	0.1/0.5	2.5×10^{13}	200	9.6×10^2	2.0×10^{14}
III	0.1/0.5	1×10^{13}	300[a]	6.7×10^2	2.2×10^{14}

[a] Linear rise time.

The sodium side of the target, on the other hand, is irradiated with an intensity of one to several times 10^{13} W/cm^2. In this study, we have used laser pulses which have a Gaussian temporal shape as well as pulses which rise linearly in time. The widths and rise time of the pulses have typically been 200–300 psec. Because of the time scales which were discussed earlier (i.e., the time scale needed to "set up" the neon plasma is 100 psec–1 nsec), the width of the sodium slab is constrained to be less than 1 μm for these types of laser pulses. This constraint is dictated by the time it takes for the ablation front to advance to the interface. Ideally, the best conditions should be achieved as the thermal wave emerges from the sodium at a temperature of approximately 300–400 eV and enters the carbon buffer. This favorable period lasts until the laser has burned through enough of the target so that the entire mass of the sodium is heated past the helium-like stage and the output in the pumping line is greatly diminished.

Table I contains more detailed information for three cases of interest. In these cases, we have chosen 0.1 μm and 0.5 μm of sodium. Again, this is somewhat dictated by the choice of the laser intensity and pulse width. Naturally, increasing the laser intensity and consequently, the energy, for a given pulse length allows for more sodium material to be heated to the proper temperature. Figure 3 shows the pumping line intensity at the Na-C boundary for the three cases which are shown in Table I. Also shown is the pumping line intensity of a Rochester implosion in which the glass microballoon contained a sodium impurity.[16] This result is discussed in ADW and is used here as a means of comparison. The pumping line intensity at line center for this Rochester experiment was found by the analysis of ADW to be 6.6×10^3 ergs/cm^2 sec Hz. The strongest line center intensity seen in the results of this paper (i.e., case I) is roughly 30% of the Rochester experimental results. However, this line is quite broad and has a width of roughly 3.0×10^{14} Hz with flux values above 10^3 ergs/cm^2 sec Hz. The profile produced in case II is also rather broad but is roughly 50% of the peak value obtained in case I at line center. From Table I, it can be seen that both the intensity incident on target and mass were increased in case I in an attempt to increase the line center intensity. Increasing the intensity without increasing the mass led to early burnout, while increasing the mass without increasing the intensity led to self-reversal in the line center. This is evident in case III. This feature appears when the main flux-producing region is behind the interface position and the flux is absorbed by dense cooler sodium. In order to remove the self-absorption, the front of the sodium must be heated to values greater than 300 eV. Therefore, increasing the mass also means that the incoming energy, or intensity for a given pulse length, must also be increased.

Figure 4 shows the density and temperature of the sodium as a function of distance from the interface at 100 psec

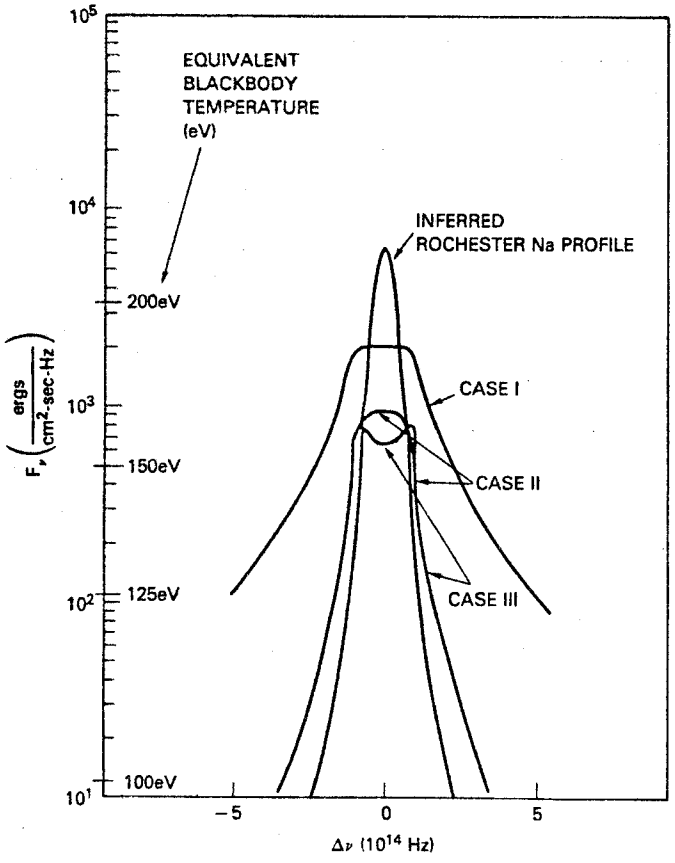

FIG. 3. Post-processed intensity profile for the 11-Å pumping line at the Na-C interface. The three cases of Table I are shown along with the inferred Rochester experimental profile. The times for case I and case II are 100 psec after the peak of the Guassian-shaped laser pulse. The time for case III is 300 psec, which is the rise time for the linear ramped pulse.

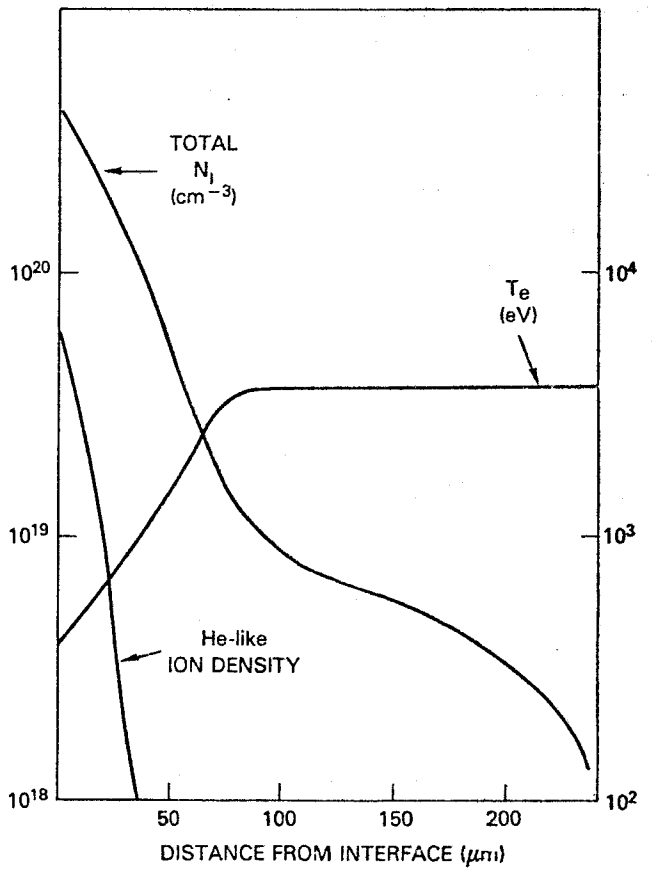

FIG. 4. Sodium density and temperature profiles for case I of Table I near the Na-C interface at 100 psec after the laser peak. Also shown is the He-like ion density.

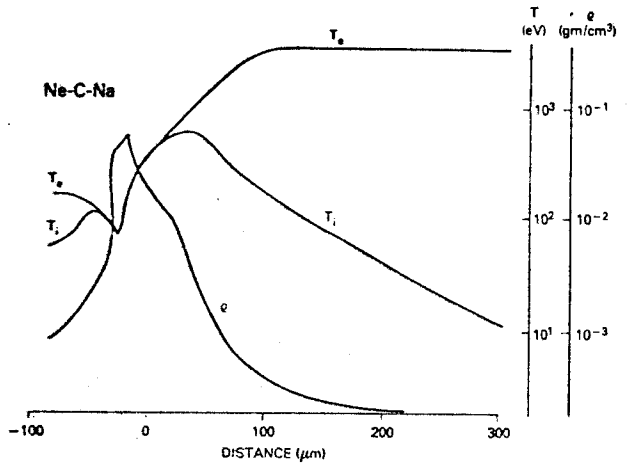

FIG. 5. Density and temperature profiles for case I of Table I at 100 psec after the laser peak.

after the peak of the laser pulse for case I. The He-like ion density is also shown. Note that this density peaks strongly at the front of the plasma where the temperature is 400 eV. The entire target including the carbon buffer and neon plasma at 100 psec is shown in Fig. 5.

The results of ADW (where the neon is assumed fully bathed in pump radiation) showed that the Rochester profile would produce a peak gain coefficient of roughly 200 cm^{-1}. For the planar targets reported here, however, the pump radiation is only incident from one side. Therefore, proportionality arguments yield gains of 30, 15, and 10 cm^{-1}, for cases I–III, respectively, for an illumination solid angle of 2π steradians.

One obvious question which might be asked is this: How much gain can be achieved in an optimized target with an optimum laser? At the present time, this question cannot be fully answered because of the large number of parameters which must be varied. However, certain issues are clear. First, the entire region of sodium near the interface must be heated close to the required temperature of 300–400 eV or self-absorption will reduce the intensity of the pumping line. Therefore, if the amount of sodium is increased to correspondingly increase the pumping power, a higher energy laser must also be used. However, a danger in going to higher intensity lasers is the production of hot electrons which could impair the effectiveness of the thermal buffer. Our present treatment does not include this effect. Second, the creation and expansion of the neon plasma dictates the operating time scale for producing the proper pump conditions. This time scale is roughly less than or equal to one nanosecond for expansion velocities of 10^7 cm/sec. Under these considerations, the optimum gain point probably lies somewhat above case I, but hot electron production may prevent it from being too far above this point.

Given the fact that the bulk of the sodium plasma is expanding with velocity 1.0×10^7 cm/sec, and the neon plasma itself is expanding in the opposite direction at 2.3×10^7 cm/sec, the question arises: have the pumped and pumping lines been Doppler-shifted out of coincidence? The line emission profiles presented here have been calculated with the stationary plasma approximation. To ascertain the effect of plasma motional broadening on the profile as seen from the neon region we consult the work of Irons.[17,18]

For the pumping sodium plasma the expansion velocity is 1.8 times the ion thermal velocity. This factor of 1.8 corresponds to Irons' parameter σ. Irons presents cases for $\sigma = 1$ and $\sigma = 3$ for pure Doppler and pure Lorentz lines, for optical depths of 10 and 10^2 (see Ref. 17, Figs. 5 and 6). The line center optical depth of the sodium pump line for case I is 40. Interpolation of Irons' calculations may be used to estimate the true profile shape. Such a procedure leads to the conclusion that, for case I, the flat-top profile which would prevail in a stationary plasma will transform to an asymmetric self-reversed profile in the presence of plasma motion. The profile would be characterized by a blue-side peak 4–5 Doppler widths (2.2×10^7 cm/sec) from line center, and a somewhat stronger red-side peak at a similar frequency spread from line center. The above shifts are quoted in the stationary laboratory frame. The neon rest frame is 2.3×10^7 cm/sec to the red of the small mass of stationary plasma between the main sodium and neon regions. Therefore, the blue peak of the pumping line would be shifted to virtually the center of the neon line in the neon rest frame. Also, as pointed out by Irons in Ref. 18, the total intensity of an optically thick line is generally greater from differentially streaming plasmas as compared to the stationary case. This is due to the fact that the Doppler shifts reduce the effective optical depth of the line, resulting in the ultimate escape of a greater fraction of collisionally created photons. Thus, the effective pumping power of the sodium line might well be greater than that calculated here, due to this mechanism. Finally, the differential expansion of the neon plasma will have the effect of reducing the resonance photon pumping of the lower lasing levels, thereby relaxing somewhat the constraints on the size of the neon region. In summary, we do not expect the motional Doppler line shifts to be significantly detrimental to the achievement of a population inversion in neon, but instead such effects may enhance the viability of the scheme.

IV. SUMMARY AND CONCLUDING REMARKS

We have examined the hydrodynamic and thermodynamic properties of a Na-Ne system irradiated on opposite sides by high-power lasers. By necessity, the laser intensity on the sodium side must be much greater than the intensity on the neon side. It was found that because of thermal considerations, a buffer is needed between the sodium and neon.

Through numerical simulation it was found that the entire sodium slab must be at or near the ideal pumping temperature of 300–400 eV to prevent self-absorption at the sodium-buffer interface. In our modeling, we used a 0.5-μm carbon slab as the buffer. The best result was found when a 0.5-μm sodium slab was irradiated with a 200-psec pulse from a 1.06-μm laser operating with a peak intensity of 5.0×10^{13} W/cm^2. When the pumping line flux emerging from the sodium was compared with that from a previously analyzed profile, it was found that the gain coefficient would be roughly 30 cm^{-1}. This gain should be measurable in an experiment of this type. It may, however, be more advantageous to employ a cylindrical or spherical configuration in order to provide compressional heating of the pump to the

requisite temperature at high density. Finally, we hope to report on a completely self-consistent transient treatment at a later date.

ACKNOWLEDGMENTS

We would like to thank the referee of a previous version of this paper who pointed out the extreme difficulty of achieving gain in a one-sided illumination target and suggested we look at alternate schemes. This work was supported in part by the Office of Naval Research.

[1]J. P. Apruzese, J. Davis, and K. G. Whitney, J. Appl. Phys. **53**, 4020 (1982).
[2]P. L. Hagelstein, Lawrence Livermore National Laboratory Report UCRL-53100 (1981).
[3]R. W. Waynant and R. C. Elton, Proc. IEEE **64**, 1059 (1976).
[4]A. W. Vinogradov, I. I. Sobel'man, and E. A. Yukov, Sov. J. Quantum. Electron **5**, 59 (1975).
[5]B. A. Norton and N. J. Peacock, J. Phys. B **6**, 989 (1975).
[6]J. P. Apruzese, J. Davis, and K. G. Whitney, J. Phys. B **11**, L643 (1978).
[7]R. H. Dixon and R. C. Elton, J. Opt. Soc. Am. B **1**, 232 (1984), and references therein.
[8]C. E. Max and C. F. McKee, Phys. Rev. Lett. **39**, 1336 (1977).
[9]R. L. Morse and C. W. Nielson, Phys. Fluids **18**, 1299 (1975).
[10]R. C. Malone, R. L. McCrory, and R. L. Morse, Phys. Rev. Lett. **34**, 721 (1975).
[11]W. M. Manheimer and H. H. Klein, Phys. Fluids **18**, 1299 (1975).
[12]F. Biggs and R. Lighthill, Sandia Report, SC-RR-71 0507 (1971).
[13]C. W. Cranfill and R. More, Los Alamos Report No. LA-7313-MS, 1978 (informal report).
[14]U. Gupta, private communication (1983).
[15]T. J. Goldsack, J. D. Kilkenny, B. J. MacGowan, P. F. Cunningham, L. S. Lewis, M. H. Key, and D. T. Rumsby, Phys. Fluids **25**, 1634 (1982).
[16]B. Yaakobi, D. Steel, E. Thorsos, A. Hauer, and B. Perry, Phys. Rev. Lett. **39**, 1526 (1977).
[17]F. E. Irons, J. Phys. B **8**, 3044 (1975).
[18]F. E. Irons, J. Phys. B **9**, 2737 (1976).

J. Quant. Spectrosc. Radiat. Transfer Vol. 34, No. 5, pp. 447–452, 1985
Printed in Great Britain.

0022–4073/85 $3.00+.00

AN ANALYTIC VOIGT PROFILE ESCAPE PROBABILITY APPROXIMATION

J. P. APRUZESE
Naval Research Laboratory, Plasma Physics Division, Plasma Radiation Branch,
Washington, DC 20375, U.S.A.

(*Received* 9 *April* 1985)

Abstract—An efficient analytic Voigt profile escape probability approximation is presented and compared to exact numerical calculations. Using this analytic approximation, the two-level-atom source function is also computed for optically thick media, which have been previously evaluated exactly by Avrett and Hummer. Comparison with a more realistic laboratory plasma case also validates the usefulness of the approximation for economical modeling of radiation transport in optically thick plasmas.

1. INTRODUCTION

Laser-produced plasmas often contain dozens to hundreds of optically thick lines, and, in many cases, the hydrodynamic evolution of such plasmas is significantly affected by radiation transported in these lines.[1,2] Realistically accounting for such effects can be especially important in plasma X-ray lasing media,[3,4] where maintenance of population inversions often depends sensitively on plasma conditions. Substantial effects of radiation transport on ion-beam driven plasmas may also occur.[5]

Unfortunately, exact multifrequency transport calculations for each optically thick line are often computationally impractical. To alleviate this problem and still provide for the maximum attainable realism in the photon transport, a technique[6,7] requiring the equivalent of only one frequency per line has been tested and benchmarked successfully against previously published two-level-atom solutions which represent a stringent test of numerical radiation transport algorithms. This technique uses a computationally efficient method for obtaining photon escape probabilities averaged over the line profile. Such methods have been described in Refs. 6 and 7 for Doppler and Lorentz profiles. While such profiles may be adequate for some applications,[6] the more general Voigt profile is more appropriate for a large class of moderate density, optically thick plasmas. The line profiles of very high-density plasmas, such as those produced in spherically symmetric laser driven compressions, are dominated by the Stark effect. Weisheit[8] has given escape probability formulae for such Stark profiles. It is the purpose of this paper to present a simple analytic escape probability parameterization for the Voigt profile, and to access its accuracy by direct comparison with previously published exact solutions, as well as with a specific optically thick plasma which has also been solved by a multifrequency radiation transport technique.

2. VOIGT PROFILE ESCAPE PROBABILITY

The technique presented in Refs. 6 and 7, and referred to above, employs as its central quantity the coupling-constant matrix C_{ij}, which is the probability that a line photon emitted in spatial cell i will be absorbed by cell j. There is one coupling-constant matrix for each line. Each pair of cells in the medium is connected by a ray, as in Fig. 1. The choice of ray angle is described in Ref. 7. In the notation of Fig. 1, the coupling constant C_{ij} is the difference in mean escape probabilities from the originating cell i to the front and rear of the receiving cell j, i.e.

$$C_{ij} = \frac{0.5}{\tau_i}\int_0^{\tau_i}[P_e(\tau + \tau_B) - P_e(\tau + \tau_B + \tau_j)]\,d\tau \quad , \tag{1}$$

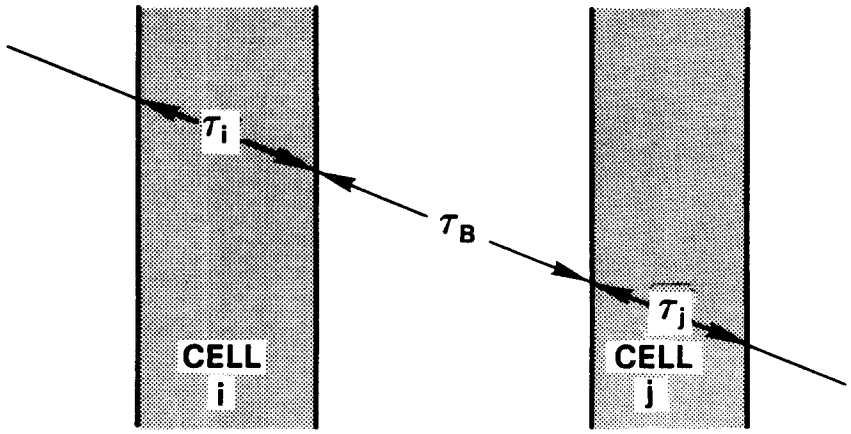

Fig. 1. Notation for photon ray tracing between a pair of cells in the medium, as applied in Eq. (1).

where the integral averages P_e over the originating cell i. In Eq. (1), the escape probability $P_e(\tau)$ is the probability that the line photon travels at least through line-center optical depth τ along the ray before being absorbed, and is given by

$$P_e(\tau) = \int \phi(\nu)\, e^{-\tau\phi(\nu)/\phi(0)}\, d\nu \quad . \tag{2}$$

In Eq. (2), $\phi(\nu)$ is the line profile function, normalized to a frequency integral of unity. The integral in Eq. (2) extends over the line profile, and $\phi(0)$ refers to the profile function at line center. Throughout this work, complete frequency redistribution is assumed. Once $P_e(\tau)$ is obtained, the C_{ij} are given by Eq. (1). The steady-state line source function can then be obtained by direct matrix inversion when the collision rates are fixed.[6,7] When the nonlinear electron density dependence affects the collision rates (as in a multistage, multilevel plasma calculation), an iteration procedure[9] is required to obtain the steady-state line source functions. The actual form of $P_e(\tau)$ for the Voigt profile is now considered.

The Voigt function is given by

$$U(a,\nu) = \frac{a}{\pi^{3/2}} \int_{-\infty}^{+\infty} \frac{e^{-y^2}\, dy}{(\nu - y)^2 + a^2} \quad . \tag{3}$$

In Eq. (3), ν is the frequency displacement from line center in Doppler widths, and a is the line-broadening parameter, which is the ratio of the sum of the inverse lifetimes of the upper and lower levels to 4π times the Doppler width. In general, the far wings of this profile are Lorenztian, i.e.

$$U(a,\nu)_{\nu\to\infty} = a/\pi\,(\nu^2 + a^2) \quad . \tag{4}$$

The transition point between a Doppler-like core and Lorentzian wings depends on a; the smaller the value of the broadening parameter, the further in frequency from line center that this transition occurs. In the limit of large optical depth, only the far wings contribute to the photon escape probability. In that case, Eq. (4) for $U(a,\nu)$ may be substituted into Eq. (2) for $\phi(\nu)$. The resulting elementary integral yields, for $a \ll 1$,

$$P_e(a,\tau) = \pi^{-1/4}\,(a/\tau)^{1/2} \tag{5}$$

as the exact optically thick limit of the Voigt escape probability for line-center optical depth τ and broadening parameter $a \ll 1$. Not surprisingly, Eq. (5) shows that a Voigt profile in the limit of large optical depth is characterized by $P_e \sim \tau^{-1/2}$, as is the case for a pure Lorentz profile.[10]

Extensive exact numerical calculations of $P_e(a,\tau)$ have been performed to determine the feasibility of simple fits to the escape probability for a Voigt profile. The simplicity of the fit is important in maintaining the computational efficiency of the coupling constant technique by which the radiative transfer is solved. Different expressions for many regimes in a and τ would substantially negate the desired economy of the method. It was not found possible to produce simple formulae with the same degree of accuracy—a few percent—achieved for Doppler and Lorentz profiles as described in Ref. 7. However, the expressions given below will be shown to be valuable for some purposes.

Two contrasting regimes in the broadening parameter a were delineated by the results of the exact calculations. For $a < 0.49$ three different regions in line-center optical depth characterized by different functional behavior in P_e exist. For $\tau \leq 1$, photons emitted throughout the line core have a significant change of escape. Between $\tau = 1$, and a critical optical depth denoted by τ_c, the behavior of the escape probability is Doppler-like ($P_e \sim \tau^{-1}$). Finally, above τ_c, only the far Lorentzian wings contribute, and the escape probability exhibits pure Voigt functional variation, i.e. $P_e \sim \tau^{-1/2}$ as in Eq. (5). Empirically, it is found that

$$\tau_c = 0.83/a(1+\sqrt{a}) \quad . \tag{6}$$

The expressions for P_e for $a < 0.49$ are

$$P_e(\tau) = \begin{cases} (1 + 1.5\tau)^{-1} & (\tau \leq 1) \quad , & \text{(7a)} \\ 0.4/\tau \quad (1 < \tau \leq \tau_c) & , & \text{(7b)} \\ 0.4/\sqrt{\tau_c \tau} & (\tau > \tau_c) \quad . & \text{(7c)} \end{cases}$$

For broadening parameters $a \geq 0.49$, the Lorentz wings are strong enough so that essentially no Doppler-like behavior occurs. In this case, the expressions adoped are

$$P_e(\tau) = \begin{cases} (1 + \tau)^{-1} & (\tau \leq 1) & \text{(8a)} \\ 0.5/\sqrt{\tau} & (\tau > 1) \quad . & \text{(8b)} \end{cases}$$

Needless to say, the sharp divisions are somewhat artificial and are set primarily to minimize inaccuracies while maintaining computational efficiency. The Voigt optical depth τ refers to the line center; it may be readily computed from the pure Doppler line-center optical depth using the ratio of polynomials given by Hui, Armstrong and Wray.[11] Equations (7) and (8) apply for all optical depths and have been tested against exact escape probability calculations for $a \geq 10^{-3}$.

Comparisons of the escape probabilities given by Eqs. (6)–(8) with exact calculations are presented in Figs. 2 and 3, for various broadening parameters ranging from 0.01 to 1.0. The simplified expressions are typically accurate to 20%, although this deteriorates to nearly 40% for a small range near $\tau = 2$ at a broadening parameter of 0.32. In some other regimes, however, the formulae are nearly exact, as shown in Figs. 2 and 3. The expressions (7) and (8) are analytically integrable; therefore the coupling constants for use in radiative transfer applications are directly obtainable using Eq. (2). The accuracy and usefulness of the present formulae to solve radiative transfer problems is now considered.

3. APPLICATION TO RADIATIVE TRANSFER

The new expressions and technique have been applied to two specific radiative transfer problems. The first of these is the planar two-level-atom case, first solved exactly by Avrett and Hummer.[12] Their chosen parameters represent a stringent test for numerical transfer algorithms, as the optical depths are high and the photon collisional quenching parameter (10^{-4}) is quite low. This latter quantity (designated here as P_Q and by Avrett and Hummer

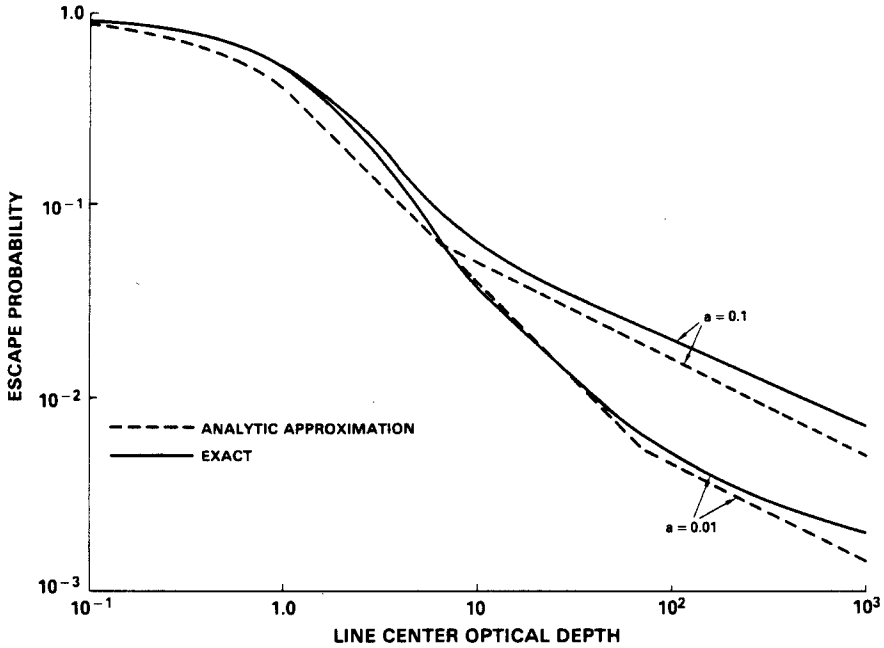

Fig. 2. Comparison of the present analytic approximation for the Voigt profile escape probability as a function of line-center optical depth with exact numerical results. Voigt-broadening parameters (a) of 0.01 and 0.1 were assumed.

as ϵ) is the probability per line photon absorption that the photon is destroyed collisionally rather than reemitted. A low P_Q coupled with high-optical-depth results in many photon scatterings. In such situations the line source function is dominated by photoexcitation, and its evaluation is therefore very sensitive to the accuracy of the radiative transfer approximation employed. Figure 4 shows comparisons of the line source function obtained with the present approximate technique to the exact results of Ref. 12. The Planck function is unity throughout the planar medium, and the line-center optical depth varies from 28 to 2.8×10^5. The Voigt-broadening parameter is 0.01. As expected, the accuracy of the approximation deteriorates with increasing optical depth. At $\tau = 28$, the maximum dis-

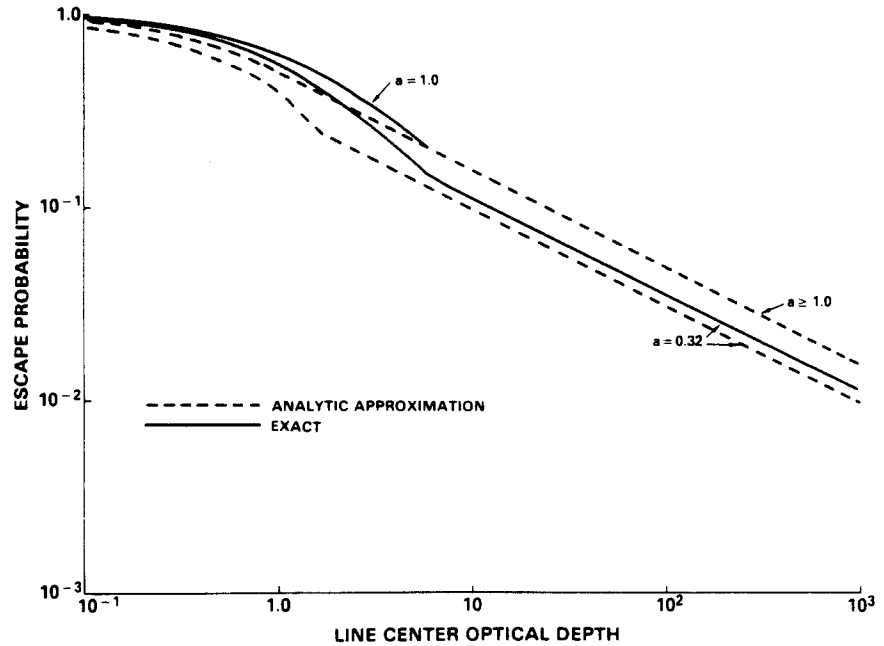

Fig. 3. As in Fig. 2, except that Voigt-broadening parameters of 0.32 and 1.0 were assumed in the exact calculation. The approximation gives the same escape probability for all $a \geq 1.0$.

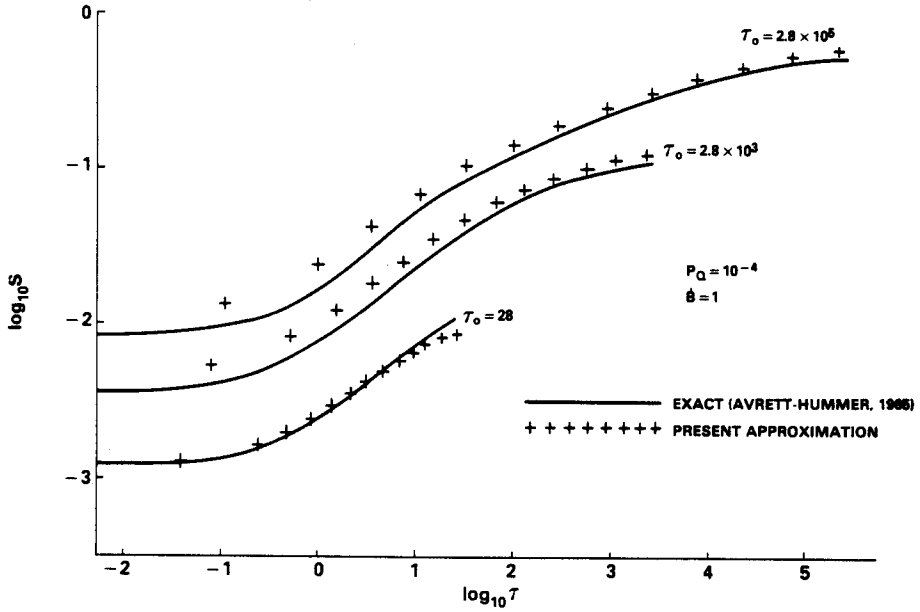

Fig. 4. A 25-cell calculation of the two-level-atom source function for planar media, using the present analytic Voigt profile escape probability approximation, is plotted along with the exact solutions of Avrett and Hummer. For the approximate calculation, every other cell is plotted as a cross. Collisional quenching probability per scattering is 10^{-4} in all cases, and the Planck function is normalized to unity. The line-center optical depths τ_0 are as indicated. The Voigt-broadening parameter is 0.01.

crepancy in the source function is 20%, but most points lie within 5% of the exact solution. In the present calculation 25 cells have been employed, and the odd-numbered cells are plotted in Fig. 4. By contrast, at $\tau = 2.8 \times 10^5$, the maximum error due to the approximation is 45%, with most points lying 10–30% from the exact source function. This latter high-optical-depth case, coupled with $P_Q = 10^{-4}$, is rarely encountered in laboratory plasmas and therefore represents a more difficult transfer problem than the present algorithm would usually be called upon to solve.

The superior accuracy of the approximation when employed in laboratory plasma simulations is demonstrated in Table 1. The problem to which the algorithm has been applied is this: Given a planar sodium plasma of fixed ion density 10^{20} cm^{-3}, electron and ion temperature of 400 eV and thickness 0.4 cm, what are the steady-state ionic stage and excited level population distributions? Table 1 shows the ratio of the helium-like Na X $1s\,2p\ ^1P_1$ level population to that of the Na X $1s^2\ ^1S_0$ ground state as a function of position in the plasma. The ratio is also presented as obtained from an exact multifrequency calculation, and is directly proportional to the line source function. A description of the atomic model and rate calculations is given in Ref. 13. The optical depth of the $1s^2\ ^1S_0 - 1s\,2p\ ^1P_1$ line is 2.6×10^2, measured from planar midpoint to outer edge. The Voigt-broadening parameter is 0.03, and $P_Q = 0.24$ for the line. As evident from Table 1 that the moderate optical depth and collisional quenching parameter, characterizing this plasma, render the transfer problem less sensitive to errors of approximation in P_e than the Avrett–Hummer cases. The maximum deviation in the line source function from the multifrequency solution is 4% near the outer boundary.

4. SUMMARY AND CONCLUSIONS

The frequency-averaged line photon escape probability for a Voigt opacity profile has been parameterized with simple analytic expressions given by Eqs. (6)–(8). The escape probability as a function of optical depth obtained from the expressions has been tested against exact calculations for Voigt-broadening parameters $\geq 10^{-3}$. Typical comparisons with the exact results are given in Figs. 2 and 3. The line source functions obtained by

Table 1. Fractional population (f) of the helium-like sodium $1s\ 2p\ ^1P_1$ excited level relative to that of the $1s^2\ ^1S_0$ ground state is tabulated as a function of distance from the boundary of a planar sodium plasma. The plasma is assumed to be homogeneous with full width 0.4 cm, ion density 10^{20} cm^{-3} and temperature of 400 eV. The last point in the table is at the plasma midpoint (0.2 cm); the populations are symmetric about this point.

Distance from the boundary (cm)	$f(1s2p\ ^1P_1) / f(1s^2\ ^1S_0)$	
	multifrequency	probabilistic
2.4×10^{-2}	4.22×10^{-3}	4.37×10^{-3}
6.0×10^{-2}	5.60×10^{-3}	5.67×10^{-3}
1.0×10^{-1}	5.92×10^{-3}	5.93×10^{-3}
1.6×10^{-1}	6.01×10^{-3}	6.02×10^{-3}
2.0×10^{-1}	6.01×10^{-3}	6.02×10^{-3}

employing these expressions in conjunction with the radiative transfer algorithm described in Refs. 6 and 7 are shown in Fig. 4 and Table 1, along with exact solutions.

The approximation presented here will probably find the most appropriate applications in laboratory plasma simulations, especially where dozens to hundreds of optically thick lines influence the plasma's hydrodynamic behavior. For most plasma applications, the calculated source function will probably deviate only a few percent from exact results, although errors of 20% are conceivable for optical depths exceeding 10^3 combined with small ($< 10^{-3}$) collisional quenching parameters. However, the realism of this approximation is greatly superior to such often-employed cruder approximations as local thermodynamic equilibrium or Planck or Rosseland mean opacities used in a diffusion approximation. Finally, for very large optical depth ($> 10^5$), low-density astrophysical applications the source function errors generated by the present method can approach 45% in certain cases. Since the present technique assumes complete frequency redistribution over the line profile, additional errors due to partial redistribution effects are also likely for extremely low-density cases. Therefore this technique is not recommended in such instances unless the errors are tolerable in the context of the problem being attacked.

Acknowledgement—This work was supported by the U.S. Defense Advanced Research Projects Agency.

REFERENCES

1. D. Duston, R. W. Clark, J. Davis and J. P. Apruzese, *Phys. Rev. A* **27**, 1441 (1983).
2. D. Duston, R. W. Clark and J. Davis, *Phys. Rev. A* **31**, 3220 (1985).
3. M. D. Rosen, P. L. Hagelstein, D. L. Matthews, E. M. Campbell, A. U. Hazi, B. L. Whitten, B. MacGowan, R. E. Turner, R. W. Lee, G. Charatis, Gar. E. Busch, C. L. Shepard and P. D. Rockett, *Phys. Rev. Lett.* **54**, 106 (1985).
4. D. L. Matthews, P. L. Hagelstein, M. D. Rosen, M. J. Eckart, N. M. Ceglio, A. U. Hazi, H. Medecki, B. J. MacGowan, J. E. Trebes, B. L. Whitten, E. M. Campbell, C. W. Hatcher, A. M. Hawryluk, R. L. Kauffman, L. D. Pleasance, G. Ramback, J. H. Scofield, G. Stone and T. A. Weaver, *Phys. Rev. Lett.* **54**, 110 (1985).
5. J. E. Rogerson, R. W. Clark and J. Davis, *Phys. Rev. A* **31**, 3323 (1985).
6. J. P. Apruzese, J. Davis, D. Duston and K. W. Whitney, *JQSRT* **23**, 479 (1980).
7. J. P. Apruzese, *JQSRT* **25**, 419 (1981).
8. J. C. Weisheit, *JQSRT* **22**, 585 (1979).
9. J. P. Apruzese, J. Davis, D. Duston and R. W. Clark, *Phys. Rev. A* **29**, 246 (1984).
10. T. Holstein, *Phys. Rev.* **72**, 1212 (1947).
11. A. K. Hui, B. H. Armstrong and A. A. Wray, *JQSRT* **19**, 509 (1978).
12. E. H. Avrett and D. G. Hummer, *MNRAS* **130**, 295 (1965).
13. J. P. Apruzese and J. Davis, *Phys. Rev. A* **31**, 2976 (1985).

J. Quant. Spectrosc. Radiat. Transfer Vol. 23, pp. 479–487
Pergamon Press Ltd., 1980. Printed in Great Britain

DIRECT SOLUTION OF THE EQUATION OF TRANSFER USING FREQUENCY- AND ANGLE-AVERAGED PHOTON ESCAPE PROBABILITIES, WITH APPLICATION TO A MULTISTAGE, MULTILEVEL ALUMINUM PLASMA

J. P. APRUZESE,† J. DAVIS, D. DUSTON,† and K. G. WHITNEY‡
Naval Research Laboratory, Plasma Radiation Group, Washington, DC 20375, U.S.A.

(*Received* 17 *August* 1979)

Abstract—A formalism is developed which permits direct steady-state solution of the transfer equation using escape probabilities averaged over angle and frequency. A matrix of probability-based coupling coefficients, which are related to the kernel function K_1, is used to obtain the source function for a Doppler profile in plane-parallel geometry. Comparison is made with exact solutions, establishing the high accuracy of the technique. The method is extendable to different physical situations by simply modifying the coupling coefficients. As an example of a more realistic application of the formalism, we have solved for the ionization-excitation state of a planar aluminum plasma at 600 eV in collisional-radiative equilibrium. The results agree well with those obtained from the conventional multifrequency-multiangle formalism. Additionally, we have used the technique to gauge the effects of transport of lines connecting excited states with each other.

1. INTRODUCTION

In the literature of radiative transfer theory, much attention has been devoted to photon escape-probability concepts as a means of aiding in the interpretation of detailed solutions to the transfer equation in astrophysical and laboratory contexts. In this paper, we develop a formalism which permits utilization of such concepts to *obtain* direct solutions of the steady-state source function. When applied to a plane-parallel, Doppler-broadened medium, the technique eliminates entirely the need for either frequency or angle integration, while yielding generally excellent agreement with previous results obtained by Avrett and Hummer.[1]

2. MULTICELL RADIATIVE COUPLING EQUATIONS

If a medium which is finite in extent in at least one direction is divided into a number N of smaller regions, line photons emitted in each region will have a finite probability of being absorbed in any of the other $N-1$ regions, as well as being reabsorbed in the local region or escaping entirely from the medium. Let C_{ij} be the probability that a line photon emitted in geometrical region i traverses the distance between regions i and j and is absorbed in region j. N_{ui} will refer to the *total* upper level population of region i, and A_{ul} stands for the spontanous transition probability ($\sec^{-1}$) for the line in question. In each region i, W_i, and D_i will stand for the total collisional population and depopulation rates, respectively, of the upper level (N_{ui}). The above concepts and notation clearly imply the following equation for the rate of change of the line upper level population in region i:

$$\frac{dN_{ui}}{dt} = N_{ei}W_i + \sum_{j=1}^{N} N_{uj}A_{ul}C_{ji} - N_{ui}(A_{ul} + D_i). \tag{1}$$

The first two terms on the r.h.s. account for local collisional population of the upper level and radiative population of the level by photons emitted from all the cells j into cell i, respectively. The final term is the sum of spontaneous and collisional depopulation of the upper level. In this paper, we will confine ourselves to the case where $dN_{ui}/dt = 0$, that is, utilization of Eq. (1) to obtain the steady state upper level population in each region, which is equivalent to finding the source function when the lower level population is known. For a large class of problems, such as those treated by Avrett and Hummer,[1] the ground state (lower level)

†Science Applications, Inc., McLean, VA 22102, U.S.A.
‡Optical Sciences Division.

population is much larger than that of the upper level and the absorption coefficient is known with high accuracy. In these cases, the steady-state version of Eq. (1) requires for its solution the inversion of one $N \times N$ matrix—to solve N linear equations in N unknowns—once the C_{ji} are calculated from the absorption coefficients. When the absorption coefficient is not known *a priori*, the appropriate version of Eq. (1) must be set up for each level considered and populations for each level must be obtained iteratively using the C_{ji} calculated from the populations (hence, absorption coefficients) of the previous iteration.

Aside from the atomic constants, calculation of the C_{ji} from the absorption coefficients to permit solution of Eq. (1) forms the heart of the mathematical problem and is now detailed.

3. CALCULATION OF THE COUPLING CONSTANTS

For the case of plane-parallel geometry and Doppler profile with a spatially constant Doppler width, it has proven possible to develop very fast and extremely accurate algorithms for obtaining the C_{ji}, primarily because of the vast amount of effort by other workers which has been devoted to probability concepts for this case.

Consider a line photon emitted at a point in cell j, in the direction of cell i, in the medium. The probability P_{ji} that the photon is absorbed in cell i is given by

$$P_{ji} = \bar{P}_e(\tau_{ji}) - \bar{P}_e(\tau_{ji} + \Delta\tau_i), \tag{2}$$

where $P_e(\tau)$ is the angle-averaged probability that a photon tranverses an optical depth τ without being absorbed or scattered. In Eq. (2), τ_{ji} is the line-center optical depth from cell j to the boundary of cell i *closest* to cell j and $\Delta\tau_i$ is the optical depth of cell i itself. The practicality of the method here described is obviously dependent upon having an efficient technique for obtaining the $\bar{P}_e$'s. Holstein[2] obtained an expression for the monodirectional escape probability P_e valid for completely redistributed Doppler-profile line photons at large optical depths. We have numerically calculated the integral

$$\bar{P}_e(\tau_0) = \int_0^1 P_e\left(\frac{\tau_0}{\mu}\right) d\mu \tag{3}$$

for a large range of optical depths and have adopted the following algorithm to obtain $\bar{P}_e$ quickly and accurately.

(a) At $\tau_0 \leq 3$, a cubic spline polynomial has been fitted to the exact result at 20 points roughly equally spaced from $\tau_0 = 0$ to $\tau_0 = 3$.

(b) For $\tau_0 > 3$, the following analytic expression is accurate to better than 7% for $\tau_0 < 5$ and 4% for $5 \leq \tau_0 \leq 3 \times 10^4$;

$$\bar{P}_e(\tau_0) = \frac{0.286}{\tau_0 \sqrt{(\ln(1.95\,\tau_0))}}.$$

At this point, it should be noted that in calculating the C_{ji} coupling cells of finite width, $\bar{P}_e$ must be averaged over the cell originating the photons. This is especially important when the originating and receiving cells are adjacent since $\bar{P}_e$ can vary by an order of magnitude or more, in some cases, from the front to the back of the originating cell. This averaging process is easily accomplished by analytically integrating the above expressions across the originating cell j so that

$$C_{ji} = \frac{1}{2(\Delta\tau)_j}\left\{\int_{\tau_{ji}}^{\tau_{ji}+\Delta\tau_j} \bar{P}_e(\tau)\,d\tau - \int_{\tau_{ji}+(\Delta\tau)_i}^{\tau_{ji}+(\Delta\tau)_i+(\Delta\tau)_j} \bar{P}_e(\tau)\,d\tau\right\}. \tag{4}$$

In Eq. (4), $(\Delta\tau)_j$ and $(\Delta\tau)_i$ are the line-center perpendicular optical depths of cells j and i and τ_{ji} is the optical depth between cells j and i, measured between the two closest boundaries. The factor of 1/2 in Eq. (4) accounts for the assumed equal probability of photon emission in either direction from cell j.

4. RELATION TO THE EXACT TRANSFER EQUATION

Avrett and Hummer[1] have written the formal solution for the source function $S(\tau)$ in a plane-parallel atmosphere of optical depth T as

$$S(\tau) = (1 - P_Q) \int_0^T K_1|(t - \tau)|S(t)\,dt + P_Q B, \tag{5}$$

where B is the Planck function for the local electron temperature, P_Q is the "quenching parameter", or probability per scattering that the photon is lost from the line and K_1 is the kernel function. In Ref. 1, Avrett and Hummer developed a useful asymptotic expansion for the Doppler kernel function and showed that, for large τ (measured at line center),

$$K_1(\tau) \sim \frac{1}{4\tau^2\sqrt{(\pi \ln \tau)}}. \tag{6}$$

Inspection of Eq. (5) reveals that $K_1(\tau)$ is the analog of the discrete probability-based coupling coefficients which are used in the present treatment. $K_1(\tau)$ couples the regions of the medium together and, since the integral is carried out over τ, it is, in analogy with Eqs. (1) and (2),

$$K_1(\tau_0) = -\frac{1}{2}\frac{d\bar{P}_e}{d\tau}\bigg|_{\tau_0}. \tag{7}$$

The rate of change of the angle-averaged escape probability $\bar{P}_e$ across optical path τ_0 determines the efficiency with which photons are absorbed per unit optical depth after crossing the path τ_0.

The analytic expression

$$\bar{P}_e(\tau_0) = 0.286/\tau_0\sqrt{[\ln(1.95\,\tau_0)]}, \tag{8}$$

which we have used computationally in the calculations presented below should, when differentiated, approach Eq. (7) closely in the limit of large τ.

Differentiating Eq. (8) yields, as $\tau \to \infty$,

$$-\frac{1}{2}\frac{d\bar{P}_e}{d\tau_{\tau\to\infty}} = \frac{1}{6.993\tau^2\sqrt{(\ln \tau)}}, \tag{9}$$

(τ measured at line center)

which differs by only 1.4% from the exact expression (6). For most cases of interest, nearly all of the coupling occurs within optical depths much smaller than 3×10^4, where Eq. (8) is usually accurate to better than 4%. Also, as seen below, errors of a few per cent in the coupling matrix do not result in large source function errors when the method is applied to specific media of finite optical depth.

5. COMPARISON WITH THE TWO-LEVEL-ATOM MODEL

To explore the computational viability of the approach detailed above, we have applied Eq. (1) to a range of plane-parallel media of varying optical depths and quenching parameters. The cases presented in Figs. 1 and 2 reflect comparisons of our approach with exact solutions obtained by Avrett and Hummer.[1] The physical interpretation of the solutions has been thoroughly discussed in Ref. 1 by Avrett and Hummer. Since the media are symmetric about the midplane, the calculation has been set up by establishing 25 or 75 cells in half the medium and coupling each cell "to itself" and to others *across* the symmetry plane, as well as by direct photon coupling *within* the *same* half of the medium. In each case, the cells are spaced logarithmically in optical depth ($\Delta\tau/\tau \sim$ constant) and the optical depths of the cells close to the boundary are less than unity to allow for the anticipated rapid change of the source function

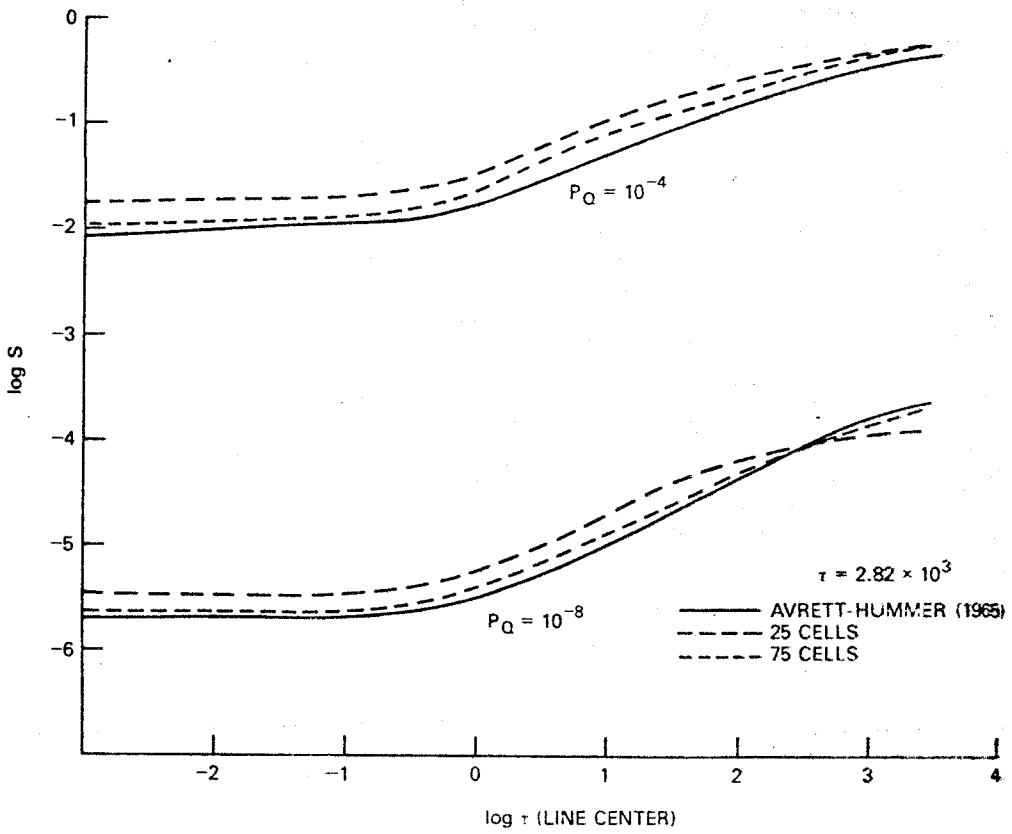

Fig. 1. The steady-state source function for a Doppler profile is shown for an optical depth of 2.82×10^3 and a Planck function $B = 1$. Results obtained from the present treatment are shown along with the exact solutions obtained by Avrett and Hummer in Ref. 1. The optical depth is measured from the center of the plane-parallel medium to the edge and at line center. Quenching parameters of 10^{-4} (effectively thick) and 10^{-8} (effectively thin) are assumed in the curves shown.

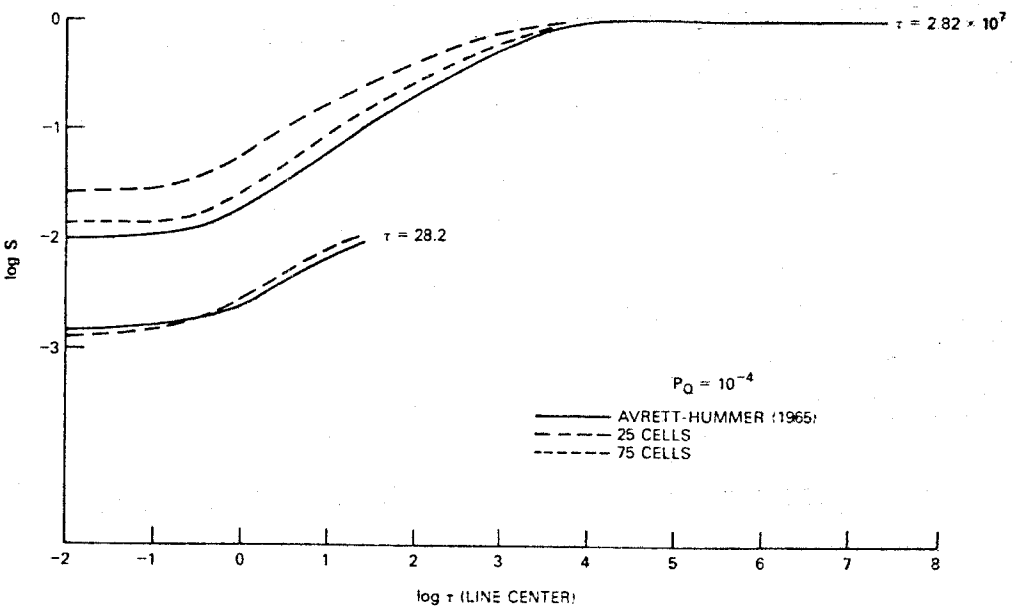

Fig. 2. As in Fig. 1, except that optical depths of 28.2 and 2.82×10^7 are shown and only one quenching parameter, 10^{-4}, is considered.

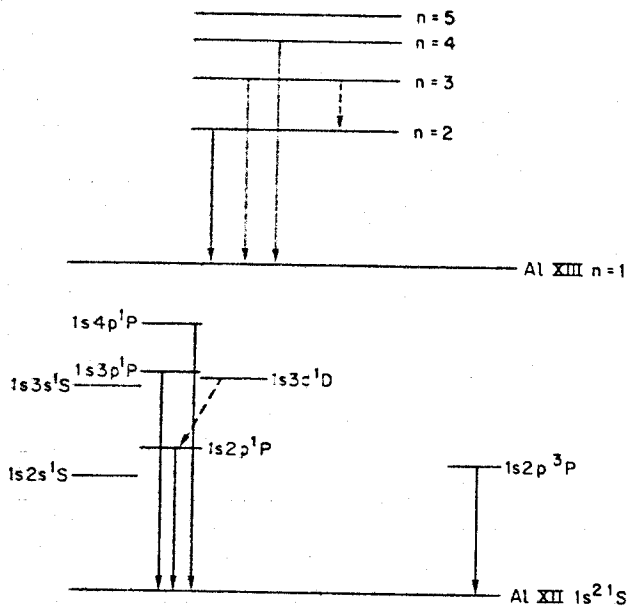

Fig. 3. The excited state structure of the Al (XII) and Al (XIII) species are indicated. Solid arrows illustrate line transported by both direct and probabilistic methods; – – – –, lines transported using the probabilistic formalism only.

near the edge of the medium. We have also computed results for 50 cells per half-slab, which are not plotted for reasons of clarity.

To obtain solutions within a few per cent of the exact values, only 25 cells need be used for optical depths of $\sim 10^2$, but 50–75 cells are necessary at $\tau \sim 10^4$. These considerations apply for both the effectively thick and the effectively thin cases. As is seen in Fig. 2, for $\tau = 2.8 \times 10^7$, the 25-cell calculation yields source functions a factor of 2.5 greater than the exact solution at small optical depths, but goes to the Planck function ($B = 1$) at the correct optical depth. The 75-cell model yields source functions about 25% too high in the nonthermalized, effectively thin regions at this very high optical depth.

6. APPLICATION TO AN ALUMINUM PLASMA

The method described here appears to hold considerable promise for computationally efficient modeling of laboratory plasmas. Detailed multi-angle, multi-frequency calculations have shown[3] that the ionization dynamics and energetics of high-temperature plasmas are significantly affected by the trapping of line and continuum radiation. Accurate simulation of such plasmas and computation of diagnostically useful line ratios requires that all optically thick lines be transported. Given these considerations, we have applied the method to determine the state of an optically thick aluminum plasma in collisional-radiative equilibrium. Specifically, we have chosen a planar plasma at a temperature of 600 eV, with a half-width of 750 μ and a total ion density of 1×10^{19} ions per cm^3. As a framework within which the technique is applied, we have used the multistage, multilevel aluminum model, which has been extensively described elsewhere.[4] The accompanying energy level diagram (Fig. 3) indicates the excited state structure and transported lines of the Al (XII) and Al (XIII) stages, which are dominant at our chosen temperature and density.† Additionally, the Al (XI) $1s^2 2s$–$2p$, $-3s$, $-3p$, $-3d$, $-4d$, and $1s2p^2$ excited states are included, with transport of the satellite line $1s^2 2p\ ^2P$–$1s2p^2\ ^2D$. This model has been extensively applied using direct methods to solve the radiative transport equation and the results will be thoroughly described for a range of plasma conditions in an upcoming paper. The salient features of the results for this particular plasma are now described in the separate sections below.

†In these calculations, photoionization has been neglected, as have radiative recombination transitions except for those onto the bare proton to form $H\,n = 1$ and $n = 2$, onto $H\,n = 1$ to form He $1s^{2\,1}S$ and $1s2p\,^3P$, and onto He $1s^{2\,1}S$ to form Li $1s^2 s^2 S$.

(a) *Comparison of Voigt and Doppler profiles*

We have performed a separate calculation for the identical plasma directly solving the transport equation with Voigt profiles for each line whose widths are determined by the total lifetime of the respective upper levels. The calculation revealed very little difference in state populations from that observed using a pure Doppler profile. At this density and size, therefore, a Doppler profile is an adequate representation of the line opacity of the plasma. At higher ion densities, the increased wings of the Voigt profile coupled with higher optical depths causes a significant lowering of the excited state densities compared to that obtained with a Doppler profile.[5]

(b) *Effect of photon pumping*

The effects of radiative pumping of the excited states on the overall state of the plasma are perceived most readily by solving for the plasma state *ignoring* radiative transfer, that is, assuming that lines which are really optically thick are instead thin. This is done in our calculation as a means of providing an initial guess as a basis for iteration to the true optically thick state. In Figs. 4 and 5, we have plotted the level densities as a function of z for helium-like (XII) and hydrogen-like (XIII) aluminum, respectively. Both the assumed thin and true optically thick solutions are shown. The most obvious feature of Figs. 4 and 5 is that the excited state densities are raised well above their optically thin values by repeated line photon scatterings (re-excitations of the level). Relative to the ground state densities, the Al (XII) $1s2p\,^1P$ population at plasma center is increased by a factor of 170 and that of the Al (XIII) $n = 2$ state is raised by a factor of 68. These values are in reasonable agreement with the

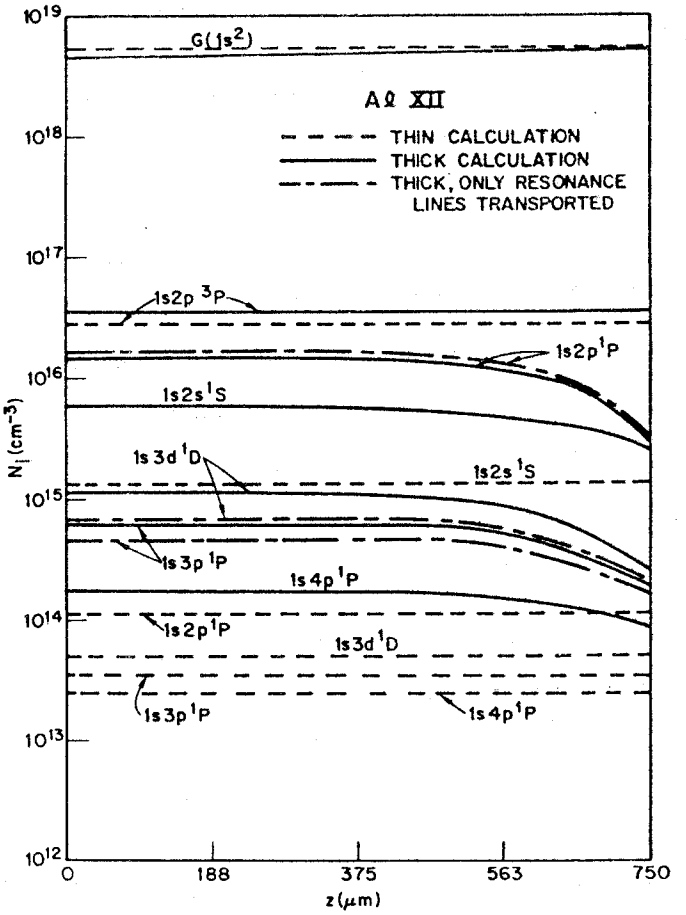

Fig. 4. Excited and ground state densities of Al (XII) are shown as functions of position in the plasma. Results are given for both thin (ignoring radiative transfer) and thick calculations. Also plotted are densities obtained when transport of excited state lines is neglected, when such densities differ appreciably from those of the full calculation.

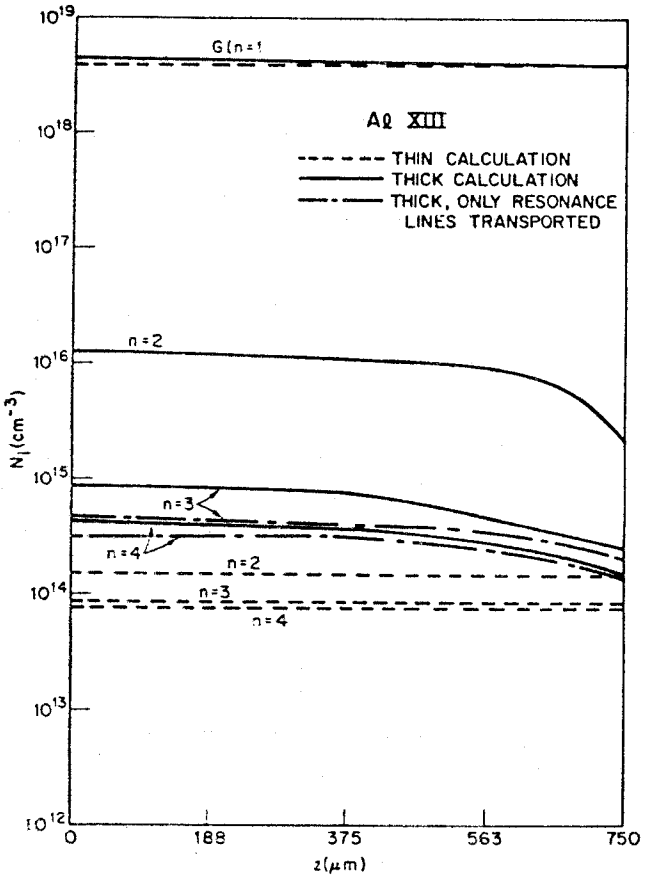

Fig. 5. As in Fig. 4, except that Al (XIII) is shown.

Table 1. Table of line power outputs (W/cm^3).

Line	Thin lines (no transport)	Thick lines; only resonance lines are transported	Full transport
Al XIII			
1-2	5.87 x 10^{11}	6.23 x 10^{11}	6.12 x 10^{11}
1-3	2.5- x 10^{10}	2.86 x 10^{10}	4.09 x 10^{10}
1-4	1.02 x 10^{1}	1.03 x 10^{10}	1.29 x 10^{10}
2-3	5.61 x 10^{9}	2.89 x 10^{10}	2.41 x 10^{10}
Al XII			
$1s^2$-$1s2p\,^3P$	1.98 x 10^{11}	1.74 x 10^{11}	1.71 x 10^{11}
$1s^2$-$1s2p\,^1P$	7.3- x 10^{11}	6.04 x 10^{11}	5.76 x 10^{11}
$1s^2$-$1s3p\,^1P$	6.1- x 10^{10}	4.12 x 10^{10}	5.42 x 10^{10}
$1s^2$-$1s-p\,^1P$	2.5- x 10^{10}	1.93 x 10^{10}	2.03 x 10^{10}
$1s2p\,^1P$-$1s3d\,^1D$	2.3- x 10^{9}	2.96 x 10^{10}	2.27 x 10^{10}

enhancement of excited state populations predicted by photon-escape theory arguments.[5] The table of line power outputs reveals that, at our chosen density of 1×10^{19}, the Al (XII) $1s^2$–$1s2p\,^1P$ line, for instance, is effectively thin. That is, even though the line center optical depth happens to be 50 in this case, the emergent power is attenuated only slightly from the optically thin value. Most of the line photons, therefore, escape the plasma after many scatterings. For the effectively thin case, N_s, the number of scatterings, is equal to P_e^{-1},[6] where P_e is the mean photon escape probability for the plasma. To produce 170 scatterings for this line requires a P_e of about 1/170 or, as revealed by Eq. (3) and the subsequent approximate expressions, an optical depth of 25. This optical depth is exactly halfway between the surface and center of the plasma, confirming the usefulness of the mean escape probability concept. Similarly, good agreement is seen for the $1\rightarrow2$ line of Al (XIII).

Figures 4 and 5 also illustrate spatial gradients in certain of the excited states of this plasma, which is of course of uniform temperature and total ion density. The gradients appear in the excited states which are controlled primarily by radiative pumping. This pumping occurs either directly to the excited state in question or to an adjoining state which is strongly collisionally coupled to the state. The $1s2p^3P$ state of Al (XII) is so strongly controlled by collisions that no significant spatial gradient appears. The gradients in the radiatively-controlled excited states are a result of the lack of pumping radiation incident on the outer edge of the plasma. This results in a lowered excited state density at the outer boundary, hence a lowered inward line photon flux emitted near the outer boundary. The interior of the plasma ($\tau \gg 1$) can thus sense the boundary of the plasma and the result is the spatial profiles of Figs. 4 and 5. These effects have been discussed in detail elsewhere.[7,8]

(c) *Effects of excited state-to-excited state photo-pumping.*

Also indicated in the power output table and plotted in Figs. 4 and 5 are the effects of photon-pumping by lines connecting excited states. This is of particular interest since the transport of such lines is usually neglected. The optical depths of such lines are strongly dependent on photon pumping of their lower levels from the ground state. Thus, they are not easily estimable and may vary extremely sensitively with temperature, density and plasma size. We plan a detailed study of these effects, which will be subsequently reported. We confine our remarks here to the specific plasma discussed above. In the particular plasma under consideration, the Al (XII) $1s2p\,^1P$–$1s3d\,^1D$ and Al (XIII) $n=2\rightarrow n=3$ lines are the only excited state lines with appreciable optical depths (0.61 and 0.38 at line center, respectively). The principal effect of neglecting transport of these lines is to underestimate, by about a factor of 2, the populations of the Al (XIII) $n=3$ and Al (XII) $1s3d\,^1D$ states. The $n=2$ level populations, which depend primarily on pumping from the ground state, are not significantly affected. Nor are the $n=4$ levels substantially increased, since lines arising from $n=2$ and $n=3$ pumping $n=4$ are optically thin in both species. The optical depths of the above mentioned $2\rightarrow3$ lines imply that about one scattering will follow collisional excitation of the lines, resulting in the doubling of the upper level populations when the transport effect is accounted for. The power output of the Al (XIII) 1–3 line increases by 43%, rather than doubling, because near the surface of the plasma the $n=3$ level's population only increases by 25%, since the pumping effects are not as large at the boundary. The level populations near the plasma edge are, of course, more important than those in the interior in determining power output. The calculated outputs of the 2–3 lines in both Al (XII) and Al (XIII) decrease when the lines are transported because of reabsorption and quenching. The optically thick calculation, however, yields a vastly greater output in these 2–3 lines than that obtained when all lines (including resonance lines) are assumed thin. This is, of course, due to resonance pumping of the $n=3$ level. It is thus seen that two-level-atom scattering theory[6] gives good results for $1\rightarrow2$ and $1\rightarrow4$ lines in this specific case but that the $1\rightarrow3$ line in Al (XIII) is significantly altered in output by radiative pumping from $n=2$.

(d) *Advantages and limitations of the formalism*

No significant differences were observed in the results obtained using conventional multi-frequency, multiangle transport compared to those yielded by the present method. Since our formalism eliminates frequency- and angle-integration, it is quite advantageous numerically.

another advantage of the coupling constant technique was achieved specifically in its use in a multistage, multilevel model. As the excited state densities build up during the "time-stepping" solution scheme,[9] the ground states change very little over 5–10 steps. Thus, the coupling constants, which depend on the ground state densities *only* for the thick resonance lines, need be updated for these lines (the vast majority of lines transported) only every 5–10 steps.

Two major limitations affect the application of the present scheme. First, efficient numerical algorithms for the cell-to-cell coupling constants have been obtained only for the case of a spatially constant line Doppler width. It is far from obvious that similar algorithms can be obtained to apply to the general case, where gradients of varying magnitudes and directions are conceivable. Second, the emitted radiation cannot be resolved in angle. This second limitation can be mitigated for the steady state case by using a detailed multi-ray procedure to compute the angular distribution of radiation once the excited state densities are determined by the more efficient coupling method. However, for a time dependent calculation calling a ray-tracing scheme every timestep to obtain angular resolution would clearly be as expensive as using the multi-frequency, multi-angle technique to directly compute the state of the plasma.

7. SUMMARY AND CONCLUSIONS

An efficient and readily adaptable technique for radiative transfer calculations has been developed which eliminates the need for angle-and-frequency integrations. A specific numerical algorithm has been developed for a Doppler profile in plane-parallel geometry and applied in a detailed analysis of multilevel coupling in a highly ionized aluminum plasma. Extension of the method to other geometries and line profiles (e.g. Voigt profiles) can be achieved by obtaining expressions for cell-to-cell photon escape and absorption probabilities for these cases. The numerical consequences of this additional physics will appear solely in the use of different coupling coefficients. Use of the technique has made possible calculations which have revealed in detail the effects of excited-state-line transport on line power outputs and level populations in an aluminum plasma. In addition, the uses and limitations of an even simpler one-cell scattering theory approach have been assessed.

Note added in proof: The 20-point cubic spline fit to $\bar{P}_e(\tau_0)$ for $\tau_0 \le 3$ is extremely accurate for both $\bar{P}_e$ and its gradient. However, a somewhat less time-consuming approximation to $\bar{P}_e(\tau_0)$ for $\tau_0 \le 3$ is given by

$$\bar{P}_e(\tau_0) = \frac{1}{1 - 1.861607\tau_0 + 0.817393\tau_0^2}$$

This expression differs from the exact P_e by a maximum of 7% for $0 \le \tau_0 \le 3$. The gradient of $\bar{P}_e$, however, is not well represented for $\tau_0 \le 0.5$. Despite this fact, use of the above simplified expression yields results which are everywhere within a few per cent of the 20-point spline results for the Avrett–Hummer cases which are illustrated in Figs. 1 and 2. Both the above expression and the one given for $\tau > 3$ in Section 3 are analytically integrable for use in Eq. (4), and are equal at the joining point $\tau_0 = 3$ to several significant figures.

Acknowledgement—This work was supported in part by the Defense Nuclear Agency.

REFERENCES

1. E. H. Avrett and D. G. Hummer, *MNRAS* 130, 295 (1965).
2. T. Holstein, *Phys. Rev.* 72, 1212 (1947).
3. J. Davis, K. G. Whitney, and J. P. Apruzese, *JQSRT* 20, 353 (1978).
4. J. Davis, and K. G. Whitney, *J. Appl. Phys.* 47, 1426 (1976).
5. J. P. Apruzese, J. Davis, and K. G. Whitney, *JQSRT* 17, 557 (1977).
6. J. P. Apruzese, J. Davis, and K. G. Whitney, *J. Phys. B.* 11, L643 (1978).
7. J. P. Apruzese, J. Davis, and K. G. Whitney, *J. Appl. Phys.* 47, 4433 (1976).
8. J. P. Apruzese, J. Davis, and K. G. Whitney, *J. Appl. Phys.* 48, 667 (1977).
9. K. G. Whitney, J. Davis, and J. P. Apruzese, *Cooperative Effects in Matter and Radiation* (Edited by C. M. Bowden, D. W. Howgate, and H. R. Robl), p. 115. Plenum Press, New York (1977).

J. Quant. Spectrosc. Radiat. Transfer Vol. 25, pp. 419–425, 1981
Printed in Great Britain.

0022-4073/81/050419-07$02.00/0
Pergamon Press Ltd.

DIRECT SOLUTION OF THE EQUATION OF TRANSFER USING FREQUENCY- AND ANGLE-AVERAGED PHOTON-ESCAPE PROBABILITIES FOR SPHERICAL AND CYLINDRICAL GEOMETRIES

J. P. APRUZESE
Science Applications, Inc., McLean, VA 22102, U.S.A.

(*Received* 2 *September* 1980)

Abstract—A previously developed technique for solving the transfer equation directly by using frequency- and angle-averaged escape probabilities in a planar, Doppler-broadened medium is generalized to encompass spherical and cylindrical geometries, as well as a Lorentz opacity profile. Two key elements permit this generalization to be made. The first is a reciprocity theorem relating the coupling constant from cell i to cell j to that from cell j to cell i. The second is the use of a universal but accurate mean angle of diffusivity.

1. INTRODUCTION

In a previous paper,[1] it has been shown that line photon-escape probabilities can be utilized to obtain exact solutions of the transfer equation in a Doppler-broadened, plane-parallel medium. The central quantity needed to apply this technique, the coupling constant C_{ij}, is equal to the probability that a photon emitted in a cell of finite size i traverses the distance between cells i and j and is absorbed in cell j. This coupling constant is simply the probability that a photon emitted in cell i reaches the closest surface of cell j minus the probability that it reaches the rear surface of cell j. The simplicity of the plane-parallel geometry allows the frequency-averaged line escape probability $P_e(\tau_0)$ to be readily angle-averaged as

$$\overline{P_e(\tau_0)} = \int_0^1 P_e\left(\frac{\tau_0}{\mu}\right) \mathrm{d}\mu. \tag{1}$$

In this paper, the plane-parallel formalism is extended to spherical and cylindrical geometries, where no such simple integral as Eq. (1) applies. In addition, the technique is extended to the case of a Lorentz profile by means of simple, but highly accurate, analytic fits to P_e. The technique developed here may also be extended to the case of a Voigt profile, provided that computationally efficient evaluations of P_e as a function of optical depth and damping constant are available.

2. CALCULATION OF THE COUPLING CONSTANTS IN SPHERICAL OR CYLINDRICAL GEOMETRY

The ease of determining photon coupling constants in planar geometry stems partially from the fact that each cell occupies 2π steradians, as measured from each other cell. In spherical or cylindrical geometry, this relation clearly does not hold and the greatest calculational difficulties are anticipated when computing the coupling constant from an outer to an inner cell, which involves complicated integration over solid angle. Use of the following reciprocity relation for coupling constants overcomes this potential difficulty:

$$C_{ji} = C_{ij}N_i/N_j, \tag{2}$$

where C_{ij} and C_{ji} are the coupling constants defined in the introduction and N_i and N_j are equal to the total number of absorbers (atoms, ions, or molecules) in cells i and j, respectively. These coupling constants are analagous to the collision probability matrix of neutron transport theory, for which a similar reciprocity relation exists.[2] To prove Eq. (2), we note that

$$C_{ji} = \sum_{m=1}^{N_i} \sum_{k=1}^{N_j} c_{km}/N_j, \tag{3}$$

where c_{km} is the coupling constant between the kth atom in cell j and the mth atom in cell i; here, the "atom" refers also to ions or molecules. Equation (3) states that the total coupling constant from cell j to cell i is the sum of the coupling constants between the individual atoms of the cells, normalized by dividing by the number of atoms in the cell originating the photon. Since the coupling constant between atom k and atom m equals that between atom m and atom k (since the photon path is the same) it follows that

$$C_{ij} = \sum_{k=1}^{N_j} \sum_{m=1}^{N_i} c_{mk}/N_i = \sum_{m=1}^{N_i} \sum_{k=1}^{N_j} c_{km}/N_i; \tag{4}$$

dividing Eq. (3) by Eq. (4) yields Eq. (2). Equation (2) allows computation of the coupling constants connecting inner to outer cells only; the outer-to-inner cell coupling constants are then obtained from the reciprocity relation.

In practice, it has proven possible to obtain quite accurate results by tracing the photon-escape probability over a single mean angle of diffusivity from the inner to the outer cell. In Fig. 1, this process is graphically illustrated for coupling cell 2 to cell 4. The ray along which the P_e are calculated intersects the radius at the mean diffusivity angle $\bar{\theta}$, the value of which is discussed below. Since the escape probabilities must be averaged over the originating cell, the coupling constant is given by

$$C_{24} = \frac{1}{\tau_a} \int_0^{\tau_a} [P_e(\tau_b + \tau) - P_e(\tau_b + \tau_c + \tau)]\, d\tau, \tag{5}$$

where τ_a, τ_b, and τ_c, are optical depths (see Fig. 1) and P_e refers to the photon-escape probability along the chosen mean ray and is not angle-averaged. Simple but quite accurate expressions for the single ray escape probability have been fitted as a function of line center optical depth τ for Doppler and Lorentz profiles. For a Doppler profile, the following expressions are used:

$$P_e(\tau) = 1/(1 + 0.65\tau + 0.29\tau^2), \qquad \tau \leqslant 5.18; \tag{6a}$$

$$P_e(\tau) = \frac{0.546847}{\tau\sqrt{\ln\tau}}, \qquad \tau > 5.18. \tag{6b}$$

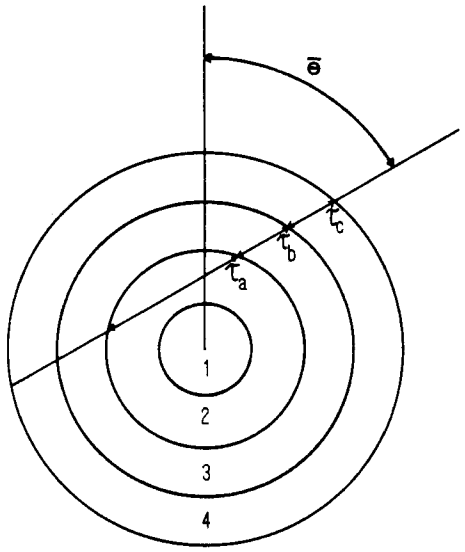

Fig. 1. The method used to obtain coupling constants connecting an inner cell (2) with an outer cell (4) is illustrated for spherical or cylindrical geometries. The quantities τ_a, τ_b, and τ_c are the line-center optical depths along the indicated segments. Escape probabilities are calculated along the ray at a mean angle θ intersecting the radial at the center of the inner cell. The determination of $\bar{\theta}$ is discussed in the text.

Equation (6a) deviates from the exact Doppler profile escape probability in its domain by a maximum of 4% and the maximum deviation of Eq. (6b) is also 4%. Holstein[3] obtained the exact expression corresponding to Eq. (6b) for $\tau \to \infty$, viz.

$$P_e(\tau) = \frac{1}{\tau\sqrt{(\pi \ln\tau)}}, \tag{6c}$$

which differs from Eq. (6b) by just over 3%. Equation (6b) is utilized rather than the infinite-optical-depth limit of Eq. (6c) because it is more accurate at lower optical depths where more photon coupling occurs and it joins smoothly at $\tau = 5.18$ to the polynomial expression given in Eq. (6a).

For a Lorentz profile, the analytic approximations to P_e are also divided into two line-center optical depth domains on each side of $\tau = 5.18$. For $\tau \leqslant 5.18$,

$$P_e(\tau) = 1./(1. + 0.58572\tau) \tag{7a}$$

is adopted whereas, for $\tau > 5.18$, the following expression is used (which is the exact limit as $\tau \to \infty$[3]):

$$P_e(\tau) = 1/\sqrt{(\pi\tau)}. \tag{7b}$$

Equations (7a) and (7b) differ from the exact escape probability by a maximum of 8%; in both cases, the maximum discrepancy occurs in the vicinity of $\tau = 5.18$. For $\tau < 3.4$ and $\tau > 13$, the accuracy is better than 3%. The two expressions join smoothly at $\tau = 5.18$.

A principal question related to the use of this technique involves the specific angle $\bar{\theta}$ along which the rays should be traced to obtain the best coupling constants. These coupling constants are directly calculated only from the inner cells to outer cells, as discussed above. Any photon emitted from cell i whose radius of curvature is much less than that of cell j will travel nearly along the local radius when it reaches the vicinity of the outer cell j. Therefore, the value of C_{ij} obtained is quite insensitive to the choice of $\bar{\theta}$ when cell i is located close to the origin relative to cell j. If the angle $\bar{\theta}$ is chosen to provide high accuracy when cells i and j have nearly the same radius of curvature (i.e., in the planar limit), the scheme represented in Fig. 1 will automatically scale the C_{ij} correctly as cell i draws closer to $r = 0$. Therefore, $\bar{\theta}$ will be chosen to give accurate results for the planar limit, viz,

$$P_e\left(\frac{\tau}{\cos\bar{\theta}}\right) \cong \int_0^1 P_e\left(\frac{\tau}{\mu}\right) \mathrm{d}\mu. \tag{8}$$

Since, according to Eqs. (6) and (7), $P_e(\tau)$ depends on the line profile, the best value of $\bar{\theta}$ will also be profile-dependent. In this paper, the analysis will be confined to the cases of astrophysical and low-to-medium density laboratory plasmas whose line cores are dominated by Doppler broadening and whose line wings are Lorentzian. Surprisingly, the $\bar{\theta}$ which are chosen according to these considerations also give excellent results for a pure Lorentz line (see below).

The value of $\bar{\theta}$ which gives exact results for large optical depth is readily obtainable from Eqs. (6c), (7b), and (8). For a Doppler profile, letting $\bar{\mu} = \cos\bar{\theta}$ where $\ln\tau \gg \ln\mu$.

$$\frac{\bar{\mu}}{\tau\sqrt{[\pi \ln(\tau/\bar{\mu})]}} = \int_0^1 \frac{\mu\,\mathrm{d}\mu}{\tau\sqrt{[\pi \ln(\tau/\mu)]}}$$

$$= \frac{1}{\tau\sqrt{(\pi \ln\tau)}}\int_0^1 \mu\,\mathrm{d}\mu = \frac{1}{2\tau\sqrt{(\pi \ln\tau)}} \Rightarrow \bar{\mu} = \frac{1}{2}. \tag{9}$$

For a Lorentz profile, we must have

$$\sqrt{\left(\frac{\bar{\mu}}{\pi\tau}\right)} = \int_0^1 \sqrt{\left(\frac{\mu}{\pi\tau}\right)} \mathrm{d}\mu \Rightarrow \bar{\mu} = \frac{4}{9}. \tag{10}$$

The errors in the angle-averaged escape probability at large τ associated with a choice of $\bar{\mu} = \cos \bar{\theta}$ are, therefore, for Doppler and Lorentz profiles

$$\frac{\Delta P_e}{P_e}(\text{Doppler}) = 2\bar{\mu} - 1 \tag{11a}$$

and

$$\frac{\Delta P_e}{P_e}(\text{Lorentz}) = \frac{3}{2}\sqrt{(\bar{\mu})} - 1, \tag{11b}$$

respectively. Thus, choice of a $\bar{\mu}$ which is not exact at large τ leads to a constant error and not a constantly increasing error in P_e. Since the photoexcitation of line radiation is generally dominated by absorption of photons in the high-opacity Doppler core which are generally emitted within a few optical depths, the condition of high accuracy at large τ cannot be the sole criterion for the choice of $\bar{\mu}$. To guide this choice, errors in the Doppler P_e associated with use of various $\bar{\mu}$ have been calculated numerically for more modest optical depths. It is found that, for $1.5 \leq \tau < \infty$, $\bar{\mu}$ somewhat larger than 0.5 is required for exact agreement; a maximum $\bar{\mu}$ of 0.54 is required at $\tau = 3.4$. For $\tau < 1.5$, $\bar{\mu}$ smaller than 0.5 is required for exact agreement; as $\tau \to 0$, all $\bar{\mu}$ tend toward the correct $P_e = 1$. In view of these results, the value $\bar{\mu} = 0.51$ has been adopted for the following calculations. This value is accurate to 2% at $\tau = \infty$ and is slightly better than $\mu = 0.50$ for the important coupling region $1.8 \leq \tau \leq 25$. Moreover, even for a pure Lorentz profile, $\bar{\mu} = 0.51$ is accurate to better than 10% for all $\tau > 1$ and, according to Eq. (11b), is accurate to 7% as $\tau \to \infty$. No claim is made here that $\bar{\mu} = 0.51$ is the best choice under all circumstances. It is, however, a reasonable choice for our applications and yields good agreement with exact solutions of several diverse transfer problems. There is also a self-compensating aspect of the coupling constant technique for solving transfer equations which tends to reduce the sensitivity of the results to the choice of $\bar{\mu}$. The source function in each cell is established by photon coupling from within the cell and from other cells. If, for example, the chosen $\bar{\mu}$ is too large, the escape probabilities from other distant cells to the cell in question will be overestimated, generally leading to an overestimate of the coupling. However, the overestimate of P_e from the local cell partially compensates for this effect by reducing the local coupling which is proportional to $(1 - P_e)$. As is shown in Ref. 1, small errors in the coupling matrix do not result in large source-function errors.

As a precaution and to ensure consistency, the N coupling constants from cell i to other cells j are renormalized, as will now be described. First, the probability of escape from the entire plasma from cell i is calculated along the chosen $\bar{\theta}$. This quantity, P_i, must be equal to $1 - \sum_{j=1}^{N} C_{ij}$. It can be found to be slightly different because of numerical noise; therefore the C_{ij} are multiplied by the factor needed to make this sum over j equal to $(1 - P_i)$.

3. COMPARISON OF RESULTS WITH EXACT SOLUTIONS

The most meaningful test of our formalism is the following: how closely are we able to reproduce exact solutions of basic transfer problems in spherical or cylindrical geometry? The technique of using the coupling constants, once obtained, to solve for the steady-state line source function is described in Ref. 1. Briefly, the equation for the steady-state upper level population of a two-level atom in cell i is written as

$$\frac{dN_{ui}}{dt} = 0 = N_{l,i} W_i + \sum_{j=1}^{N} N_{uj} A_{ul} C_{ji} - N_{ui}(A_{ul} + D_i), \tag{12}$$

where N_{ui} and N_{li} are the upper and lower level populations of cell i, respectively, A_{ul} is the spontaneous transition probability (sec^{-1}), C_{ji} is the coupling constant from cell j to cell i as previously defined, and W_i and D_i are the total collisional population and depopulation rates, respectively, of the upper level in cell i. For the cases studied, the absorption coefficient and

hence the C_{ij} are fixed. A fixed absorption coefficient also allows the lower level populations N_{li} to be written in terms of the upper level population N_{ui} for a two-level atom since

$$k \propto N_l B_{lu} - N_u B_{ul},$$

where the B are the stimulated absorption and emission probabilities. Solving Eq. (12) for the two-level-atom, thus reduces to an inversion of an $N \times N$ matrix. The requirements imposed on the W, D and A_{ul} stem from the fact that the comparison cases specify the Planck function spatially and also the quenching parameter $P_{q'}$ which is the ratio of collisional to total decay of the upper state. The W, D and A_{ul} of Eq. (12) are chosen to be compatible with the specified Planck function and quenching parameter. The C are calculable from the fixed absorption coefficient.

The results of comparisons with previously published solutions to basic transfer problems are presented in Figs. 2–4. In Fig. 2, comparison is made with the hollow-sphere calculations of Kunasz and Hummer.[4] The cylindrical calculations of Avery *et al.*[5] are repeated with the present method and the results exhibited in Fig. 3. The comparisons of Fig. 3 are confined to cases where the cylinders are long compared to their widths, since the present techniques apply to infinite cylinders. Finally, since the mean diffusivity angle used in these calculations is most accurate for a Doppler profile, a comparison with pure Lorentz profile solutions obtained by Avrett and Hummer[6] is presented in Fig. 4 to determine the applicability of $\bar{\mu} = 0.51$ to Lorentz and hence to Voigt profiles.

It is self-evident from the three figures that the method yields very good accuracy. The maximum deviation of the calculated source function from that given by accurate solutions is 25% for the cylindrical and spherical cases, with most of the curves lying within 15% of the previously obtained values. For the planar Lorentz profile, the maximum error is 10%. Although exact solutions are clearly not obtained by using this formalism, the accuracy is more than acceptable considering that the technique obviates entirely the need for either frequency- or angle-integration. As might be expected, the largest number of cells required to obtain this accuracy (75) was needed for the stringent test of the Kunasz–Hummer cases, where both the absorption coefficient and the Planck function vary as r^{-2}. The smallest number of cells was

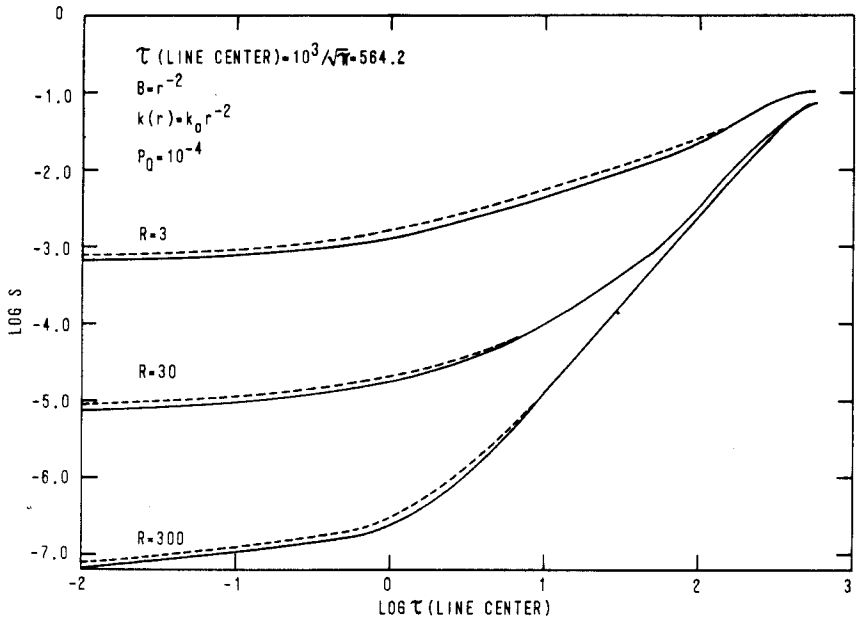

Fig. 2. Steady-state source functions obtained by use of the presently described method (dotted line) are compared with exact spherical solutions obtained in Ref. 4 by Kunasz and Hummer (solid line). In obtaining the present approximate solutions, we used 75 cells logarithmically spaced in τ. The radius of the inner boundary of each hollow sphere is 1 and each curve is labeled by the radius of the outer boundary. The Planck function and absorption coefficient vary as indicated. A pure Doppler profile is assumed with line center optical depth $10^3/\sqrt{\pi} = 564.2$.

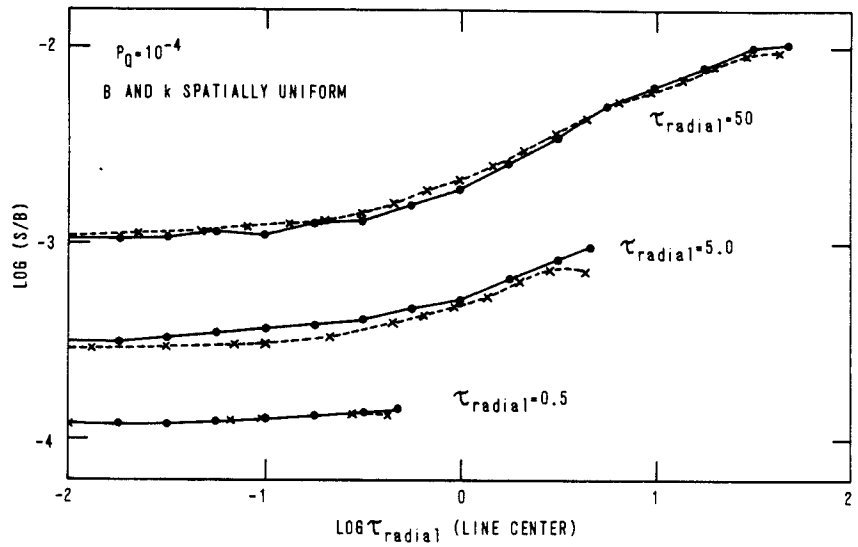

Fig. 3. Steady-state source functions obtained by the present method (dotted lines) are compared with the Monte Carlo cylindrical solutions obtained in Ref. 5 (solid lines). The curves are differentiated by line center optical depth along the cylinder radius. In obtaining the present approximate solutions, 20 cells logarithmically spaced in τ were used, with selected cells plotted. The lines connecting the points are intended to guide the eye rather than to suggest interpolated values.

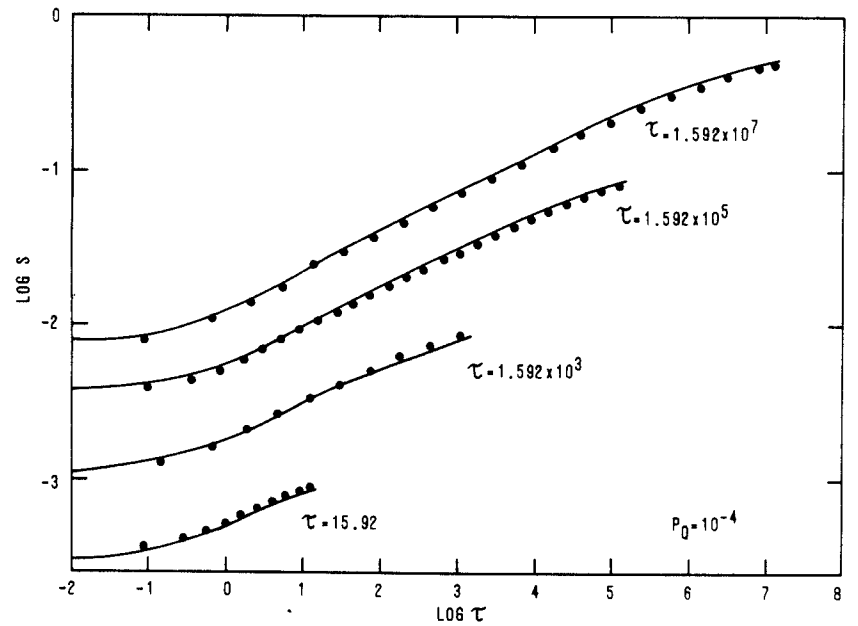

Fig. 4. Steady-state source functions obtained by the present method (circles) are compared with the exact planar. Lorentz-profile solutions obtained in Ref. 6 (solid lines). The Planck function is assumed to be spatially uniform and equal to 1. The number of cells (logarithmically spaced in τ) presently used is 10, 10, 25, and 40, in ascending order of optical depth. The value of the source function at the center of each cell is indicated by the circles, except for $\tau = 1.592 \times 10^7$, for which every other cell plus the innermost cell are plotted.

used (10) in calculating the low-optical-depth planar Lorentz cases for which the Planck function was spatially uniform.

4. SUMMARY AND CONCLUSIONS

It has been shown that the use of escape probability techniques to obtain solutions to the radiative transfer equation may be extended from planar to cylindrical and spherical geometries. The formalism for line transfer requires that the line-profile-averaged photon escape probability along a ray be known as a function of optical depth. Convenient analytic fits

to these quantities are given for the cases of pure Doppler and pure Lorentz line profiles. The technique presented is quite advantageous numerically in that it eliminates frequency and angle integrations at small cost in accuracy. It is also readily adaptable to different physical situations. For instance, for high-density plasmas for which Stark broadening dominates the line profile, the escape probability formulae given by Weisheit[7] could be readily employed.

Perhaps the main drawback to our approach (and the principal area for further work on this technique) is that profile-averaged escape probabilities are most easily obtained and used for spatially constant line profiles. When density and/or temperature gradients are present in such degree as to affect $P_e(\tau)$ significantly, the accuracy of this approach will deteriorate. Obtaining fits to $P_e(\tau)$ in the presence of such gradients is the only way to restore accuracy.

Acknowledgment—This work was supported by the Naval Research Laboratory.

REFERENCES

1. J. P. Apruzese, J. Davis, D. Duston, and K. G. Whitney, *JQSRT* **23**, 479 (1980).
2. I. Carlvik, *Proceedings of the Third International Conference on the Peaceful Uses of Atomic Energy*, Vol. 2, p. 225. International Atomic Energy Agency, Vienna (1965).
3. T. Holstein, *Phys. Rev.* **72**, 1212 (1947).
4. P. B. Kunasz and D. G. Hummer, *MNRAS* **166**, 16 (1974).
5. L. W. Avery, L. L. House, and A. Skumanich, *JQSRT* **9**, 519 (1969).
6. E. H. Avrett and D. G. Hummer, *MNRAS* **130**, 295 (1965).
7. J. C. Weisheit, *JQSRT* **22**, 585 (1979).

J. Quant. Spectrosc. Radiat. Transfer Vol. 34, No. 5, pp. 447–452, 1985
Printed in Great Britain.

0022–4073/85 $3.00+.00

AN ANALYTIC VOIGT PROFILE ESCAPE PROBABILITY APPROXIMATION

J. P. APRUZESE
Naval Research Laboratory, Plasma Physics Division, Plasma Radiation Branch,
Washington, DC 20375, U.S.A.

(*Received* 9 *April* 1985)

Abstract—An efficient analytic Voigt profile escape probability approximation is presented and compared to exact numerical calculations. Using this analytic approximation, the two-level-atom source function is also computed for optically thick media, which have been previously evaluated exactly by Avrett and Hummer. Comparison with a more realistic laboratory plasma case also validates the usefulness of the approximation for economical modeling of radiation transport in optically thick plasmas.

1. INTRODUCTION

Laser-produced plasmas often contain dozens to hundreds of optically thick lines, and, in many cases, the hydrodynamic evolution of such plasmas is significantly affected by radiation transported in these lines.[1,2] Realistically accounting for such effects can be especially important in plasma X-ray lasing media,[3,4] where maintenance of population inversions often depends sensitively on plasma conditions. Substantial effects of radiation transport on ion-beam driven plasmas may also occur.[5]

Unfortunately, exact multifrequency transport calculations for each optically thick line are often computationally impractical. To alleviate this problem and still provide for the maximum attainable realism in the photon transport, a technique[6,7] requiring the equivalent of only one frequency per line has been tested and benchmarked successfully against previously published two-level-atom solutions which represent a stringent test of numerical radiation transport algorithms. This technique uses a computationally efficient method for obtaining photon escape probabilities averaged over the line profile. Such methods have been described in Refs. 6 and 7 for Doppler and Lorentz profiles. While such profiles may be adequate for some applications,[6] the more general Voigt profile is more appropriate for a large class of moderate density, optically thick plasmas. The line profiles of very high-density plasmas, such as those produced in spherically symmetric laser driven compressions, are dominated by the Stark effect. Weisheit[8] has given escape probability formulae for such Stark profiles. It is the purpose of this paper to present a simple analytic escape probability parameterization for the Voigt profile, and to access its accuracy by direct comparison with previously published exact solutions, as well as with a specific optically thick plasma which has also been solved by a multifrequency radiation transport technique.

2. VOIGT PROFILE ESCAPE PROBABILITY

The technique presented in Refs. 6 and 7, and referred to above, employs as its central quantity the coupling-constant matrix C_{ij}, which is the probability that a line photon emitted in spatial cell i will be absorbed by cell j. There is one coupling-constant matrix for each line. Each pair of cells in the medium is connected by a ray, as in Fig. 1. The choice of ray angle is described in Ref. 7. In the notation of Fig. 1, the coupling constant C_{ij} is the difference in mean escape probabilities from the originating cell i to the front and rear of the receiving cell j, i.e.

$$C_{ij} = \frac{0.5}{\tau_i}\int_0^{\tau_i}[P_e(\tau + \tau_B) - P_e(\tau + \tau_B + \tau_j)]\,d\tau \quad , \tag{1}$$

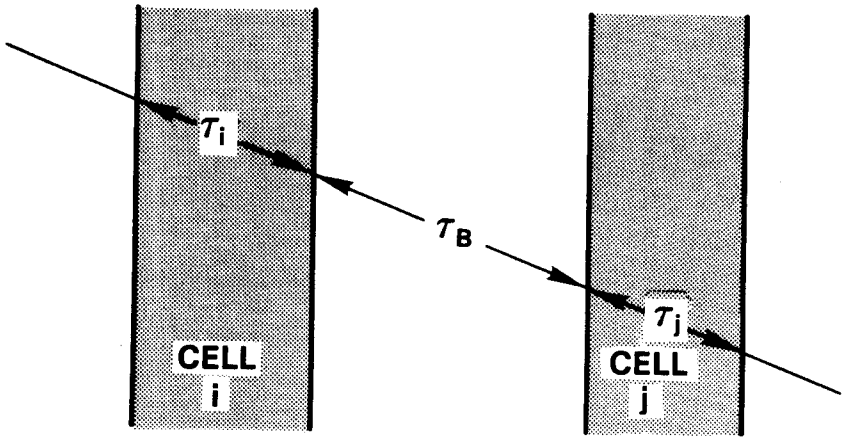

Fig. 1. Notation for photon ray tracing between a pair of cells in the medium, as applied in Eq. (1).

where the integral averages P_e over the originating cell i. In Eq. (1), the escape probability $P_e(\tau)$ is the probability that the line photon travels at least through line-center optical depth τ along the ray before being absorbed, and is given by

$$P_e(\tau) = \int \phi(\nu)\, e^{-\tau\phi(\nu)/\phi(0)}\, d\nu \quad . \tag{2}$$

In Eq. (2), $\phi(\nu)$ is the line profile function, normalized to a frequency integral of unity. The integral in Eq. (2) extends over the line profile, and $\phi(0)$ refers to the profile function at line center. Throughout this work, complete frequency redistribution is assumed. Once $P_e(\tau)$ is obtained, the C_{ij} are given by Eq. (1). The steady-state line source function can then be obtained by direct matrix inversion when the collision rates are fixed.[6,7] When the nonlinear electron density dependence affects the collision rates (as in a multistage, multilevel plasma calculation), an iteration procedure[9] is required to obtain the steady-state line source functions. The actual form of $P_e(\tau)$ for the Voigt profile is now considered.

The Voigt function is given by

$$U(a,\nu) = \frac{a}{\pi^{3/2}} \int_{-\infty}^{+\infty} \frac{e^{-y^2}\, dy}{(\nu - y)^2 + a^2} \quad . \tag{3}$$

In Eq. (3), ν is the frequency displacement from line center in Doppler widths, and a is the line-broadening parameter, which is the ratio of the sum of the inverse lifetimes of the upper and lower levels to 4π times the Doppler width. In general, the far wings of this profile are Lorenztian, i.e.

$$U(a,\nu)_{\nu\to\infty} = a/\pi\,(\nu^2 + a^2) \quad . \tag{4}$$

The transition point between a Doppler-like core and Lorentzian wings depends on a; the smaller the value of the broadening parameter, the further in frequency from line center that this transition occurs. In the limit of large optical depth, only the far wings contribute to the photon escape probability. In that case, Eq. (4) for $U(a,\nu)$ may be substituted into Eq. (2) for $\phi(\nu)$. The resulting elementary integral yields, for $a \ll 1$,

$$P_e(a,\tau) = \pi^{-1/4}\,(a/\tau)^{1/2} \tag{5}$$

as the exact optically thick limit of the Voigt escape probability for line-center optical depth τ and broadening parameter $a \ll 1$. Not surprisingly, Eq. (5) shows that a Voigt profile in the limit of large optical depth is characterized by $P_e \sim \tau^{-1/2}$, as is the case for a pure Lorentz profile.[10]

Extensive exact numerical calculations of $P_e(a,\tau)$ have been performed to determine the feasibility of simple fits to the escape probability for a Voigt profile. The simplicity of the fit is important in maintaining the computational efficiency of the coupling constant technique by which the radiative transfer is solved. Different expressions for many regimes in a and τ would substantially negate the desired economy of the method. It was not found possible to produce simple formulae with the same degree of accuracy—a few percent—achieved for Doppler and Lorentz profiles as described in Ref. 7. However, the expressions given below will be shown to be valuable for some purposes.

Two contrasting regimes in the broadening parameter a were delineated by the results of the exact calculations. For $a < 0.49$ three different regions in line-center optical depth characterized by different functional behavior in P_e exist. For $\tau \leq 1$, photons emitted throughout the line core have a significant change of escape. Between $\tau = 1$, and a critical optical depth denoted by τ_c, the behavior of the escape probability is Doppler-like ($P_e \sim \tau^{-1}$). Finally, above τ_c, only the far Lorentzian wings contribute, and the escape probability exhibits pure Voigt functional variation, i.e. $P_e \sim \tau^{-1/2}$ as in Eq. (5). Empirically, it is found that

$$\tau_c = 0.83/a(1+\sqrt{a}) \quad . \tag{6}$$

The expressions for P_e for $a < 0.49$ are

$$P_e(\tau) = \begin{cases} (1 + 1.5\tau)^{-1} & (\tau \leq 1) \quad , & (7a) \\ 0.4/\tau & (1 < \tau \leq \tau_c) \quad , & (7b) \\ 0.4/\sqrt{\tau_c \tau} & (\tau > \tau_c) \quad . & (7c) \end{cases}$$

For broadening parameters $a \geq 0.49$, the Lorentz wings are strong enough so that essentially no Doppler-like behavior occurs. In this case, the expressions adoped are

$$P_e(\tau) = \begin{cases} (1 + \tau)^{-1} & (\tau \leq 1) & (8a) \\ 0.5/\sqrt{\tau} & (\tau > 1) \quad . & (8b) \end{cases}$$

Needless to say, the sharp divisions are somewhat artificial and are set primarily to minimize inaccuracies while maintaining computational efficiency. The Voigt optical depth τ refers to the line center; it may be readily computed from the pure Doppler line-center optical depth using the ratio of polynomials given by Hui, Armstrong and Wray.[11] Equations (7) and (8) apply for all optical depths and have been tested against exact escape probability calculations for $a \geq 10^{-3}$.

Comparisons of the escape probabilities given by Eqs. (6)–(8) with exact calculations are presented in Figs. 2 and 3, for various broadening parameters ranging from 0.01 to 1.0. The simplified expressions are typically accurate to 20%, although this deteriorates to nearly 40% for a small range near $\tau = 2$ at a broadening parameter of 0.32. In some other regimes, however, the formulae are nearly exact, as shown in Figs. 2 and 3. The expressions (7) and (8) are analytically integrable; therefore the coupling constants for use in radiative transfer applications are directly obtainable using Eq. (2). The accuracy and usefulness of the present formulae to solve radiative transfer problems is now considered.

3. APPLICATION TO RADIATIVE TRANSFER

The new expressions and technique have been applied to two specific radiative transfer problems. The first of these is the planar two-level-atom case, first solved exactly by Avrett and Hummer.[12] Their chosen parameters represent a stringent test for numerical transfer algorithms, as the optical depths are high and the photon collisional quenching parameter (10^{-4}) is quite low. This latter quantity (designated here as P_Q and by Avrett and Hummer

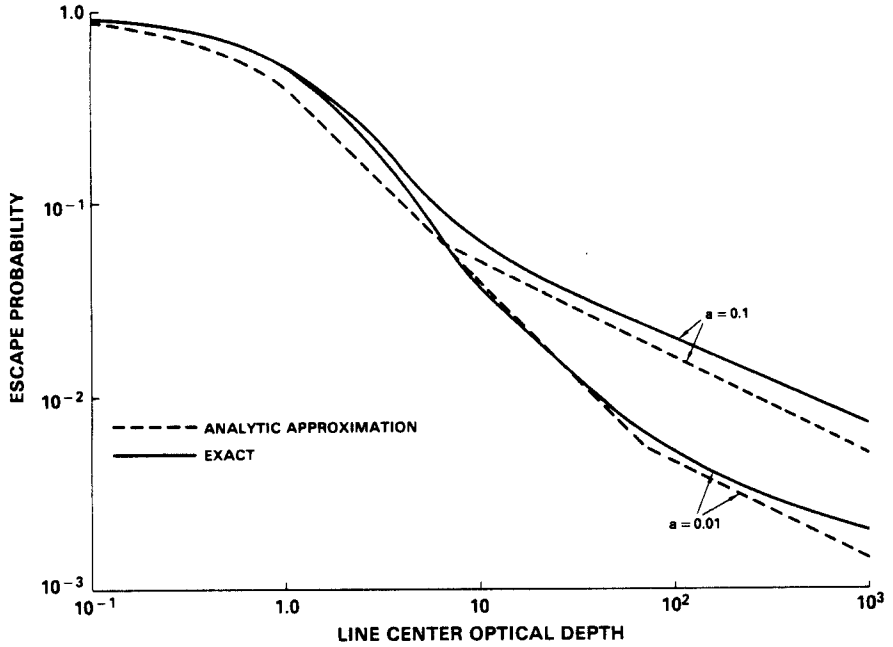

Fig. 2. Comparison of the present analytic approximation for the Voigt profile escape probability as a function of line-center optical depth with exact numerical results. Voigt-broadening parameters (a) of 0.01 and 0.1 were assumed.

as ϵ) is the probability per line photon absorption that the photon is destroyed collisionally rather than reemitted. A low P_Q coupled with high-optical-depth results in many photon scatterings. In such situations the line source function is dominated by photoexcitation, and its evaluation is therefore very sensitive to the accuracy of the radiative transfer approximation employed. Figure 4 shows comparisons of the line source function obtained with the present approximate technique to the exact results of Ref. 12. The Planck function is unity throughout the planar medium, and the line-center optical depth varies from 28 to 2.8×10^5. The Voigt-broadening parameter is 0.01. As expected, the accuracy of the approximation deteriorates with increasing optical depth. At $\tau = 28$, the maximum dis-

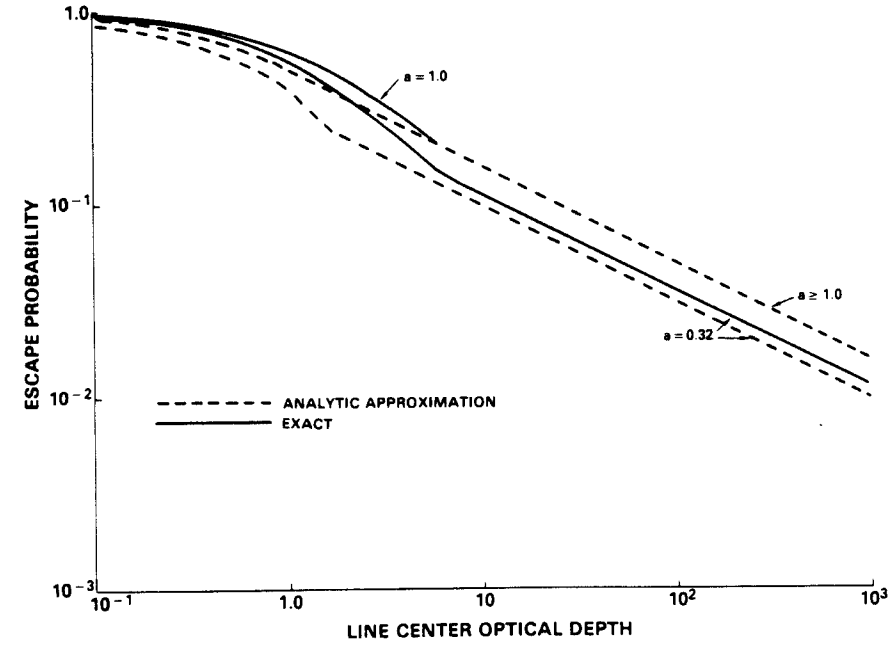

Fig. 3. As in Fig. 2, except that Voigt-broadening parameters of 0.32 and 1.0 were assumed in the exact calculation. The approximation gives the same escape probability for all $a \geq 1.0$.

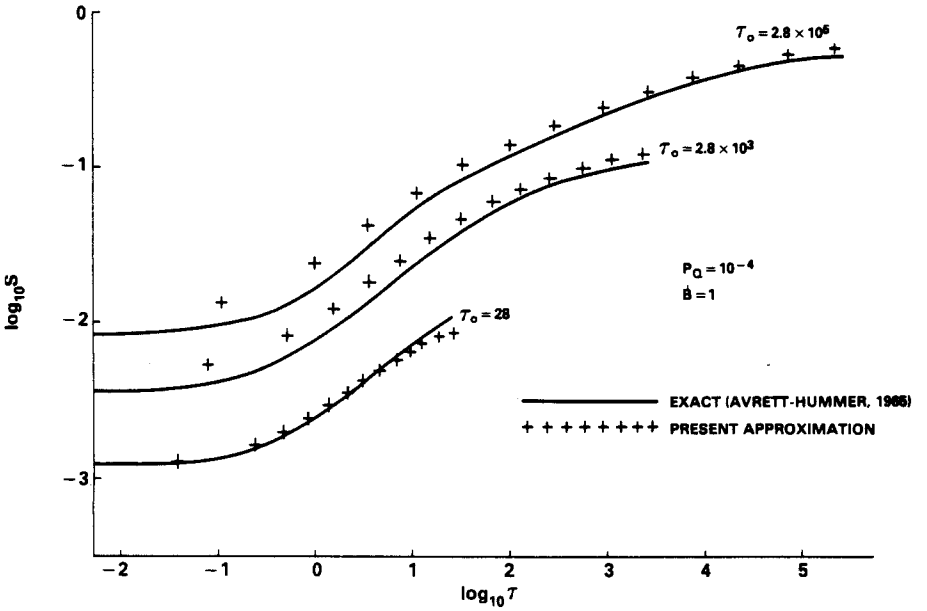

Fig. 4. A 25-cell calculation of the two-level-atom source function for planar media, using the present analytic Voigt profile escape probability approximation, is plotted along with the exact solutions of Avrett and Hummer. For the approximate calculation, every other cell is plotted as a cross. Collisional quenching probability per scattering is 10^{-4} in all cases, and the Planck function is normalized to unity. The line-center optical depths τ_0 are as indicated. The Voigt-broadening parameter is 0.01.

crepancy in the source function is 20%, but most points lie within 5% of the exact solution. In the present calculation 25 cells have been employed, and the odd-numbered cells are plotted in Fig. 4. By contrast, at $\tau = 2.8 \times 10^5$, the maximum error due to the approximation is 45%, with most points lying 10–30% from the exact source function. This latter high-optical-depth case, coupled with $P_Q = 10^{-4}$, is rarely encountered in laboratory plasmas and therefore represents a more difficult transfer problem than the present algorithm would usually be called upon to solve.

The superior accuracy of the approximation when employed in laboratory plasma simulations is demonstrated in Table 1. The problem to which the algorithm has been applied is this: Given a planar sodium plasma of fixed ion density 10^{20} cm^{-3}, electron and ion temperature of 400 eV and thickness 0.4 cm, what are the steady-state ionic stage and excited level population distributions? Table 1 shows the ratio of the helium-like Na X $1s\,2p\ ^1P_1$ level population to that of the Na X $1s^2\ ^1S_0$ ground state as a function of position in the plasma. The ratio is also presented as obtained from an exact multifrequency calculation, and is directly proportional to the line source function. A description of the atomic model and rate calculations is given in Ref. 13. The optical depth of the $1s^2\ ^1S_0 - 1s\,2p\ ^1P_1$ line is 2.6×10^2, measured from planar midpoint to outer edge. The Voigt-broadening parameter is 0.03, and $P_Q = 0.24$ for the line. As evident from Table 1 that the moderate optical depth and collisional quenching parameter, characterizing this plasma, render the transfer problem less sensitive to errors of approximation in P_e than the Avrett–Hummer cases. The maximum deviation in the line source function from the multifrequency solution is 4% near the outer boundary.

4. SUMMARY AND CONCLUSIONS

The frequency-averaged line photon escape probability for a Voigt opacity profile has been parameterized with simple analytic expressions given by Eqs. (6)–(8). The escape probability as a function of optical depth obtained from the expressions has been tested against exact calculations for Voigt-broadening parameters $\geq 10^{-3}$. Typical comparisons with the exact results are given in Figs. 2 and 3. The line source functions obtained by

Table 1. Fractional population (f) of the helium-like sodium $1s\ 2p\ ^1P_1$ excited level relative to that of the $1s^2\ ^1S_0$ ground state is tabulated as a function of distance from the boundary of a planar sodium plasma. The plasma is assumed to be homogeneous with full width 0.4 cm, ion density 10^{20} cm^{-3} and temperature of 400 eV. The last point in the table is at the plasma midpoint (0.2 cm); the populations are symmetric about this point.

Distance from the boundary (cm)	$f(1s2p\ ^1P_1) / f(1s^2\ ^1S_0)$	
	multifrequency	probabilistic
2.4×10^{-2}	4.22×10^{-3}	4.37×10^{-3}
6.0×10^{-2}	5.60×10^{-3}	5.67×10^{-3}
1.0×10^{-1}	5.92×10^{-3}	5.93×10^{-3}
1.6×10^{-1}	6.01×10^{-3}	6.02×10^{-3}
2.0×10^{-1}	6.01×10^{-3}	6.02×10^{-3}

employing these expressions in conjunction with the radiative transfer algorithm described in Refs. 6 and 7 are shown in Fig. 4 and Table 1, along with exact solutions.

The approximation presented here will probably find the most appropriate applications in laboratory plasma simulations, especially where dozens to hundreds of optically thick lines influence the plasma's hydrodynamic behavior. For most plasma applications, the calculated source function will probably deviate only a few percent from exact results, although errors of 20% are conceivable for optical depths exceeding 10^3 combined with small ($< 10^{-3}$) collisional quenching parameters. However, the realism of this approximation is greatly superior to such often-employed cruder approximations as local thermodynamic equilibrium or Planck or Rosseland mean opacities used in a diffusion approximation. Finally, for very large optical depth ($> 10^5$), low-density astrophysical applications the source function errors generated by the present method can approach 45% in certain cases. Since the present technique assumes complete frequency redistribution over the line profile, additional errors due to partial redistribution effects are also likely for extremely low-density cases. Therefore this technique is not recommended in such instances unless the errors are tolerable in the context of the problem being attacked.

Acknowledgement—This work was supported by the U.S. Defense Advanced Research Projects Agency.

REFERENCES

1. D. Duston, R. W. Clark, J. Davis and J. P. Apruzese, *Phys. Rev. A* **27**, 1441 (1983).
2. D. Duston, R. W. Clark and J. Davis, *Phys. Rev. A* **31**, 3220 (1985).
3. M. D. Rosen, P. L. Hagelstein, D. L. Matthews, E. M. Campbell, A. U. Hazi, B. L. Whitten, B. MacGowan, R. E. Turner, R. W. Lee, G. Charatis, Gar. E. Busch, C. L. Shepard and P. D. Rockett, *Phys. Rev. Lett.* **54**, 106 (1985).
4. D. L. Matthews, P. L. Hagelstein, M. D. Rosen, M. J. Eckart, N. M. Ceglio, A. U. Hazi, H. Medecki, B. J. MacGowan, J. E. Trebes, B. L. Whitten, E. M. Campbell, C. W. Hatcher, A. M. Hawryluk, R. L. Kauffman, L. D. Pleasance, G. Ramback, J. H. Scofield, G. Stone and T. A. Weaver, *Phys. Rev. Lett.* **54**, 110 (1985).
5. J. E. Rogerson, R. W. Clark and J. Davis, *Phys. Rev. A* **31**, 3323 (1985).
6. J. P. Apruzese, J. Davis, D. Duston and K. W. Whitney, *JQSRT* **23**, 479 (1980).
7. J. P. Apruzese, *JQSRT* **25**, 419 (1981).
8. J. C. Weisheit, *JQSRT* **22**, 585 (1979).
9. J. P. Apruzese, J. Davis, D. Duston and R. W. Clark, *Phys. Rev. A* **29**, 246 (1984).
10. T. Holstein, *Phys. Rev.* **72**, 1212 (1947).
11. A. K. Hui, B. H. Armstrong and A. A. Wray, *JQSRT* **19**, 509 (1978).
12. E. H. Avrett and D. G. Hummer, *MNRAS* **130**, 295 (1965).
13. J. P. Apruzese and J. Davis, *Phys. Rev. A* **31**, 2976 (1985).

APPLICATIONS OF X-RAY TRANSPORT EFFECTS IN DENSE, HIGHLY IONIZED PLASMAS

J. P. APRUZESE

NAVAL RESEARCH LABORATORY

COLLABORATORS

J. DAVIS

D. DUSTON

K. WHITNEY

R. CLARK

P. KEPPLE

F. COCHRAN

C. COULTER

A. HAUER

P. BURKHALTER

OUTLINE OF THE PRESENTATION

- BASIC EFFECTS AND TERMINOLOGY
- NUMERICAL APPROACH
- IMPACT ON X-RAY DIAGNOSTICS
- EFFECT ON PLASMA ENERGETICS
- LINE OPACITY BROADENING AND RESONANT PUMPING

IMPORTANCE OF X-RAY OPACITY IN PLASMAS

TYPICAL LINE CROSS SECTION

$\sigma \simeq 10^{-16}$ (OSC) ($\lambda(\mathring{A})$) $(AMU/T)^{1/2}$ cm^2

OSC $\simeq$ 0.5; $\lambda = 1200/Z^2$; AMU = 2Z

$T = 4\ Z^2$ eV

$\sigma \simeq \frac{4.2 \times 10^{-14}}{Z^{2.5}}$ (7×10^{-17} cm^2 for Al, requiring only 1.5μm for $\tau = 1$ at ion density 10^{20} cm^{-3})

BOUND-FREE CROSS SECTION

$\sigma \simeq 7.9 \times 10^{-18} \frac{n}{Z^2}$ (4.7×10^{-20} cm^2 for Al XIII n = 1, requiring 0.2 cm for $\tau = 1$ at the above density)

FREE-FREE CROSS SECTION

assume $N_e = N_I\ Z$

$\sigma \simeq 1.3 \times 10^{-49}\ Z^3\ T_{eV}^{-1/2}\ \lambda\ (\mathring{A})^3\ N_I$ cm^2

(3.8×10^{-25} cm^2 for Al, requiring 2.6×10^4 cm for $\tau = 1$ at ion density 10^{20} cm^{-3})

EQUATION OF TRANSFER ALONG A RAY

$$\frac{\partial I_\nu}{\partial s} = j_\nu - k_\nu I_\nu - \frac{1}{c}\frac{\partial I_\nu}{\partial t}$$

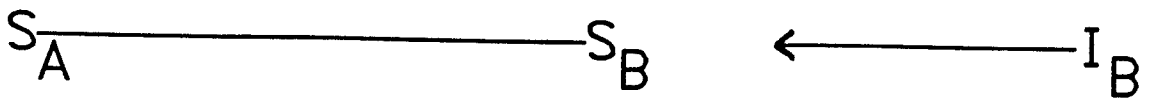

TIME-INDEPENDENT FORMAL SOLUTION

$$\tau_\nu(S) = \int_{S_A}^{S} k_\nu(x)dx$$

$$I_\nu(S_A) = \int_{S_A}^{S_B} j_\nu(s)e^{-\tau_\nu(s)}ds + I_{\nu B}e^{-\tau_{\nu B}}$$

LINE PHOTON ESCAPE PROBABILITY P_E

$$P_E = \int_{\text{PROFILE}} \phi(\nu) \, \text{EXP} \, (-\tau_0 \, \phi(\nu) / \phi(0)) \, d\nu$$

WHERE

$$\int_{\text{PROFILE}} \phi(\nu) \, d\nu = 1$$

AND τ_0 = LINE CENTER OPTICAL DEPTH

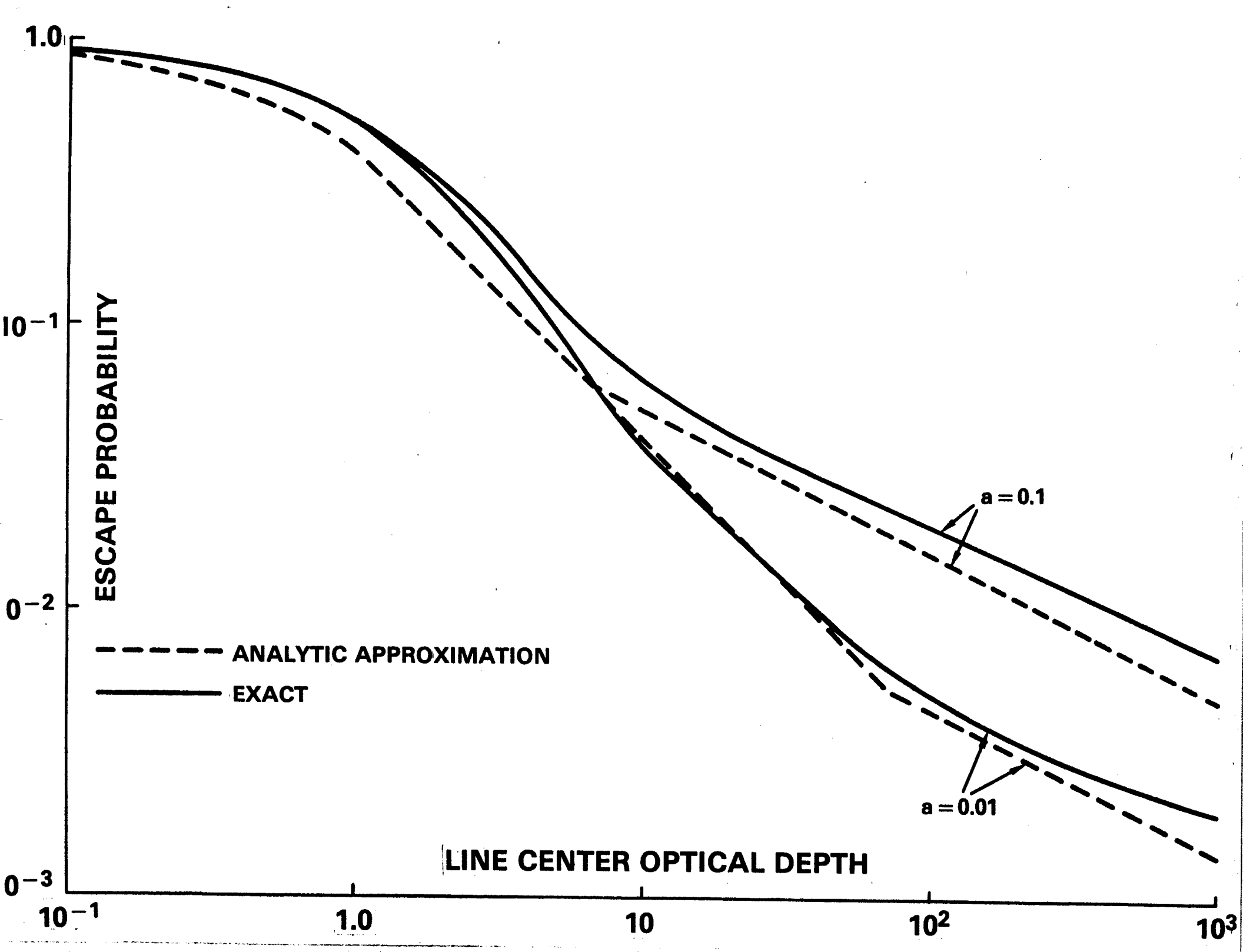
1.0
10^{-1}
0^{-2}
0^{-3}
ESCAPE PROBABILITY
ANALYTIC APPROXIMATION
EXACT
a = 0.1
a = 0.01
LINE CENTER OPTICAL DEPTH
10^{-1}
1.0
10
10^2
10^3

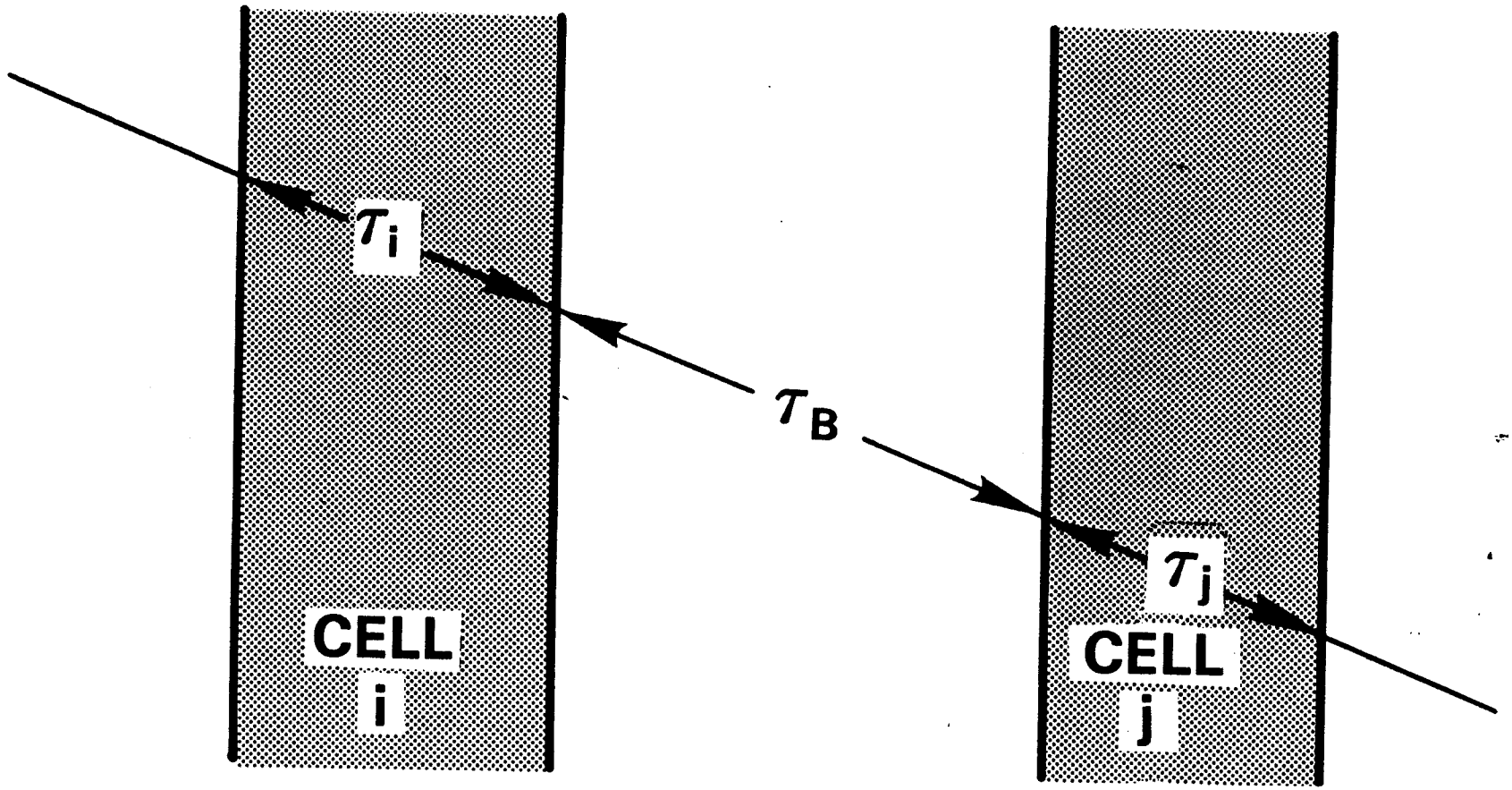
τ_i
τ_B
τ_j
CELL
i
CELL
j

COUPLING CONSTANT CALCULATION

$$C_{ij} = \frac{0.5}{\tau_i} \int_0^{\tau_i} \left[P_e\left(\tau+\tau_B\right) - P_e\left(\tau+\tau_B+\tau_j\right) \right] d\tau$$

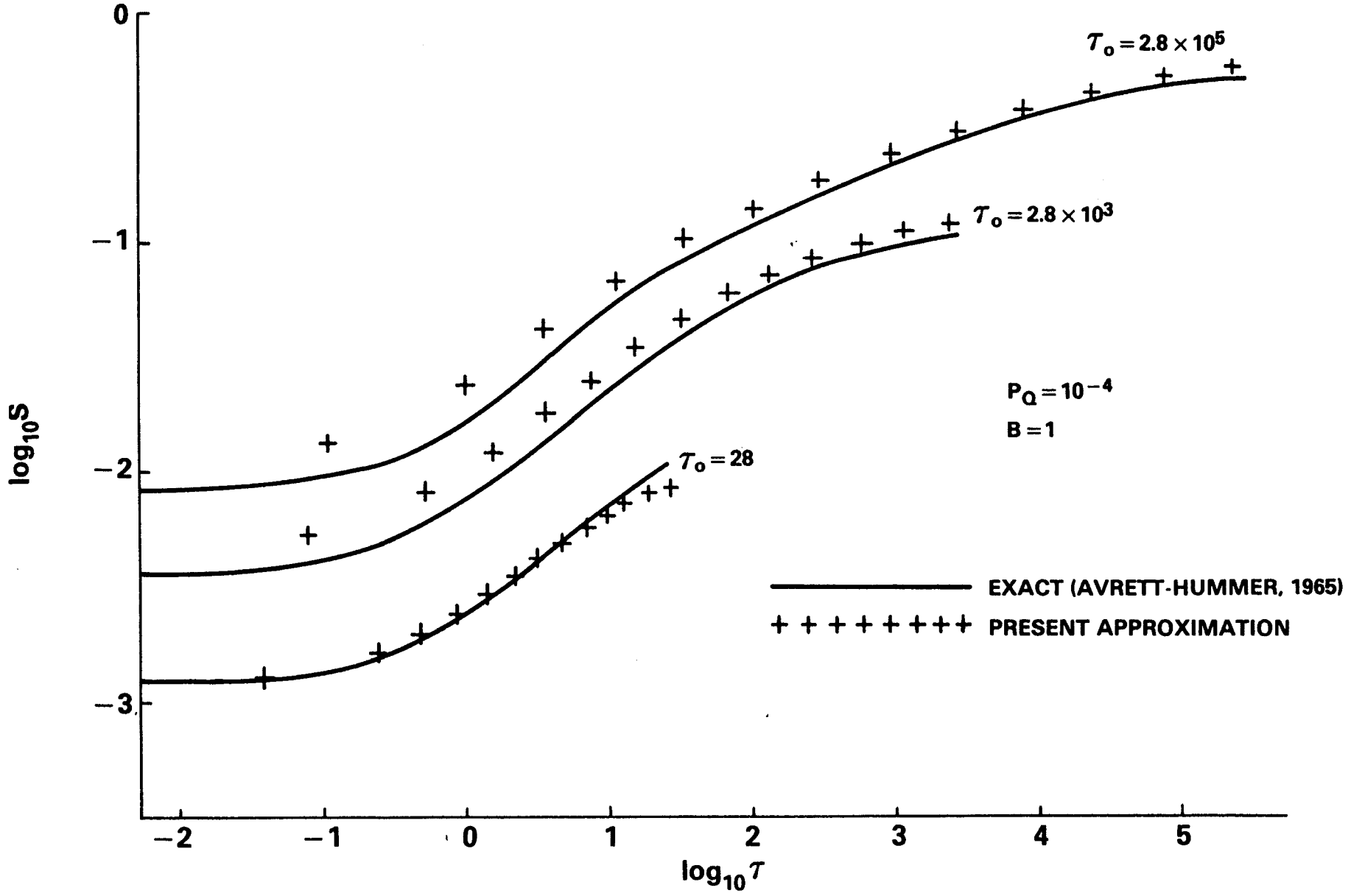
0
−1
−2
−3
$\log_{10} S$
−2
−1
0
1
2
3
4
5
$\log_{10} \tau$
$\tau_o = 2.8 \times 10^5$
$\tau_o = 2.8 \times 10^3$
$\tau_o = 28$
$P_Q = 10^{-4}$
B = 1
EXACT (AVRETT-HUMMER, 1965)
PRESENT APPROXIMATION

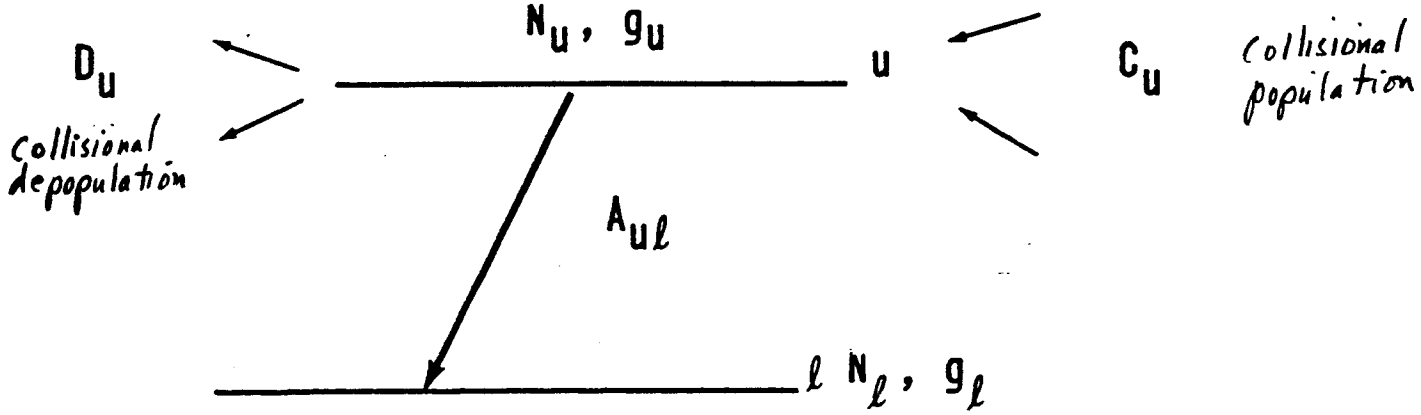

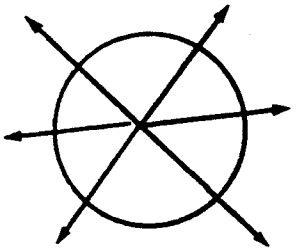

P_e

$$P_q = \frac{D_u}{A_{ul} + D_u}$$

quenching probability

STEADY STATE CONDITION FOR UPPER LEVEL

$$C_u = N_u \, (D_u + A_{ul} P_e) \quad (cm^{-3} \ sec^{-1})$$

thin case $P_e = 1$

$$\frac{N_u \ (thick)}{N_u \ (thin)} = \frac{D_u + A_{ul}}{D_u + A_{ul} P_e} = \frac{1}{P_q + P_e (1 - P_q)} \geqslant 1$$

ULTIMATE LINE PHOTON ESCAPE PROBABILITY

$$P_u = \frac{N_u \, A_{ul} \, P_e}{C_u \, (1 - P_q)} = \frac{P_e}{P_q + P_e (1 - P_q)}$$

ESCAPE PROBABILITY AFTER SCATTERINGS (P_u)

Al XII $1s^2$-$1s2p$ ^1P LINE, T = 300 eV

λ = 7.76Å

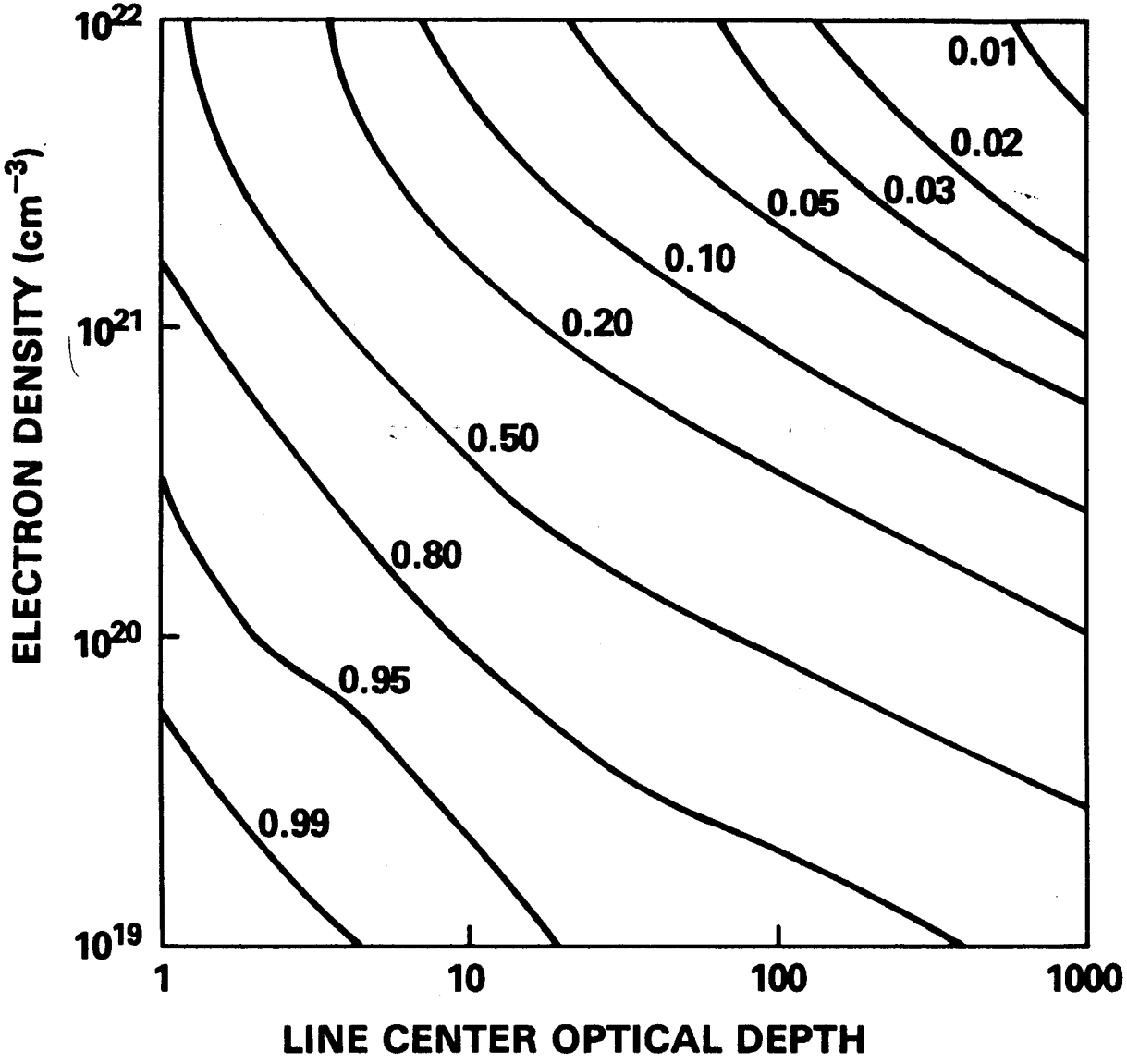

ESCAPE PROBABILITY AFTER SCATTERINGS (P_e)

Cu XXVIII $1s^2$-$1s2p$ ^1P LINE, T = 1600 eV

$\lambda = 1.48$Å

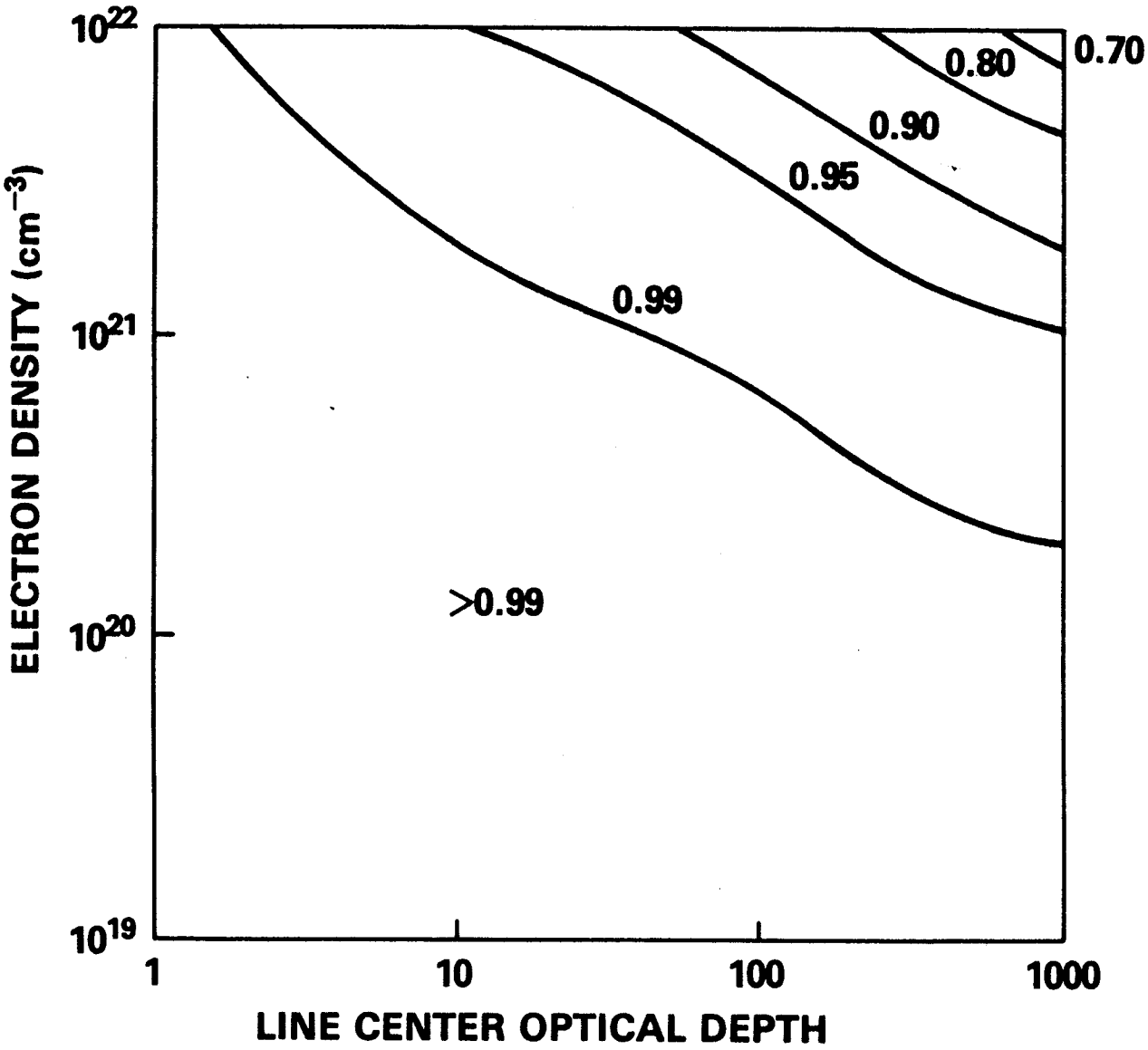

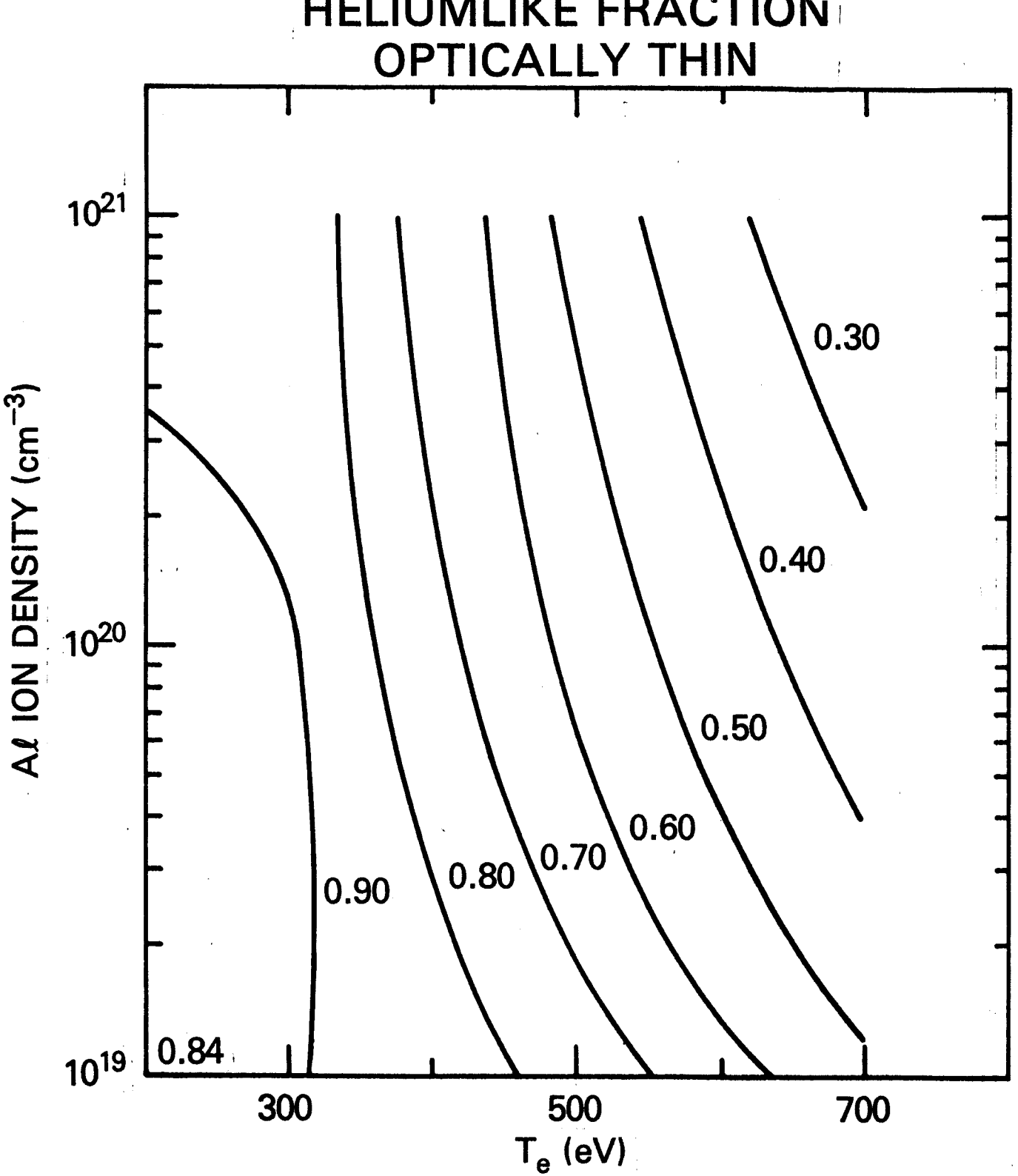
HELIUMLIKE FRACTION
OPTICALLY THIN
10^{21}
10^{20}
10^{19}
Aℓ ION DENSITY (cm^{-3})
0.30
0.40
0.50
0.60
0.70
0.80
0.90
0.84
300
500
700
T_e (eV)

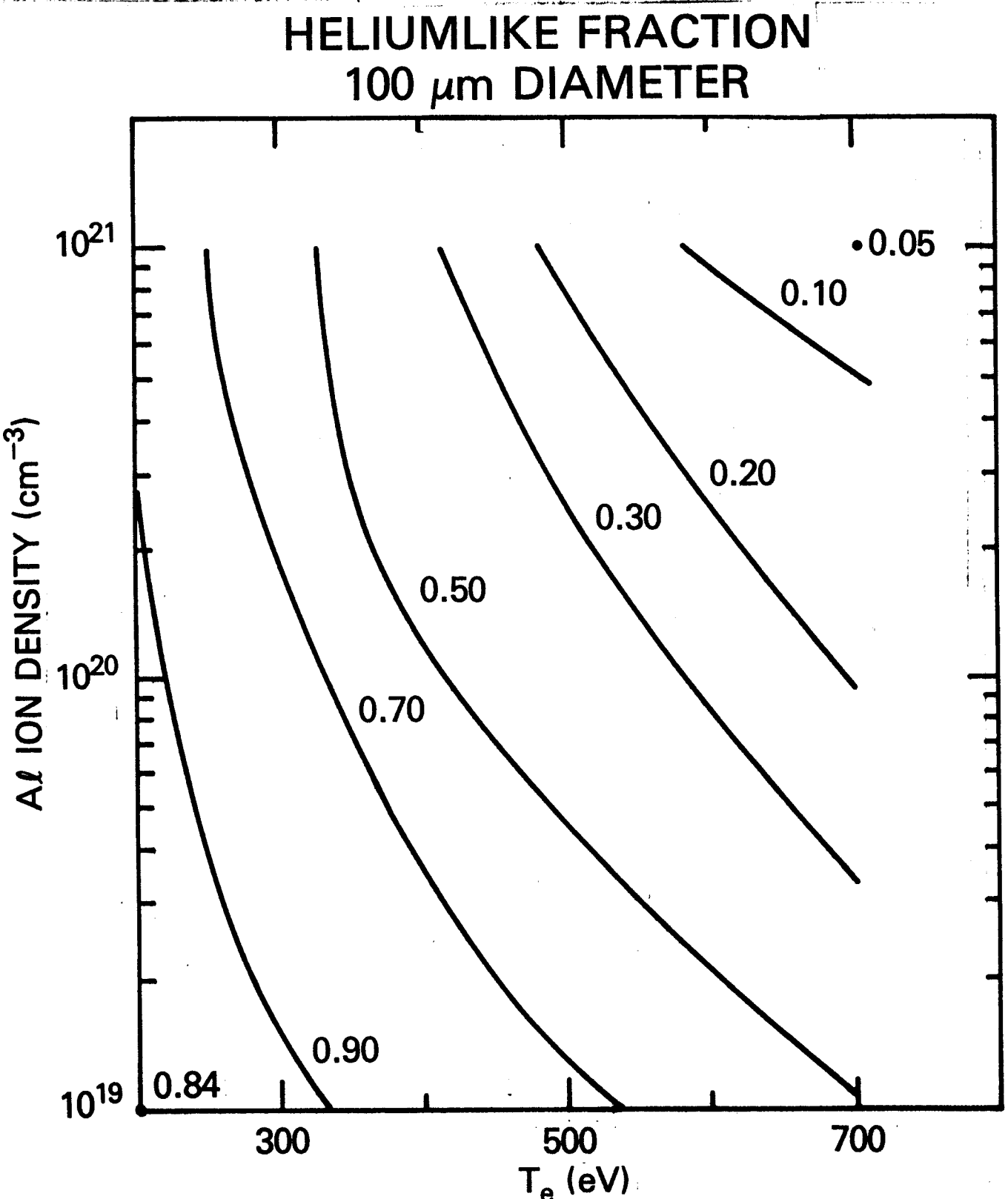
HELIUMLIKE FRACTION
100 μm DIAMETER
Aℓ ION DENSITY (cm⁻³)
10²¹
10²⁰
10¹⁹
•0.05
0.10
0.20
0.30
0.50
0.70
0.84
0.90
300
500
700
Te (eV)

STARK LINEWIDTH AS A DENSITY DIAGNOSTIC FOR SPHERICAL COMPRESSED PLASMAS

OPTICALLY THIN CASE

WIDTH OF PROFILE, $\Delta\upsilon \sim N_e^{2/3}$

OPTICALLY THICK CASE

$\tau_\upsilon \sim N_e r \sim N_e^{2/3}$ (FIXED SPHERICAL MASS) $\left(r \sim \frac{1}{N_e^{1/3}}\right)$

WIDTH OF PROFILE, $\Delta\upsilon \sim \tau_\upsilon = 1$ POINT ON LINE WING

$$\tau_\upsilon \sim N_e^{2/3}\, \phi(\Delta\upsilon) \sim N_e^{2/3} \left(\frac{\Delta\upsilon}{N_e^{2/3}}\right)^{-9/4}$$

$$\Delta\upsilon(\tau_\upsilon = 1) \sim N_e$$

OPACITY BROADENING PLUS STARK WIDTH PLUS DEPENDENCE OF τ_υ ON N_e

$\Longrightarrow$ ENHANCED SENSITIVITY OF $\Delta\nu$ ON N_e

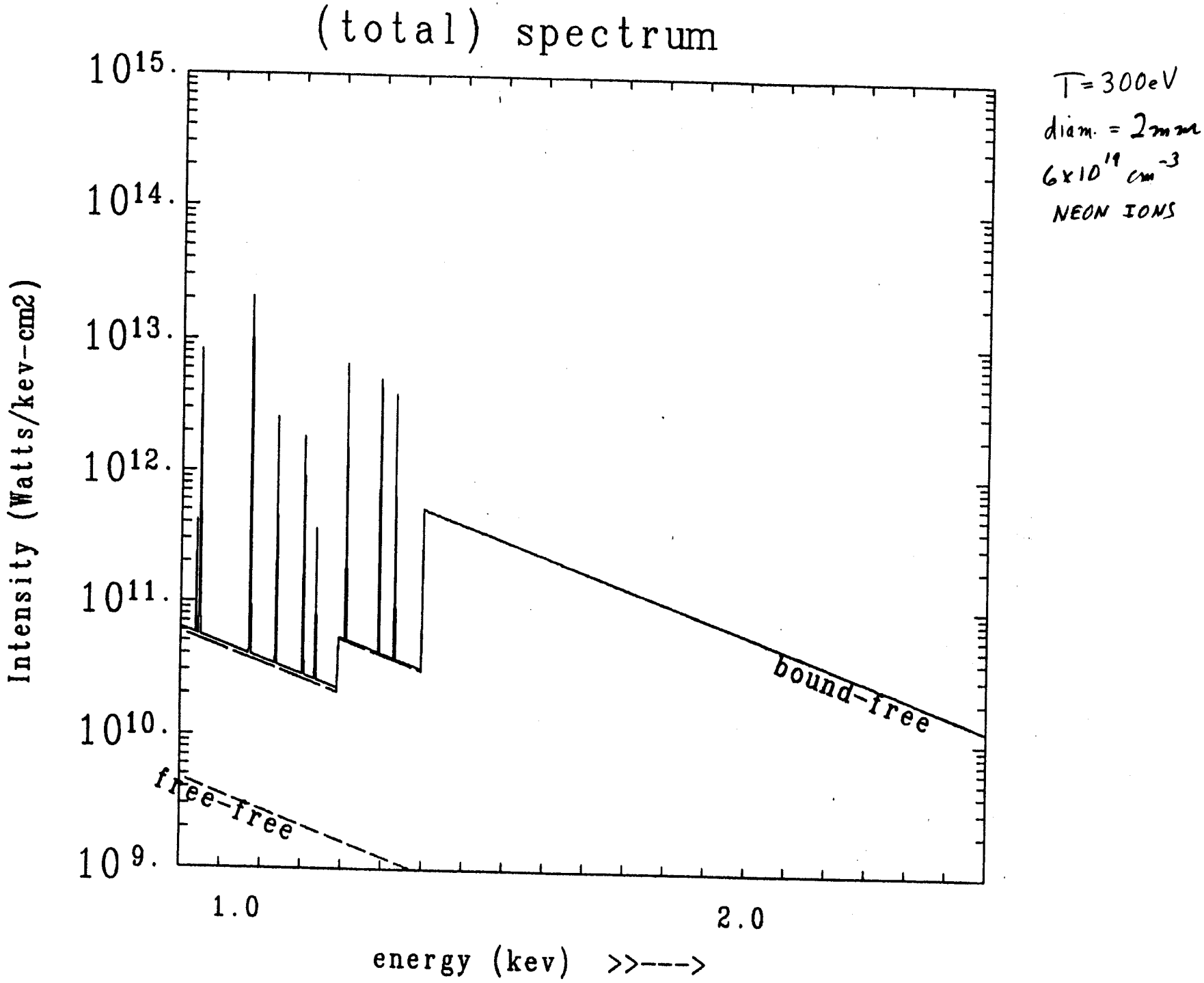
(total) spectrum
T=300eV
diam. = 2mm
6x10^19 cm^-3
NEON IONS
Intensity (Watts/kev-cm2)
10^15.
10^14.
10^13.
10^12.
10^11.
10^10.
10^9.
bound-free
free-free
1.0
2.0
energy (kev) >>--->
NEON

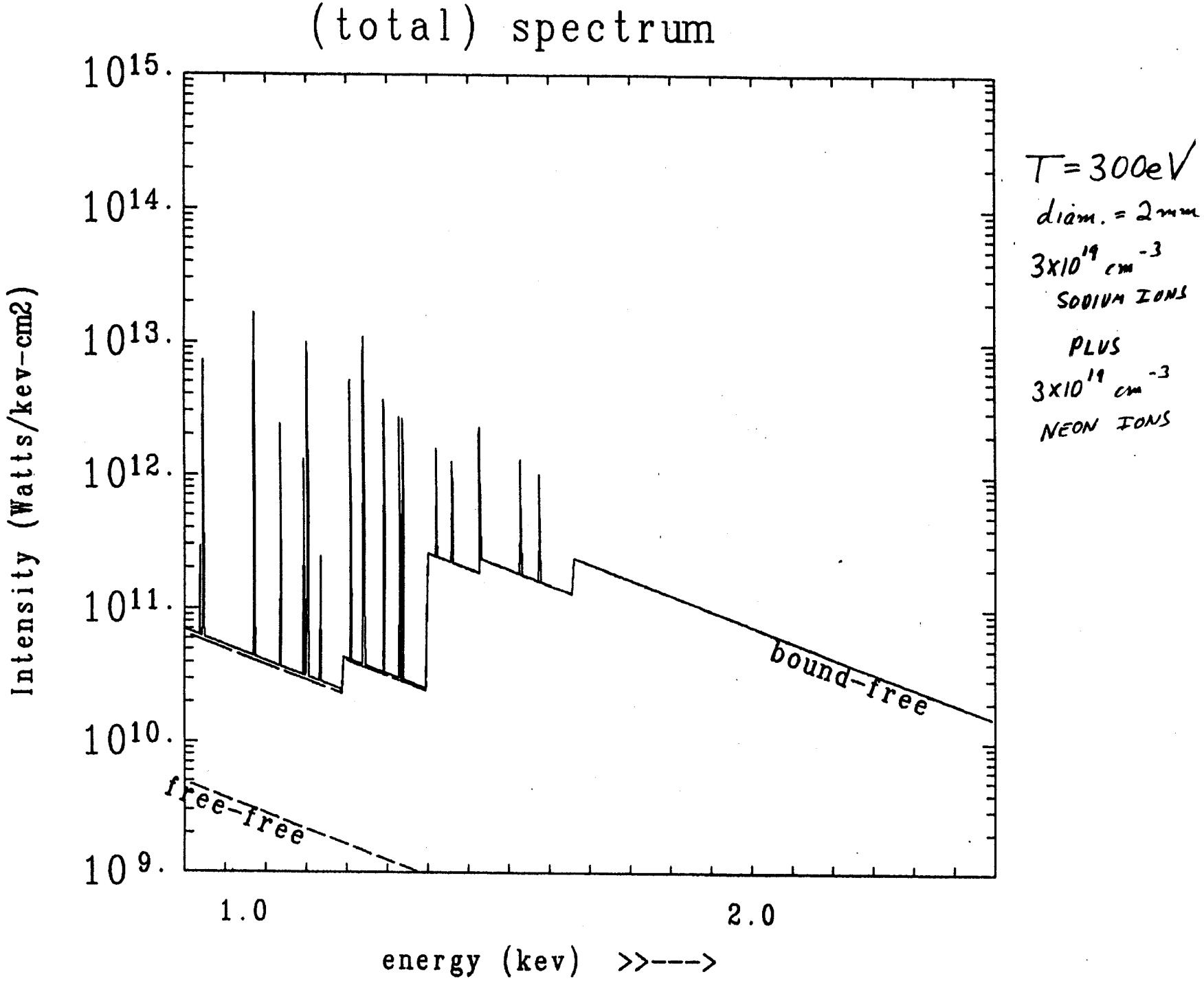

T = 300eV
diam. = 2mm
3×10^{19} cm^{-3}
SODIUM IONS
PLUS
3×10^{19} cm^{-3}
NEON IONS

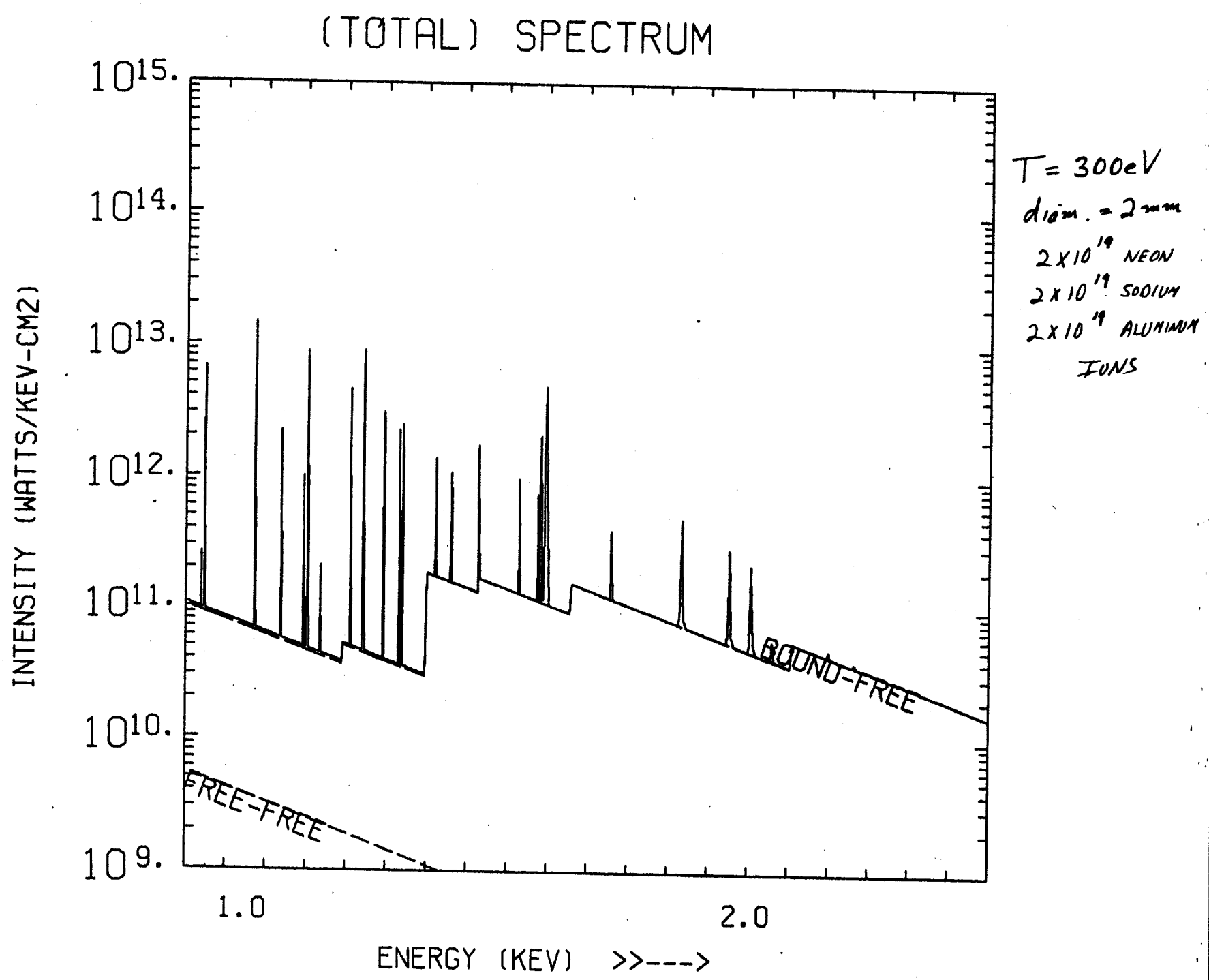
(TOTAL) SPECTRUM
INTENSITY (WATTS/KEV-CM2)
10^15.
10^14.
10^13.
10^12.
10^11.
10^10.
10^9.
1.0
2.0
ENERGY (KEV) >>--->
BOUND-FREE
FREE-FREE
T = 300eV
diam. = 2mm
2X10^19 NEON
2X10^19 SODIUM
2X10^19 ALUMINUM
IONS
NEON/SODIUM/ALUM

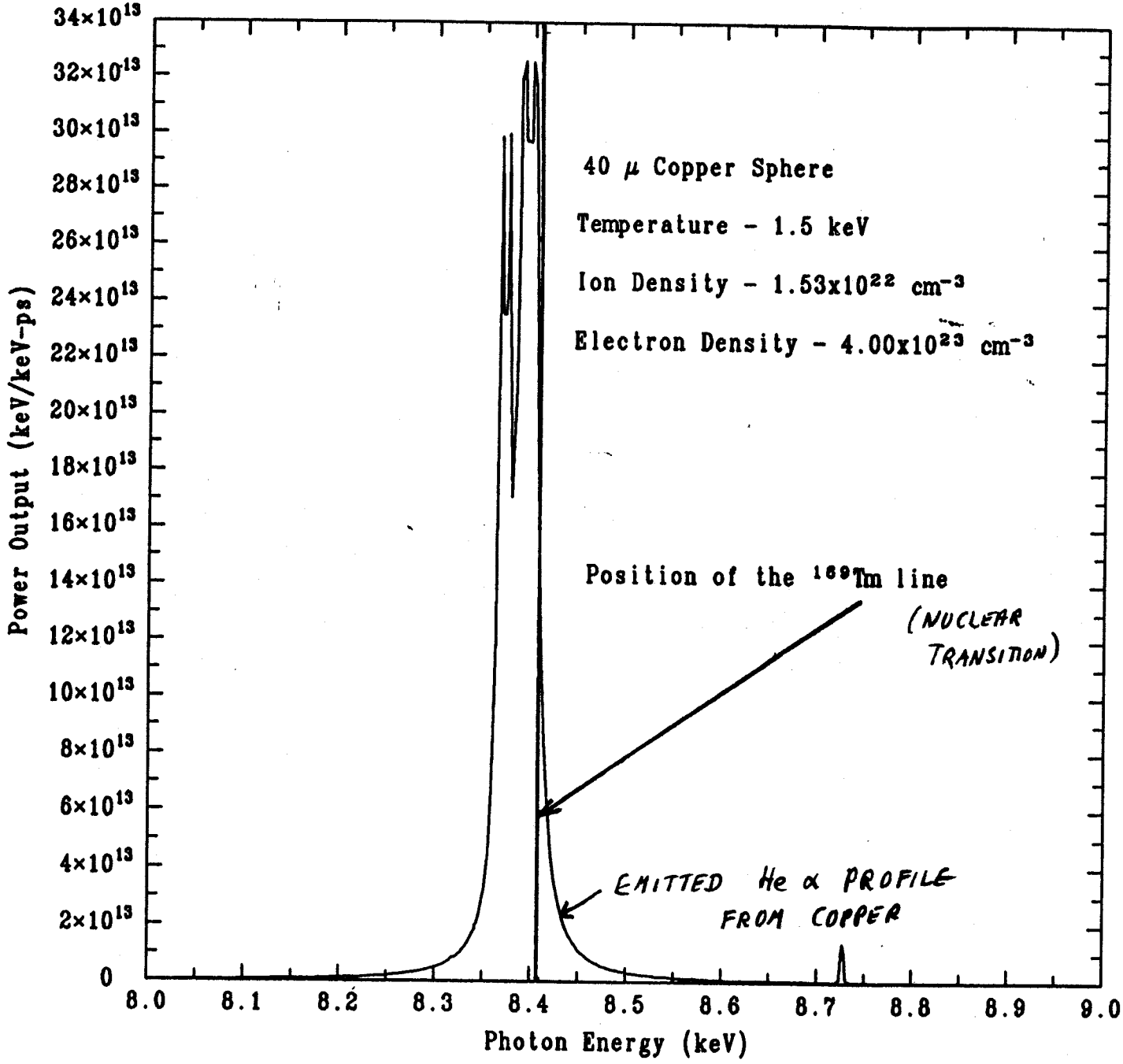
34×10^13
32×10^13
30×10^13
28×10^13
26×10^13
24×10^13
22×10^13
20×10^13
18×10^13
16×10^13
14×10^13
12×10^13
10×10^13
8×10^13
6×10^13
4×10^13
2×10^13
0
Power Output (keV/keV-ps)
8.0
8.1
8.2
8.3
8.4
8.5
8.6
8.7
8.8
8.9
9.0
Photon Energy (keV)
40 μ Copper Sphere
Temperature - 1.5 keV
Ion Density - 1.53x10^22 cm^-3
Electron Density - 4.00x10^23 cm^-3
Position of the 169Tm line
(NUCLEAR TRANSITION)
EMITTED He α PROFILE FROM COPPER

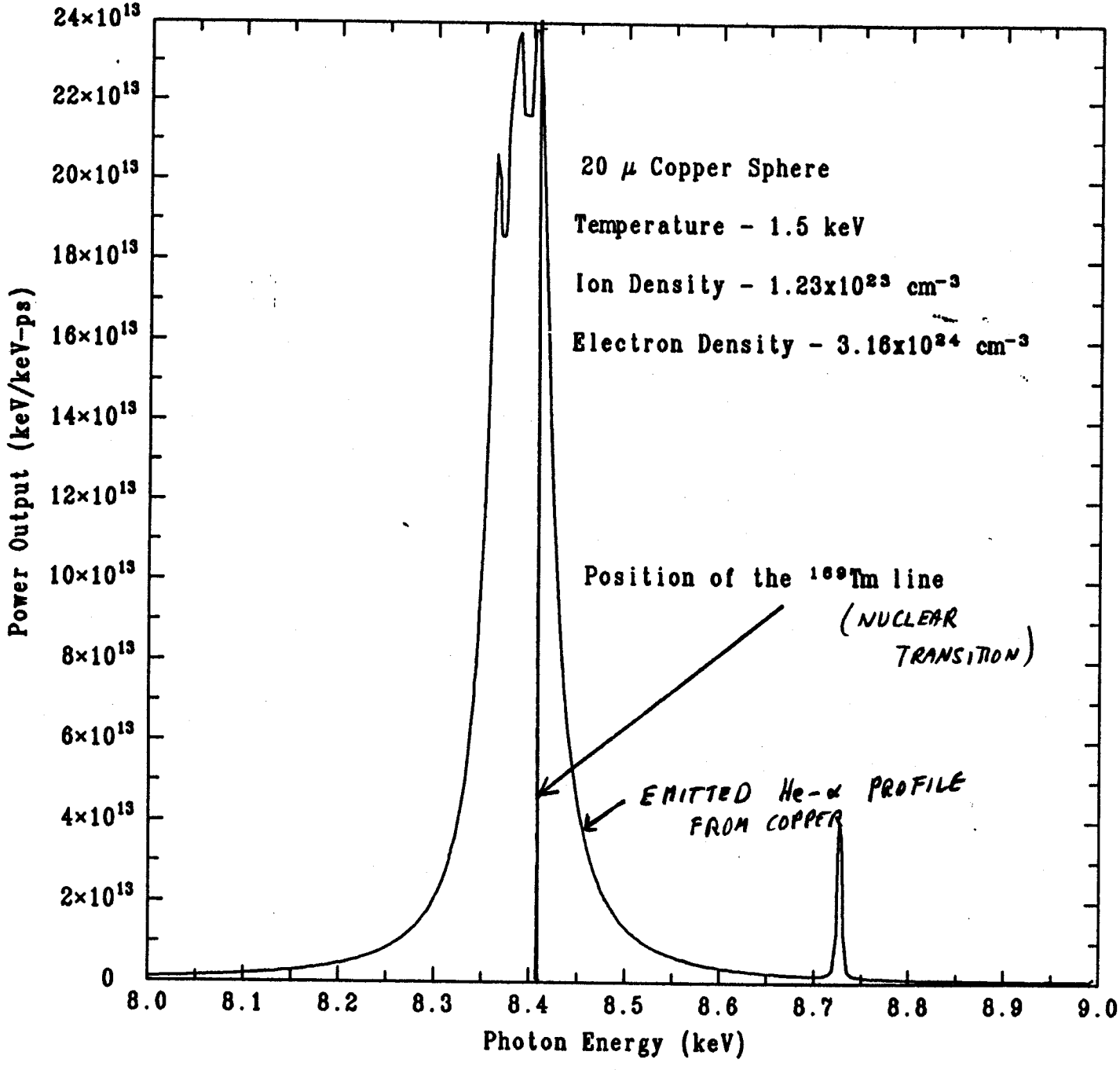
24×10^13
22×10^13
20×10^13
18×10^13
16×10^13
14×10^13
12×10^13
10×10^13
8×10^13
6×10^13
4×10^13
2×10^13
0
Power Output (keV/keV-ps)
8.0
8.1
8.2
8.3
8.4
8.5
8.6
8.7
8.8
8.9
9.0
Photon Energy (keV)
20 μ Copper Sphere
Temperature - 1.5 keV
Ion Density - 1.23x10^23 cm^-3
Electron Density - 3.16x10^24 cm^-3
Position of the 169Tm line
(NUCLEAR TRANSITION)
EMITTED He-α PROFILE FROM COPPER